



# Charge Carrier Recombination and Open Circuit Voltage in Organic Solar Cells: From Bilayer-Model Systems to Hybrid Multi-Junctions

## Dissertation

zur Erlangung des akademischen Grades  
*doctor rerum naturalium* (Dr. rer. nat.)  
in der Wissenschaftsdisziplin Experimentalphysik

Eingereicht an der  
Mathematisch-Naturwissenschaftlichen Fakultät  
der Universität Potsdam

von

**Steffen Roland**

Berlin, im Februar 2017

Published online at the  
Institutional Repository of the University of Potsdam:  
URN urn:nbn:de:kobv:517-opus4-397721  
<http://nbn-resolving.de/urn:nbn:de:kobv:517-opus4-397721>

# Abstract

Tremendous progress in the development of thin film solar cell techniques has been made over the last decade. The field of organic solar cells is constantly developing, new material classes like Perovskite solar cells are emerging and different types of hybrid organic/inorganic material combinations are being investigated for their physical properties and their applicability in thin film electronics. Besides typical single-junction architectures for solar cells, multi-junction concepts are also being investigated as they enable the overcoming of theoretical limitations of a single-junction. In multi-junction devices each sub-cell operates in different wavelength regimes and should exhibit optimized band-gap energies. It is exactly this tunability of the band-gap energy that renders organic solar cell materials interesting candidates for multi-junction applications. Nevertheless, only few attempts have been made to combine inorganic and organic solar cells in series connected multi-junction architectures. Even though a great diversity of organic solar cells exists nowadays, their *open circuit voltage* is usually low compared to the band-gap of the active layer. Hence, organic low band-gap solar cells in particular show low *open circuit voltages* and the key factors that determine the voltage losses are not yet fully understood. Besides *open circuit voltage* losses the recombination of charges in organic solar cells is also a prevailing research topic, especially with respect to the influence of trap states.

The exploratory focus of this work is therefore set, on the one hand, on the development of hybrid organic/inorganic multi-junctions and, on the other hand, on gaining a deeper understanding of the *open circuit voltage* and the recombination processes of organic solar cells.

In the first part of this thesis, the development of a hybrid organic/inorganic triple-junction will be discussed which showed at that time (Jan. 2015) a record power conversion efficiency of 11.7%. The inorganic sub-cells of these devices consist of hydrogenated amorphous silicon and were delivered by the Competence Center Thin-Film and Nanotechnology for Photovoltaics in Berlin. Different recombination contacts and organic sub-cells were tested in conjunction with these inorganic sub-cells on the basis of optical modeling predictions for the optimal layer thicknesses to finally reach record efficiencies for this type of solar cells.

In the second part, organic model systems will be investigated to gain a better understanding of the fundamental loss mechanisms that limit the *open circuit voltage* of organic solar cells. First, bilayer systems with different orientation of the donor and acceptor molecules were

---

investigated to study the influence of the donor/acceptor orientation on non-radiative voltage loss. Secondly, three different bulk heterojunction solar cells all comprising the same amount of fluorination and the same polymer backbone in the donor component were examined to study the influence of long range electrostatics on the *open circuit voltage*. Thirdly, the device performance of two bulk heterojunction solar cells was compared which consisted of the same donor polymer but used different fullerene acceptor molecules. By this means, the influence of changing the energetics of the acceptor component on the *open circuit voltage* was investigated and a full analysis of the charge carrier dynamics was presented to unravel the reasons for the worse performance of the solar cell with the higher *open circuit voltage*. In the third part, a new recombination model for organic solar cells will be introduced and its applicability shown for a typical low band-gap cell. This model sheds new light on the recombination process in organic solar cells in a broader context as it re-evaluates the recombination pathway of charge carriers in devices which show the presence of trap states. Thereby it addresses a current research topic and helps to resolve alleged discrepancies which can arise from the interpretation of data derived by different measurement techniques.

# Zusammenfassung

In der Photovoltaikforschung spielen neuartige Dünnschichtsolarzellen eine immer größere Rolle. Neben innovativen Design und Anwendungskonzepten sind Material und Kostenreduzierung in der Herstellung die größten Triebfedern für die Entwicklung neuer Technologien. Hier sind neben den vielversprechenden Perowskitsolarzellen insbesondere organische Solarzellen zu nennen, die sich durch ihre chemische Vielseitigkeit, einfache Verarbeitung und stetige Weiterentwicklung in Bezug auf ihre Effizienz auszeichnen. Diese Vielseitigkeit ermöglicht die Herstellung organischer Solarzellen mit unterschiedlicher spektraler Empfindlichkeit, was wiederum Vorteile für den Einsatz in seriengeschaltete Mehrschichtsolarzellen bietet. Diese erlauben es, fundamentale Limitierungen von Einschichtsolarzellensystemen zu überwinden.

Der erste Teil dieser Arbeit befasst sich daher mit der Entwicklung einer neuartigen hybriden Multischichtsolarzelle, die sowohl aus anorganischen als auch organischen Subzellen besteht und zum Zeitpunkt ihrer Veröffentlichung einen neuen Effizienzrekord für diese Klasse von Solarzellen aufzeigte. Der zweite Teil der Arbeit befasst sich mit fundamentalen physikalischen Prozessen in organischen Solarzellen, da viele Funktionsmechanismen noch nicht im Detail geklärt sind. An verschiedenen organischen Modellsolarzellensystemen wurde daher unter anderem der Einfluss molekularer Orientierung von Donor- und Akzeptorkomponenten der Solarzelle oder der Einfluss von Fluorinierung des Donors auf die Leerlaufspannung der Solarzelle untersucht. Auf diese Weise konnten neue wichtige Erkenntnisse über den Einfluss von verschiedenen Verlustkanälen und der Energetik auf die Leerlaufspannung gewonnen werden. Der letzte Teil der Arbeit widmet sich der Entwicklung eines neuen Modells, welches den Rekombinationsprozess von Ladungen in einer bestimmten organischen Solarzelle beschreibt. Dieses neue Modell wurde anhand umfangreicher Experimente validiert und ermöglicht es, insbesondere den Einfluss freier und in sogenannten Fallenzuständen gefangener Ladungen auf die Rekombination zu trennen. Damit hat dieses Modell eine weitreichende Bedeutung, zum einen für die Beurteilung von typischen Rekombinationsexperimenten in organischen Solarzellen und zum anderen für die Bewertung des Einflusses von Fallenzuständen auf den Rekombinationsstrom.

# Contents

<b>1. Introduction</b>	<b>1</b>
<b>2. Fundamental Concepts of Organic and Multi-Junction Solar Cells</b>	<b>5</b>
2.1. Organic Semiconductors . . . . .	5
2.2. Organic Solar Cells . . . . .	6
2.3. Fundamental Solar Cell Characterization . . . . .	9
2.3.1. Power Conversion Efficiency . . . . .	9
2.3.2. Photovoltaic External Quantum Efficiency . . . . .	9
2.4. Shockley-Queisser Limit . . . . .	10
2.5. Series Connected Multi-Junction . . . . .	11
<b>3. Open Circuit Voltage and Recombination of Charges</b>	<b>13</b>
3.1. Open Circuit Voltage . . . . .	13
3.2. Non-Geminate Recombination of Charges and Effective Bimolecular Recombination . . . . .	17
<b>4. Experimental Methods</b>	<b>27</b>
4.1. Current Voltage Characteristics . . . . .	27
4.2. Photovoltaic External Quantum Efficiency Measurement . . . . .	28
4.3. External Quantum Efficiency of the Electroluminescence . . . . .	28
4.4. Time Delayed Collection Field . . . . .	29
4.5. Bias Assisted Charge Extraction . . . . .	30
<b>5. Hybrid Triple-Junction Solar Cells</b>	<b>32</b>
5.1. The Hybrid Concept. Advantages of Combining Inorganic and Organic Sub-Cells	32
5.2. Hybrid Triple-Junction Device Structure . . . . .	33
5.3. Optical Modeling of the Photocurrent in a Multi-Junction Solar Cell. . . . .	36
5.4. Optimization of Hybrid Multi-Junctions . . . . .	38
5.5. Discussion and Outlook . . . . .	42
<b>6. Experimental Investigation of the Open Circuit Voltage and Free Charge Carrier Recombination in Organic Solar Cells</b>	<b>44</b>
6.1. Open Circuit Voltage in Bilayer Solar Cells . . . . .	47
6.1.1. Device Structure and Solar Cell Performance . . . . .	47

6.1.2.	The Open Circuit Voltage of p-SIDT(FBTTh <sub>2</sub> ) <sub>2</sub> / C <sub>60</sub> Bilayer Solar Cells	50
6.1.3.	Discussion . . . . .	54
6.2.	Three Methods of Backbone Fluorination and the Effects on Open Circuit Voltage . . . . .	56
6.2.1.	Chemical Structure and Device Preparation . . . . .	56
6.2.2.	Comparisson of Fundamental Photovoltaic Parameters . . . . .	57
6.2.3.	Steady State and Transient Recombination Measurements . . . . .	58
6.2.4.	Open Circuit Voltage and CT Energy . . . . .	62
6.2.5.	Conclusion . . . . .	67
6.3.	Open Circuit Voltage in PCBM or ICBA based Solar Cells . . . . .	68
6.3.1.	Device Structure and Device Performance . . . . .	68
6.3.2.	Open Circuit Voltage in FTAZ:ICBA and FTAZ:PCBM . . . . .	69
6.3.3.	Generation of Free Charge Carriers . . . . .	71
6.3.4.	Recombination and Extraction of Free Charges in FTAZ:ICBA and FTAZ:PCBM Solar Cell . . . . .	72
6.3.5.	Simulation of <i>JV</i> -curves in FTAZ:ICBA and FTAZ:PCBM Solar Cell	75
6.3.6.	Conclusion . . . . .	77
<b>7.</b>	<b>Effective Bimolecular Recombination in PMDPP3T:PCBM Solar Cells</b>	<b>79</b>
7.1.	Energetics and Open Circuit Voltage . . . . .	80
7.2.	Steady State Recombination evaluated from Recombination Current Measurements . . . . .	82
7.3.	Steady State Recombination evaluated from Charge Carrier Density Measurements . . . . .	85
7.4.	Transient Recombination - TDCF . . . . .	90
7.5.	Extraction of Charges - the Effective Mobility . . . . .	95
7.6.	Simulation of the <i>JV</i> -Characteristics for Different Illumination Intensities . .	97
7.7.	Discussion . . . . .	100
<b>8.</b>	<b>Conclusion</b>	<b>103</b>
	<b>Bibliography</b>	<b>107</b>
<b>A.</b>	<b>Appendix Chapter 4</b>	<b>119</b>
A.1.	Calibration Routine for Absolute EL Measurements . . . . .	119
<b>B.</b>	<b>Appendix Chapter 5</b>	<b>121</b>
B.1.	Triple-Junction Layer Stack . . . . .	121
B.2.	Contour Pots of PMDPP3T:PCBM based Triple-Junction . . . . .	123
B.3.	Contour Plots of Si-PCPDTBT:PCBM based Triple-Junctions . . . . .	124
B.4.	SEM pictures of flat or rough a-Si:H tandem . . . . .	125

<b>C. Appendix Chapter 6</b>	<b>126</b>
C.1. Molecular Orientation of p-SIDT(FBTTh <sub>2</sub> ) <sub>2</sub> Films . . . . .	126
C.2. Interfacial Mixing of C <sub>60</sub> into edge-or face-on oriented p-SIDT(FBTTh <sub>2</sub> ) <sub>2</sub> layers	127
C.3. Pinholes in the neat Edge-On oriented p-SIDT(FBTTh <sub>2</sub> ) <sub>2</sub> Layer . . . . .	127
C.4. <i>JV</i> -Characteristics of the Bilayer Devices at UCSB and UP . . . . .	128
C.5. UPS measurements of Edge- or Face-On oriented Films of p-SIDT(FBTTh <sub>2</sub> ) <sub>2</sub> .	130
C.6. Field dependence of Charge Carrier Generation of the Bilayer Systems . . . . .	130
C.7. Electroluminescence and Photovoltaic External Quantum Efficiency Spectra .	132
C.8. CT-Emission of FTAZ:PCBM Solar Cells in Dependence of the Active Layer Thickness . . . . .	132
C.9. Transmission Electron Microscopy of the 50% Blends . . . . .	133
C.10. Photoluminescence measurements of pure FTAZ or FTTPC or FTIC blends . .	133
C.11. SCLC measurements of FTTPC and FTIC devices at UNC . . . . .	134
<b>D. Appendix Chapter 7</b>	<b>135</b>
D.1. Gaussian Fits of the External Quantum Efficiency Spectra of the PMDPP3T:PCBM Solar Cell . . . . .	135
D.2. Uncertainty in the Determination of the Absolute $EQE_{EL}$ . . . . .	135
D.3. Differentially Determined Light Ideality Factor for the PMDPP3T:PCBM So- lar Cell . . . . .	136
D.4. Trapped Charge Carrier Density . . . . .	137
<b>Publications</b>	<b>139</b>
<b>Danksagung</b>	<b>142</b>
<b>Eigenständigkeitserklärung</b>	<b>144</b>

# Chapter 1

## Introduction

The sun is a unique, reliable power source - at least for the next few billion years - capable of covering the increasing energy demands of mankind. Unfortunately, solar radiation is not equally accessible on earth, neither temporally nor locally, and energy storage is fundamentally connected to photovoltaics in terms of reliably providing access to electricity. In recent years tremendous progress in battery technology has been made, also driven by the emerging e-mobility economy. Furthermore, the infrastructure of power grids is changing to embrace the versatile renewable energy technologies contributing to the power supply, shifting the focus from large power plants to more delocalized energy supply. This large flexibility also enables different types of photovoltaic devices to become more and more important. Thin film solar cells are especially promising due to potential mechanical and processing advantages compared to conventional silicon wafer cells. Thin film cells with a maximum thickness of only a few micrometers can, e.g., be produced on flexible substrates in roll to roll processing. Integration of solar cells in facades or windows of buildings is gaining more and more interest, especially as semi-transparent applications can be realized and energetic amortization of thin film cells is in general achieved much faster than for conventional silicon wafer cells.[1]

Nowadays only a few thin film technologies are established on the market as e.g. cadmium-telluride (CdTe), copper-indium-gallium-selenide (CIGS) and hydrogenated amorphous or micro-crystalline silicon (a-Si:H/ $\mu$ c-Si:H). These examples are all based on inorganic material combinations and are all build up as p/n or p/i/n junctions. The last example of an a-Si:H/ $\mu$ c-Si:H solar cell introduces the concept of a multi-junction, here two solar cells with different band-gap energies are series connected to absorb efficiently over the whole spectral range of the sun. At the same time thermalization losses can be reduced in such a solar cell architecture. Unfortunately, although established for many years, in a-Si:H/ $\mu$ c-Si:H multi-junction solar cells, especially the deposition of the  $\mu$ c-Si:H layer is time consuming.

$\mu\text{c-Si:H}$  is an indirect semiconductor and relatively thick layers are needed to realize efficient absorption, while at the same time growth rates for  $\mu\text{c-Si:H}$  layer deposition are low in a typical plasma enhanced chemical vapor deposition (PECVD). Exchanging this  $\mu\text{c-Si:H}$  layer with an organic solar cell, that can, e.g., be processed from solution, was suggested to circumvent these processing limitations. Several examples of such hybrid multi-junctions already exist, but high efficiencies could not be realized so far.[2–4] Therefore, the exploratory focus of this work is, on the one hand, to improve hybrid multi-junctions with suitable low band-gap organic solar cells and, on the other hand, to gain a better understanding of these low band-gap cells in general. The idea of exchanging the  $\mu\text{c-Si:H}$  cell in a a-Si:H/ $\mu\text{c-Si:H}$  multi-junction with an organic solar cell requires the organic cell to absorb efficiently in the near infrared (NIR) spectral region. At the same time a low band-gap impedes reaching high *open circuit voltage* ( $V_{OC}$ ) which is directly related to the efficiency of a solar cell.

*The first part of this thesis* describes the development of efficient hybrid multi-junction solar cells, comprising two a-Si:H sub-cells and one low band-gap organic solar cell. Two low band-gap materials were tested in the organic sub-cell. Optical modeling was applied to predict best layer thicknesses in these multilayer systems. Intermediate transparent recombination layers were optimized. External quantum efficiency measurements (EQE) with sufficient background illumination were realized to probe the generated currents in each sub-cell and finally light scattering was introduced to increase the absorption in especially the a-Si:H sub-cells. Finally, efficient hybrid multi-junctions are presented, reaching *power conversion efficiencies* (PCE) of above 11%. This PCE set a new record for this type of hybrid cells at that time (Jan. 2015).[5]

*In the second part of this thesis* fundamental properties of organic solar cells, especially the *open circuit voltage*, will be discussed based on the findings of different model systems. Particular attention is paid to the *open circuit voltage* as in organic solar cells energetic losses, with respect to the band-gap of the photoactive material, are large compared to other solar cell techniques.

In Figure 1.1 a) typical values of the band-gap energy and *open circuit voltage* are depicted for common solar cell techniques. The values are extracted from Green et al. and Zhao et al. for the organic solar cell reference considering an efficient organic solar cell with a power conversion efficiency of about 11%.[6, 7] In Figure 1.1 b) the energetic losses between band-gap energy and actual open circuit voltage are depicted and it becomes clear that even the most efficient organic and a-Si:H solar cells suffer from significant potential losses compared to, e.g., gallium-arsenide (GaAs). Especially for organic solar cells the reasons for these losses are not yet fully understood and predictions of *open circuit voltages* are often based on empirical relationships.[8]

To gain a better understanding of the *open circuit voltage* and apparent potential losses different organic solar cell systems were studied in the course of this thesis. At first two bilayer

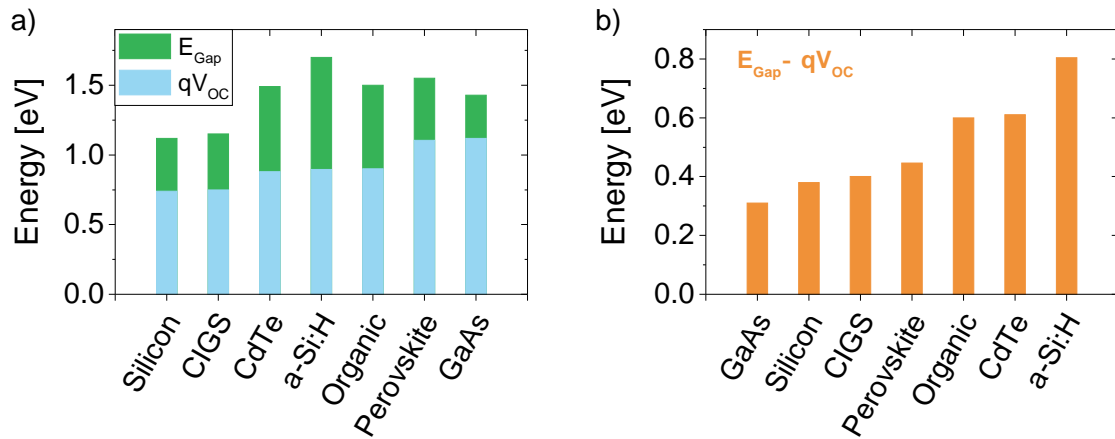


**Figure 1.1.:** a) Band-gap energies and open circuit voltages of typical solar cell technologies. The data represent examples of today's most efficient systems and are extracted from Green et al. and Zhao et al. for the organic solar cell.[6, 7] b) The potential loss between the band-gap energy and the open circuit voltage data shown in a) is depicted from low to high losses for the compared solar cell techniques.

solar cells will be discussed, that are based on the same donor/acceptor material combination, but differ in the orientation of their donor molecules at the interface to the acceptor. This architecture allowed one to study orientation effects on the *open circuit voltage* and especially on the non-radiative loss of charges. Secondly, measurement results of three different solar cell systems, which all incorporate the same amount of fluorine atoms attached to the donor polymer back-bones will be presented. All three systems use the same fullerene acceptor molecule and the basic structure of the donor polymer is also not changed. The difference of the three systems arises from the way fluorine atoms are incorporated. This has been achieved in three fashions: Chains of fully fluorinated polymer in which each monomer contains two fluorine atoms is physically mixed with non-fluorinated chains, chains are synthesized in which fluorinated and non fluorinated monomers are coupled in an alternating fashion, or every monomer unit only contains one fluorine atom. Incorporating fluorine instead of hydrogen is known to alter the energetics of organic materials and with that it has a direct influence on the *open circuit voltage*. [9–13] The way of how the fluorine affects the *open circuit voltage* is investigated, focusing on the question if the direct donor/acceptor interaction or rather long range electrostatic effects dominate. Furthermore, the effect on *open circuit voltage* of altering the energetics of the acceptor molecule by exchanging the fullerene derivative with a higher adduct fullerene derivative in a bulk heterojunction (BHJ) architecture will be addressed. The change in *open circuit voltage* by exchanging the acceptor was carefully investigated and the recombination mechanisms of these two different systems were measured. By studying the recombination mechanism of charge carriers in these devices the origin of the voltage losses with respect to the band-gaps of the respective systems were determined. Furthermore, the *fill factor* changes of both systems were investigated and simulations of the current-voltage

characteristics were conducted revealing the accuracy of the applied measurement methods and models.

*In the third part of this thesis* the organic sub-cell of the best performing triple-junction is discussed with respect to its *open circuit voltage* and its recombination mechanism. A new way of understanding the recombination in certain organic solar cells is presented with the intention of shedding light on the ongoing debate about the influence of trap-assisted vs. free charge carrier recombination as the dominant recombination mechanism in organic solar cells.[14, 15] These findings are made possible by comprehensive studies of the steady state and time dependent recombination behavior, as well as the application of a new model describing the possible recombination pathways in the presence of charge carrier traps.

# Chapter 2

## Fundamental Concepts of Organic and Multi-Junction Solar Cells

To introduce the concept of organic semiconductors, a brief excerpt of historical milestones, paving the way for efficient organic solar cells, is given. There was a large research interest in molecular crystals in the 1960s through the 1980s. For example, in 1963 Pope et al. were able to show electroluminescence from an anthracene crystal.[16] The concept of doping organic  $\pi$ -conjugated systems to increase the conductivity by MacDiarmid, Shirakawa and Heeger presented in the late 1970s was another important development in this field.[17] Their finding was ultimately rewarded with the Nobel Prize in Chemistry in 2000. A milestone in the development of organic solar cells (OSC) was the bilayer cell comprising of a donor and an acceptor organic compound, introduced by Tang in 1986.[18] Herein, the concept of a donor/acceptor interface with different energetics of the molecular orbitals to facilitate efficient singlet exciton splitting is introduced. In 1995 Friend et al. and Heeger et al. processed organic photodiodes with an active layer consisting of a donor/acceptor blend with an increased donor/acceptor interface.[19, 20] By this means the generated photocurrent could be increased significantly. Up to day the concept of a donor/acceptor blend is still the most promising approach in producing efficient OSCs and most progress in recent years is based on the development of new donor and acceptor materials.

### 2.1. Organic Semiconductors

Semiconducting properties of inorganic materials are based on their crystalline structure. However, in organic materials, as used in organic electronics, the model of a periodic lattice

fails as many organic materials show amorphous or semi crystalline morphologies. Semiconducting properties in organic materials are based on the nature of the chemical carbon bonds. In chains and rings of  $sp$  and  $sp^2$  hybridized carbon atoms, the unhybridized p-orbitals form bonding  $\pi$  and anti-bonding  $\pi^*$  molecular orbitals, whereas the hybridized s and p-orbitals form so called  $\sigma$  and  $\sigma^*$  molecular orbitals. The electrons in the  $\pi$  orbitals are delocalized that means they cannot be explicitly assigned to a certain atom or bond anymore. The electrons are somewhat free to move along the conjugated segment. One approach to approximate the energy of the molecular orbitals is the *linear combination of atomic orbitals* (LCAO). The electron wave functions of the participating atomic orbitals will interfere positively or negatively, when they are linearly combined, leading to enhanced or reduced electron densities in the formed molecular orbitals. This establishes molecular orbitals with binding or anti-binding character and with lower or higher energy, respectively. If the molecular orbitals are filled with the valence electrons, the *highest occupied molecular orbital* (HOMO) and the *lowest unoccupied molecular orbital* (LUMO) are of major importance as the energetic difference between them defines the band-gap. The band-gap decreases with increasing conjugation lengths. Conjugation in a polymer chain is unlikely to be preserved over the whole lengths of the chain as the polymer tends to coil up and kinks or defects in the chain will distort the conjugation (each conjugated segment is also referred to as chromophore). This introduces several conjugation lengths in one system and concomitant a distribution of energies for the binding and anti-binding molecular orbitals and the band-gap energies. Furthermore, the energetics are influenced by inter- and intramolecular interactions. This results in statistically distributed energy levels energetically close to each other, creating an inhomogeneously broadened density of states distribution.

## 2.2. Organic Solar Cells

Today's efficient organic solar cells are built up of a blend of so called donor and acceptor materials. This fundamental concept of a bulk heterojunction solar cell is based on the nature of excitons formed by light absorption in typical organic materials. The relative permittivity in organic semiconducting materials is low compared to the permittivity in inorganic semiconductors, which is caused by less screened electron – electron interaction in organics.[21] This leads to a larger coulomb attraction between electron and hole in an organic semiconductor compared to inorganic ones. The exciton binding energy in organic semiconductors is in the range of a few hundred millivolts. To split these excitons the implementation of donor/acceptor interfaces is crucial. In Figure 2.1 all the essential steps of generation and extraction of free charge carriers in a bulk heterojunction solar cell are sketched. The donor material is defined as the material with the higher lying LUMO energy, the acceptor as the material with the lower lying LUMO energy, respectively. If the energetic difference between the LUMO or HOMO levels of the donor and acceptor exceeds the exciton binding energy,

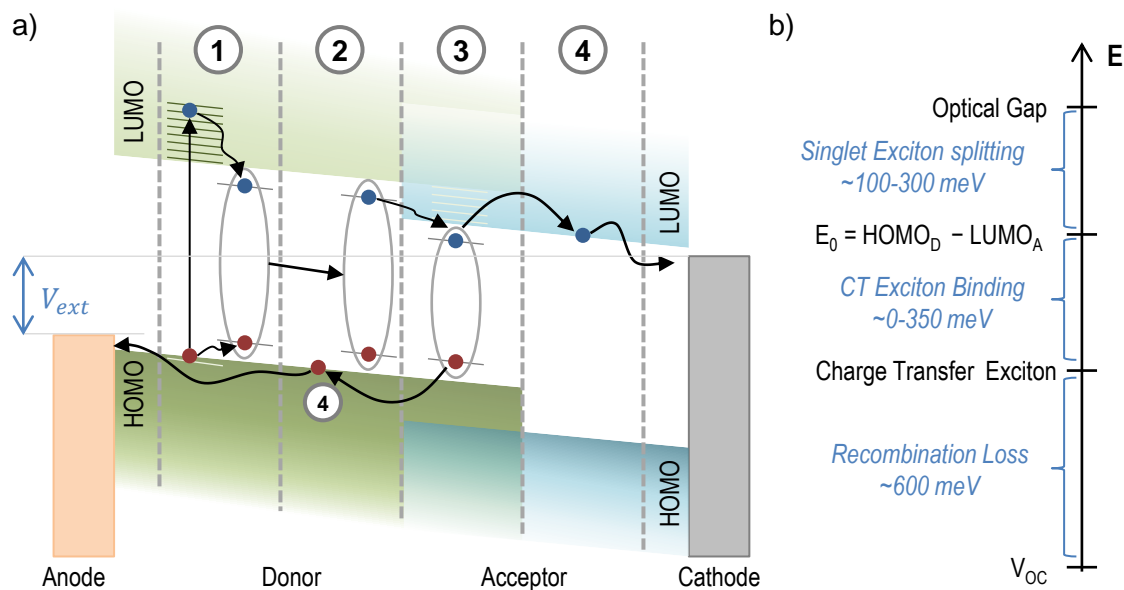


**Figure 2.1.:** a) Energy diagram scheme describing the fundamental steps in the generation and extraction of free charges in OSCs. The process is sketched for an initial excitation of the donor material but is valid for the excitation of the acceptor as well. 1) Upon absorption of a photon with energy larger than the optical band-gap of donor or acceptor an electron is excited from its ground state to an vibronic level of an excited state, depending on the excitation energy. The electron will lower its energy by thermalization and Coulomb binding to the hole it left behind. By this means a coulombically bound exciton is formed. 2) This exciton moves diffusively and potentially reaches an acceptor interface 3), where the electron energy can be lowered by going over to the acceptor LUMO and thus splitting the exciton. The electron on the acceptor LUMO and the hole on the donor HOMO are then forming a CT-state still being bound coulombically. This potentially lowers the energy of the CT-state below the energy of the CS-state, the latter being the difference between donor HOMO and acceptor LUMO. This CT-state can split up into free charges, that then move through the bulk at an applied external voltage ( $V_{ext}$ ) 4) before they get extracted at the electrodes. All these processes are competing with potential recombination of the electron with a hole. In b) typical values for the energetic losses are denoted which finally limit the  $V_{OC}$  in OSC.

the exciton – located on the donor or acceptor material – can potentially be split up into a hole, located in the donor HOMO, and an electron in the acceptor LUMO. This splitting of excitons requires the exciton to be close to a donor/acceptor interface as the exciton itself can not be driven by an electric field and needs to diffuse to the interface in the time span of its lifetime. Otherwise the excitation will be lost to recombination; referred to as *geminate* recombination if the electron and hole originate from the same excitation event.

Prior to the dissociation of the exciton into a free hole located in the donor HOMO and an electron in the acceptor LUMO, called the *charge separated state* (CS-state), a *charge transfer state* (CT-state) is formed. The CT-state is formed by an electron in the acceptor LUMO and a hole in the donor HOMO that are bound by Coulomb attraction. The CT-

state energy ( $E_{CT}$ ) is lower than the CS-state energy ( $E_{CS}$ ) by the Coulomb binding energy. The CT-state can be formed in different ways. A singlet exciton on the donor or acceptor that reaches the interface can form the CT-state exciton by transferring the electron or hole to the acceptor LUMO or donor HOMO, respectively, or two free charge carriers in their respective molecular orbitals get bound by their mutual Coulomb attraction forming a CT-exciton if they are spatially close to each other. Furthermore, the CT-state can directly be excited by photons of appropriate energy, although the coupling to the ground state is usually low and thus the absorption of the CT-state is very weak. In Figure 2.1 only the first of the mentioned processes is sketched, with the initial exciton created on the donor domain (denoted in the figure as process 1) and diffuses to the interface (2) where it forms a CT-exciton (3). This CT-exciton is subsequently split into free charges (4). The initial exciton on either donor or acceptor and also the CT-exciton can have a "hot" character, meaning that they are not in their respective ground state. This implies for an exciton on either donor or acceptor that its diffusion lengths is increased and that the likelihood of reaching the interface is increased. For the CT-exciton a beneficial effect of a "hot" CT-exciton for the generation of free charge carriers is reported by measuring increased photovoltaic internal quantum efficiencies for such "hot" CT-state excitations.[22] Furthermore, ultrafast pump-probe experiments have indicated that free charges can be probed on timescales  $< 100$  fs,[22, 23] promoting a so called "hot" process. Either free charges are directly formed from the excited singlet states of the donor or acceptor or the initial excitation of higher lying singlet states results in "hot" CT-states effectively promoting the generation of free polarons.[22] In contradiction to such a "hot" mechanism, it was found for several systems that excess energy does not yield a higher generation efficiency than what is measured upon direct excitation of relaxed CT-states.[24, 25] Furthermore, a correlation between the generation efficiency of free charges and the difference between relaxed CT-state and CS-state energy is found.[25] Although "hot" processes can be found, their overall contribution to the exciton splitting is of minor importance in typical OSCs. The relaxed CT-state was shown to be the important precursor state in understanding the pathway of generation of free charges in OSCs.[24–26] The CT-state might however recombine before dissociation. If the CT-state was formed by charge carrier pair of a mutual excitation event, e.g. by a singlet exciton on the donor domain that transfers its electron to the acceptor, then the recombination of the CT-state is referred to as *geminate*. Otherwise, if additionally free charges, that are in the donor and acceptor domain, form CT-states and recombine before they can be extracted at the contacts, this recombination process is referred to as *non-geminate* and will be discussed in section 3.2 to greater detail. The overall performance of the solar cell is furthermore influenced by the extraction of the free charges, which is competing with the *non-geminate* recombination. How well a hole or electron can be transported on the donor or acceptor, can be expressed by hole or electron mobilities ( $\mu_h$  and  $\mu_e$ ). These mobilities depend, amongst other, also on the morphology of the material and especially organic blend systems show very complex morphologies with crystalline and amorphous regions. Hence, charge transport

is often described best by a thermally activated hopping process between energetically and spatially distributed sites.[27]

## 2.3. Fundamental Solar Cell Characterization

### 2.3.1. Power Conversion Efficiency

The *power conversion efficiency* ( $PCE$ ) of a solar cell is determined by the ratio of the electric power output of the cell to the radiative input power. The voltage at which the measured current is zero is defined as the *open circuit voltage* ( $V_{OC}$ ), the current density measured at zero volt is called the *short circuit current density* ( $J_{SC}$ ). The *maximum power point* ( $MPP$ ) is defined as the voltage and corresponding current density for which the electrical output power is maximal. The voltage and current density are defined as  $V_{MPP}$  and  $J_{MPP}$ , respectively. The *fill factor* ( $FF$ ) is defined as the ratio of the maximum electrical power and the product of  $V_{OC}$  and  $J_{SC}$ :

$$FF = \frac{V_{MPP} \cdot J_{MPP}}{V_{OC} \cdot J_{SC}}. \quad (2.1)$$

Although the  $FF$  is easily measured, the fundamental processes which determine it are rather complex as it depends on the charge carrier transport and the recombination of charges. With the intensity of the sun simulator  $Int_{in}$  the  $PCE$  is determined by:

$$PCE = \frac{J_{SC} \cdot V_{OC} \cdot FF}{Int_{in}}. \quad (2.2)$$

### 2.3.2. Photovoltaic External Quantum Efficiency

The *photovoltaic external quantum efficiency* ( $EQE_{PV}$ ) is defined as the ratio of incident photons to extracted electrons. The  $EQE_{PV}$  depends on the energy  $E$  of the incident photons and can be split up in several factors  $\eta$  depending on the efficiency of absorption in the active layer (abs), exciton diffusion(ED), charge transfer between donor and acceptor (CT) and extraction of free charges (CE).

$$EQE_{PV}(E) = \eta_{abs}(E) \cdot \eta_{ED} \cdot \eta_{CT} \cdot \eta_{CE} = \eta_{abs} \cdot IQE \quad (2.3)$$

The last three factors can be summed up in the *internal quantum efficiency* ( $IQE$ ). The  $EQE_{PV}$  is of major importance as it allows one to calculate the *short circuit current* ( $J_{SC}$ ) of a solar cell for illumination with known photon flux  $\phi(E)$ , assuming the  $EQE_{PV}$  is determined

without an external electric field applied ( $V = 0$ , short circuit conditions).

$$J_{SC} = q \int EQE_{PV}(E) \cdot \phi(E) dE. \quad (2.4)$$

## 2.4. Shockley-Queisser Limit

In order to approach the limitations of solar cells in a more general way and to motivate the concept of series connected multi-junction solar cells, the key ideas of Shockley and Queisser, to calculate the upper efficiency limit of a solar cell, presented in 1961, are discussed.[28] The idea is based on the assumption of *detailed balance* between absorption with subsequent generation of an electron-hole pair and radiative emission of recombining electron-hole pairs. The basic assumptions made by Shockley and Queisser are:

1. Photons with an energy larger than the band-gap ( $E_1 > E_G$ ) of the material are perfectly absorbed and create charge carriers that are extracted. There is no absorption of photons with an energy smaller than the band-gap ( $E_2 < E_G$ ).
2. All photons with an energy  $E_1 > E_G$  have exactly the same effect as photons with an energy  $E_G$ .
3. All recombination is radiative.

This implies on the one hand that the lower the band-gap energy of the material is, the more photons can be absorbed and potentially higher  $J_{SC}$  yields are possible. On the other hand a small band-gap energy directly results in larger thermalization losses. This trade-off of higher potential energy, resulting in a higher  $V_{OC}$  with increasing band-gap and simultaneous decrease of photogenerated current results in an ideal band-gap energy close to 1.1 eV for a single absorber material. In that case, with the cell at a temperature of 0 K and surrounded by a black-body emitter at sun temperature, the maximum power conversion efficiency would reach almost 45%. In a less idealized description with a planar cell at room temperature and the light incident from a small solid angle element, corresponding to the solid angle element the sun appears at in its distance to earth under an azimuthal angle of incidence (AM 1.5G conditions), Shockley and Queisser calculated the upper limit for a single junction solar cell to be about 32%. [28] In an organic solar cell with donor and acceptor the effective band-gap is not determined just by the band-gap of one component, but an additional potential loss due to the exciton splitting at the donor/acceptor interface has to be accepted. The efficiency limit for an organic single-junction, based on a donor and acceptor, is about 11% for a donor band-gap of 1.5 eV and a LUMO offset between donor and acceptor of 0.3 eV. [29] The assumptions made in that work were rather conservative and partially based on empirical findings concerning  $V_{OC}$ ; today's champion devices already have reached efficiencies of about 11%. [7, 30] The lack of a valid Shockley-Queisser type limit for organic solar cells is mainly

due to limits of fundamentally understanding of what exactly determines the  $V_{OC}$  of such donor/acceptor type solar cells. Especially, the role of non-radiative voltage losses needs to be mentioned and to what extent they can be avoided. To partially circumvent the aforementioned trade-off, series connected multi-junctions can be used.

## 2.5. Series Connected Multi-Junction

In the previous section the trade-off between high achievable current or high voltages was introduced, resulting in a optimum band-gap for a single-junction solar cell. The same consideration can be made for multi-junction solar cells. By taking into account different sub-cells, each with different band-gap energies, the thermalization losses can be reduced. In a series connected multi-junction the first sub-cell (with respect to the incident light) needs to have the highest band-gap of all sub-cells in order to only absorb high energy photons. This sub-cell will generate a *short circuit current density*  $J_{SC,1}$  at a reasonably high *open circuit voltage*  $V_{OC,1}$ . The  $i$ -th sub-cell will give a current density  $J_{SC,i}$  and voltage  $V_{OC,i}$ . According to Kirchhoff's rules the *open circuit voltage* of each sub-cell will add up to the total *open circuit voltage*  $V_{OC,total}$  if recombination losses between the sub-cells can be avoided. Furthermore, the current through all cells needs to be the same.

In order to determine the theoretical resulting *short circuit current* of the multi-junction the  $JV$ -characteristics of each sub-cell can be used to determine the  $JV$ -characteristic of the multi-junction by adding the voltages of each sub-cell at the same current density. In a multi-junction made up of sub-cells with reasonably high  $FF$ s the lowest  $J_{SC}$  of all sub-cells usually gives a good measure of the total expectable *short circuit current density*  $J_{SC,total}$ . As a general rule of thumb it can be stated that the current limiting sub-cell should have a high  $FF$  to preserve a high  $FF$  in the series connected multi-junction.

$$J_{SC,total} \approx \min(J_{SC,i}), \quad (2.5)$$

$$V_{OC,total} = \sum_{i=1}^N V_{OC,i}. \quad (2.6)$$

In such a series connection of solar cells the total current will be lower as in a typical single junction as all cells absorb a smaller fraction of the incident light. Nevertheless, the  $V_{OC}$ s of all cells add up, with a potentially highest  $V_{OC}$  for the cell with the largest band-gap. In 1980 De Vos calculated the maximum efficiency of multi-junctions as a function of the band-gap energies of the sub-cells.[31] These calculations are based on the same assumptions that were used by Shockley and Queisser. For a tandem solar cell device the best band-gap combinations would be  $E_{G,1} = 1.9 \text{ eV}$  and  $E_{G,2} = 1.0 \text{ eV}$  and for a triple junction  $E_{G,1} =$

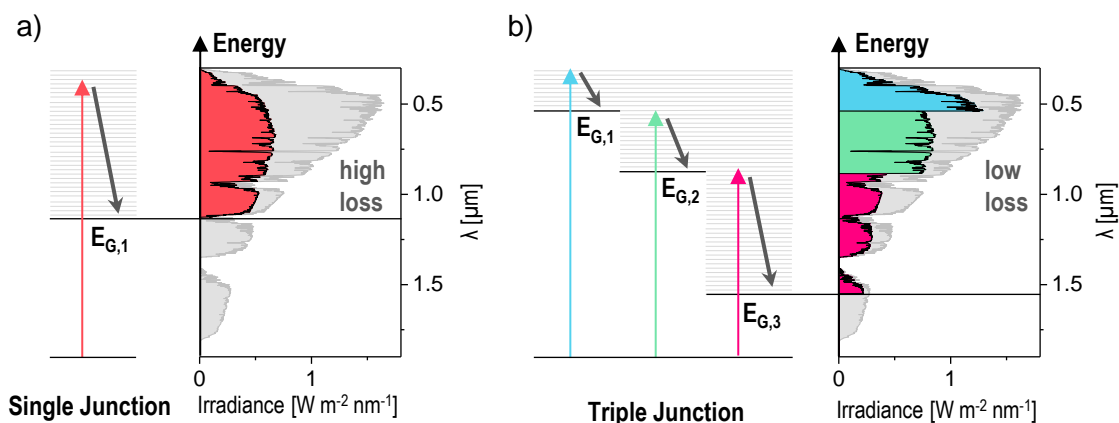


**Figure 2.2.:** Energiediagram of a single- (a) and a multi- (b) junction in combination with the spectral irradiance of standardized one sun illumination (gray line). The colored areas denote the energy that can be used by the solar cell. The difference between incident irradiance and the usable energy is lost to thermalization.

2.3 eV and  $E_{G,2} = 1.4$  eV and  $E_{G,3} = 0.8$  eV.[31] In Figure 2.2 a) and b) the concept of energy dependent absorption and thermalization losses is visualized for a single junction and a triple junction with their optimum band-gaps. It becomes clear that thermalization losses are diminished in a multi-junction by comparing the usable energy yield of each cell (colored areas in Figure 2.2) compared to the incident AM 1.5 G irradiance. With similar assumptions as for the single junction the efficiency maximum for a tandem junction is 42% and 49% for a triple junction. As soon as organic sub-cells are taken into account the efficiency would again be lower as reasoned in section 2.4. Nevertheless, the reduction of thermalization losses is an essential advantage of series connected multi-junctions of any kind compared to single junction architectures. Aside of the mere potential efficiency increase, multi-junctions have other beneficial properties. In a series connected multi-junction high operating voltages are obtained that are required to, e.g., perform water splitting.[32, 33]

# Chapter 3

## Open Circuit Voltage and Recombination of Charges

In this chapter a theoretical approach to the *open circuit voltage* ( $V_{OC}$ ) is introduced based on the reciprocity between the photovoltaic quantum efficiency and the electroluminescence of the CT-states of organic solar cells. This approach has proven to have powerful implications on the understanding of  $V_{OC}$ ,[34] and it relates it to steady state emission and photovoltaic quantum efficiency spectra. Furthermore, recombination models of photogenerated free charges inside the solar cell will be discussed and the concept of an effective, free carrier recombination coefficient is introduced.

### 3.1. Open Circuit Voltage

In the previous chapter the concept of series connected multi-junctions was introduced. The subsequent stacking of cells with decreasing effective band-gap energies requires the use of low band-gap materials in multi-junction solar cells. In section 2.2 the donor/acceptor type organic solar cells and the concept of a *charge transfer state* (CT-state) were introduced. The existence of such states in organic solar cells was shown by sensitive  $EQE_{PV}$  measurements to prove its absorbing character,[35, 36] and by its photo- or electro-luminescence ( $EQE_{EL}$ ) spectra.[37–39] The low effective band-gap of a donor/acceptor type organic solar cell will automatically restrict the maximum accessible  $V_{OC}$  of such an organic sub-cell in a multi-junction. Unfortunately, the full potential of the effective band-gap can also never be exploited in a solar cell as radiative and non-radiative losses of charges will additionally limit the  $V_{OC}$ . Therefore a fundamental understanding of these losses is crucial in order to optimize organic solar cells with respect to the  $V_{OC}$ . An elegant way of connecting the  $V_{OC}$

and the radiative and non-radiative  $V_{OC}$  losses to CT-state emission and absorption spectra of organic materials was presented by Vandewal in 2010.[34] The derivation is based on the principle of *detailed balance* and quasi-equilibrium conditions and will be explained in detail. First of all, Kirchhoff's law of radiation states that a reciprocity between absorption and emission exist under thermodynamic equilibrium conditions.[40] Hence, the emission of thermal radiation of a gray body equals the black-body radiation of the surrounding with equal temperature multiplied by the absorptance of the gray body. The thermal *photon flux of a black-body*  $\phi_{BB}$  is given as a function of energy and the temperature  $T$  of the black-body as famously derived by Max Planck:[41]

$$\phi_{BB}dE = \frac{2\pi}{c^2h^3} \frac{E^2}{\exp\left(\frac{E}{k_B T}\right) - 1} dE, \quad (3.1)$$

with  $c$  the speed of light,  $k_B$  the Boltzmann constant and  $h$  Planck's constant. Secondly, Würfel introduced a generalized radiation law extending the radiation law of Kirchhoff for non-equilibrium conditions by introducing a chemical potential  $\mu$ .[42, 43] This has the important consequence that by increasing the chemical potential of a gray body the emission will not change spectrally, but the intensity of emission will increase exponentially with the applied chemical potential. Finally, in 2007 Rau extended this concept and connected the *total emitted photon flux*  $\phi_{em}$  and the *photovoltaic external quantum efficiency* ( $EQE_{PV}$ ) of a solar cell,[44] via the black-body spectrum  $\phi_{BB}$ .

$$\phi_{em}(V) = \int EQE_{PV}(E)\phi_{BB}(E)dE \left[ \exp\left(\frac{qV}{k_B T}\right) - 1 \right]. \quad (3.2)$$

Following the reasoning of Rau an *emitted photon flux*  $\phi_{em}$  is caused under equilibrium conditions by an *injected current density*  $J_{em,0}$ .

$$J_{em,0} = \phi_{em} \cdot q. \quad (3.3)$$

With this the detailed balance of light absorption with subsequent charge carrier collection and charge carrier injection with subsequent light emission is introduced. In a real device, however, not every free charge carrier will recombine radiatively and the injected charge carrier density  $J_{em,0}$  which leads to radiative recombination is actually lower than the total injected charge carrier density  $J_{em}$ . The *quantum efficiency of electroluminescence* ( $EQE_{EL}$ ), that is the number of emitted photons divided by the injected number of charges can be measured by calibrated electroluminescence measurements as outlined in section 4.3. The

### 3.1. Open Circuit Voltage

---

$EQE_{EL}$  might itself be voltage dependent as the non-radiative recombination process can depend on the applied voltage. This finally results in:

$$\begin{aligned}
 J_{em}(V) &= \frac{1}{EQE_{EL}(V)} J_{em,0}(V) \\
 &= \frac{q}{EQE_{EL}(V)} \phi_{em}(V) \\
 &= \frac{q}{EQE_{EL}(V)} \int EQE_{PV}(E) \phi_{BB}(E) dE \left[ \exp\left(\frac{qV}{k_B T}\right) - 1 \right] \\
 &= J_0(V) \left[ \exp\left(\frac{qV}{k_B T}\right) - 1 \right],
 \end{aligned} \tag{3.4}$$

with the *dark saturation current density*  $J_0(V)$  defined as:

$$J_0(V) = \frac{q}{EQE_{EL}(V)} \int EQE_{PV}(E) \phi_{BB}(E) dE. \tag{3.5}$$

If the solar cell is illuminated in addition to this injected current density, the photogenerated current density  $J_{Ph}$  needs to be considered. At voltages larger than  $\approx 4k_B T/q \approx 100$  mV the error by neglecting the contribution from the  $(-1)$  term in Equation 3.4 is less than 2%. For open circuit conditions, when the total current density of the solar cell under illumination is zero, Equation 3.6 for the  $V_{OC}$  can be derived, neglecting the  $(-1)$  term as typical  $V_{OC}$  is larger than 100 mV.

$$V_{OC} = \frac{k_B T}{q} \ln\left(\frac{J_{Ph}}{J_0(V)}\right). \tag{3.6}$$

Under the assumption of no non-radiative losses, meaning  $EQE_{EL}$  is unity, the radiative limit of the solar cell can be determined from the photogenerated current density  $J_{Ph}$ , the  $EQE_{PV}$  and the black-body spectrum. The black-body spectrum is exponentially decreasing with higher energy and only the low energy portion of the  $EQE_{PV}$  contributes to the recombination current. The radiative limit of the *open circuit voltage*  $V_{OC,Rad-Lim}$  is then given by:

$$V_{OC,Rad-Lim} = \frac{k_B T}{q} \ln\left(\frac{J_{Ph}}{q \int EQE_{PV} \phi_{BB} dE}\right). \tag{3.7}$$

If non-radiative losses are taken into account ( $EQE_{EL} < 1$ ), the  $V_{OC}$  can be derived as:

$$V_{OC,calc.1} = \frac{k_B T}{q} \ln\left(\frac{J_{Ph}}{q \int EQE_{PV} \phi_{BB} dE}\right) + \frac{k_B T}{q} \ln(EQE_{EL}). \tag{3.8}$$

This reveals, that by carefully measuring the electroluminescence and the photovoltaic quantum efficiency the  $V_{OC}$  of an organic solar cell can be determined. Unfortunately though, no direct connection between an effective band-gap and radiative losses can be made from these findings. In 2010, however, Vandewal et al. presented an equation for the  $V_{OC}$  based on the CT-state energy and the radiative and non-radiative  $V_{OC}$  losses.[34] The crucial idea herein is to describe the absorption and emission spectrum of the CT-states by Gaussian functions based on Marcus Theory.[34, 45, 46] In subsection 2.3.2 the internal quantum efficiency ( $IQE$ ) was shown to relate the absorption and the  $EQE_{PV}$ . Therefore, also the  $EQE_{PV}$  can be described by a Gaussian function depending on the CT-state energy  $E_{CT}$  and the reorganization energy  $\lambda$ .  $EQE_{PV}$  is then given by:[34]

$$EQE_{PV}(E) = \frac{f}{E\sqrt{4\pi\lambda k_B T}} \exp\left(\frac{-(E_{CT} + \lambda - E)^2}{4\lambda k_B T}\right). \quad (3.9)$$

Herein,  $f$  contains information about the CT-state density, the  $IQE$  and the strength of the electronic coupling between donor and acceptor, and does not itself depend on energy. Therefore, the line shape of the modeled Gaussian  $EQE_{PV}$  spectrum is determined only by  $E_{CT}$  and  $\lambda$ , while  $f$  scales the Gaussian in order to fit the measured  $EQE_{PV}$  spectrum of the CT-state. The emission spectrum is Stokes shifted compared to the absorption or  $EQE_{PV}$  spectrum, respectively. The Stokes shift is given by  $\approx 2\lambda$ . The emission rate of electroluminescence ( $EL$ ) is then determined by:

$$EL = \frac{E f_{EL}}{\sqrt{4\pi\lambda k_B T}} \exp\left(\frac{-(E_{CT} - \lambda - E)^2}{4\lambda k_B T}\right), \quad (3.10)$$

where  $f_{EL}$  is also dependent on the strength of the electronic coupling between donor and acceptor.[46] By simultaneously simulating the measured  $EQE_{EL}$  and  $EQE_{PV}$  by Equation 3.9 and Equation 3.10 the factors  $f_{EL}$  and  $f$  as well as the CT-state energy  $E_{CT}$  and the reorganization energy  $\lambda$  can be obtained. Finally, Vandewal determined a formula for  $J_0$  by evaluating Equation 3.5 under the assumption that the  $EQE_{PV}$  of the CT-state is given by Equation 3.9 and by approximating the black-body spectrum  $\phi_{BB}$  for energies  $E \gg k_B T$ . By this means an analytical formula for the  $V_{OC}$  was presented, directly relating the  $V_{OC}$  to  $E_{CT}$  and a non-radiative and radiative loss term.

$$V_{OC} = \frac{E_{CT}}{q} + \frac{k_B T}{q} \ln\left(\frac{J_{Ph} h^3 c^2}{f q 2\pi (E_{CT} - \lambda)}\right) + \frac{k_B T}{q} \ln(EQE_{EL}). \quad (3.11)$$

This formula has important implications as it not only defines the effective band-gap between donor and acceptor to be the CT-state energy, but it also provides the opportunity to directly

determine the amount of radiative and non-radiative  $V_{OC}$  loss from the measurement of the  $EQE_{EL}$  and  $EQE_{PV}$ .

## 3.2. Non-Geminate Recombination of Charges and Effective Bimolecular Recombination

In section 2.2 the basic ideas of charge carrier generation and recombination have been outlined, discriminating between *geminate* and *non-geminate* processes. In this section *non-geminate* recombination – the recombination of free charge carriers – will be discussed with focus on the special case of bimolecular recombination (BMR). It will be discussed how interfacial CT-states determine the recombination current in organic solar cells and a model by Burke et al. is introduced resolving the discrepancy of BMR coefficients in OSCs and predictions from Langevin theory.[47] Recombination orders larger than two, yielded occasionally from charge extraction experiments in typical OSCs, will be discussed and accommodated to the energetic picture put forward by Burke et al. Finally, the concept of an effective BMR coefficient  $k_{2,eff}$ , which explicitly characterizes the free charge carrier recombination, is introduced in order to help resolve contradicting findings about recombination mechanisms in OSCs.

Once free charge carriers are generated in a device they need to be effectively extracted at the electrodes before they can recombine. The competition between recombination and extraction directly influences the *fill factor* in organic solar cells,[48, 49] which highlights the importance of gaining a better understanding of the actual *non-geminate* recombination process. In general the *non-geminate* recombination rate  $R$  can be expressed in terms of the charge carrier density  $n$ , the recombination coefficient  $\gamma$  and the recombination order  $\beta$ .

$$R = -\frac{dn}{dt} = \gamma n^\beta \quad (3.12)$$

If the recombination rate depends linearly on the charge carrier density, meaning  $\beta = 1$ , the process is referred to as monomolecular recombination. If  $\beta = 2$  the recombination process is called bimolecular. Higher order processes such as Auger recombination do not play a significant role in organic solar cells as they would only occur at very high charge carrier densities that are rather uncommon in these devices under AM 1.5G illumination conditions. Monomolecular recombination occurs when the main loss channel of free charges is trap assisted as was described by Shockley, Read and Hall in 1952 with respect to inorganic semiconductors.[50, 51] In organic solar cells the most important loss mechanism is found to be bimolecular in nature and depends on the product of free electron and hole density which

can be assumed to be equal ( $n = p$ ), if they are photogenerated by mutual excitation events. The recombination rate is then described by:

$$R_{BMR} = -\frac{dn}{dt} = k_2 n^2, \quad (3.13)$$

in which  $k_2$  denotes the bimolecular recombination coefficient. Usually  $k_2$  is described in the framework of Langevin recombination theory. This theory was developed by Langevin to describe recombination of ions in gases.[52] It states that the BMR coefficient depends linearly on the sum of electron and hole mobilities ( $\mu_e$  and  $\mu_h$ );  $k_{2,Langevin} = \frac{q}{\epsilon\epsilon_0}(\mu_e + \mu_h)$ . This theory is based on the assumption that every encounter<sup>1</sup> of two oppositely charged ions leads to recombination (for organic electronics electron and holes are considered instead of ions). However, Langevin theory fails in describing the recombination coefficients for today's efficient OSCs. Typical recombination coefficients are found to be 1 to 3 orders of magnitude lower than predicted.[47, 53, 54] This has led to the introduction of a reduced Langevin recombination coefficient, suggesting that either free charges encounter each other less often than assumed by the mobilities or that not every encounter leads to recombination. Burke et al. recently showed that the latter assumption becomes meaningful when considering equilibrated population of CT- and CS-states. This means that CT-states split up several times into free charges before finally recombining.[47] Furthermore, they are able to relate the recombination current at  $V_{OC}$  conditions to the CT-state energetics, implying that, if an equilibrium between CS- and CT-states is established, the relevant recombination mechanism is bimolecular and always mediated via the CT-state. The recombination current density according to Burke et al. is given by:[47]

$$J_{rec} = \frac{qn_{CT}d}{\tau_{CT}} = \frac{qN_{CT}d}{\tau_{CT}} \exp\left(-\frac{E_{CT} - \frac{\sigma^2}{2k_B T} - qV_{OC}}{k_B T}\right), \quad (3.14)$$

with  $d$  the active layer thickness,  $n_{CT}$  the total number of occupied CT-states,  $N_{CT}$  the total number of CT-states,  $\tau_{CT}$  the average lifetime of the CT-states and  $\sigma$  the standard deviation of the Gaussian CT-state distribution. It is important to note that this recombination current density is independent of the total charge carrier density  $n$ , implying that the recombination current is only determined by the charge carrier density of the CT-states. The scheme presented in Figure 3.1 a) is adapted from Burke et al. showing the rate coefficients which establish the aforementioned equilibrium and the loss of charges by recombination of the CT-state to its ground-state. This, however implies that under equilibrium conditions, meaning  $k_{CT} \ll k_s$ , the charge carrier density of CT-states  $n_{CT}$  and the free charge carrier density of electrons and holes ( $n = p = n_{free} = p_{free}$ ) are only related by the rate coefficient  $k_m$ , for

---

<sup>1</sup>Encounter means in this case that the distance between the charges is smaller than their mutual Coulomb capture radius.

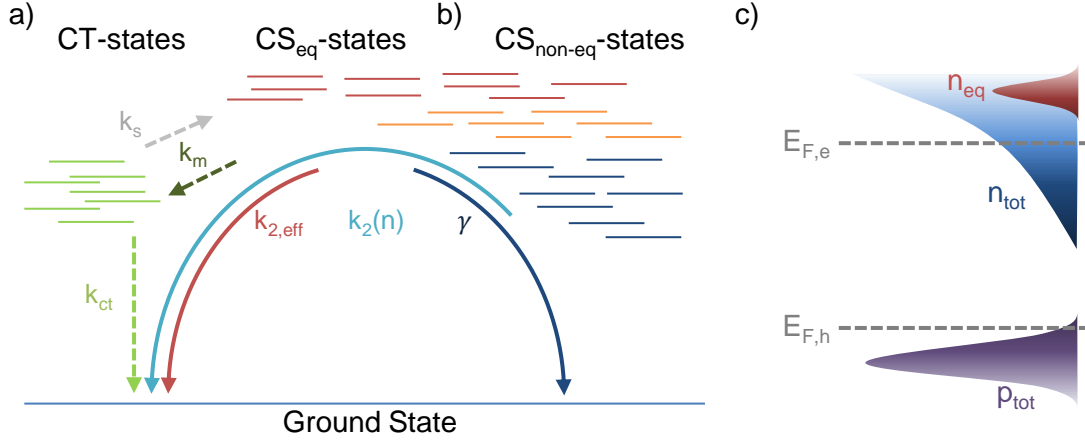


**Figure 3.1.:** a) Recombination pathway scheme adapted from Burke et al.[47] showing the equilibrium between CT- and  $CS_{eq}$ -states denoted by  $k_s$  and  $k_m$  as well as the coefficient  $k_{CT}$  for CT- to ground-state recombination as dashed arrows. The red full arrow indicates the effective BMR coefficient  $k_{2,eff}$ . b)  $CS_{non-eq}$ -states that are not in equilibrium with the CT-states can be below or above their quasi-Fermi level, depicted as blue or orange lines, respectively. The light blue arrow indicates the recombination rate taking into account also the trapped  $CS_{non-eq}$ -states resulting in a charge carrier density dependent recombination coefficient  $k_2(n)$ . The dark blue arrow indicates recombination with a different order via trapped states, represented by a constant coefficient  $\gamma$ . c) Example sketches of density of state distributions related to a) and b); filled with a total electron concentration  $n_{tot}$  with a substantial amount of charges below the quasi-Fermi level (for electrons  $E_{F,e}$ ) and a free hole concentration  $p_{tot}$ . Indicated in red is the DOS distribution of  $CS_{eq}$ -states filled with a free charge carrier concentration  $n_{eq}$  which may recombine bimolecularly via a CT-state. This representation only considers electron traps but the same conclusion can be drawn if only holes or both, electron and holes can be trapped.

forming the CT-states and  $k_s$ , the rate coefficient for splitting them:

$$k_s n_{CT} = k_m n_{free} p_{free} = k_m n p = k_m n^2. \quad (3.15)$$

In this case, where  $n = p = n_{free} = p_{free}$ ,  $k_m$  can also be expressed by  $k_2$ , the bimolecular recombination coefficient. Additionally, Burke et al. show, that if  $k_{CT} \gg k_s$ , Langevin theory applies and the reduction factor approaches one.[47]

The suggested picture includes an interfacial mixed region between donor and acceptor with  $CS$ -states ( $CS_{eq}$ ) that are in equilibrium with CT-states and additionally aggregated regions of either donor or acceptor with  $CS$ -states of different energy which are not in equilibrium with the CT-states ( $CS_{non-eq}$ ). The recombination current, and with that the  $V_{OC}$  would only be dominated by the charge carrier density of the CT-states, as outlined before. This however means, that only the free charges  $n_{eq}$  in the  $CS$ -states in equilibrium with the CT-states ( $CS_{eq}$ ) define the recombination current. Nevertheless, the additional charges in  $CS$ -states, which are not in equilibrium with the CT-state ( $CS_{non-eq}$ ), would significantly increase the

total charge carrier density and, as the recombination current is not affected by these extra charges, the total carrier lifetime.[47] Hence, Burke et al. suggest introducing energy cascades in order to preserve high  $V_{OC}$ , determined by the CT-state energy, while at the same time enabling higher  $J_{SC}$ .

This picture also allows one to assume a broad distribution of energetically disordered charge separated states in the aggregated region that may even act as traps, if they are located below their respective quasi-Fermi level ( $E_{F,e}$  for electrons and  $E_{F,h}$  for holes). In this sense not all CS-states are necessarily free; in Figure 3.1 b) such (low lying) CS-states are sketched in blue as part of the manifold of  $CS_{non-eq}$ -states. In this picture the recombination is nevertheless mediated via the CT-states in equilibrium with the  $CS_{eq}$ -states. To discriminate whether  $CS_{non-eq}$ -states include trapped states or not, recombination measurements can be conducted. In the case of only free carrier recombination the recombination order will be 2, independent of the total charge carrier density. However, in a typical charge extraction experiment all charges, free and also trapped ones, are extracted from the device with high extraction voltages. This, implies that the total extracted charge carrier density is larger than the free charge carrier density ( $n > n_{eq}$ ) which is located in  $CS_{eq}$ -states and directly contributes to the recombination current. Overestimation of free charges in extraction experiments leads to underestimation of the recombination coefficient. A more meaningful recombination coefficient,  $k_{2,eff}$  which describes recombination only of free charges can be significantly higher than the measured  $k_2$ . The distinction whether or not traps exist in the manifold of  $CS_{non-eq}$ -states is possible by examining the charge carrier density dependence of  $k_2$ . If  $k_2$  is itself charge carrier density dependent, a significant amount of states below the respective quasi-Fermi level are present. In Figure 3.1 a) and b) this is indicated by a light blue arrow indicating the pathway of recombination. In contrast to this charge carrier density dependent coefficient the effective BMR coefficient  $k_{2,eff}$  is always related only to the  $CS_{eq}$ -states. The charges in these states are located well above their quasi-Fermi levels resulting in a  $k_{2,eff}$  independent of charge carrier density. In Figure 3.1 c) density of state distributions (DOS) are sketched for electrons and holes with respect to their potential quasi-Fermi levels. A narrow DOS with most states below the quasi-Fermi level is sketched for holes, filled with a total hole concentration  $p_{tot}$ . The DOS for electrons is denoted as exponentially distributed, with states well below the quasi-Fermi level for electrons. A total electron concentration  $n_{tot}$  fills these states according to Fermi-Dirac statistics. The number of electrons above the quasi-Fermi level that are in equilibrium with the interfacial CT-states are denoted as  $n_{eq}$ . The DOS of  $CS_{eq}$ -states that are filled up by  $n_{eq}$  is sketched in red as a narrow Gaussian distribution. This sketch obviously is only one of several optional idealized DOS distributions that might occur in OSCs due to the complex energetic landscapes determined by molecular orbital interactions in complex morphologies. Nevertheless, it is sufficient to explain apparent higher recombination orders that have been observed experimentally and were related to trapped tail states.[15, 55, 56] To understand this relation it is sufficient to examine the charge carrier recombination via the recombination rate as given in Equation 3.12. If the rate is measured

at open circuit conditions, by e.g. charge extraction experiments, the recombination rate  $R$  is known to be equal to the generation rate  $G$  to fulfill zero net current conditions. Furthermore the generation rate can be expressed by the generation current density  $J_G$  divided by the device thickness  $d$  and the elementary charge  $q$ .

Hence, at  $V_{OC}$  the recombination current  $J_R$  can be expressed as:

$$J_R = J_G = qd\gamma n^\beta. \quad (3.16)$$

The charge carrier density in a semiconductor is related to the energetics via the density of states function (DOS) and the occupation probability, given by the Fermi-Dirac distribution. In the classical semiconductor theory with a valence and conduction band, sharp band edges and by applying the Boltzmann-approximation for the Fermi-Dirac distribution the charge carrier densities of electrons  $n$  and holes  $p$  can be calculated.[42] The product of electron and hole charge carrier density is given by:

$$\begin{aligned} np &= N_e N_h \exp\left(-\frac{E_C - E_V}{k_B T}\right) \exp\left(\frac{E_{F,e} - E_{F,h}}{k_B T}\right) \\ &= N_e N_h \exp\left(-\frac{E_G}{k_B T}\right) \exp\left(\frac{E_{F,e} - E_{F,h}}{k_B T}\right) \\ &= n_i^2 \exp\left(\frac{E_{F,e} - E_{F,h}}{k_B T}\right) \\ &= n_i^2 \exp\left(\frac{qV_{OC}}{k_B T}\right), \end{aligned} \quad (3.17)$$

with  $N_{e/h}$  the effective density of states for electrons/holes,  $n_i$  the intrinsic charge carrier density of electrons and holes and the band-gap ( $E_G$ ) between conduction and valence band edge energy,  $E_C$  and  $E_V$  respectively. By this means a dependence of charge carrier density and  $V_{OC}$  is found and for  $n = p$  follows:

$$n = n_i \exp\left(\frac{qV_{OC}}{2k_B T}\right). \quad (3.18)$$

For an exponential tail-state distribution for electrons and holes with a tail slope defined by the energy  $E_U = k_B T_0$  and with the ratio  $m = \frac{T_0}{T}$  the  $V_{OC}$  dependence of charge carrier density is given by:

$$\begin{aligned} n &= n_i \exp\left(\frac{qV_{OC}}{2mk_B T}\right) \\ &= n_i \exp(\zeta V_{OC}), \end{aligned} \quad (3.19)$$

with  $\zeta = \frac{q}{2mk_B T}$  as also shown by Kirchartz et al.[56] By recalling Equation 3.16 and expressing  $n$  as shown in Equation 3.19 the general recombination current density  $J_R$  is obtained:

$$\begin{aligned}
 J_R &= qd\gamma n^\beta \\
 &= qd\gamma n_i^\beta \exp\left(\frac{qV_{OC} \cdot \beta}{2mk_B T}\right) \\
 &= J_0 \exp\left(\frac{qV_{OC} \cdot \beta}{2mk_B T}\right) \\
 &= J_0 \exp(\beta\zeta \cdot V_{OC}) \\
 &= J_0 \exp\left(\frac{qV_{OC}}{n_{id}k_B T}\right),
 \end{aligned} \tag{3.20}$$

with  $J_0$  the dark generation current density and  $n_{id}$  the ideality factor. It becomes clear that the ideality factor is a function of the recombination order  $\beta$  and the disorder parameter  $m$  or alternatively  $\zeta$ :

$$n_{id} = \frac{2m}{\beta} = \frac{q}{\beta\zeta k_B T}. \tag{3.21}$$

The case of bimolecular recombination of free charges that are described by the Boltzmann approximation, where  $m = 1$  and  $\beta = 2$ , results in an ideality factor  $n_{id} = 1$ . Alternatively, by assuming exponential DOS distributions for electrons and holes and regarding recombination of free electrons/holes with exponentially trapped holes/electrons, where the trapped charge carrier concentration is given by  $n_T \propto \exp(qV/2E_U)$ , with  $E_U$  the Urbach energy, the ideality factor is found to be temperature dependent as originally showed for a-Si:H diodes by Berkel et al.: [57]

$$n_{id} = \left(\frac{1}{2} + \frac{k_B T}{2E_U}\right)^{-1} = \left(\frac{1}{2} + \frac{T}{2T_0}\right)^{-1}. \tag{3.22}$$

Whether the recombination in organic solar cells is dominated by such tail states or by free charge carrier recombination is still highly debated.[58–63] An important recent finding by Tvingstedt, however, shows that for a variety of typical organic solar cells the ideality factor is not temperature dependent and usually closer to 1 (pure bimolecular recombination).[14] This conclusion is also in better agreement with the model by Burke et al. where the recombination current is mediated via CT-states in equilibrium with free CS-states,[47] or Wetzelaer et al. who come to the conclusion that CT-state emission originates from free carrier bimolecular recombination and not from a trap assisted process.[63] Hawks et al. however extract the energy  $E_0$  from the slope of the photocurrent response of the low energy part of the CT-state, describing an exponential band tail density of states, which in their case would result

in temperature dependent ideality factors for several tested organic solar cell systems.[15] Tvingstedt however, explicitly examined the solar cells under open-circuit conditions where the recombination current can be expressed as shown in Equation 3.20. For voltage conditions  $V < V_{OC}$  transport and series resistance effects need to be considered. This becomes clear from the modified non-ideal Shockley-Equation under illumination which includes the illumination intensity dependent, generated photocurrent density  $J_G$ , as well as shunt and series resistance ( $R_{shunt}$  and  $R_{series}$ ).[14]

$$J = J_0 \left[ \exp \left( \frac{q(V - JR_{series})}{n_{id}k_B T} \right) - 1 \right] + \frac{V - JR_{series}}{R_{shunt}} - J_G. \quad (3.23)$$

At  $V_{OC}$  conditions the total current density  $J$  equals zero and all series resistance related terms cancel out. This allows one to evaluate the ideality factor independently of series resistance by measuring  $J_G(V_{OC})$  at different light intensities. This method is referred to as  $J_{SC}$  vs.  $V_{OC}$  method and it was first conducted by Wolf and Rauschenbach in 1963.[64] It is similar to the transient suns- $V_{OC}$  method by Sinton et al.[65] whose applicability to organic solar cells was investigated before. [66, 67] The impact of transport resistance losses was also examined by Würfel et al. who showed that the externally applied voltage  $V_{ext}$  to a diode with low charge carrier mobilities becomes irrelevant and instead the effective quasi-Fermi level splitting ( $\Delta E_{F,eff}$ ) needs to be considered as it defines the internal voltage  $qV_{int} = \Delta E_{F,eff}$ . [68] Neher et al. extended this picture by relating the actual internal voltage to a new figure of merit  $\alpha$ , relating bimolecular free carrier recombination and transport properties.[49]

$$\alpha = \sqrt{\frac{qk_2 d^3 J_G}{4\mu_e \mu_h (k_B T^2)}}, \quad (3.24)$$

with  $d$  the device thickness,  $\mu_{e/h}$  the electron and hole mobilities and  $k_2$  denoting the BMR coefficient. The internal voltage is then related to the externally applied voltage  $V_{ext}$  and the  $V_{OC}$  via:[49]

$$V_{int} = \frac{1}{1 + \alpha} V_{ext} + \frac{\alpha}{1 + \alpha} V_{OC}. \quad (3.25)$$

By this means an analytical modified Shockley-equation is found which fully describes the  $JV$ -curve of transport limited OSCs in terms of free carrier recombination and mobilities.[49]

$$J = J_G \left\{ \exp \left[ \frac{q}{k_B T (1 + \alpha)} (V_{ext} - V_{OC}) \right] - 1 \right\}. \quad (3.26)$$

Similar approaches have proven to be useful to describe the  $FF$  of a great variety of OSCs, as for example shown by Bartesaghi et al.[48]

In the discussion so far several important aspects were pointed out. First of all a model by Burke et al. was introduced showing how to explain Langevin reduction factors by a model that assumes recombination currents are mediated via CT-states that are in equilibrium with charge separated states and connects the  $V_{OC}$  to the CT-state energetics.[47] Then it was outlined how the introduction of trap states explains higher recombination orders and temperature dependent ideality factors. Hawks et al. indeed found temperature dependent ideality factors for several solar cell systems and concluded that a main charge carrier recombination channel is via trap states.[15] In contrast, Tvingstedt et al. found ideality factors to be temperature independent for a variety of different organic solar cells by  $J_{SC}$  vs.  $V_{OC}$  measurements, concluding that in most cases the recombination cannot be dominated by trap states.[14] Finally, the work of Würfel and Neher was presented, who showed that for solar cells with transport limitations the ideal Shockley-equation is not appropriate to describe the  $JV$ -characteristics. The modified Shockley-equation, introduced by Neher et al., was presented based on a figure of merit, relating bimolecular recombination and charge extraction. In the following passage the main idea of an effective bimolecular recombination coefficient will be introduced, which is in agreement with all the presented theories and experiments.

The idea of an effective, free carrier recombination coefficient is to describe the recombination process of an organic solar cell in a simplified way, by only taking into account the actual free charge carriers in the device. This discrimination of charges becomes reasonable by recalling the different, previously discussed findings. In the pictures of Burke and Neher, recombination of free charge carriers that are not in their Fermi-gap dominates the recombination current of many typical OSCs. This is in agreement with the experiments by Tvingstedt who finds temperature independent ideality factors for several different OSCs that are close to one. That means that in these cases the recombination current is indeed dominated by one BMR pathway, described by one fixed BMR coefficient. Referring to Figure 3.1 this recombination coefficient is the effective or free, bimolecular recombination coefficient  $k_{2,eff}$  and it will not depend on the total charge carrier density that can be extracted from the solar cell. However, in a situation with additional exponentially trapped electrons and holes,<sup>2</sup> meaning  $m = \frac{T_0}{T} \neq 1$ , charge extraction experiments will reveal a  $n(V_{OC})$  dependence according to Equation 3.19 and recombination orders  $\beta \neq 2$  and this also demands that the ideality factor is temperature dependent, according to Equation 3.22. Therefore, it is important to note that depending on the measurement technique, different conclusions would be drawn if these additional trapped charges do not directly contribute to the recombination current. As a consequence, by only applying the  $J_{SC}$  vs.  $V_{OC}$  method the series resistance free ideality factors will point to a strong influence of bimolecular recombination. At the

<sup>2</sup>In chapter 7 the case where only one charge carrier type is exponentially trapped will be discussed as well. It will be shown that this model representation also results in temperature dependent ideality factors.

same time charge extraction experiments will point to a substantial influence of trap states on the recombination process. This apparent discrepancy is resolved by splitting the total amount of charges in free and trapped charges, energetically located outside and inside the Fermi-gap, respectively. This results in a recombination current that is dominated by only the free charges in the device that recombine bimolecularly, described by an effective, free carrier coefficient  $k_{2,eff}$  while at the same time charge extraction experiments reveal the presence of trapped charges. This means that if trapped charges indeed do not directly contribute to the recombination current or the total current, only the effective recombination coefficient will be relevant. This can easily be understood in the simplified picture shown in Figure 3.1 c); in a charge extraction experiment almost all charges  $n_{tot}$  and  $p_{tot}$  would be extracted, but actually only the free charges  $n_{eq}$  in equilibrium with the CT-state would contribute to the recombination current. The modified Shockley-equation Equation 3.26 by Neher et al. explicitly considers only free charge carrier recombination and is in agreement with the assumption of an effective recombination coefficient.

In order to test this hypothesis it is necessary to determine the effective recombination coefficient and prove its applicability by fitting measured  $JV$ -characteristics with the modified Shockley-equation. The effective recombination coefficient can be measured with a charge extraction experiment where the recombination rate can be measured as a function of the extracted charge carrier density. This will reveal the recombination order and concomitantly the recombination coefficient according to Equation 3.12. In a situation where no trap states are present the recombination will be bimolecular. If however trap states are present the dependence of the recombination rate on the charge carrier density will reveal a recombination order  $\beta \neq 2$ , although the main recombination pathway may still be established via free charges located outside the Fermi-gap. As discussed before, this is a direct consequence of the extraction experiment in which trapped charges are also extracted. Therefore, in order to measure the actual free effective recombination coefficient, it becomes necessary to increase the free charge carrier density so high that the influence of the additionally extracted and previously trapped charges on the recombination rate becomes negligible. In the ideal case the order of recombination will then approach  $\beta = 2$  and the effective bimolecular recombination coefficient can be determined. To actually measure the effective recombination coefficient the charge extraction technique time delayed collection field (section 4.4) can be conducted. In this charge extraction experiment the initial charge carrier densities in the solar cells can be tuned by the intensity of the laser excitation that is used to generate charges. By this means the ratio of initially free and trapped charges can be changed and the effective, free recombination coefficient can be determined by examining the recombination rate dependence on the charge carrier density at high charge carrier densities. The experimental tools needed to achieve this challenge will be discussed in the following chapter. It should be highlighted at this point, that a full analysis of not only the charge carrier density dependence of the recombination current and  $V_{OC}$ , but also the  $J_{SC}$  vs.  $V_{OC}$  method and the series resistance free determination of the ideality factor are necessary to draw final conclusions on the recombi-

nation mechanism. In chapter 7 a full analysis of a typical low band-gap bulk heterojunction solar cell is presented and the applicability of this new model will be proven. This work sheds new light on the influence of trapped charges on the recombination process, a topic that has yet remained controversial within the field.

# Chapter 4

## Experimental Methods

In this chapter the most important measurement techniques used to collect the presented data will be introduced. Besides standard measurement techniques like the measurement of *current density vs. applied voltage* (*JV*-characteristics) under standardized illumination conditions or the measurement of the *external quantum efficiency of photogenerated current* ( $EQE_{PV}$ ), more sophisticated pump-probe experiments such as time delayed collection field (TDCF) and bias assisted charge extraction (BACE) were utilized to examine recombination behavior of free charges in the solar cells. Furthermore, the spectrally resolved *external quantum efficiency of electroluminescence* ( $EQE_{EL}$ ) was measured to gain knowledge about the energetics of charge transfer states and subsequently the *open circuit voltage*. For all extraction experiments (BACE and TDCF) small pixel sizes were used ( $\sim 1 \text{ mm}^2$ ) in order to achieve small RC-times a necessary condition to realize good time resolution when voltage steps are applied. For all external quantum efficiency measurements big pixels ( $\sim 16 \text{ mm}^2$ ) are needed to either efficiently absorb or emit light. *JV*-measurements, however, can be done at all pixel sizes. If not stated otherwise these pixel sizes are valid for all presented samples and respective measurement methods.

### 4.1. Current Voltage Characteristics

For standardized illumination conditions, air mass 1.5G irradiation with an intensity of  $100 \text{ mW cm}^{-2}$  (Oriel 91160, 300 W) calibrated by a NREL certified standard silicon cell was used and current was measured at applied voltages with a Keithley 2400 digital source meter. Temperature dependent *JV*-measurements were conducted both with a Peltier cooled sample holder at the sun simulator and in a helium cooled cryostat with LED illumination.

## 4.2. Photovoltaic External Quantum Efficiency Measurement

To spectrally resolve how efficiently incident photons are converted into extracted electrons the current output of the solar cell was measured with a lock in amplifier (EG&G Princeton Applied Research Model 5302) for chopped monochromatic illumination conditions. As a light source a 200 W halogen lamp was used and the wavelength was selected by a monochromator (LOT-Oriel). The frequency of the mechanically chopped light signal was used as the reference frequency for the lock in amplifier. The calibration of the light source was performed with either a UV enhanced silicon photodiode calibrated by Newport (Newport 818-UV) or a germanium photodiode (Newport 818-IR) for the visible or near infrared part of the light spectrum, respectively. In order to measure the  $EQE_{PV}$  of different sub-cells of a multi-junction solar cell it became necessary to modify the standard setup. The sub-cell of interest should be the current limiting cell in a multi-junction as the measured current is determined by the lowest current in a series connection of different current sources. Therefore, in addition to the monochromatic probe light a background illumination was provided by high power LEDs of certain wavelengths to saturate the current of the sub-cells that are not of interest.[69] The LEDs used for this purpose had wavelengths of 470 nm (Alustar 9008098), 592 nm (Alustar 9008098) and 740 nm (Roithner H2A1-H740). The  $EQE_{PV}$  measurement in series connected multi-junctions includes some uncertainties. It is very sensitive to the current saturation of the sub-cells. Slight variation of the intensity of the LED light can have a significant influence on the resulting absolute current values. The light induced charge carriers in the saturated sub-cells additionally introduce a photovoltage.[69] Thus, the field distribution, especially within the sub-cell of interest, is not known. Therefore the exact voltage condition for measuring the  $J_{SC}$  in the sub-cell is not known. However, from high  $FFs$  of a multi-junction device it reasons that a small field deviation from  $J_{SC}$  conditions has only minor influence on the derived current density.

## 4.3. External Quantum Efficiency of the Electroluminescence

To acquire the electroluminescence spectra of the solar cells at low injection currents an Andor SR393i-B spectrometer equipped with a silicon (Si) (DU420ABR-DD) and an indium-gallium-arsenide (InGaAs) (DU491A-1.7) detector was used. As the two detectors have different spectral sensitivity, spectra were taken with each for the same injection conditions to combine the near infra red portion, measured with the InGaAs detector, and shorter wavelengths, covered by the Si detector, to construct a single broad emission spectrum. Current injection was accomplished with a Keithley 2400 source meter. To get absolute emission spectra, the absolute photon flux from the cells was measured with a calibrated silicon photodiode for the same injection conditions as for the spectral measurement. In order to obtain a reliable calibration measurement, either all photons leaving the cell need to be collected or a

reference measurement, in the same setup geometry, needs to be taken with a light emitting diode (LED) with calibrated emission. In lack of a calibrated LED the experimental setup was modified in the course of this thesis. Measurements at different distances from the emitting OSC were taken and the collected photocurrent of the silicon diode was corrected as outlined in section A.1. This corrected photocurrent ( $I_{Diode,meas.}$ ), which accounts for the total emission into the half sphere, was used to correct the normalized emission spectra at the very same injection conditions to finally yield the absolute emission spectrum. The determined emission current into the half sphere that was detected by a silicon photodiode with known spectral irradiance was then compared to the hypothetical current that was calculated from the normalized emission spectrum and the known spectral irradiance function of that calibrated silicon photodiode ( $I_{Diode,calc.}$ ). By this comparison, the factor which was needed to scale the normalized emission spectrum was obtained and the absolute emission spectrum can be constructed.

## 4.4. Time Delayed Collection Field

The time delayed collection field (TDCF) measurement is an important tool to track the decay dynamics of free charges in an OSC and will only be introduced briefly, as it has been described in detail before.[70, 71] In the TDCF experiments laser pulses from a diode pumped, Q-switched Nd:YAG laser (NT242, EKSPLA) with 6 ns pulse duration and a typical repetition rate of 500 Hz were used to generate charges in the device. This charge generation was realized at different applied pre-voltages,  $V_{pre}$ . After a variable delay, a high reverse bias,  $V_{coll}$ , was applied to extract all the charges in the device.

A pulse generator (Agilent 81150A) was used to apply the pre- and collection bias which are amplified by a home-built amplifier. The currents flowing through the OSC were measured via a  $50\ \Omega$  resistor and recorded with an oscilloscope (Yokogawa DL9140). The pulse generator was triggered with a fast photodiode (EOT, ET-2030TTL). By applying the shortest possible delay between excitation and extraction of 4–6 ns the generation of free charge carriers could be measured; by increasing the delay and tracking the amount of extracted charges, by measuring the photocurrent transients, non-geminate recombination was quantified. In Figure 4.1 a) the basic measurement scheme is sketched with the applied voltage and extracted photocurrent as a function of time. By integrating the photocurrent transients either up to when the extraction voltage was applied or from when the extraction voltage was applied the charge carrier density can be split into pre- and collection charge carrier density,  $n_{pre}$  and  $n_{coll}$ , respectively. The sum is equal to the total extracted charge carrier density and the decay of this total charge carrier density with delay time contains information of the recombination process.

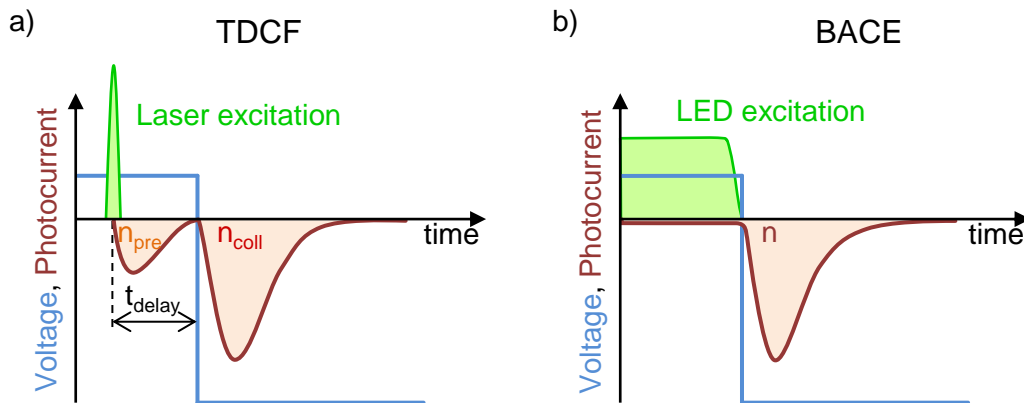


**Figure 4.1.:** a) Sketched representation of the TDCF measurement as a function of time. The applied voltage, the measured photocurrent and the initial laser excitation are shown. The charge carrier density is split into  $n_{pre}$  and  $n_{coll}$  for charges leaving the device before and after the extraction pulse is applied. b) Representation of the BACE measurement as a function of time. A constant illumination with a laser diode and an applied pre bias establish steady state conditions. After the shortest delay possible ( $\sim 10$  ns) the extraction voltage is applied and the photocurrent transient is measured. The applied pre bias is close to  $V_{OC}$  in this sketch as almost no current is measured before the extraction voltage is applied.

## 4.5. Bias Assisted Charge Extraction

The experimental setup required for bias assisted charge extraction (BACE) measurements was similar to the TDCF setup, except for the illumination conditions. With BACE, steady state charge carrier densities in the device can be measured; steady state conditions were established by a high power 1 W, 445 nm laser diode (insaneware) with a switch off time of about 10 ns. The LED was operated at 500 Hz with a duty cycle of at least 90% of one period. This realized 1.8 ms of illumination before the diode was switched off for 200  $\mu$ s. By this measurement routine, steady state conditions were established for any applied voltage, e.g.  $V_{OC}$  conditions. After switching off the laser diode, a high reverse bias was applied and all charges were extracted. The fast switch off time of the diode and the fast pulse generator (Agilent 81150A) allowed for charge extraction as fast as 10–20 ns after the switch off. This prevented severe non-geminate recombination losses. The current transients were measured via a 50  $\Omega$  resistor and recorded with an oscilloscope (Yokogawa DL9140) in the same way as for the TDCF measurement. The current transient, integrated from when extraction bias first was applied onwards, yields the total amount of charges that were in the device under the steady state conditions as defined by the illumination intensity and the applied pre bias. In Figure 4.1 b) the time line of a typical BACE measurement scheme is illustrated. Additionally, the full current voltage characteristics were measured for the same illumination intensities with the laser diode operated in continuous wave mode. By this means the generation current and the  $V_{OC}$  were known for a particular light intensity. By extracting the steady state charge

carrier density at  $V_{OC}$  conditions and simultaneously knowing the generation rate  $G$  from the generation current, the recombination order was determined according to Equation 3.12 as at  $V_{OC}$  the recombination and generation rate are equal ( $G = R$ ).

Furthermore, as outlined by Albrecht et al. BACE additionally allows to extract the effective mobility  $\mu_{eff}$  of the device. The effective mobility can be related to the electron and hole mobilities,  $\mu_e$  and  $\mu_h$  respectively, via:

$$\mu_{eff} = \frac{2\mu_e\mu_h}{\mu_e + \mu_h}. \quad (4.1)$$

Additionally, the injected charge carrier density for an applied bias can be determined. Therefore the BACE measurement was done without illumination at a pre bias condition for which a measurement of the injected charge carrier density was desired. This ensured that no photogenerated charges were in the device and only charges that had been injected at that pre bias  $V_{pre}$  were extracted with the extraction pulse  $V_{extr}$ . The capacitive charging due to applying the extraction pulse was corrected for by subtracting the capacitive charge determined by keeping the device at  $V_{pre} = 0$  before applying an extraction pulse with the same voltage step between pre and extraction voltage as used for the measurement at an applied pre bias  $V_{pre} \neq 0$ .

# Chapter 5

## Hybrid Triple-Junction Solar Cells

In this chapter the development of an efficient hybrid triple-junction (TJ) will be discussed. Key issues such as proper choice of a low band-gap system, establishing an efficient recombination contact between the sub-cells, predicting the best thicknesses of each layer, incorporating the concept of light scattering as well as setting up suitable measurement routines for the  $JV$ -characteristics and the  $EQE_{PV}$  will be introduced. Finally, a record efficiency of 11.7% is presented for a triple-junction consisting of two series connected amorphous silicon cells and one series connected low band-gap, organic solar cell.[5] This set the overall record for such a device type in the beginning of 2015. Recently, the efficiency of a similar triple-junction was increased to 13.2% by Tan et al. showing the potential for further improvements of such devices.[72].

### 5.1. The Hybrid Concept. Advantages of Combining Inorganic and Organic Sub-Cells

Hydrogenated amorphous silicon (a-Si:H) is an inorganic wide band-gap ( $\sim 1.7$  eV) semiconductor usually build up in a p-i-n structure with very high internal quantum efficiencies in the i-layer. The maximum efficiency is stuck at about 10% with *open circuit voltages* of about 0.9 V for device thicknesses of  $\sim 250$  nm (thin film technology).[6] The  $V_{OC}$  is very low compared to the band-gap energy of a-Si:H of about 1.7 eV, as already discussed in the introduction. This low  $V_{OC}$  is the main drawback of this technology in terms of efficiency. Therefore, further improvements can only be achieved by using a multi-junction architecture incorporating other materials with lower band-gaps. As mentioned in chapter 1, a-Si:H is usually combined in tandem or triple-junction architectures with hydrogenated microcrystalline Si:H ( $\mu c$ -Si:H)

reaching a record efficiency of 13.6%.<sup>[73]</sup> However,  $\mu\text{c-Si:H}$  is an indirect semiconductor and suffers from small absorption coefficients in the near infrared (NIR) spectral range.<sup>[74]</sup> This leads to the need of rather thick  $\mu\text{c-Si:H}$  layers ( $> 1\mu\text{m}$ ) to absorb most of the NIR photons. Layer stacks of such p-i-n devices are built up by plasma enhanced chemical vapor deposition (PECVD) and the growth of  $\mu\text{c-Si:H}$  requires low deposition rates ( $\approx 0.5\text{ nm s}^{-1}$ ), which makes the  $\mu\text{c-Si:H}$  deposition especially time and energy consuming. Alternatively, all organic, thin film multi-junctions have been developed. The active layers are either built from small molecules reaching a record efficiency of 13.2%,<sup>[75]</sup> or from polymers mixed with molecules reaching an efficiency of 11.5%.<sup>[76]</sup> The drawback of small molecule cells is that all layers need to be deposited under high vacuum conditions, whereas the polymer blends can be processed from solution in a less energy and time consuming way. However, in purely solution processed devices orthogonal solvents are needed to not destroy previously prepared layers.

The best wide band-gap sub-cell that has been used so far consist of poly(3-hexylthiophene-2,5-diyl) (P3HT) as donor and the fullerene derivative indene- $\text{C}_{60}$  bisadduct (ICBA) as acceptor material; the best efficiencies in P3HT:ICBA single junction solar cells were reported to reach about 6.5%.<sup>[77]</sup> Hence, a-Si:H is still better in terms of efficiency than typical wide band-gap organic solar cells. These preliminary considerations motivate the combination of inorganic and organic sub-cells to circumvent either performance or preparation limitations which any of those techniques show. In Figure 5.1 the extinction coefficients for a-Si:H,  $\mu\text{c-Si:H}$  and both organic solar cells used in this study are shown together with the photon flux of the AM 1.5G spectrum indicating the absorption potential of the hybrid combinations. The concept of combining a-Si:H sub-cells together with organic solar cells in a series connected multi-junction has been presented before, but only very few publications on tandem devices of one a-Si:H and one organic sub-cell with rather low efficiencies had been published before the work for this thesis was started.<sup>[2, 3]</sup> In 2014 Albrecht et al. developed an efficient tandem cell, which set the starting point for the development of the hybrid triple-junctions presented in this work.<sup>[78]</sup> Introducing another a-Si:H sub-cell to a hybrid tandem device might be counterintuitive by looking at Figure 5.1 as another a-Si:H sub-cell does not cover a different spectral region than the first cell, but by using two a-Si:H cells the thicknesses of both cells can be optimized separately. Therefore, the expected  $V_{OC}$  will increase and by using a rather thin front a-Si:H sub-cell and a thicker middle a-Si:H sub-cell, both a-Si:H sub-cells should be able to absorb enough photons to generate reasonable photocurrents, while at the same time a high  $FF$  can be preserved.

## 5.2. Hybrid Triple-Junction Device Structure

The hybrid triple-junction devices presented in this work were built in close collaboration with the Competence Centre Thin-Film- and Nanotechnology for Photovoltaics Berlin (PVcomB).

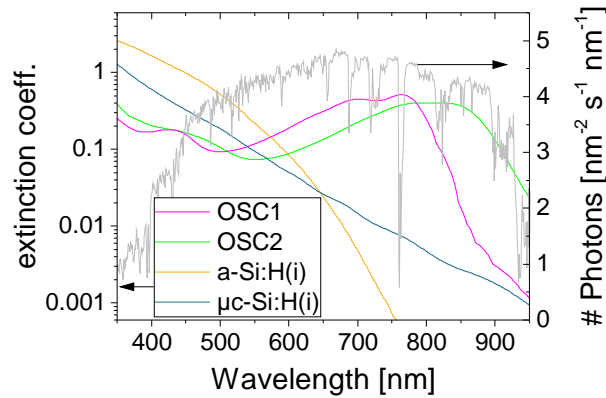


**Figure 5.1.:** (left scale) Extinction coefficient of a-Si:H  $\mu$ c-Si:H and the two organic solar cells used in the triple-junction (OSC1: Si-PCPDTBT:PC<sub>60</sub>BM, OSC2: PMDPP3T:PC<sub>60</sub>BM). (right scale) Photon flux density of the AM 1.5G standardized sun spectrum. Figure adapted from Albrecht et al.[78]

At PVcomB the inorganic part of the hybrid triple-junction was built and transferred to the laboratory at the university of Potsdam where the recombination contact, the organic sub-cell and the back electrode were prepared. Though the inorganic sub-cells are of major importance for the efficient development of the triple-junction, their preparation routine will be discussed only in brevity, as the main focus of this work has been the efficient combination of state of the art inorganic techniques with organic solar cells.

In Figure 5.2 the full layer stack is sketched showing the active layers, recombination contacts and electrodes, prepared on a glass substrate. The transparent front electrode is made of sputtered aluminum doped zinc oxide (AZO) and the standard back electrode consists of calcium (Ca) capped with silver (Ag). The recombination contact between the two a-Si:H cells is a tunnel recombination junction formed by the adjacent n- and p-doped layers. The recombination layer between the a-Si:H tandem and the organic sub-cell was either built up by a sputtered AZO or indium tin oxide (ITO) layer in combination with either the conductive polymer poly(3,4-ethylenedioxythiophene) polystyrene sulfonate (PEDOT:PSS), purchased from Hereaus (Clevios P VP AI 4083) or a 1 nm thick silver layer covered with molybdenum trioxide (MoO<sub>3</sub>). The a-Si:H devices were prepared by PECVD of the a-Si:H layers on the AZO electrode. In the PECVD process silane (SiH<sub>4</sub>) and hydrogen (H<sub>2</sub>) act as precursor gases to build up the i-layer in the a-Si:H. Admixture of TMB (C<sub>3</sub>H<sub>9</sub>B) and phosphine (PH<sub>3</sub>) facilitates creation of p- and n-doped layers which cause the build up of an electric field to separate and collect the charge carriers in the i-layer. The full layer stack of the optimized devices is shown in section B.1. The doped hydrogenated micro crystalline silicon oxide ( $\mu$ c-SiOx) mitigates parasitic light absorption.[79, 80] The aperture shown in Figure 5.2, was attached to the front side of the glass substrate for the *JV* measurements on the sun simulator to avoid overestimating the current produced

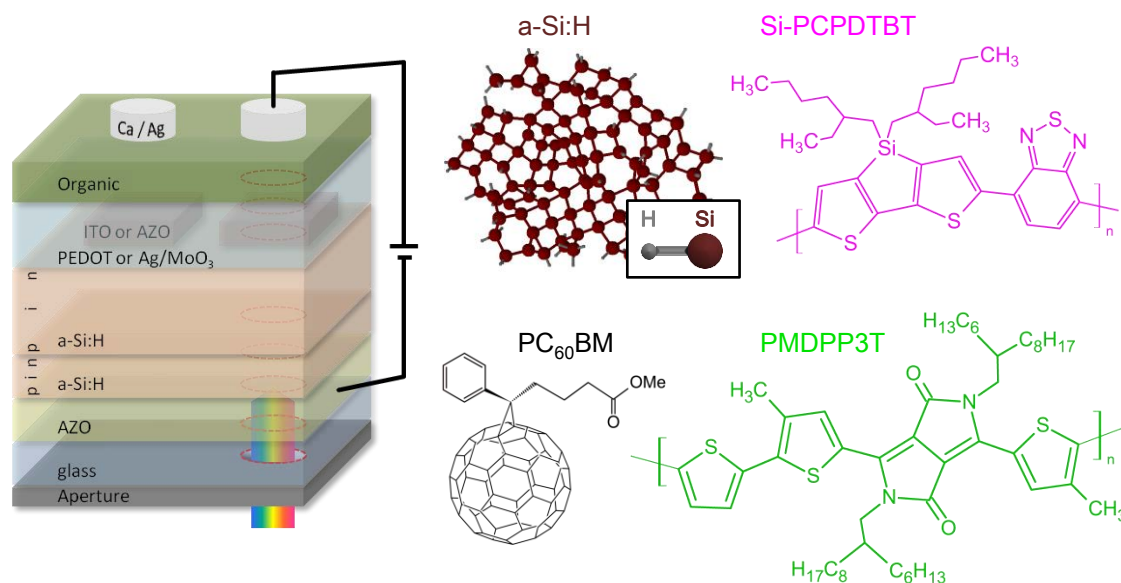


**Figure 5.2.:** (left) Schematic layer structure of the triple-junction device stack. Aperture as used for the  $JV$ -measurements is included (right) Chemical structure of the materials used in the active layers of the sub-cells.

by the a-Si:H tandem. This became necessary as the intermediate sputtered ITO or AZO layers were slightly larger than the evaporated back electrode on the organic. The total pixel area is therefore defined by the aperture and the evaporated metal electrode, both with a size of  $4.16 \text{ mm}^2$ . The organic low band-gap solar cells used in the presented triple-junctions are based on either the low band-gap donor poly[2,1,3-benzothiadiazole-4,7-diyl][4,4-bis(2-ethylhexyl)-4H-silolo[3,2-b:4,5-b'] dithiophene-2,6-diyl] (Si-PCPDTBT)<sup>1</sup> or the donor polymer poly[[2,5-bis(2-hexyldecyl)-2,3,5,6-tetrahydro-3,6-dioxopyrrolo[3,4-c]pyrrole-1,4-diyl]-alt-[3',3''-dimethyl-2,2':5',2' -terthiophene]-5,5''-diyl] (PMDPP3T)<sup>2</sup> which has an even more red shifted absorption spectrum. As acceptor the fullerene derivative [6,6]-phenyl C61 butyric acid methyl ester (PC<sub>60</sub>BM) is used. The extinction coefficients of both donor acceptor combinations are shown in Figure 5.1. The chemical structure of Si-PCPDTBT, PMDPP3T, PC<sub>60</sub>BM are displayed in Figure Figure 5.2. Si-PCPDTBT:PCBM films were prepared from dichlorobenzene solution with a total concentration of 36 g/L in a donor/acceptor weight ratio of 1:1.5. The solution was kept at 100°C for several hours and cooled to 70°C before spin coating. PMDPP3T:PCBM was prepared with a weight ratio of 1:3 from a chloroform:dichlorobenzene solution (volume ratio of 4:1) with a total concentration of 20 g/L, dissolved at 55°C and spin coated at room temperature. Several other low band-gap materials were tested that did not improve the overall performance and are therefore not considered in this thesis.

<sup>1</sup>Si-PCPDTBT was synthesized according to Scharber et al.[81] and provided by Sybille Allard and Prof. Ulrich Scherf of University of Wuppertal, Germany

<sup>2</sup>PMDPP3T was synthesized by Polyera and first published by Li et al.[82]

### 5.3. Optical Modeling of the Photocurrent in a Multi-Junction Solar Cell.

In order to optimize a multi-layer structure with respect to the generated photocurrents in the active layers the optimum thicknesses of each layer needs to be known. In this section it will be explained how the optimized layer thicknesses can be predicted with the help of a transfer matrix model and the results for hybrid triple-junctions with either an PMDPP3T:PCBM or an Si-PCPDTBT:PCBM sub-cell are presented. Each layer has a different absorption spectrum in the triple-junction layer stack depending on the light that reaches that layer, its wavelength dependent extinction coefficient and the thickness of each layer. By knowing the complex refractive indices of all layers, a transfer matrix formalism can be used to describe the propagation of an electromagnetic wave through such a layer stack.[83] The complex refractive indexes used in this work were either provided by the PVcomB or determined from the transmission and reflection spectra of several layer thicknesses of the material of interest.<sup>3</sup> By this means the absorption in each layer of the multi-layer stack can be calculated in dependence of each layer's thickness. In subsection 2.3.2 it is shown how the  $EQE_{PV}$  is obtained from the absorption spectrum, if the internal quantum efficiency is known. By assuming reasonable  $IQEs$  of 1.0 for the a-Si:H layers[85] and 0.8 for both organic solar cells[81, 82] the  $EQE_{PV}$  was determined and the expected  $J_{SC}$  of each active layer was calculated according to Equation 2.4. Under the assumption of reasonably high  $FFs$  for each active layer, Equation 2.5 can then be used to give an estimate of the  $J_{SC}$  of the multi-junction. The transfer matrix model that has been used in this work is an open source software developed by George F. Burkhard and Eric T. Hoke from Stanford University.[86–88] The original software allows one to calculate the fraction of the incident photons that are absorbed by a respective layer in the full layer stack as a function of the incident photon's wavelength. In order to predict the current density as described above, the program was first extended by James Blakesley at the University of Potsdam to calculate the current densities for two active layers with varying thicknesses and later on in the course of this work it has been extended to three active layers.

The non-active layers, such as the electrode and recombination contact materials are taken into consideration for the optical modeling, though their thicknesses are not varied. The extinction coefficients of these layers are low and their influence on the absorption in the active layers is of minor importance. The full layer stack and the thicknesses of all layers that have not been varied are shown in section B.1. Furthermore, reasonable thickness ranges were chosen for the active layers in order to maintain reasonably high  $FFs$ . The front a-Si:H sub-cell is varied between 40 and 80 nm in 2 nm steps, the organic back-cell is varied

<sup>3</sup>The extinction coefficients were determined with a program written by Matthias Gohlke in 2012 at the University of Potsdam.[84] The Program is based on a reverse transfer matrix formalism that calculates the extinction coefficient of a material from transmission and reflection spectra of films consisting of that material with known thicknesses.

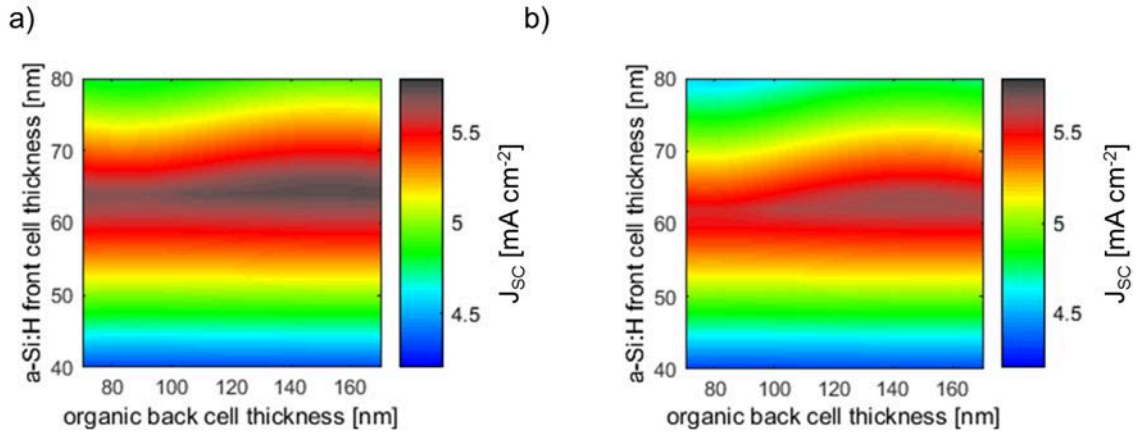


**Figure 5.3.:** Contour plots showing  $J_{sc}$  [ $\text{mA cm}^{-2}$ ] of the triple-junction based on PMDPP3T:PCBM a) or Si-PCPDTBT:PCBM b) in dependence of the a-Si:H front- and organic back-cell thickness. The middle-cell thickness is set to 400 nm in both cases.

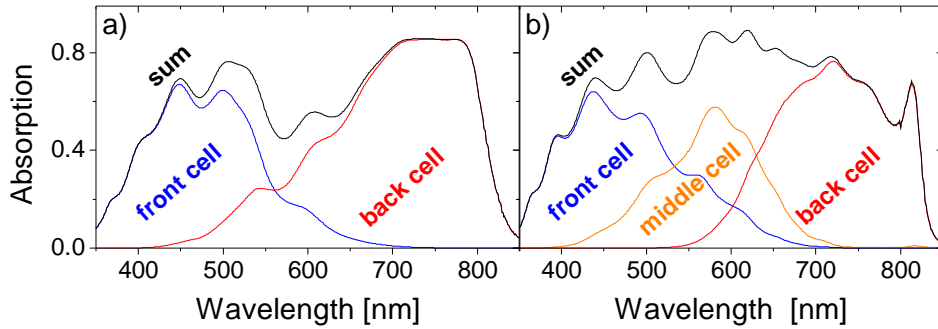


**Figure 5.4.:** Modeled absorption spectra of a) the best tandem cell presented by Albrecht et al.[78] and b) the PMDPP3T:PCBM based triple-junction presented in this work. The total absorption of each cell stack is denoted as black line, the absorption spectra of the modeled sub-cells are colored.

between 70 and 170 nm in 2 nm steps and for the middle a-Si:H sub-cell four thicknesses were tested from 300 to 450 nm in 50 nm steps. In general a thicker middle-cell thickness should give more photocurrent, but as the  $FF$  of a-Si:H cells is known to drop for intrinsic layer thicknesses above 400 nm,[89] the supplied a-Si:H tandem cells on a flat AZO electrode were limited to an intrinsic middle cell thickness of 400 nm. In section B.2 and section B.3 contour plots are shown displaying  $J_{sc}$  of each sub-cell as a function of the a-Si:H front- and the organic back-cell thickness. For each of the four middle-cell thicknesses and for both organic sub-cell materials an extra plot is shown. In Figure 5.3 contour plots in accordance with Equation 2.5 are shown, displaying the lowest of all sub-cell's  $J_{sc}$ s as a function of the front- and back-cell thickness for a middle-cell thickness of 400 nm. Assuming high  $FF$ s of the sub-cells this value should give a good estimate of the total current density that can be expected for triple-junctions using each organic layer.

According to Figure 5.3 the best device efficiency is expected at a front-cell thickness of about 65 nm and a organic back-cell thickness of about 130 to 150 nm for both types of multi-junction. In Figure 5.4 a) the absorption spectra modeled for the best performing tandem device presented before by Albrecht et al.[78] is shown in comparison to Figure b) the modeled absorption spectra of the best performing triple-junction that will be presented in this work. This figure underlines the expected benefit upon introducing another a-Si:H sub-cell to a hybrid tandem device. Especially at intermediate wavelengths (500–700 nm) a considerable absorption enhancement can be seen. Together with the higher *IQE* of the a-Si:H cells, compared to the organic sub-cells, the higher  $V_{OC}$  expected and, at the same time, maintaining high *FFs* this should increase the efficiency of such a triple-junction significantly. The highest expected  $J_{SC}$  for a triple-junction based on PMDPP3T:PCBM with an ITO/PEDOT:PSS recombination contact is  $J_{SC} = 5.79 \text{ mA cm}^{-2}$  and for the Si-PCPDTBT:PCBM based triple-junction  $J_{SC} = 5.59 \text{ mA cm}^{-2}$ . This optical modeling routine set the thickness ranges that should experimentally be realized in the real device to reach these maximum currents. In the next section a closer look will be taken on the actual working devices that were built according to these optimized thickness predictions.

## 5.4. Optimization of Hybrid Multi-Junctions

The big advantage of the hybrid approach is surely the combination of the well established a-Si:H technique with the great flexibility of organic materials. Therefore it was possible to get well working a-Si:H tandem devices with a 65 nm thick active front-cell and a 400 nm thick second active a-Si:H layer with matched sub-cell  $J_{SC}$ s from the PVcomB. The main challenge in building a well working triple-junction is therefore to establish a well working recombination contact between the a-Si:H tandem and the organic sub-cell and to find a suitable low band-gap system to efficiently generate charges in the NIR spectral region, in addition to all processing and measurement difficulties that needed to be solved. Two different types of recombination contacts were tested as the inorganic tandem device could either be delivered with a transparent, sputtered AZO or ITO back contact. The recombination contact needs to efficiently transport charges away from both adjacent sub-cells and ensure ohmic recombination. Therefore high conductivities are in general desirable, however conductivities that are too high will enhance the vertical transport and the collection of leakage current. Based on previous work several PEDOT:PSS formulations with different conductivities<sup>4</sup> and also evaporated silver/molybdenum oxide (Ag/MoO<sub>3</sub>) layers were tested on both AZO and ITO.[78] Working devices were built with different material combinations but the best layer combinations that resulted in the highest *FFs* and efficiencies were AZO/Ag/MoO<sub>3</sub> and ITO/PEDOT:PSS(AI4083). The AZO and ITO layer are both

<sup>4</sup>All different PEDOT:PSS formulations were purchased from Hereaus just like the standard AI4083 with a rather low conductivity compared to the others

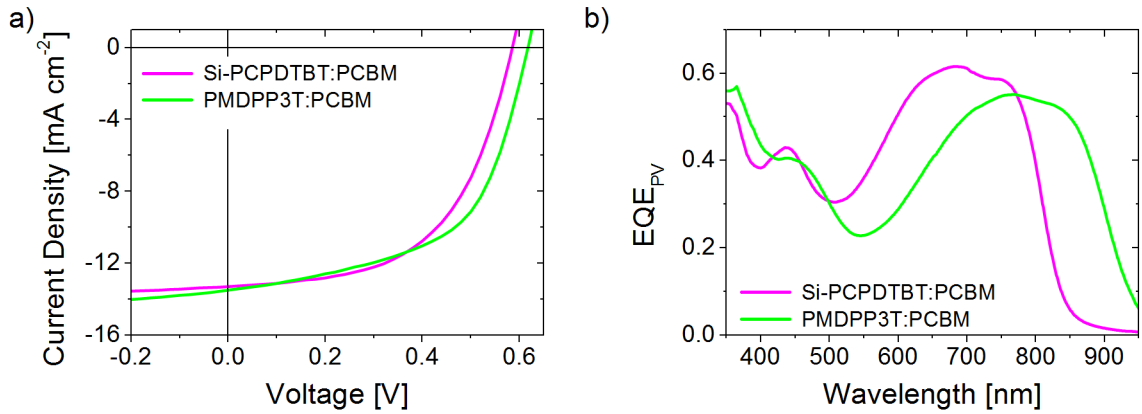


**Figure 5.5.:** Single-junction  $JV$ -characteristics a) and the *photovoltaic external quantum efficiency* b) of Si-PCPDTBT:PCBM and PMDPP3T:PCBM.

about 100 nm thick with either 1 nm silver and 10 nm MoO<sub>3</sub> or 30 nm PEDOT:PSS, respectively. The first triple-junction cells were built with Si-PCPDTBT:PCBM sub-cells that had already proven to work well in the tandem structure.[78] Unfortunately, the best working triple-junction based on Si-PCPDTBT:PCBM only reached an efficiency of 9.7% which is only slightly higher than for the a-Si:H tandem device as can be seen in Table 5.1 where all the best efficiencies of the sub-cells and all triple-junctions are summarized. Nevertheless, the Si-PCPDTBT:PCBM based triple-junction proves the fundamental concept and by comparing the  $V_{OC}$ s it becomes clear that the recombination contact works efficiently. Almost no voltage loss occurs due to series connecting the a-Si:H tandem with an initial  $V_{OC}$  of 1.7 V and the Si-PCPDTBT:PCBM sub-cell with an  $V_{OC}$  of 0.59 V. The Si-PCPDTBT:PCBM triple-junction with an ITO/PEDOT:PSS recombination contact showed a  $V_{OC}$  of 2.27 V and with an AZO/Ag/MoO<sub>3</sub> recombination contact, a  $V_{OC}$  of 2.28 V. At the same time high  $FF$ s of about 78% were established and the predicted  $J_{SC}$ s were nearly reached. The  $J_{SC}$  value expected from the optical modeling is given in Table 5.1 as  $J_{SC}(\text{Sim})$ .

Furthermore, Table 5.1 reveals that the a-Si:H tandem cell  $J_{SC}$  value could not be preserved in the triple-junction. This could either be caused by limiting current from the subsequent organic cell, or due to the fact that in the a-Si:H tandem the second a-Si:H cell benefits from back scattered light at the metal electrode, which would be reduced by another series connected organic cell with an overlapping absorption spectrum. In order to reduce such a potential limitation an alternative low band-gap system was introduced as mentioned earlier. Although the single-junction characteristics of the Si-PCPDTBT:PCBM and the PMDPP3T:PCBM cell are very similar (Table 5.1 and Figure 5.5), the respective currents are generated in different spectral regions. This is indicated by the substantially red shifted absorption of PMDPP3T:PCBM compared to Si-PCPDTBT:PCBM, as shown in Figure 5.1, and finally proven by the  $EQE_{PV}$  measurements of both organic cells depicted in Figure 5.5. To measure the actual sub-cells current densities,  $EQE_{PV}$  measurements with monochro-

**Table 5.1.:** Solar cell parameters for all sub-cells and triple-junctions either with an AZO or ITO based recombination contact. The  $J_{SC}$  is given either as extracted from the  $JV$ -characteristics ( $J_{SC}(JV)$ ), as determined from the  $EQE_{PV}$  measurement ( $J_{SC}(EQE)$ ) or as simulated by optical modeling ( $J_{SC}(Sim)$ ).

System		$V_{OC}$ [V]	$J_{SC}$ [ $\text{mA cm}^{-2}$ ] (JV) (EQE) (Sim)	$FF$ [%]	$PCE$ [%]
a-Si:H/a-Si:H	DJ(ITO)	$1.70 \pm 0.01$	$6.93 \pm 0.07$	$78.2 \pm 0.2$	$9.2 \pm 0.1$
	DJ(AZO)	$1.71 \pm 0.01$	$6.95 \pm 0.08$	$78.0 \pm 0.5$	$9.3 \pm 0.2$
Si-PCPDTBT:PCBM	SJ	$0.59 \pm 0.01$	$13.24 \pm 0.09$	$55.2 \pm 0.4$	$4.2 \pm 0.1$
	TJ(ITO)	$2.27 \pm 0.01$	$5.36 \pm 0.02$   5.28   5.59	$77.6 \pm 0.2$	$9.4 \pm 0.1$
	TJ(AZO)	$2.28 \pm 0.01$	$5.45 \pm 0.01$   5.36   5.51	$77.8 \pm 0.2$	$9.7 \pm 0.1$
PMDPP3T:PCBM	SJ	$0.62 \pm 0.01$	$13.4 \pm 0.2$	$55 \pm 1$	$4.6 \pm 0.2$
	TJ(ITO)	$2.31 \pm 0.01$	$5.82 \pm 0.06$   5.68   5.79	$79.6 \pm 0.2$	$10.7 \pm 0.1$
	TJ(AZO)	$2.31 \pm 0.01$	$5.77 \pm 0.04$   5.70   5.73	$77.3 \pm 0.8$	$10.3 \pm 0.2$
rough front AZO	TJ(ITO)	2.26	6.83	75.8	11.7
rough front AZO	TJ(AZO)	2.29	6.80	73.8	11.5

matic background illumination were performed as described in section 4.2. By this means the actual current limiting sub-cell can be identified and its  $J_{SC}$  value, determined from the  $EQE_{PV}$  according to Equation 2.4, is denoted as  $J_{SC}(EQE)$  in Table 5.1. The measured  $EQE_{PV}$  spectra of the sub-cells of hybrid triple-junctions with an ITO/PEDOT:PSS recombination contact and either a Si-PCPDTBT:PCBM or PMDPP3T:PCBM organic sub-cell are displayed in Figure 5.6.

It is important to note that the a-Si:H tandem cells are exactly the same for both displayed triple-junctions. The front-cells have almost identical  $J_{SC}$  of about  $6.5 \text{ mA cm}^{-2}$ , but the a-Si:H middle-cell of the PMDPP3T:PCBM based triple-junction shows significantly higher  $EQE_{PV}$  in the intermediate wavelength regime from  $\sim 530\text{--}700 \text{ nm}$ , resulting in a middle-cell  $J_{SC}$  of 5.28 and  $5.68 \text{ mA cm}^{-2}$  for the Si-PCPDTBT:PCBM and PMDPP3T:PCBM based triple-junctions, respectively. The  $EQE_{PV}$  of the Si-PCPDTBT:PCBM organic back-cells yields a  $J_{SC}$  value of 6.70 and  $8.84 \text{ mA cm}^{-2}$  for the PMDPP3T:PCBM cell, respectively. Therefore, the a-Si:H middle-cell is current limiting in both triple-junctions, with a higher current for the PMDPP3T:PCBM based triple-cell. This higher  $EQE_{PV}$  and with that  $J_{SC}$  in the a-Si:H middle-junction is displayed in Figure 5.6 and reasoned by the red shifted absorption of the PMDPP3T:PCBM compared to the Si-PCPDTBT:PCBM cell. This shifted absorption of the organic sub-cell causes a larger fraction of photons in the intermediate wavelength regime that were not absorbed when they passed the a-Si:H layers for the first time, to be reflected off the metal electrode on top of the organic and subsequently be absorbed by the a-Si:H middle-cell when they reach it a second time. Additionally, the PMDPP3T:PCBM sub-cell produces significantly higher current than the Si-PCPDTBT:PCBM sub-cell which is beneficial as well due to less influence of the worse organic  $FFs$  compared to the a-Si:H cells. Therefore it was possible to increase the efficiency of the triple-junction by about 10%

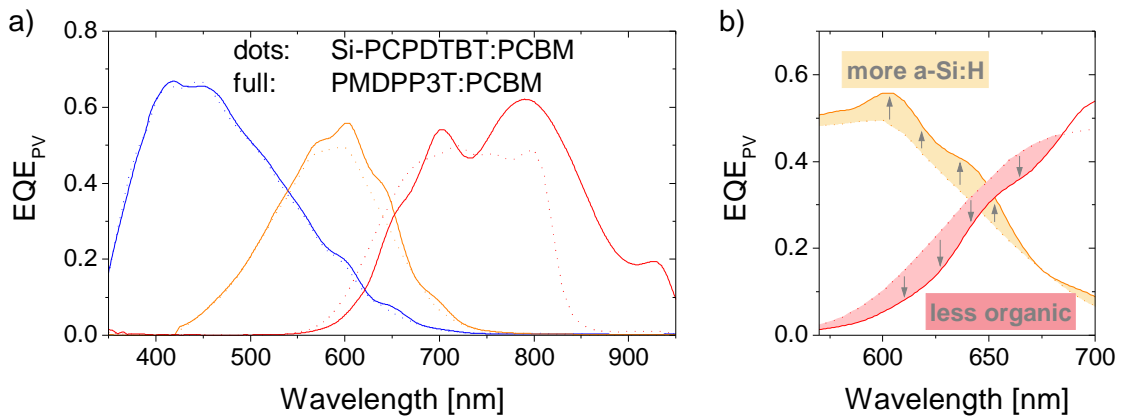


**Figure 5.6.:** a) Sub-cell  $EQE_{PV}$  spectra of both best performing triple-junction solar cells. The a-Si:H front- and middle-cell are displayed in blue and orange, respectively. The organic back-cell is depicted in red. Full lines belong to the PMDPP3T:PCBM and dotted lines to the Si-PCPDTBT:PCBM based TJ. The important intermediate wavelength range for the middle- and the back-cell is again shown in b) and the differences in sub-cell  $EQE_{PV}$  for the middle- and back-cells are highlighted in light red and orange.

to a total PCE of  $10.7 \pm 0.1\%$  with a very high  $FF$  of  $\sim 80\%$ . There is good agreement between the  $J_{SC}$  from  $EQE_{PV}$ ,  $JV$  measurements and from optical modeling with only slightly lower values from the  $EQE_{PV}$  measurements that can be reasoned with uncertainties in the  $EQE_{PV}$  measurements as outlined in section 4.2. In order to circumvent the current limitations of the a-Si:H middle-cell, the absorption needs to be increased in this layer. This can either be achieved by increasing the cell thickness or by scattering the incoming light to increase the absorption pathway in the cell. To realize scattering, the transparent front electrode, composed of AZO, is etched in dilute hydrochloric acid (HCl) which increases the surface roughness. The subsequent a-Si:H layers were deposited as described before with slight modifications in i-layer thickness (60 and 500 nm) to ensure current matching in the a-Si:H tandem sub-cell. Additionally, the n-layer of the front-cell was modified by adding a 20 nm thick  $\mu c$ -SiO<sub>x</sub> layer that mitigates the detrimental effects of local shunts related to the growth on the textured front AZO to retain a high  $V_{OC}$ . [90, 91] As the optimized organic layer thickness is about 150 nm, it is important that the roughness of the front AZO is not too pronounced, because of the inability of the deposited a-Si:H cells to flatten out the roughness of the electrode completely, as can be seen in section B.4 where Scanning Electron Microscopy (SEM) pictures of an a-Si:H tandem on either a flat or a rough front AZO are displayed. This could hamper the homogeneous film formation of the organic, increasing leakage currents and limiting the  $FF$  as seen by Kim et al. for an a-Si:H organic tandem cell. [92] The rough a-Si:H tandem cells as shown in section B.4 could however be fully covered with a closed organic layer of PMDPP3T:PCBM which can be seen from the cross section SEM picture of the triple-junction (Figure 5.7 b)). By incorporating light scattering, finally a record efficiency of 11.7% was achieved for a PMDPP3T:PCBM based triple-junction. The  $JV$ -characteristics

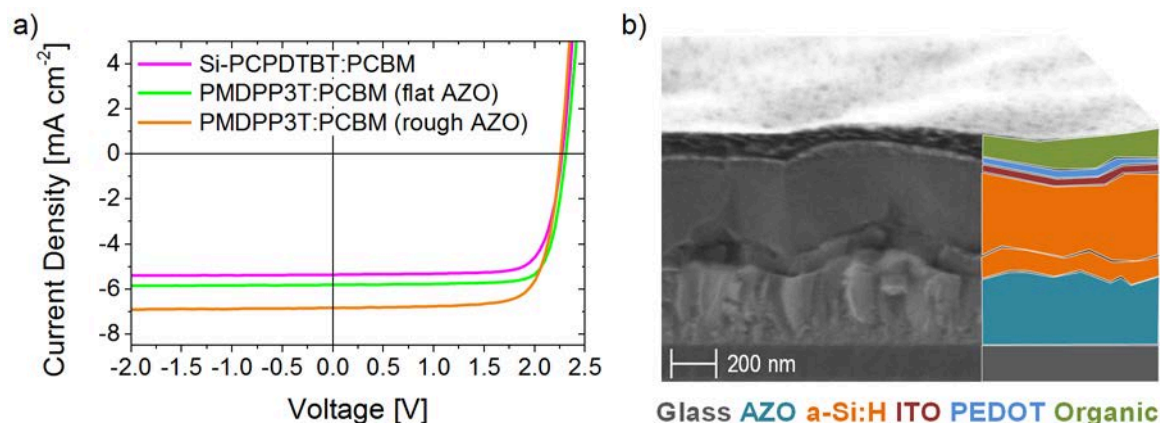


**Figure 5.7.:** a)  $JV$ -characteristics of the best TJs with the best performing PMDPP3T:PCBM based TJ on a rough front AZO. b) Scanning Electron Microscope picture of the final TJ layer stack on a rough front AZO without the Ca/Ag back electrode.

of the best working triple-junctions based on Si-PCPDTBT:PCBM or PMDPP3T:PCBM are shown in Figure 5.7 a). The Si-PCPDTBT:PCBM based cell was only produced on a flat front AZO, the PMDPP3T:PCBM based triple-junction is displayed for a flat or rough front AZO. Optical modeling and  $EQE_{PV}$  measurements were not applicable for the rough triple-junction. Optical modeling relies on a transfer matrix model which only accounts for perpendicular light propagation in the layers. The spot of the probe light for the  $EQE_{PV}$  measurements is of nearly the size of the pixel and due to the light scattering too much of the probe light is scattered out of the active area making the reference measurement with the available setup meaningless. Nevertheless, the  $JV$ -characteristics gave reliable results with an increased current density of  $\sim 1 \text{ mA cm}^{-2}$  and almost no  $V_{OC}$  loss compared to the triple-junction with a flat front electrode (Figure 5.7). The  $FF$  decreased, but less than 5%, allowing for the very efficient performance. The  $FF$  decrease can be reasoned by two effects; on the one hand side due to the thicker a-Si:H layer and on the other hand, because of better balanced sub-cell currents increasing the influence of the worse  $FF$  of the organic sub-cell.

## 5.5. Discussion and Outlook

Overall, a high efficiency hybrid multi-junction was realized by the close collaboration of inorganic and organic photovoltaic research groups. The solar cell presented in this thesis held the efficiency record for this type of thin film hybrid multi-junction solar cells for about one year and it demonstrated the potential of this type of hybrid device.[5] Recently a hybrid multi-junction, also comprising of PMDPP3T:PCBM and a-Si:H sub-cells was presented by Tan et al. with an efficiency of 13.2%, [72] showing the potential of the herein presented type of multi-junctions. Different measures can be taken to further increase the efficiency of this type of solar cell. First of all, there is ongoing research to find better low band gap materials

that enable efficient charge carrier generation in the NIR, while at the same time yielding high  $V_{OC}$ . [93, 94] Furthermore, there is still room for optimization of the electrodes, making them highly transparent and improving the scattering front electrodes to increase the light pathway in the cells or introducing micro cavities. [72] This type of multi-junction with high *open circuit voltage* is also attractive for alternative applications such as water splitting. [32, 33] Concluding, it should be mentioned that, although the efficiencies of this type of cells will always be limited, the combination of a well studied inorganic solar cell technology that is established on the market with rather new organic solar cell techniques bares interesting opportunities for future research and might pave the way for cost effective improvements of inorganic thin film multi-junctions as time and energy consuming plasma enhanced chemical vapor deposition steps can be exchanged with solution based processing. Nevertheless, the fundamental drawback of this type of hybrid multi-junction solar cells is their overall low *open circuit voltage*. This becomes clear by considering which wavelength regime is relevant for the absorption of each sub-cell and comparing the low energy onset of the absorption – or  $EQE_{PV}$ , as shown in Figure 5.6 – with the  $V_{OC}$  of the respective sub-cell. The first, thin a-Si:H sub-cell mainly generates photocurrent at wavelengths  $\lambda < 600$  nm, which corresponds to an energy gap of  $E_g \approx 2$  eV, while the best performing a-Si:H single-junction solar cells reach a  $V_{OC}$  of only  $\approx 0.85$  V. For the second a-Si:H sub-cell the onset of relevant photocurrent generation is determined to be approximately at  $\lambda \approx 680$  nm, corresponding to  $E_g \approx 1.8$  eV. For the organic solar cell the onset is determined to be at  $\lambda \approx 950$  nm and  $E_g \approx 1.3$  eV. If we assume that a  $V_{OC}$  of 0.85 V can be reached in each a-Si:H sub-cell and by taking the  $V_{OC}$  value of the PMDPP3T:PCBM solar cell of  $V_{OC} = 0.62$  V, a total  $V_{OC}$  of approximately 2.52 V is expected. The summed up value of the sub-cells gap energies is  $E_g \approx 5.1$  eV and therefore a factor of  $\approx 2$  larger than the total  $V_{OC}$ . This rough approximation reveals a severe limitation of such hybrid multi-junctions. A better understanding of what determines  $V_{OC}$  and the respective losses, especially with respect to the less understood mechanisms in organic solar cells, is necessary.

# Chapter 6

## Experimental Investigation of the Open Circuit Voltage and Free Charge Carrier Recombination in Organic Solar Cells

In this chapter experimental results concerning the *open circuit voltage* ( $V_{OC}$ ) in organic solar cells will be presented. The  $V_{OC}$  is closely related to the CT-state energy and the radiative and non-radiative losses in many organic solar cells, as already discussed in section 3.1. The CT-states themselves form at the interface between donor and acceptor. Therefore, many aspects such as molecular orientation, degree of crystallization of the donor and acceptor and the overall mesoscale morphology are found to influence the CT-state energy.[95–99] Furthermore, the role of delocalization of the CT-state on the generation efficiency has been discussed[96, 100] and the role of donor acceptor orientation on the device performance and interfacial energetics have largely been studied by means of theoretical calculations and/or model bilayer systems.[97–104] The  $V_{OC}$  can also be changed by simply exchanging the chemical composition of organic solar cell systems, reasoned by the different energetics that are present in various conjugated materials used in organic photovoltaics. Besides high extinction coefficients it is this variety of materials and energetics, which can be tuned by changing the chemical compositions, that make organic semiconductors interesting for solar cell applications.

The experimental work, presented in this chapter, is split into three sections each following different approaches to understand what determines  $V_{OC}$ , covering many of the aforementioned topics. All investigations were done in collaboration with either the University of Santa Barbara (UCSB), or the University of North Carolina (UNC) who build the respective solar cells, while measurements concerning the  $V_{OC}$  were almost exclusively done in the course of this thesis at the University of Potsdam (UP). The absorptive and emissive character of the

---

CT-states is utilized, as described by Vandewal et al.[34] and outlined in chapter 3, to gain a better understanding of  $V_{OC}$  in the different investigated model situations. A sensitive spectrometer setup with an InGaAs detector, as described in section 4.3, is used to measure CT emission even in the near infrared spectral region. By this means several open questions regarding  $V_{OC}$  are addressed experimentally, corroborating existing theories or incentivizing the scientific community. Prior to the experimental discussion, here the key topics related to each experimental part are first outlined in a broader context.

- In the first part of this chapter the effects of molecular orientation of the polymer on  $V_{OC}$  are studied for a model bilayer solar cell system. So far changes in  $V_{OC}$  were often solely related to a change of the HOMO positions due to altered orientations.[99, 105, 106] Theoretical approaches by means of Density Functional Theory (DFT) were also used to determine the CT-state energy's dependence on molecular orientation at the interface.[100] A big drawback of most experimental approaches however is related to non ideal hetero-junctions between donor and acceptor. Molecular diffusion has been shown to manipulate ordered interfaces,[107, 108] and often interfacial roughness limits a perfect orientation.[97] Thus the influence of the molecular orientation on the radiative and non-radiative loss channels has not been studied experimentally so far. Whereas radiative losses are unavoidable due to the laws of thermodynamics,[36, 44] reduction of non-radiative losses should in principle be possible, but so far only little is known about these losses and how they relate to molecular orientation. This issue is addressed by explicitly measuring non-radiative losses and CT energies in perfectly ordered edge- or face on oriented bilayers in combination with the fullerene acceptor  $C_{60}$ .
- In the second part of this chapter the influence on the  $V_{OC}$  of three different ways of introducing fluorination to the same polymer backbone is examined. It is well known that fluorination can influence the morphology of bulk hetero-junctions and it is known to lower the HOMO energy of the polymer.[9, 11, 109] By this means the  $V_{OC}$  can typically be increased due to fluorination compared to the non-fluorinated version of the donor polymers in combination with the common fullerene acceptor PCBM.[9, 109] Furthermore, for ternary blends with two different acceptor molecules and the same donor it was found before that the  $V_{OC}$  is not dominated by the lower energy gap between donor and the respective acceptor, but rather shifts with the ratio of the two different acceptors.[110–113] The  $V_{OC}$  of a physical ternary blend of fluorinated and non-fluorinated donor (ratio 1:1) with the fullerene acceptor PCBM will be examined. This ternary blend can then also be compared to two other systems that consist of the same polymer backbone and also PCBM as acceptor, but introduce the 1 to 1 ratio of fluorinated and non-fluorinated units by either exchanging only one hydrogen on every monomer unit with fluorine or by building the polymer of completely fluorinated and non-fluorinated monomer units that are randomly distributed. This provides three different systems that all will adapt varying local donor/acceptor interfaces, but have

the same relative amount of fluorine atoms attached to the same polymer backbone. Hereby it will be possible to discuss the influence of the local distribution of fluorinated units on the energetics of these donor/acceptor systems and the resulting  $V_{OC}$ .

- In the third part of this chapter the changes in  $V_{OC}$  that accompany the exchange of the acceptor molecule are investigated. The indene-  $C_{60}$  bisadduct (ICBA) has been regarded as a promising alternative to PCBM in organic solar cells as it provides higher  $V_{OC}$ s,[114–116] this is reasoned by the higher LUMO energy of ICBA compared to PCBM, which is found to be larger by  $\sim 0.2$  eV.[114] And indeed it has been shown that the *power conversion efficiency* can be increased by 50% by using ICBA instead of PCBM with the well studied poly(3-hexylthiophene) (P3HT) as donor material.[77] However, P3HT seems to be an exception and usually the overall performance is inferior upon using ICBA instead of PCBM as a acceptor. Different reasons have been put forward to explain this issue, like too low driving force for CT-state generation,[117–120] inefficient exciton quenching and charge generation, which are found to be connected to the energy differences between CT-state and minimal absorption onset energy in typical polymer/fullerene systems,[120, 121] energy back-transfer from the CT-exciton to the singlet exciton and subsequent rapid recombination,[122] or inefficient generation related to unfavorable morphology[115, 117] and low electron mobilities in ICBA devices that impede the charge transport.[115, 121, 123] Herein, the fluorinated donor polymer PBnDT-FTAZ (FTAZ) is tested with ICBA. FTAZ has proven to reach high efficiencies of about 7% in thick devices with PCBM[10, 109, 124] and it is of particular interest as it has a similar band-gap as P3HT, but shows a  $V_{OC}$  that is  $\approx 0.2$  eV higher, with PCBM as acceptor. Unfortunately, FTAZ is no exception to what is measured for many donor polymers and the efficiency could not be improved by exchanging PCBM with ICBA. Besides the examination of the  $V_{OC}$ , charge carrier dynamics are measured and a conclusive picture is derived, explaining the overall performance of these ICBA based cells. By this means several of the theories concerning the device performance of ICBA based cells are reviewed.

## 6.1. Open Circuit Voltage in Bilayer Solar Cells comprising C<sub>60</sub> and either Face- or Edge-On oriented Donor Molecules

The donor molecule p-SIDT(FBTTh<sub>2</sub>)<sub>2</sub> has proven to give high efficiencies in BHJ solar cells with PCBM.[125] Furthermore, it has been shown that p-SIDT(FBTTh<sub>2</sub>)<sub>2</sub> shows high levels of self organization and large crystalline domains have been realized.[125] It is possible to process layers of p-SIDT(FBTTh<sub>2</sub>)<sub>2</sub> with exceptional high fractions of either edge-on (94%) or face-on (99.5%) oriented molecules which makes it possible to process bilayers with a very well controllable donor/acceptor orientation in combination with evaporated C<sub>60</sub>. The  $V_{OC}$  investigation of those bilayers, as detailed below, is part of a comprehensive study including morphological and charge generation investigations, and has recently been submitted for publication.[126] Device preparation and morphology investigations were performed by collaborators and will be discussed briefly in this thesis to show the controllability of donor orientation.

### 6.1.1. Device Structure and Solar Cell Performance

The donor molecule p-SIDT(FBTTh<sub>2</sub>)<sub>2</sub> was originally tailored to achieve high  $V_{OC}$ s in combination with the electron acceptor PCBM. The chemical structure of p-SIDT(FBTTh<sub>2</sub>)<sub>2</sub> is shown in Figure 6.1. It consists of electron rich (dithiophene and silaindacenodithiophene (SIDT)) and electron deficient (fluorobenzothiadiazole) units.[125] This structure leads to an optical band-gap of 1.84 eV and a HOMO level of  $-5.45$  eV.[125] It was shown by grazing incidence wide-angle X-ray scattering (GIWAXS) that neat p-SIDT(FBTTh<sub>2</sub>)<sub>2</sub> films are well ordered and preferentially oriented face-on with  $\pi$ -stacking that prolongs through the whole thickness of the film.[125] However, the orientation of p-SIDT(FBTTh<sub>2</sub>)<sub>2</sub>, processed on top of the transparent conductive polymer poly(3,4-ethylenedioxythiophene) polystyrene sulfonate (PEDOT:PSS), can be altered to a preferentially edge-on configuration by adding diiodooctane (DIO) as a solvent additive to chlorobenzene (CB) in a volume ratio of 0.4% v/v. This ratio is very sensitive and small changes will decrease the percentage of edge-on oriented molecules. Thus the actual orientation of the film needs to be measured carefully. The actual ratio can be determined from GIWAXS measurements of the films. The anisotropy of the scattered  $\pi$ -stacking peak as a function of angle is shown in section C.1. In order to make reliable connections between  $V_{OC}$  losses and molecular orientation of donor and acceptor it is necessary to have very well defined edge- or face-on donor orientation of p-SIDT(FBTTh<sub>2</sub>)<sub>2</sub>. The p-SIDT(FBTTh<sub>2</sub>)<sub>2</sub> films cast on PEDOT:PSS from CB show a molecular orientation with 99.5% face-on character; films from CB with 0.4% v/v DIO led to an edge-on orientation of 94%. Additionally GIWAXS measurements can be used to learn about the quality of the donor/acceptor interface and if there is intermixing of the evaporated C<sub>60</sub> into the edge- or face-on oriented p-SIDT(FBTTh<sub>2</sub>)<sub>2</sub> layer. GIWAXS pictures were taken of films with

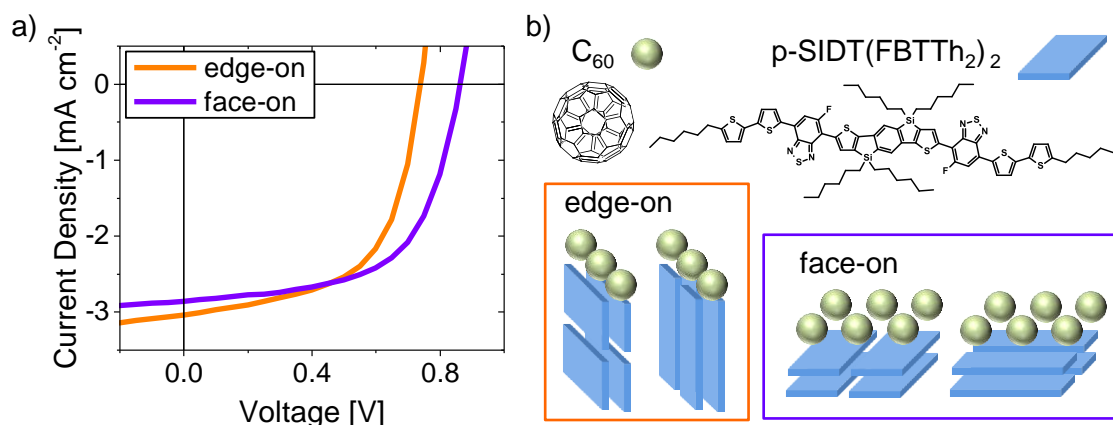


**Figure 6.1.:** a)  $JV$ -characteristics of edge- or face-on oriented bilayers of p-SIDT(FBTTh<sub>2</sub>)<sub>2</sub> and C<sub>60</sub> b) Chemical structure of p-SIDT(FBTTh<sub>2</sub>)<sub>2</sub> and C<sub>60</sub> and representations of the orientations of p-SIDT(FBTTh<sub>2</sub>)<sub>2</sub> to C<sub>60</sub>. The edge-on configuration allows both edge- or end-on, but in both cases the  $\pi$ -faces of C<sub>60</sub> and p-SIDT(FBTTh<sub>2</sub>)<sub>2</sub> are not facing each other.

edge- or face-on oriented donor molecules with either 0, 1, 5, 10 or 30 nm of C<sub>60</sub> evaporated on top, as well as a neat C<sub>60</sub> film for the reference. By comparing the integrated intensity of the C<sub>60</sub> scattering peak as a function of C<sub>60</sub> thickness it can be tracked how well the evaporated C<sub>60</sub> forms a closed layer that actually scatters the incoming X-rays. For a perfect layer formation without any intermixing a direct dependence of integrated, scattered intensity and layer thickness is expected. In section C.2 intensity cross sections of corresponding GIWAXS pictures are shown for different C<sub>60</sub> thicknesses. The integrated intensities of the C<sub>60</sub> peaks for edge- and face-on oriented p-SIDT(FBTTh<sub>2</sub>)<sub>2</sub> are normalized corresponding to the neat C<sub>60</sub> film and plotted in Figure 6.2 b). Both films show nearly linear increase of integrated scattering intensity of the C<sub>60</sub> peak with increasing C<sub>60</sub> thickness, indicating that intermixing is not strong. In fact, the weak deviation from linearity for the edge-on sample is reasoned by pinholes in the neat edge-on p-SIDT(FBTTh<sub>2</sub>)<sub>2</sub> layer as can be seen in section C.3. Further proof for the remarkably well ordered layers is found by cross-section, high-resolution - transmission electron microscopy (HR-TEM) of both layers (Figure 6.2) which do not show any disturbance at the donor/acceptor interfaces.

After it was shown that the molecular orientation of p-SIDT(FBTTh<sub>2</sub>)<sub>2</sub> can efficiently be changed from a face- to edge-on orientation and evaporation of C<sub>60</sub> does not interfere significantly with the topmost molecular p-SIDT(FBTTh<sub>2</sub>)<sub>2</sub> layers, bilayer solar cells with very well oriented interfaces were built with p-SIDT(FBTTh<sub>2</sub>)<sub>2</sub> as donor and C<sub>60</sub> as acceptor layer. The full layer stack consists of ITO/PEDOT:PSS (35 nm)/p-SIDT(FBTTh<sub>2</sub>)<sub>2</sub>(45 nm)/ C<sub>60</sub> (45 nm)/BCP (4 nm)/Al (80 nm) with bathocuproine (BCP) and aluminum (Al) forming the cathode. The processing of the PEDOT:PSS and the active layers was performed exclusively at UCSB and cells were shipped without the cathode to UP. The solar cells have then been

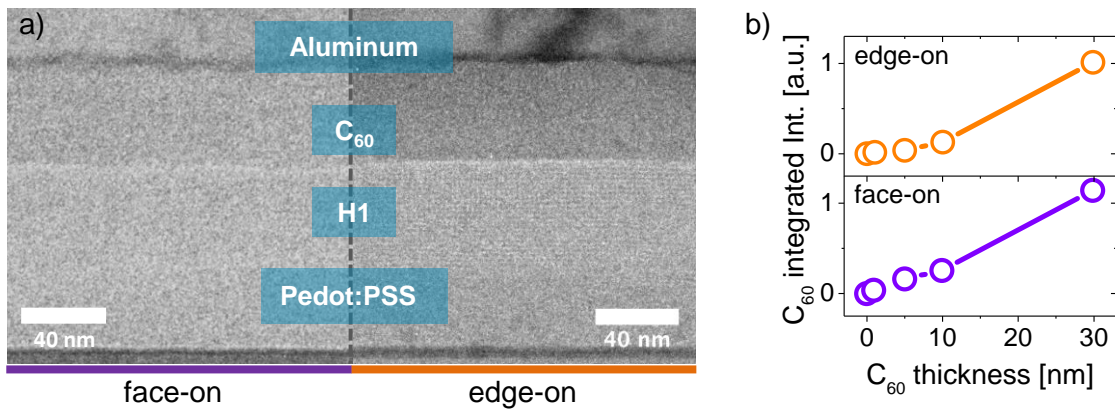


**Figure 6.2.:** a) HR-TEM cross-section pictures of bilayer films with edge- or face-on oriented p-SiDT(FBTTh<sub>2</sub>)<sub>2</sub> covered with evaporated C<sub>60</sub>. b) Integrated intensity of the C<sub>60</sub> scattering peak in dependence of C<sub>60</sub> thickness.

finalized at UP by evaporating the back electrode to avoid its oxidation during shipping. This procedure has given comparable device performance with slightly higher  $V_{OC}$  values for the edge-on devices finalized at UP compared to those measured at UCSB (section C.4). In Figure 6.1 the  $JV$ -curves of the devices on which most of the electroluminescence measurements were performed on, are displayed. These cells showed rather similar device performance as the references measured at UCSB. Although there are performance deviations from device to device (Figure C.4) the  $V_{OC}$  difference between edge- and face-on bilayers is always present and ranges from  $\sim 100$  to at maximum 150 mV. The biggest  $V_{OC}$  difference was found for the devices prepared without shipping. Interestingly only the  $V_{OC}$  values of the edge-on films vary significantly; the face-on devices show a  $V_{OC}$  in the range of  $\sim 0.84$ – $0.86$  V, whereas the  $V_{OC}$  of the edge-on devices can differ by 50 mV for different devices.

The pinholes in the edge-on films raise the question if the lower  $V_{OC}$  is an artifact of this and introduced by direct contact of C<sub>60</sub> and the PEDOT:PSS layer. To clarify this issue the edge-on and face-on oriented bilayers were build also on a molybdenum trioxide (MoO<sub>3</sub>) layer with significantly higher work function than the PEDOT:PSS layer. The resulting  $JV$ -characteristics are shown in section C.4. The average  $V_{OC}$  shift between both configurations again is at  $\sim 110$  mV and the  $V_{OC}$ s are close to the values measured on a PEDOT:PSS electrode. This shows that the  $V_{OC}$  difference is indeed determined by the molecular interaction between donor and acceptor instead of a potential interaction between C<sub>60</sub> and the electrodes. The differences in  $V_{OC}$  of these bilayer systems were investigated carefully by evaluating the  $EQE_{EL}$  and  $EQE_{PV}$  spectra as outlined in section 3.1 and are discussed in the following section.

### 6.1.2. The Open Circuit Voltage of p-SIDT(FBTTh<sub>2</sub>)<sub>2</sub>/ C<sub>60</sub> Bilayer Solar Cells

The close connection between  $V_{OC}$  and the electroluminescent and photovoltaic quantum efficiency spectra under the assumption of quasi-equilibrium conditions was discussed in section 3.1. The implication of applying Marcus-theory to describe emission and absorption of the CT-state is that their respective maxima are shifted by two times the reorganization energy  $\lambda$  and that the CT-state energy is exactly the midpoint between emission and absorption maxima, as it is the free energy difference between the CT ground and excited state. This assumption should hold true if not only the absorption and emission of a single CT-state is taken into account but also an inhomogeneously broadened CT-state manifold, as shown by Burke et al.[47] They showed that the spectra of such a CT-state manifold can still be described by Gaussian functions but yield temperature dependent, effective CT- and reorganization energies. The experimentally measured CT-state energy however already includes the effects of disorder and so the effective band-gap should be identified with the measured CT-state energy at zero Kelvin.

By referring to Equation 3.11 it becomes clear that temperature dependent measurements of the  $V_{OC}$  should extrapolate to that CT-state energy at zero Kelvin. In Figure 6.3 temperature dependent  $V_{OC}$  measurements performed for the edge- or face-on bilayers are summarized. The CT-state energy values, extracted by linear extrapolation to zero Kelvin, are  $1.40 \pm 0.02$  eV and  $1.31 \pm 0.02$  eV for the face-on and, respectively edge-on oriented cells. The average of three different intensities and three different measurements is taken. One measurement includes the averaged  $V_{OC}$  values of six different pixels of Peltier cooled samples at a sun simulator and four different pixels of cryostat cooled samples with LED illumination.

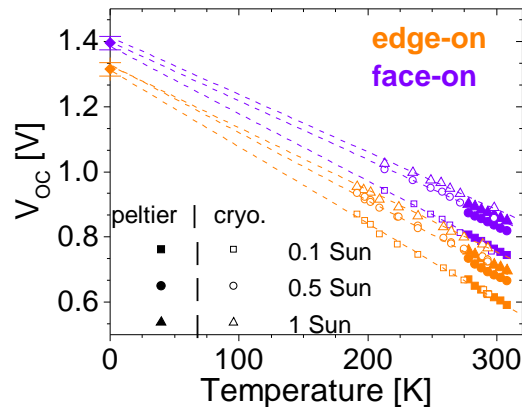


**Figure 6.3.:** Temperature dependent  $V_{OC}$  data for edge- and face-on based solar cells. Measurements were performed either in a cryostat with illumination by a LED with three different intensities close to 100, 50 or 10  $\text{mW cm}^{-2}$ , or with a Peltier cooled sample holder at the sun simulator diluted by optical density filters.

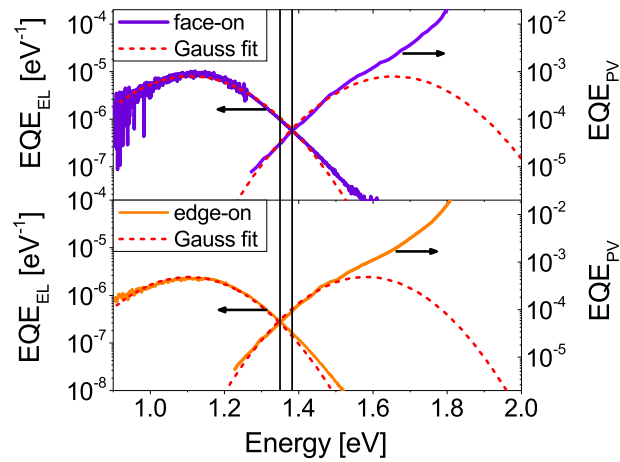


**Figure 6.4.:** Photovoltaic and electroluminescence external quantum efficiency spectra of the edge- and face-on oriented bilayer systems. The red dashed lines denote the Gaussian fits to the data according to Equation 3.9 and Equation 3.10.

Additionally, the CT-state energy can be determined from the Gaussian fits to the electroluminescence and photovoltaic external quantum efficiency spectra according to Equation 3.10 and Equation 3.9. Electroluminescence spectra were collected for three different edge- or face-on devices at different injection currents. In Figure 6.4 the  $EQE_{EL}$  and  $EQE_{PV}$  are displayed in combination with the Gaussian fits for one edge- and one face-on sample at the lowest injected current measured for that respective device; in section C.7 the spectra of the other devices are displayed. The injection voltage for the electroluminescence measurements needs to be as low as possible for quasi-equilibrium conditions. Gaussian fits yield a CT-state energy of  $1.38 \pm 0.01$  eV and  $1.33 \pm 0.02$  eV for the face-on and edge-on oriented cells, respectively. These values are in close agreement with those obtained from the temperature dependent  $V_{OC}$  measurement. Furthermore, the shift in CT-state energy is in agreement with the shift of the HOMO energy of face- or edge-on oriented p-SIDT(FBTTh<sub>2</sub>)<sub>2</sub> layers as determined by UPS of about 60 meV (section C.5). This shift is however too small to explain the shift in  $V_{OC}$  of up to 150 meV indicating that the recombination losses are different in edge- or face-on based bilayers, with larger  $V_{OC}$  losses in the edge-on case.

Recalling Equation 3.11 allows for the calculation of the radiative  $V_{OC}$  loss with the parameters obtained by the Gaussian fits and the respective photogenerated currents of each device. This generation current is approximated by the averaged short circuit current of each device as reasonably high  $FF$ s are measured and no strong field dependence of generation was observed (section C.6). In Table 6.1, for each device, the extracted values determining the  $V_{OC}$  are summarized, including the radiative loss, the non-radiative loss (determined by the  $EQE_{EL}$  that was measured for the lowest injected current), the parameter  $f$  (section 3.1), the CT-state energy, the reorganization energy and the averaged  $V_{OC}$  values for each device as determined from the  $JV$  measurements. The non-radiative  $V_{OC}$  loss is calculated from the absolute  $EQE_{EL}$  as shown in section 3.1. For the edge-on device e3 and the face-on

**Table 6.1.:**  $V_{OC}$  losses determined from the spectral analysis of  $EQE_{EL}$  and  $EQE_{PV}$ .

sample	$V_{OC,meas.}$ [V]	$J_{SC}$ [mA cm <sup>-2</sup> ]	$E_{CT}$ [eV]	$\lambda$ [eV]	$f$ [eV <sup>2</sup> ]	$\Delta V_{OC,Rad}$ [V]	$\Delta V_{OC,Non-Rad}$ [V]	$V_{OC,calc.}$ [V]
edge-on								
e1	0.741	3.6	1.325	0.260	2.5E-4	0.183	0.379	0.763
e2	0.746	3.5	1.320	0.260	2.3E-4	0.178	0.386	0.756
e3	0.749	4.0	1.340	0.250	2.2E-4	0.177	0.359	0.804
face-on								
f1	0.856	3.4	1.380	0.290	4.5E-4	0.200	0.317	0.863
f2	0.867	4.0	1.375	0.270	3.0E-4	0.186	0.331	0.858
f3	0.840	4.0	1.380	0.285	4.0E-4	0.193	0.327	0.860

device f3 only one injection current was used and the non-radiative loss, that is shown in Table 6.1, is given for that injection condition. For the other devices (edge-on: e1, e2 and face-on: f1, f2) the injection conditions were varied and the non-radiative loss is given for the lowest injection currents. By comparing the measured ( $V_{OC,meas.}$ ) and the calculated ( $V_{OC,calc.}$ ) *open circuit voltage* it becomes clear that a better agreement is achieved for the devices in which the losses are determined at lower injection current. This, however, implies that the non-radiative losses and thus  $EQE_{EL}$  depend on the injection current. Overall the variation between measured and calculated  $V_{OC}$  is in the range of only 10 to 50 mV, showing the accuracy of the used evaluation method.

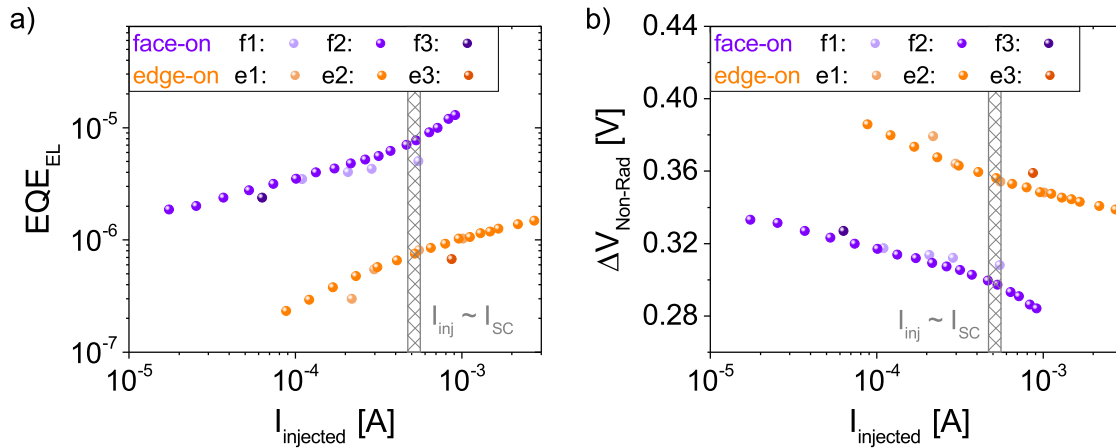


**Figure 6.5.:** Absolute  $EQE_{EL}$  a) and non-radiative  $V_{OC}$  loss determined from the emission spectra at different injected current. The results for three different edge- and face-on samples are summarized. For devices e2 and f2 a large range of injection currents was probed.

In order to investigate the voltage dependence of the  $EQE_{EL}$ , samples e2 and f2 were measured at various injection currents. In Figure 6.5 a) the injection current dependence of  $EQE_{EL}$  is shown and in Figure 6.5 b) the corresponding  $V_{OC}$  loss is depicted. If the non-radiative losses of the edge- and face-on devices are compared at similar injection currents,

e.g. at injection currents corresponding to the short circuit current, the difference in the non-radiative  $V_{OC}$  loss is apparent and about 50–60 mV. In Figure 6.6 a) the full, injection current dependent  $EQE_{EL}$  spectra of device e2 and f2 are shown; the integrated spectra give the absolute  $EQE_{EL}$  shown in Figure 6.5 a). The lowest/highest applied voltages were 0.74/1.1 V and 0.78/1.15 V for the edge- and face-on devices, respectively. The lowest applied voltages were close to or even below  $V_{OC}$  conditions. Figure 6.6 a) also reveals that even at very low injection currents the emission spectra show additional emission peaks at energies of about 1.7 to 1.8 eV. This emission can be explained by singlet state emission from the pure p-SIDT(FBTTh<sub>2</sub>)<sub>2</sub>. The normalized electroluminescence of a pure, face-on oriented p-SIDT(FBTTh<sub>2</sub>)<sub>2</sub> film is shown in Figure 6.6 a) as well. The pure fullerene emission usually is found at similar energies ( $\sim 1.6$ – $1.7$  eV)[122], but the spectral shape and the dependence of the emission strength on molecular orientation suggests that the emission at energies larger than  $\sim 1.5$  eV is due to pure p-SIDT(FBTTh<sub>2</sub>)<sub>2</sub> emission. To give a rough estimate of the influence of this singlet emission on the absolute  $EQE_{EL}$  value, the  $EQE_{EL}$  spectra have been split and integrated separately for energies less and greater than 1.5 eV. In Figure 6.6 b) the obtained values are plotted together with the total  $EQE_{EL}$  of the full spectrum. The singlet emission has only little effect on the absolute  $EQE_{EL}$ , and with that the non-radiative  $V_{OC}$  loss for low injection conditions. This qualitative statement holds true for both systems, although the singlet emission is stronger in the face-on oriented cases.

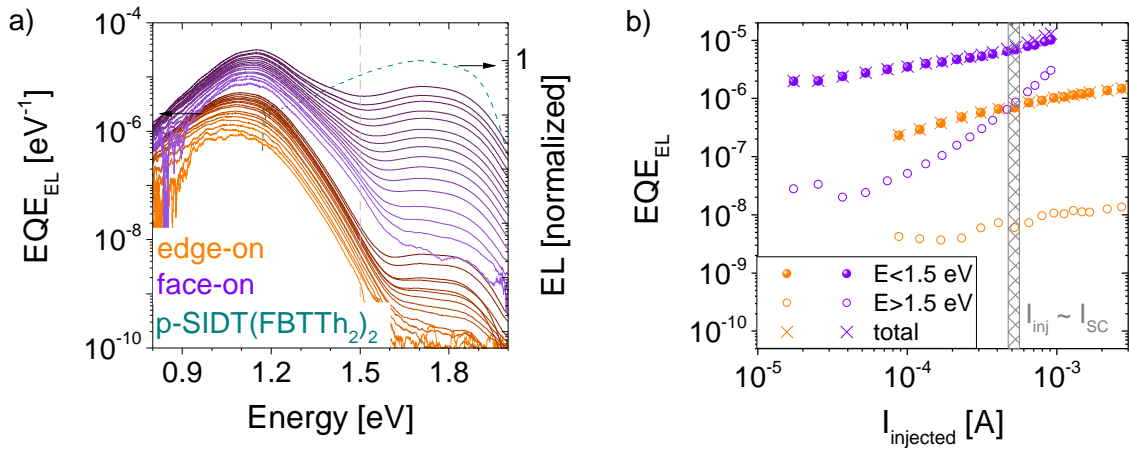


**Figure 6.6.:** External quantum efficiency spectra of device e2 and f2 for different injection conditions. The integrated full spectra give the  $EQE_{EL}$  values depicted in Figure 6.5 a). The normalized electroluminescence spectrum of a pure p-SIDT(FBTTh<sub>2</sub>)<sub>2</sub> film (face-on) is depicted in dark cyan. The line at 1.5 eV roughly separates the CT-emission at lower energies from the donor singlet emission at larger energies. In b) the integrated  $EQE_{EL}$  for the CT-emission, the singlet emission and the sum of both is shown. The singlet emission has almost no effect on the total emission at low injection conditions. The gray shaded area denotes the short circuit current range of edge- and face-on oriented bilayer solar cells.

Singlet emission has previously been observed to be more dominant as the CT-state emission gets energetically closer to the optical band-gap of the whole system.[120] This observation

holds true for the studied bilayers as well, even though no quantitative statements can be made. Further conclusions as a decreased short circuit current being correlated to increased singlet emission[120] or singlet emission being caused by direct injection of electrons into the donor LUMO[122] could not be confirmed for the bilayer systems. The fact that singlet emission is seen at injection conditions even below  $V_{OC}$  conditions rather suggests an equilibrium between occupation of CT-states and singlet-states, which shifts towards higher population of the singlet-states as the CT-energy approaches the singlet energy. Nevertheless the effect of this extra emission on the total  $EQE_{EL}$ , and with that, on the calculated non-radiative voltage losses, is negligible for low injection currents.

### 6.1.3. Discussion

Overall a significant change in non-radiative voltage loss is observed by changing the molecular orientation of the donor molecules at the interface with the  $C_{60}$  layer. The total amount of losses differs slightly between investigated cells, which reasoned to be due to less ideal edge-on configurations at the interface. To obtain perfectly oriented edge-on layers p-SIDT(FBTTh<sub>2</sub>)<sub>2</sub> solutions need to contain a very precise amount of solvent additive. The ratio of solvent to solvent additive is very sensitive and small deviations immediately result in a larger amount of face-on oriented p-SIDT(FBTTh<sub>2</sub>)<sub>2</sub> molecules, disrupting the preferred edge-on configuration. Additionally, one can speculate that the edge-on configuration is less stable and  $C_{60}$  molecules could interact with the topmost p-SIDT(FBTTh<sub>2</sub>)<sub>2</sub> layer. This also gives a reasonable explanation why the  $V_{OC}$  difference in freshly produced bilayers measured at UCSB was always slightly larger compared to the bilayer cells shipped to UP. The edge-on character might get lost over time concomitant with inter-diffusion of  $C_{60}$  molecules introducing locally more face-on oriented interfaces between p-SIDT(FBTTh<sub>2</sub>)<sub>2</sub> and  $C_{60}$ . The face-on configuration in the bilayer cells is more stable with respect to the  $V_{OC}$  (compare the values in section C.4 for the face-on oriented bilayers measured at UCSB and UP). This suggested reason for the small increase in  $V_{OC}$  for the shipped devices is speculative and could be addressed by future work. Nevertheless, the difference in non-radiative loss is significant and necessary, in combination with the measured CT-state energy, to explain the measured  $V_{OC}$  differences. These findings are further backed up by a recent publication studying the effect of molecular orientation by means of DFT calculations.[127] Herein the authors show a significant increase of non-radiative losses in an edge-on configuration of pentacene molecules compared to a face-on orientation with respect to  $C_{60}$  acceptor molecules. For the face-on orientation a significant decrease in the overlap of hole and electron density was determined by considering more and more donor molecules in the calculation. Additional molecules lead to hole delocalization away from the interface and as a consequence a decrease in the nonadiabatic coupling of the CT-state to the ground state.[127] These findings are in perfect agreement with what is measured for the bilayers investigated experimentally in this thesis.

Bilayer solar cells consisting of the donor molecule p-SIDT(FBTTh<sub>2</sub>)<sub>2</sub> and the fullerene acceptor C<sub>60</sub> have been presented with exceptional well controlled interfacial molecular orientation of donor toward acceptor. The orientation of p-SIDT(FBTTh<sub>2</sub>)<sub>2</sub> is almost completely face- or edge-on with respect to the surface and the  $\pi$ -stacking direction. This well defined interface enabled the study of molecular orientation effects on  $V_{OC}$ . Clear evidence is presented that not just the energetics of the interfacial CT-states change and influence the  $V_{OC}$ , but that additionally the non-radiative voltage loss can change significantly with molecular orientation at the donor/acceptor interface. Recent DFT calculations predict exactly the observed behavior and larger non-radiative losses for edge-on oriented interfaces between fullerene acceptors and small molecules. The explicit experimental proof for the influence of molecular orientation on the non-radiative  $V_{OC}$  loss is of major importance for further improvements of the  $V_{OC}$  of organic solar cell systems.

## 6.2. Three Methods of Backbone Fluorination and the Effects on Open Circuit Voltage

Recent work on ternary blends with one donor and two acceptors with different LUMO energies showed that the  $V_{OC}$  of such blends is not limited by the donor/acceptor combination with the smaller HOMO/LUMO gap, but lies between the  $V_{OC}$  of both donor/acceptor binary combinations. Several theories have been proposed to explain this behavior, such as filling a joint density of states,[128] a shift of energy levels of the components caused by molecular aggregation,[129] or alloy formation with delocalized wavefunctions over several molecules.[113] In this thesis a ternary blend of two donors PBnDT-FTAZ (FTAZ), PBnDT-HTAZ (HTAZ), which only differ in substitution of two fluorine for hydrogen atoms attached to the backbone, and the acceptor PC<sub>60</sub>BM will be examined. The fully fluorinated donor polymer FTAZ has proven to be superior to its non-fluorinated counterpart HTAZ in combination with the fullerene acceptor PC<sub>60</sub>BM in binary bulk hetero-junction solar cells.[10, 109]

By studying a series of these block copolymers with fluorinated and non-fluorinated monomer sub-units, the increased efficiency could be explained by increased hole mobilities correlated to fluorination, which improved  $\pi$ -stacking and face-on orientation in the fully fluorinated system.[109] In addition to the increased hole mobility, slightly higher  $V_{OC}$  was measured related to the lower lying HOMO level of FTAZ compared to HTAZ. The ternary device consisting of FTAZ/HTAZ/PC<sub>60</sub>BM is investigated and compared to two additional donor/acceptor binary blends that bear great resemblance to the ternary blend. Both donor polymers of the binaries are based on the same polymer backbone as FTAZ and HTAZ and include, on average, the same amount of fluorination (50%) as the ternary blend. These three systems are interesting model systems to investigate the influence of fluorination and of the local donor/acceptor interaction on the  $V_{OC}$  and the overall device performance.

### 6.2.1. Chemical Structure and Device Preparation

The average amount of 50% fluorination is achieved in three different ways. The chemical structures of the three different systems are shown in Figure 6.7. The fluorination is introduced by replacing hydrogen atoms with fluorine atoms at the benzothiadiazole (BT) unit of the block copolymer PBnDT-DTBT.[130] In the first case the devices are built from a mono fluorinated version of the donor polymer again in combination with PC<sub>60</sub>BM as acceptor (monoF). The second option is the ternary blend of pure HTAZ, FTAZ and PC<sub>60</sub>BM with a FTAZ:HTAZ ratio of 1:1 (H:F 1:1). The third donor/acceptor combination consists of a block copolymer based on 50% fully fluorinated and 50% non-fluorinated monomer units that are randomly ordered, again with the acceptor PC<sub>60</sub>BM (F50). All solar cells were prepared on pre-structured indium tin oxide covered with  $\sim 50$  nm of PEDOT:PSS spun cast at 2000 rpm

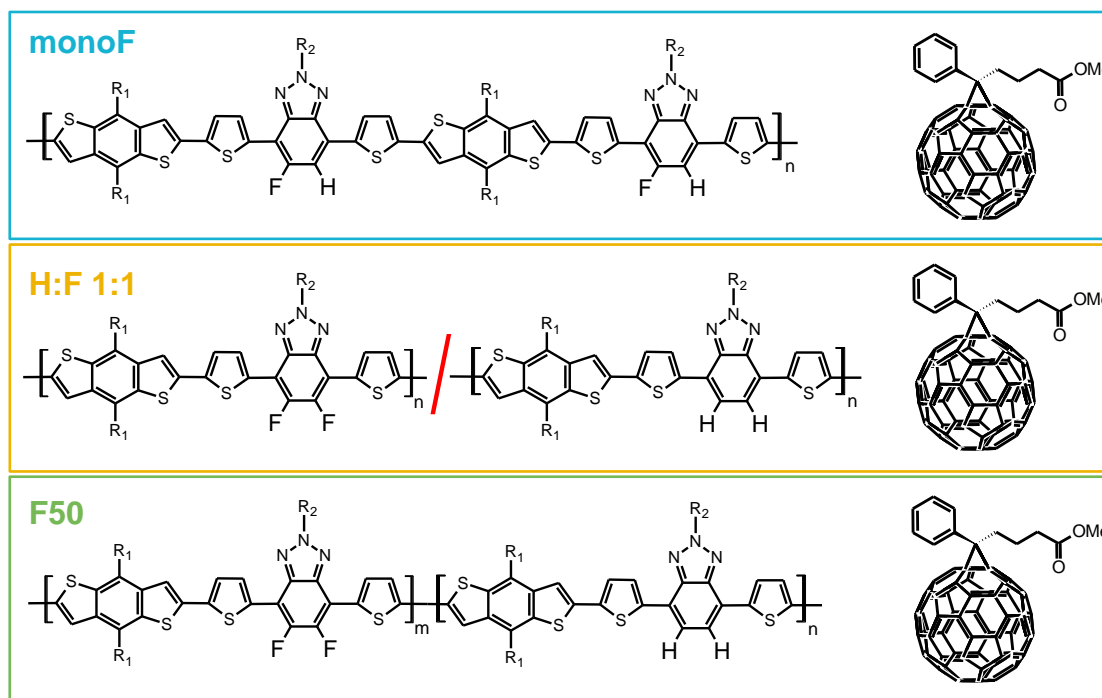


**Figure 6.7.:** Chemical composition of the three 50% fluorinated solar cell systems.  $R_1 =$  3-butylnonyl and  $R_2 =$  2-butyloctyl.

and annealed at 130°C for 15 minutes. The active layers were spun cast from trichlorobenzene solutions with a total donor concentration of 12 g/L and a donor acceptor weight ratio of 1:2. Films were spin cast at 400-800 rpm to reach final thicknesses of about 200-250 nm. The films were dried under vacuum for 30 minutes and 30 nm calcium and 100 nm aluminum were evaporated as cathode. For the H:F 1:1 ternary blends the donor consisted of a 1 to 1 mixture of the pure donor polymers HTAZ and FTAZ. Except for the cathode evaporation all processing steps were conducted at the University of North Carolina (UNC) and reference devices were prepared and compared to the *JV*-characteristics measured at UP. Only when the device performance was comparable to what had been measured at UNC were further experiments conducted.

### 6.2.2. Comparison of Fundamental Photovoltaic Parameters

At first glance the donor components in all three systems could adopt different morphological characteristics. In the ternary blend (H:F 1:1) HTAZ and FTAZ might phase separate to some degree resulting in fluorine rich or deficient domains interacting with the fullerene acceptor. In the mono fluorinated system (monoF) the fluorine content is expected to be spread most uniformly over the whole donor phase. In the randomly ordered block copolymer (F50) fluorine is expected to be spread over the whole polymer chains as well, but less homogeneously than for monoF. Furthermore it was shown for another system that random

and regular copolymers can, in general, adopt different morphologies.[131] Hence, by taking into account the differences of the chemical composition of the three systems, one might speculate that properties like the charge carrier transport or recombination or the CT-state energetics might actually differ significantly for all 50% systems.

However, typical  $JV$ -curves of all 50% systems show a strong resemblance in every aspect; the curves are plotted in Figure 6.8 and the averaged device performance is given in Table 6.2. The measured  $V_{OC}$ , as well as the  $FF$ , lie between the values for a pure FTAZ or HTAZ donor system. This has already been reported for the F50 device in a previous study.[109] In that work the external generation efficiency ( $EGE$ ) was determined for the non-fluorinated system HTAZ:PCBM (HTPC), the fully fluorinated system FTAZ:PCBM (FTPC) and the F50 system and it was shown that the  $EGE$  is field independent in all cases. Herein, the field dependence of generation was also measured for the monoF and the H:F 1:1 system in the same way. The  $EGE$ , as measured with the TDCF setup for different applied voltages, is shown in Figure 6.9 c) for all 50% systems. No severe field dependence of generation was measured for any of the 50% systems and the total generation efficiency is close to 75% for all systems. These findings are in agreement with the rather high  $FF$  (Table 6.2), suggesting that there should not be a strong field dependence of generation for any of the 50% systems. In summary, very similar  $J_{SC}$ ,  $V_{OC}$ ,  $FF$  and  $EGE$  result in similar steady state performances of all three systems.

**Table 6.2.:** Performance data of the 50% systems and pure HTAZ:PCBM (HTPC) and FTAZ:PCBM (FTPC) solar cells

sample	$V_{OC}$ [V]	$J_{SC}$ [mA cm <sup>-2</sup> ]	$FF$ [%]	$PCE$ [%]	Thickness [nm]
HTPC	$0.761 \pm 0.002$	$10.4 \pm 0.4$	$49.7 \pm 0.7$	$3.9 \pm 0.2$	$247 \pm 31$
FTPC	$0.81 \pm 0.01$	$11.5 \pm 0.4$	$72.5 \pm 1.1$	$6.7 \pm 0.3$	$233 \pm 11$
monoF	$0.769 \pm 0.004$	$11.0 \pm 0.5$	$62.9 \pm 1.4$	$5.3 \pm 0.3$	$208 \pm 3$
H:F 1:1	$0.768 \pm 0.004$	$10.8 \pm 0.4$	$61.4 \pm 1.9$	$5.1 \pm 0.2$	$245 \pm 33$
F50	$0.768 \pm 0.006$	$11.6 \pm 0.2$	$59.7 \pm 3.1$	$5.3 \pm 0.2$	$198 \pm 3$

### 6.2.3. Steady State and Transient Recombination Measurements

The dependence of the recombination rate on carrier density governs important properties like the  $V_{OC}$  but also the  $FF$ . In order to understand what determines the  $V_{OC}$  it is therefore important to learn about the recombination mechanism that is dominant at  $V_{OC}$  conditions in the device. As discussed in section 3.2 there are different modeled situations describing recombination that are found to depend on, amongst other things, the charge carrier densities of electrons and holes in their respective density of states. However, it was shown before that the energy levels, and thus the density of states of pure polymer or mixed polymer/fullerene phases can change significantly upon mixing.[132] Furthermore, it was shown that in many

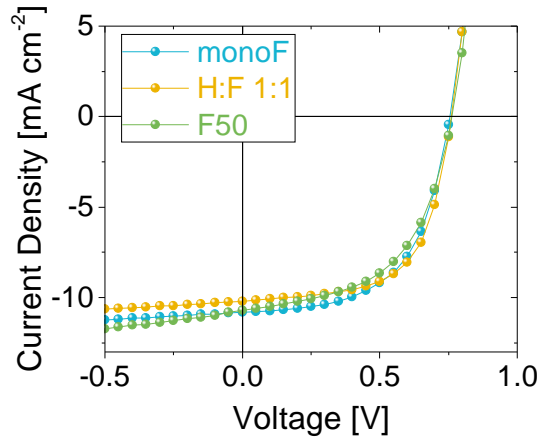


**Figure 6.8.:** *JV*-characteristics of all three 50% solar cells

organic solar cell systems the CT-state energy is closely connected to the  $V_{OC}$ . [34, 36] The CT-state exciton is formed either upon illumination at the interfaces between donor and acceptor by electron transfer from the donor to the acceptor or by free charges in the donor and acceptor coming close to each other. It stands to reason, and it was argued previously, that the recombination of free charges is mediated via CT-states. [47] Different approaches can be taken to determine the order of recombination at  $V_{OC}$  conditions. At  $V_{OC}$  the generation rate  $G$  needs to equal the recombination rate  $R$  at steady state conditions; the recombination rate  $R$  can be described in a very general way according to Equation 3.12 where  $\gamma$  is the recombination coefficient and the generation rate  $G$  depends linearly on the generation current. As long as the generation current linearly increases with increasing light intensity  $I_{LED}$ , the following relation is valid, where  $n$  is the measured charge carrier density:

$$R = -\frac{dn}{dt} = \gamma n^\beta = G \propto I_{LED}. \quad (6.1)$$

The BACE method (section 4.5) determines the steady state charge carrier densities in a working solar cell device as a function of the illumination intensity. Therefore, the recombination order  $\beta$  can be directly determined from measurements of charge carrier density at  $V_{OC}$  conditions for different illumination intensities. The measured charge carrier density  $n$  for several light intensities at  $V_{OC}$  is plotted for all three 50% systems in Figure 6.9 b). By linear fitting of the data in the double logarithmic plot the recombination orders are derived and given in the legend of Figure 6.9 b). The derived order is very close to 2 in all cases, meaning that the steady state recombination at  $V_{OC}$  is dominated by a bimolecular process. However, transient experiments have revealed that time dependent, dispersive recombination processes can be present in organic solar cells implying e.g. a slow down of carrier motion after initial excitation. [71, 133] The presence of such effects is not measurable by the BACE technique but can be addressed by TDCF (section 4.4). In a TDCF experiment charges are

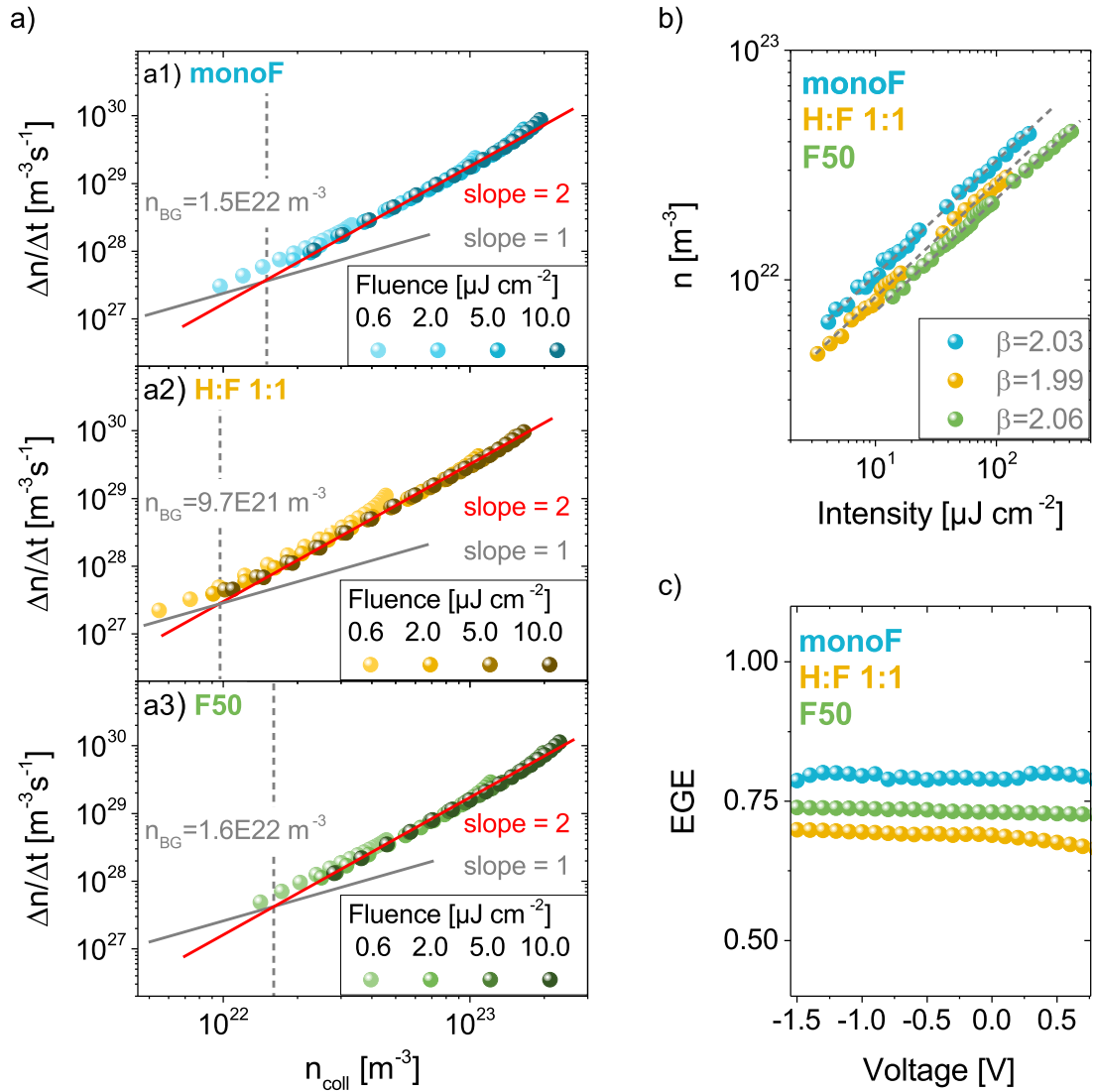


**Figure 6.9.:** a) Differential decay of photogenerated charges as determined with TDCF at different excitation intensities as a function of the extracted charge carrier density. The injected background charge carrier density is denoted as a gray dashed line. The slope of the differential data denotes the apparent recombination order. Lines with slopes of 1 and 2 are shown as guides to the eye. In a1), a2) and a3) the data are plotted for monoF, H:F 1:1 and F50 solar cells, respectively. b) Steady state charge carrier densities as determined by the BACE technique for the three different solar cells. The gray lines are linear fits with the slopes  $\beta$  according to Equation 6.1 proving bimolecular recombination in steady state. c) External generation efficiency (EGE) determined by TDCF. A constant generation efficiency with applied voltage is measured for all three systems with only small deviations of the total EGE between the three systems. The excitation fluence of the 532 nm laser excitation was in the range of 0.2 to  $0.3 \mu\text{J cm}^{-2}$  for all measurements.

generated by a short laser pulse and extracted after a variable delay time. By this means the recombination of charges in the device with time can be tracked. By measuring the

charge carrier density of the photogenerated charges in the device ( $n_{tot}$ ) for different fluences and delay times, the recombination rate  $R = -\Delta n_{tot}(t_d)/\Delta t_d$  can be obtained. If dispersive recombination is present the recombination rate should explicitly depend on delay time, whereas when thermalized charges dominate, the differential decay data should fall on one line for all fluences. This would mean that the recombination rate is solely a function of charge carrier density and not of the delay time.

As outlined in section 4.4 the total extracted charge in a TDCF experiment can be split into pre charge carrier density  $n_{pre}$ , extracted before the collection bias is applied, and collected charge carrier density  $n_{coll}$  for the charges extracted with the collection bias. If the recombination rate is plotted as a function of the collected charge the recombination order can be derived from these plots as the recombination rate, determined by TDCF, can be depicted as follows:

$$R = -\frac{dn_{tot}}{dt} = \gamma((n_{coll} + n_{BG})^\beta - n_{BG}^\beta). \quad (6.2)$$

Herein the dark injected background charge carrier density  $n_{BG}$  at the corresponding pre voltage conditions needs to be considered and the resulting recombination rate needs to be subtracted, because TDCF measures only the charge and recombination induced upon illumination, as was shown by Albrecht et al.[134] and in the PhD thesis of Juliane Kniepert.[135] The injected background charge carrier density is determined by BACE experiments in the dark as discussed in section 4.5. In the case of bimolecular recombination the order of recombination is 2 and Equation 6.2 can be rewritten as:

$$R = -\frac{dn}{dt} = k_2(n_{coll}^2 + 2n_{coll}n_{BG}), \quad (6.3)$$

with  $k_2$  the bimolecular recombination coefficient. This means that if the injected background charge becomes larger than the collected charge carrier density a linear dependence of the recombination rate on  $n_{coll}$ , as determined with TDCF, is expected. In the case where  $n_{coll}$  is dominant a quadratic dependence is expected. In Figure 6.9 a) the differential recombination data are shown for all three systems as function of  $n_{coll}$  and for different fluences, as denoted in the legend. The delay times were in the range of 4 ns to 8  $\mu$ s after laser excitation and the pre bias was set to 0.76 V for each system to be close to open circuit conditions for each of the 50% solar cells. From these plots a few conclusions can be drawn. First, there are no strong thermalization effects present for the devices and the bimolecular recombination coefficients are basically not delay time dependent. As the thermalization and recombination depends on the energetic disorder,[27] this implies that the density of states distributions are similar or that any differences are not meaningful for the recombination dynamics at the measurement time scales. Second, the rates of the thermalized charges at any particular  $n_{coll}$  are very similar resulting in the same power-law dependence of the rate  $R$  on  $n_{coll}$  for all systems.

The lines with slope 1 or 2 in Figure 6.9 a) are guides to the eye which are set to cross at the respective injected background charge  $n_{BG}$  of each 50% system. For  $n_{coll} > n_{BG}$  all data clearly follow a slope of 2; this is in very good agreement with the steady state findings from the BACE experiments, implying that the recombination mechanism, as determined at steady state conditions, is largely determined by thermalized charges. The resemblance of the recombination process in all three systems becomes clear by comparison of the bimolecular recombination coefficient obtained by fitting the TDCF data with Equation 6.3 and steady state recombination coefficient  $\gamma$  from the steady state data fit according to Equation 6.1. The coefficients are given in Table 6.3.

**Table 6.3.:** Recombination coefficients as determined with BACE or TDCF for all three 50% solar cell systems.

sample	$k_2$ [ $10^{-17}\text{m}^3\text{s}^{-1}$ ] TDCF (transient)	$k_2$ [ $10^{-17}\text{m}^3\text{s}^{-1}$ ] BACE (steady state)
monoF	1.0	$0.5 \pm 0.1$
H:F 1:1	2.0	$0.9 \pm 0.2$
F50	1.2	$1.1 \pm 0.2$

There is very little deviation between  $k_2$  values measured by BACE and TDCF, and between the three systems. All of the measured  $k_2$  values fall within a factor of 2 of  $1 \times 10^{-17} \text{ m}^3\text{s}^{-1}$ . This is remarkable considering the different measurement settings, transient or steady state conditions and the stress the devices are facing during the measurements with applying high extraction pulses and generating charges at high fluences. Apparently, the recombination mechanism at  $V_{OC}$  conditions is largely the same no matter how the fluorine is introduced into the system and unambiguously bimolecular. This strongly suggests that the recombination pathway and mechanism are dominated rather by the total ratio of fluorine to hydrogen than by very localized molecular interactions between donor polymers and their neighboring fullerene molecules.

#### 6.2.4. Open Circuit Voltage and CT Energy

The similar *open circuit voltages*, as determined by the  $JV$ -measurement, and the similarities of the recombination mechanisms and rates hint at similar CT-state energetics for all 50% systems. In order to gain knowledge about the CT-state energies of the three 50% systems the emissive and absorptive CT-state properties were determined for each solar cell. Again, the luminescent and photovoltaic external quantum efficiencies were measured and evaluated as outlined before (section 3.1). In Figure 6.10 the  $EQE_{EL}$  and  $EQE_{PV}$  measurements of all three 50% devices and of the pure HTAZ:PCBM (HTPC) and FTAZ:PCBM (FTPC) cells are compared. For all displayed emission spectra the applied voltages were close to  $V_{OC}$  conditions, not to infringe upon the quasi equilibrium conditions. According to section 3.1

and subsection 6.1.2 the CT-state energies were determined from the  $EQE_{EL}$  and  $EQE_{PV}$  spectra. By fitting these spectra with Gaussian functions, as it was reasoned in the framework of Marcus-theory, and scaling both fits in a way that their maximum values are the same, the CT-energy is simply the crossing point of both fits. The shift of the peak of CT emission and absorption, with respect to the CT energy, is caused by the reorganization energy  $\lambda$ . Those crossing points are marked with vertical dashed lines in Figure 6.10. The CT-energies of all 50% systems are almost identical and they fall in between the CT-state energies of the fully fluorinated and the non-fluorinated systems. The shift in CT-state energies of HTPC ( $E_{CT} = 1.34$  eV) and FTTC ( $E_{CT} = 1.4$  eV) is in good agreement with the shift in the HOMO energies of  $-5.29$  eV and  $-5.36$  eV for HTAZ and FTAZ, respectively as published by Price et al.[10] This great similarity of the CT energies of all three systems is quite remarkable and a very important finding. It shows that the CT state energetics are not determined by local donor/acceptor interactions at the interface, which can differ from system to system due to the changing chemical composition. This finding can be reasoned by two different models that have recently been put forward and both are related to electrostatic effects.

In the framework of the first model, introduced by Poelking et al., it was shown that long range electrostatic effects, that are a result of the mesoscale structural ordering at donor/acceptor interfaces of small molecules, are necessary to correctly predict the relevant energy levels of a system.[95] Herein, the authors show that mesoscale structural order on a length scale of  $> 100$  nm needs to be taken into account to correctly describe the energetics of a system. The core argument of that work is that the long-range charge-quadrupole interactions need to be considered to describe the ionization potentials and electron affinities of the system. Although these findings are related to interfaces between small molecules in evaporated bilayer systems, they show that long range electrostatic effects must not be neglected in order to fully predict  $V_{OC}$ .

The second model, introduced by Sweetnam et al., is based on investigations on bulk heterojunctions with varying donor/acceptor ratios. It predicts similar tail state distributions, and with that similar CT energies and  $V_{OC}$ s, of the densities of states functions of each system.[132] By different mixing ratios of donor and acceptor a significant shift in the donor HOMO and acceptor LUMO peak positions is measured, but the CT energy and the corresponding  $V_{OC}$ s are not changed significantly. The main argument put forward by the authors is that the low energy tail states of the DOS are caused by a nonuniform electrostatic background of dipole interactions at the donor/acceptor interfaces that broadens the energy levels of all lattice sites.[132] Hence, despite the different HOMO and LUMO positions found for different mixing ratios, the CT energies and  $V_{OC}$ s are hardly affected.

In the case of the three 50% blends studied in this thesis, the mixing ratios of donor and acceptor are kept constant, but the donor component is slightly changed. The donor backbone is, however, always the same and the total ratio of fluorination is also kept constant for all three 50% systems. Therefore, it stands to reason that the electrostatic background, averaged over all dipole interactions at the donor/acceptor interfaces, is also similar for all

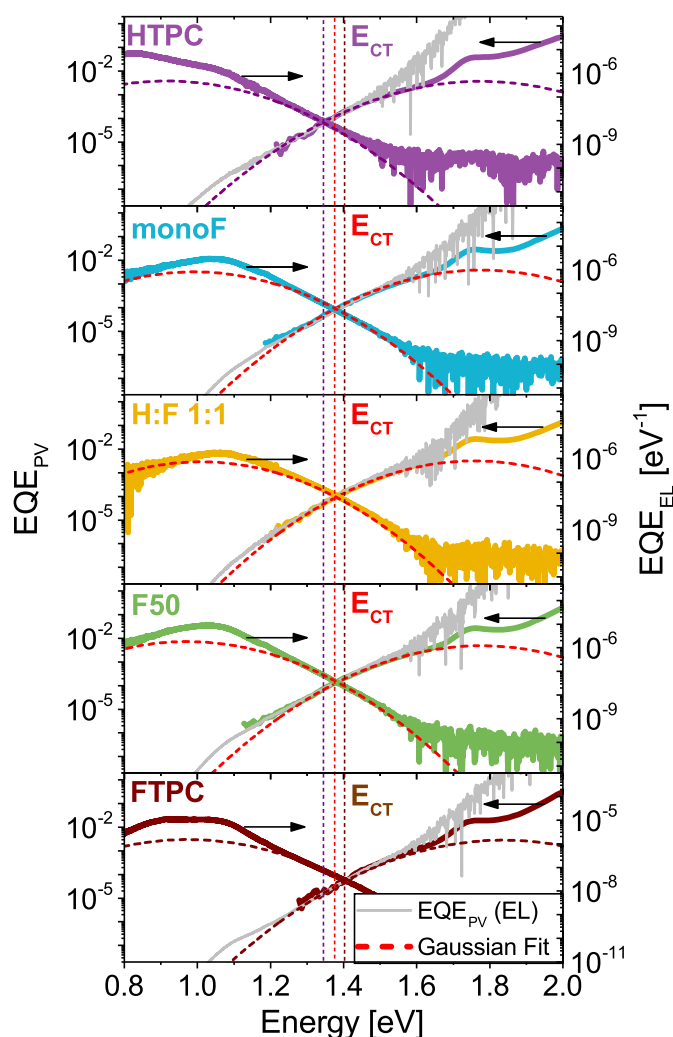


**Figure 6.10.:**  $EQE_{EL}$  and  $EQE_{PV}$  for all three 50% systems compared to the fully non- or fully fluorinated HTAZ or FTAZ systems. The  $EQE_{PV}$  calculated from the  $EQE_{EL}$  at 300 Kelvin is shown as gray line. The Gaussian fits to the spectra is denoted in red for the 50% systems and in purple or brown for HTAZ or FTAZ, respectively. The dashed vertical lines are guides to the eyes at the position of each respective  $E_{CT}$ .

systems and that a similar tail state distribution is obtained. Both models however highlight the importance of taking into account the electrostatic interactions summed up over a mesoscale morphology.

To investigate the morphology of the films transmission electron microscope (TEM) images were taken of the  $\sim 200$  nm thick films and are shown in section C.9 a) to c) (images taken at UNC). The TEM images bear great resemblance with each other for all systems. Furthermore, energy filtered TEM was used and the resulting sulfur maps show similarly good intermixing of donor and acceptor for all 50% systems (section C.9 d) to f). Most importantly there are also no big differences for the ternary blend (H:F 1:1) which suggests

that the miscibility of HTAZ and FTAZ is high. This can be reasoned by the similar morphologies and mixing of HTAZ and FTAZ with PCBM as published before.[109, 130] The similar morphology picture is in good agreement with the similar device performance.

Apparently, the performance of all 50% systems investigated in this thesis depend more on the total fluorine to hydrogen ratio in the device than on the local donor/acceptor encounters. This means that all systems might actually show a greater resemblance of the mesoscale morphology and their electrostatic interaction than what would be expected by looking locally at an isolated donor/acceptor interaction. Furthermore, it was shown for all the 50% systems that the  $V_{OC}$  values are very similar, which leads to the conclusion that the total voltage loss between CT energy and  $V_{OC}$  also must be similar. To look into this issue more closely, the actual voltage losses will be examined carefully by analyzing the luminescence and photovoltaic quantum efficiency spectra as done before (subsection 6.1.2).

However, the shape of the measured emission spectra of all 50% devices is in these cases not entirely described by a single Gaussian function and the influence of this deviation on the drawn conclusions needs to be addressed. This deviation is even more apparent for the pure HTAZ and FTAZ devices. The reason for this deviation is yet not fully understood, but it is likely caused by interference effects. This assumption is backed up by the emission spectra of different film thicknesses in the case of the fully fluorinated system FTAZ:PCBM. A comparison of normalized spectra of FTTC films of different thicknesses is presented in section C.8 and even though the high energy shoulder is nearly identical in both cases the thicker film shows a distinct extra emission peak at about 0.9 eV. This issue needs further clarification and could not be examined further in the course of this thesis.

Nevertheless, it is possible to evaluate the  $V_{OC}$  without assuming a perfect single Gaussian emission spectrum for the CT-state emission and absorption. This is an important test, as one could argue the validity of applying Marcus-theory and assuming perfect Gaussian emission and absorption spectra for the CT-state. In order to determine the  $V_{OC}$  directly from the measured spectra Equation 3.7 is recalled in which the radiative limit of the  $V_{OC}$  is connected to the dark saturation current  $J_0$  (Equation 3.5), in the case of only radiative losses (meaning  $EQE_{EL}$  equals unity). In order to determine  $J_0$  the  $EQE_{PV}$  needs to be known for low energies with great accuracy. By making use of the optical reciprocity  $EQE_{PV}(\hbar\omega) \propto EQE_{EL}(\hbar\omega)/\Phi_{BB}(\hbar\omega)$  the  $EQE_{PV}$  in the low energy range, which is not accessible with the measurement setup, can be calculated from the  $EQE_{EL}$  and the black-body spectrum at room temperature. If the reciprocity between emission and absorption holds and the measurements indeed were conducted under quasi equilibrium conditions, the shape of the calculated  $EQE_{PV}$  should match the measured  $EQE_{PV}$ . The respective calculated  $EQE_{PV}$  is plotted as a gray line in Figure 6.10; the agreement with the measured  $EQE_{PV}$  is very good at a temperature of 300 K. In Table 6.4 the radiative voltage limits for each of the 50% cells are given. Furthermore, by evaluating the absolute value of the  $EQE_{EL}$  according to section 3.1 the non-radiative losses are determined. These values are given in Table 6.4 for an applied voltage of 0.76 V for each cell. The non-radiative losses

are comparable for all cells, as can be seen from Table 6.4. The agreement of the  $V_{OC}$  values determined by the  $JV$  measurement or by evaluating  $EQE_{PV}$  and  $EQE_{EL}$  spectra is very good and the deviation is less than 10 mV in all cases. This proves the accuracy of the detailed balance approach at quasi equilibrium conditions to determine the  $V_{OC}$ . In Table 6.4 the  $V_{OC}$  values based on the analysis of the Gaussian fits according to Equation 3.11 are given as  $V_{OC,calc.2}$ . The deviation between the  $V_{OC}$  determined by the  $JV$ -measurement ( $V_{OC,JV}$ ) and by the Gaussian fits ( $V_{OC,calc.2}$ ) is considerably larger than what is obtained by comparing  $V_{OC,JV}$  and  $V_{OC,calc.1}$  the  $V_{OC}$  calculated by the radiative limit from the actual measured spectra. This shows the advantage of determining the radiative limit from the actual measured  $EQE_{EL}$  and  $EQE_{PV}$  spectra. The universal character of this method only takes into account the actual measured spectra, without the need of initially assuming any spectral line shape of the CT-state. This highlights that the accurate determination of the absolute  $EQE_{EL}$  value is critical, especially if the  $EQE_{EL}$  depends on the applied voltage and with that the injected current. To fulfill quasi equilibrium conditions the injected current should be as low as possible.

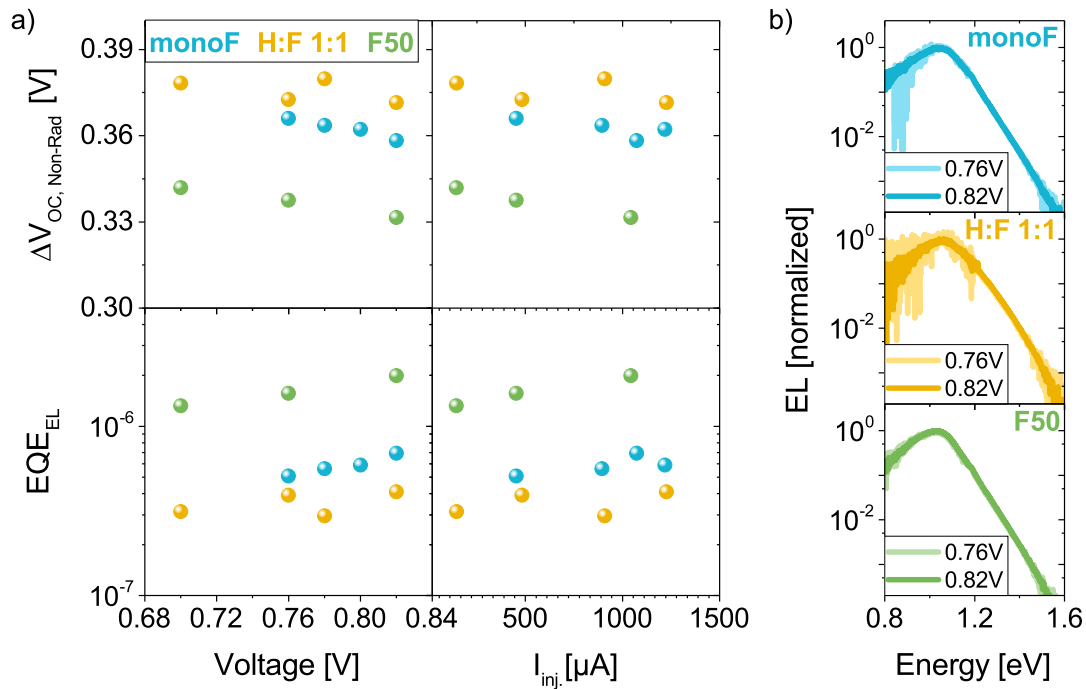


**Figure 6.11.:** a)  $EQE_{EL}$  and the corresponding non-radiative  $V_{OC}$  loss in dependence of either the applied voltage or the corresponding injected current. b) Comparison of the normalized emission spectra of the emission at  $\sim V_{OC}$  conditions or at higher applied voltage of 0.82 V.

In Figure 6.11 a) the absolute  $EQE_{EL}$  and the corresponding non-radiative voltage loss are shown as function of the applied voltage or the respective injection currents for all 50% systems. The losses are similar overall with slightly higher values (lower  $EQE_{EL}$  values) for the

F50 system. For applied voltages close to  $V_{OC}$  conditions the  $EQE_{EL}$  is only weakly voltage dependent and the emission spectra do not change their shape upon slightly higher injection currents. This can be seen from the normalized spectra at  $\sim V_{OC}$  conditions compared to the spectra at 0.82 V, depicted for each of the three 50% systems in Figure 6.11 b). The weak voltage dependence of the integrated  $EQE_{EL}$  can already influence the accurate determination of the non-radiative voltage loss and the non-radiative voltage loss values should always be evaluated at injection conditions close to  $V_{OC}$ .

**Table 6.4.:**  $V_{OC}$  and CT-state energies of the 50% systems as determined from the spectral analysis of  $EQE_{EL}$  and  $EQE_{PV}$ .

		monoF	H:F 1:1	F50	determined by
$E_{CT}$	[eV]	1.38	1.38	1.37	
$V_{OC,Rad-Lim}$	[V]	1.14	1.15	1.11	
$\Delta V_{OC,Rad}$	[V]	0.24	0.23	0.26	$E_{CT} - V_{OC,Rad-Lim}$
$\Delta V_{OC,Rad}$	[V]	0.22	0.22	0.21	Gauß fit, Equation 3.11
$\Delta V_{OC,Non-Rad}$	[V]	0.366	0.373	0.337	$k_B T/q \cdot \ln(EQE_{EL})$
$V_{OC,JV}$	[V]	0.769	0.768	0.768	$JV$ measurement
$V_{OC,calc.1}$	[V]	0.774	0.777	0.773	$V_{OC,Rad-Lim} - \Delta V_{OC,Non-Rad}$
$V_{OC,calc.2}$	[V]	0.794	0.787	0.823	Gauß fit, Equation 3.11

The very similar radiative and non-radiative voltage losses are in good agreement with the previous findings, where a great resemblance of the recombination process was shown for all 50% systems. Bimolecular recombination of free charges via the CT-states, formed at the donor/acceptor interfaces, is the dominant recombination mechanism for these organic solar cell systems. These great similarities are rather surprising considering the different compositions of each of the donor materials.

### 6.2.5. Conclusion

By employing several different measurement techniques the steady state and transient recombination behavior, as well as the CT-state energetics and radiative and non-radiative voltage losses were determined for three bulk heterojunction solar cells utilizing the same polymer backbone and all incorporating the same total amount of fluorination. A conclusive picture of the charge recombination mechanism is drawn in full agreement with the voltage losses found by spectral analysis of the CT-state. The strong resemblance of all measured parameters in all aspects clearly shows that the CT-state energetics are determined by mesoscale electrostatic interactions rather than by the properties of individual donor/acceptor pairs. Herein, for the first time, a direct comparison of systems with a similar mesoscale electrostatic interaction, determined by the same donor backbone component with overall the same amount of fluorination, but locally different donor/acceptor properties was possible. The striking resemblance in every performance aspect is an experimental proof for the importance of long range electrostatic interactions in organic donor/acceptor solar cell systems.

### 6.3. Open Circuit Voltage in PCBM or ICBA based Solar Cells

The  $V_{OC}$  is known to increase upon blending typical donor materials with the fullerene acceptor ICBA instead of PCBM due to a higher lying LUMO level. In this section the effects of blending the donor polymer PBnDT-FTAZ (FTAZ) with IC<sub>60</sub>BA instead of PC<sub>60</sub>BM (abbreviated as ICBA and PCBM in this chapter) are discussed. FTAZ has already been introduced in section 6.2 and the superior performance of solar cells comprising of FTAZ:PCBM compared to the non-fluorinated version HTAZ:PCBM was discussed before.[10, 109] It was shown that FTAZ:PCBM solar cells have good  $FFs$  ( $\sim 73\%$ ) and reasonably high  $J_{SC}s$  ( $\sim 11 \text{ mA cm}^{-2}$ ).[10] Nevertheless, the *open circuit voltage* only reached values of  $\sim 0.8 \text{ V}$  while the optical band-gap of pure FTAZ is at about 2 eV.[10, 109] Hence, ICBA was tested as alternative acceptor and it will be shown that although the  $V_{OC}$  indeed could be increased the efficiency of the FTAZ:ICBA devices were inferior to FTAZ:PCBM. In the following sections the reasons for the increased  $V_{OC}$  and the overall worse performance of FTAZ:ICBA compared to FTAZ:PCBM will be addressed in detail. The results presented in this chapter are adapted by a paper that is currently prepared for resubmission.[136]

#### 6.3.1. Device Structure and Device Performance

The solar cells studied in this chapter were built on PEDOT:PSS covered ITO electrodes. Blends of either FTAZ:PCBM or FTAZ:ICBA both with a weight ratio of 1:2 and a polymer concentration of 7 g/L were dissolved in 1,2,4-trichlorobenzene at 130°C for 6 hours and spun cast on the PEDOT:PSS layer with optimized spin speeds to realize defined active layer thicknesses of  $110 \pm 5 \text{ nm}$ . The wet processing steps were performed at UNC by Liang Yang. The back electrodes, consisting of calcium (10 nm) and aluminum (100 nm), were evaporated at UP. The chemical structures of the two compared systems are shown in Figure 6.12. Solar

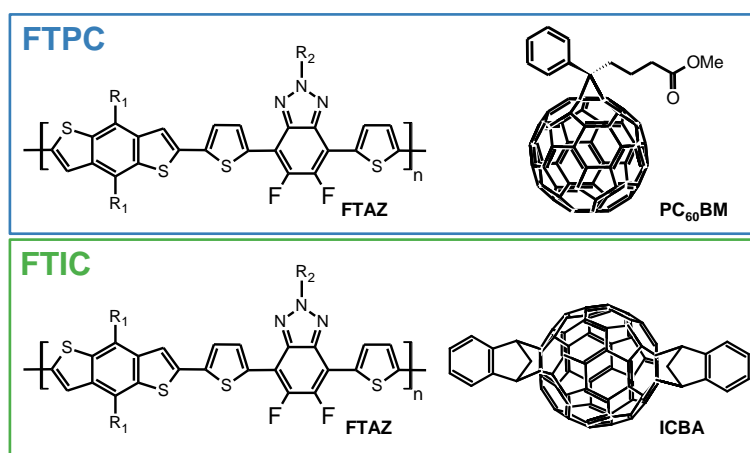


**Figure 6.12.:** Chemical components of FTAZ:PCBM and FTAZ:ICBA solar cells.  $R_1 = 3$ -butylonyl and  $R_2 = 2$ -butyloctyl.

cells consisting of FTAZ:PCBM or FTAZ:ICBA will be referred to as FTPC or FTIC in the following. Typical  $JV$ -characteristics and  $EQE_{PV}$  spectra are shown in Figure 6.13 a) and b), respectively. Apparently the  $V_{OC}$  does increase upon exchanging PCBM by ICBA, however,  $FF$  and  $J_{SC}$  decrease significantly. Averaged performance values are given in Table 6.5. The shape of the  $EQE_{PV}$  spectrum does not change significantly upon exchanging PCBM with ICBA Figure 6.13 b) but the FTIC spectrum is overall lower by a factor of approximately 2, which is in good agreement with the measured  $J_{SC}$  values.

**Table 6.5.:** Performance data of the FTPC and FTIC solar cells

sample	$V_{OC}$ [V]	$J_{SC}$ [mA cm <sup>-2</sup> ]	$FF$ [%]	$PCE$ [%]	Thickness [nm]
FTPC	$0.79 \pm 0.01$	$8.3 \pm 0.2$	$71.7 \pm 0.9$	$4.7 \pm 0.1$	$110 \pm 5$
FTIC	$1.02 \pm 0.01$	$4.7 \pm 0.2$	$53.3 \pm 0.6$	$2.5 \pm 0.1$	$110 \pm 5$

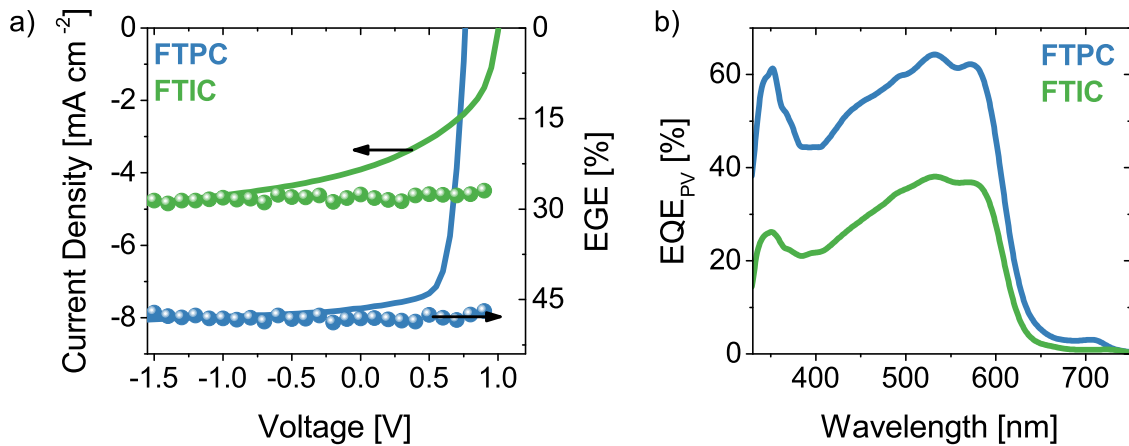


**Figure 6.13.:** a) left-axis:  $JV$ -characteristics of FTPC and FTIC solar cells at one sun illumination conditions (AM 1.5G  $100 \text{ mW cm}^{-2}$ ). Right-axis: External generation efficiency of FTPC and FTIC. b)  $EQE_{PV}$  data for FTPC and FTIC.

### 6.3.2. Open Circuit Voltage in FTAZ:ICBA and FTAZ:PCBM

The  $V_{OC}$  of FTPC and FTIC is examined with the same measurement approach as presented in section 3.1 and used in the previous chapters section 6.1 and section 6.2. The CT-state energetics and radiative and non-radiative voltage losses are discussed and the accuracy of the approach is validated by comparing its results with the  $V_{OC}$  determined by the  $JV$ -measurement. In subsection 6.2.4 the quantum efficiency spectra of a thick FTPC solar cell ( $\sim 200 \text{ nm}$ ) has already been presented and in section C.8 the  $EQE_{EL}$  spectra of a thin ( $\sim 100 \text{ nm}$ ) and the thick FTPC cell are compared. This section will focus on the thin cell for better comparison with the equally thick ICBA based cells. In Figure 6.14 the  $EQE_{EL}$  and  $EQE_{PV}$  spectra of FTPC and FTIC are shown. The  $EQE_{EL}$  spectra were measured close to

$V_{OC}$  conditions with low current injection to assure quasi-equilibrium conditions. The data were evaluated according to subsection 6.2.4 and the extracted information is summarized in Table 6.6. First of all, a distinct shift in the CT-state energy can be observed; the CT-state energy of the FTPC cell is  $\sim 0.2$  eV lower than the CT-state energy of FTIC cell. This difference is similar to the shift in LUMO energies reported for PCBM and ICBA.[77, 114] More interestingly, the  $V_{OC}$  difference of FTPC and FTIC cells is also found to be about 0.2 V. This however implies that the radiative and non-radiative voltage losses  $\Delta E_{NG} = E_{CT} - V_{OC}$ , determined between the CT-state energy and the measured  $V_{OC}$  are similar for both cells.

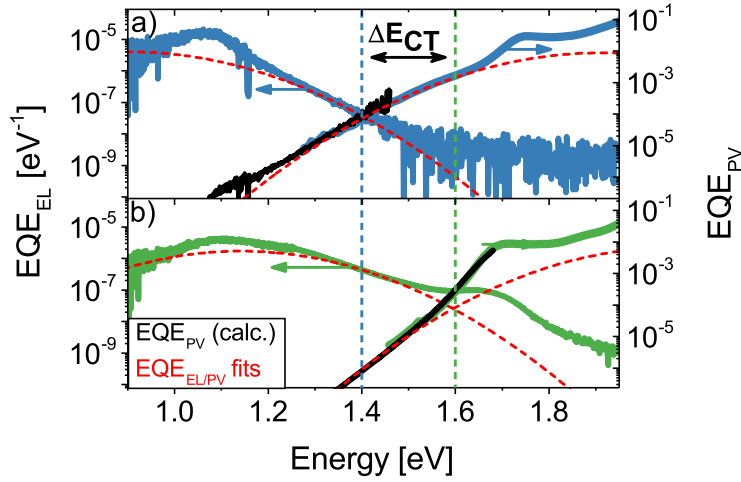


**Figure 6.14.:** Comparison of the  $EQE_{EL}$  and  $EQE_{PV}$  spectra of FTPC a) and FTIC b) solar cells. The dashed lines denote the respective CT-state energy. The  $EQE_{PV}(\text{calc.})$ , calculated from the emission spectrum, is shown as black line. Gaussian fits to the spectra are shown as red dashed lines.

In Table 6.6 the corresponding values and the differences,  $\Delta$ , between the FTPC and FTIC cell are listed. Furthermore, the optical gap  $E_{opt.}$ , determined from the absorption onset, is set for both solar cell types by the fullerene derivative and is  $\sim 1.65$  eV in both cases. Hence, the energy difference  $\Delta E_{CS} = E_{opt.} - E_{CT}$ , regarded as the exciton separation energy, is close to zero in the case of FTIC. The convergence of the CT-state energy of FTIC and its optical gap energy leads to less well resolved  $EQE_{PV}$  features of the CT-state from the  $EQE_{PV}$  measurement. Here again the reciprocity relation between  $EQE_{EL}$  and  $EQE_{PV}$  helps to extend the measured  $EQE_{PV}$  into the low energy range (black line in Figure 6.14) as it was shown before in section 6.2. The reciprocity holds very well, which can be seen by the good agreement of the shape of the measured  $EQE_{PV}$  and the  $EQE_{PV}$  that has been calculated from the  $EQE_{EL}$  spectrum and a temperature of 300 K. With the extended  $EQE_{PV}$  the radiative  $V_{OC}$  limit of both cells is determined according to subsection 6.2.4 and the values are shown in Table 6.6. The radiative  $V_{OC}$  loss is then given by the difference of CT-state energy and the radiative limit of the  $V_{OC}$  whereas the non-radiative voltage loss is

obtained from the absolute  $EQE_{EL}$  spectra (section 3.1). The main conclusion that is drawn from these results is that there is a large resemblance of the radiative and non-radiative loss mechanisms in FTPC and FTIC solar cells. The  $V_{OC}$  differences emerge mainly from the shifted LUMO energies of the two fullerene acceptors which directly translate to a shift of the CT-state energies. By comparing the  $EQE_{EL}$  spectra of FTPC and FTIC this resemblance is surprising. The FTIC spectrum is not only shifted to higher energies but it also shows an extra emission peak at  $\sim 1.65$  eV that is present even for low injected currents below  $V_{OC}$  conditions ( $\sim 0.3$  mA cm $^{-2}$  at an applied voltage of 0.94 V). Direct injection of holes into the HOMO of ICBA was put forward as a reason for singlet emission in other polymer/fullerene blend systems, which becomes more likely at high injection currents.[122] At injection conditions even below  $V_{OC}$  conditions this process is unlikely to occur. A more reasonable explanation is the establishment of an equilibrium between CT- and fullerene singlet states.[120] It was argued that at  $V_{OC}$  an additional non-geminate recombination pathway via such singlet states is established that speeds up the non-geminate recombination.[120] However, for the FTIC and FTPC cells neither a significant difference in the absolute  $EQE_{EL}$  nor in  $\Delta E_{NG} = E_{CT} - V_{OC}$  was measured, which means that the presence of singlet emission in FTIC devices does not change the impact of non-radiative and radiative recombination of charge.

**Table 6.6.:** Open circuit voltage and energetics in FTPC and FTIC solar cells.

sample	$V_{OC}$ [V]	$E_{opt.}$ [eV]	$E_{CT}$ [eV]	$\Delta E_{CS}$ [eV]	$\Delta E_{NG}$ [eV]	$V_{OC, Rad-Lim}$ [V]	$\Delta V_{OC, Rad}$ [V]	$\Delta V_{OC, Non-Rad}$ [V]
FTPC	0.79	1.66	1.40	0.26	0.61	1.14	0.26	0.32
FTIC	1.02	1.64	1.60	0.04	0.60	1.33	0.27	0.34
$\Delta$	0.21	0.02	0.20	0.22	0.01	0.19	0.01	0.02

### 6.3.3. Generation of Free Charge Carriers

The previous experiments revealed similar radiative and non-radiative voltage losses at steady state conditions indicating a similar recombination rate at  $V_{OC}$  at the respective charge carrier densities of the FTPC and FTIC solar cells at one sun standard illumination conditions. The  $EQE_{PV}$  and  $J_{SC}$  data strongly suggest that the generation of charges is initially lower in the FTIC case compared to the FTPC cells. The low  $FF$  of the FTIC solar cell could furthermore be caused by a more pronounced field dependence of charge carrier generation, as seen in other systems.[137, 138] Prior to investigating the actual recombination mechanism in the devices it is necessary to determine if the generation of free and extractable charges itself is a field dependent process. This can be tested with the TDCF setup, already described in section 6.2 and section 6.1. In Figure 6.13 a) the *external generation efficiency* ( $EGE$ ) is determined for a pulse fluence of  $0.2 \mu\text{J cm}^{-2}$  for FTPC and FTIC. The  $EGE$  in the FTIC case is indeed smaller by 40% compared to the FTPC cell and generation of charges is field independent in both devices for the applied pre bias range. This means that the lower

$FF$  is not caused by a precursor state with stronger coulomb binding in the case of FTIC compared to FTTPC. Otherwise, this state would split up more easily upon applying higher fields. The lower generation of photocurrent is therefore caused by initially less charges. Inefficient generation was connected to low values of  $\Delta E_{CS}$ , meaning a low energy difference between the CT-state and the energetically closest singlet state (either from the donor or acceptor).[120, 121] Critical threshold values for efficient generation were found ranging from 0.26 eV to 0.81 eV for different systems.[120, 121] The measured difference of  $\Delta E_{CS}$  for FTTPC and FTIC scales with the shift in CT-state energy and for FTIC  $\Delta E_{CS}$  is only 0.04 eV. The photoluminescence (PL) of a neat FTAZ film compared to either a FTTPC or FTIC blend film however reveals similar quenching for ICBA and PCBM containing films (section C.10). This indicates that inefficient singlet exciton splitting is not the reason for the lower  $EGE$ . Another explanation for low  $J_{SC}$  was suggested to be an efficient energy transfer from the CT-state to strongly bound singlet excitons which competes with free carrier formation. Singlet emission is indeed found even for low injection conditions in the electroluminescence spectra of the FTIC solar cell (Figure 6.14), however the contribution of this singlet emission to the full emission spectrum and accordingly its contribution to the recombination is rather small. Another explanation for the low current was found for small donor molecules mixed with either PCBM or ICBA from transient absorption spectroscopy (TAS) measurements by Kyaw et al.[133] The authors report an initial fast first order loss of charges caused by ICBA islands formed in the donor domain. These acceptor islands would effectively act as traps for electrons that recombine with mobile holes and thus reducing the amount of free charges that can be extracted 6 ns after laser excitation. A full morphology study on FTTPC and FTIC had not been finished in the course of this thesis but first results from resonant soft X-ray scattering measurements indeed revealed the presence of impurities in the domains.

#### 6.3.4. Recombination and Extraction of Free Charges in FTAZ:ICBA and FTAZ:PCBM Solar Cell

After addressing the generation limitations in the FTIC devices and determining that there is no field dependence of free charge carrier generation, the lower  $FF$  needs to be a consequence of the interplay between recombination and extraction of free charges. If charges are inefficiently extracted due to low charge carrier mobilities the recombination probability increases as the bimolecular recombination rate depends quadratically on the charge carrier density in the device. Furthermore the recombination process itself can have different efficiencies, expressed by the recombination coefficient as defined by Equation 3.12. Therefore, charge carrier mobilities are examined either as single carrier mobilities or by determining the effective mobility, measured with the BACE technique as outlined by Albrecht et al.[139] Furthermore, the steady state recombination mechanism is also studied by BACE. First of all single carrier mobilities were determined at UP and UNC. The device structure is

outlined in section C.11. From the  $JV$  data of a single carrier device the respective mobility can be found according to Mott-Guerney Law:[140, 141]

$$J = \frac{9}{8} \epsilon_0 \epsilon_r \frac{V^2}{d^3}. \quad (6.4)$$

With  $\epsilon_0$  the permittivity of free space and  $\epsilon_r$  the relative permittivity of the blend layer that is set to 3, a typical value for polymer blend systems,[21]  $\mu$  the mobility,  $V$  the voltage drop across the device and  $d$  the film thickness.  $JV$  data of the single carrier devices measured at UP are shown in Figure 6.15 for a) FTPC and b) FTIC. Data measured at UNC by Liang Yan are shown in section C.11. The mobility results for all measured devices at UP and UNC are summarized in Table 6.7.

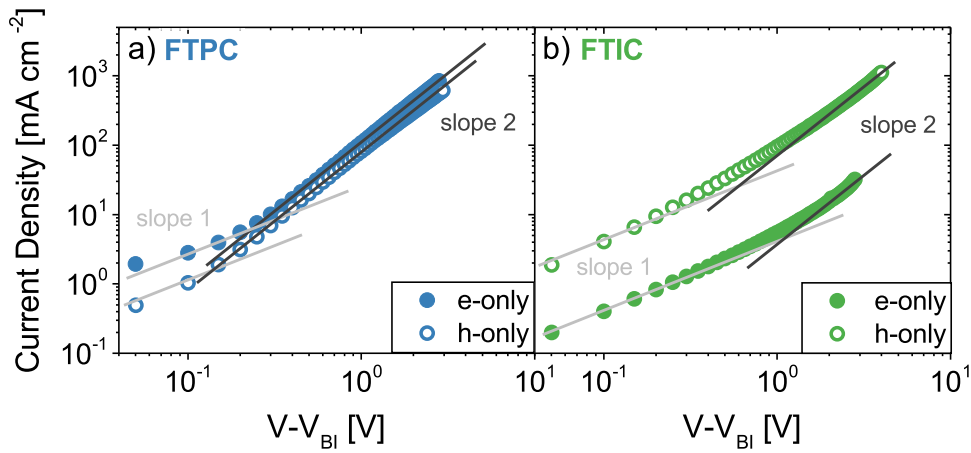


**Figure 6.15.:** Space Charge Limited Currents of a) FTPC and b) FTIC devices. Closed circles show the electron only device currents and open circles the hole only device currents. The applied voltage was corrected for a build in voltage  $V_{Bi}$ .

**Table 6.7.:** SCLC and effective mobilities of FTIC and FTPC.

Mobility $\times 10^{-4} \text{ cm}^2 \text{ V}^{-1} \text{ s}^{-1}$	FTPC	FTIC	PCBM	ICBA
Electron (UP)	$4.2 \pm 0.1$	$0.14 \pm 0.04$		
Electron (UNC)	$6 \pm 3$	$0.3 \pm 0.1$	$77 \pm 41$	$0.8 \pm 0.3$
Hole (UP)	$4.3 \pm 0.9$	$3.1 \pm 0.1$		
Hole (UNC)	$3 \pm 1$	$3 \pm 1$		
Effective calc. (UP)	4.2	0.27		
Effective calc. (UNC)	4.2	0.47		
Effective BACE	$3.1 \pm 0.8$	$0.37 \pm 0.2$		

The space charge limited current (SCLC) mobility values are in good agreement for devices measured at UP or at UNC. Apparently the electron mobility in the ICBA containing devices is significantly lower than in the PCBM devices. The initial electron mobility of pure films of ICBA and PCBM was also compared at UNC and it is confirmed that electron mobilities are already lower in pure ICBA films compared to PCBM in agreement with literature re-

ports.[115] According to Equation 4.1 the effective mobility can be calculated from the single carrier SCLC mobilities and the results are also given in Table 6.7 (Effective calc.). Furthermore, Albrecht et al. presented a way to directly determine the effective mobility from BACE measurements.[139] According to their work the effective mobility is given by:

$$\mu_{eff}(n, V) = \frac{J(V)d}{2e \cdot n(V) \cdot (V - V_{OC})}. \quad (6.5)$$

With  $n(V)$  the charge carrier density in the device at certain voltage and illumination conditions,  $V_{OC}$  the open circuit voltage at different illumination condition but at the same charge carrier density  $n$ ;  $J(V)$  the generated current density,  $d$  the device thickness and  $e$  the elementary charge. This approach allows for determination of the effective mobility in the device taking into account drift and diffusion currents. In Figure 6.16 the corresponding measurements are shown as functions of the applied voltage for a) FTPC and b) FTIC. On the right axis the current density is shown and on the left axis the charge carrier density is depicted on a logarithmic scale. The red dashed line is a fit to the  $n(V_{OC})$  data and the different colors are denoting data collected each for three distinct illumination conditions.

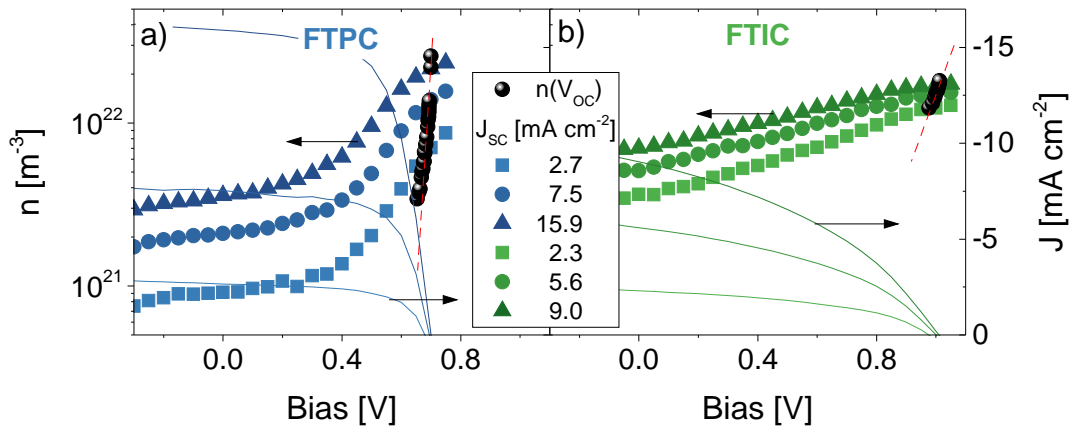


**Figure 6.16.:** a) FTPC and b) FTIC; left axis: Charge carrier density for different illumination conditions either at an applied voltage  $V$  or at  $V_{OC}$  conditions; right axis: Current density measured at each three different illumination conditions resulting in the  $J_{SC}$  values given in the legend.

The effective mobilities determined for the FTPC and FTIC solar cells by the BACE technique are given in Table 6.7 for comparison with the effective mobility calculated from the single carrier mobilities according to Equation 4.1. The agreement between both methods is very good indicating that the effective mobility is a good measure of how efficient charges can be extracted from the devices. As a direct consequence of the lower effective mobility the charge carrier densities in the FTIC device are high compared to the charge carrier densities in the FTPC device for comparable electric field and illumination conditions. This can be seen from Figure 6.16 by comparing the charge carrier densities at voltages below the respective

$V_{OC}$ . In the FTPC device a strong drop in charge carrier density with increasing field is seen, meaning charges are able to leave the device even for low applied fields, pointing to high effective mobility values; however, in the FTIC solar cell the drop in charge carrier density is much less pronounced for each illumination condition and charges are more prone to stay in the device. This could be caused by lower mobilities and thus enhances non-geminate recombination of free charge carriers, which are not extracted fast enough from the device. In order to gain a better understanding of the recombination mechanism, the generation rate is determined from the generated photocurrent at  $V_{OC}$  conditions for each of the three displayed  $JV$ -curves in Figure 6.16. With that rate and the extracted charge carrier density at the corresponding  $V_{OC}$  conditions a BMR coefficient can be determined according to Equation 3.13. If, however, the recombination rate at  $V_{OC}$ ,  $R$ , does not exactly depend on the square of charge carrier density  $n$ , then this implies that the extracted BMR coefficient is charge carrier density dependent. While for FTPC the recombination order is determined to be indeed close to 2, meaning a strong influence of bimolecular recombination, for FTIC a higher recombination order is extracted. On the one hand, this indicates that the recombination mechanism might be more complex than what is expected for pure bimolecular recombination. On the other hand, the correct determination of the generation current  $J_G$ , which determines the generation rate at  $V_{OC}$ , is problematic for the FTIC devices. The measured current was not saturated for the applied reverse biases and a certain error in the correct determination of  $J_G$  was unavoidable. In section 3.2 and in the last chapter of this thesis the appearance of higher recombination orders will be addressed in detail. In this chapter the focus is set on the influence of BMR of free charges in the devices and therefore the recombination coefficients are compared at LED illumination conditions that gave currents closest to  $J_{SC}$  under AM 1.5G 100 mW cm<sup>-2</sup>. The corresponding coefficients are  $2.0 \times 10^{-17}$  m<sup>3</sup>s<sup>-1</sup> and  $1.8 \times 10^{-17}$  m<sup>3</sup>s<sup>-1</sup> for the FTPC and FTIC cell, respectively. Hence, at one sun standard illumination conditions the bimolecular recombination is similar for FTIC and FTPC, meaning that the inferior  $FF$  of the FTIC cell is mainly caused by the lower electron mobility, that was measured for those cells.

### 6.3.5. Simulation of $JV$ -curves in FTAZ:ICBA and FTAZ:PCBM Solar Cell

In order to confirm the experimental findings that inefficient generation of free charges and worse extraction cause the inferior performance of FTPC compared to FTIC the  $JV$ -curves presented in Figure 6.16 were simulated by the modified Shockley-Equation discussed in section 3.2 which was recently published by Neher et al.[49] The newly introduced figure of merit  $\alpha$  (Equation 3.24) includes the competition between free charge carrier recombination and extraction and is used to connect the externally applied voltage with the internal voltage which is a direct measure of the quasi-Fermi level splitting. Therefore,  $\alpha$  was calculated from the generation current density, the BMR coefficients and the effective mobilities for the

FTPC and the FTIC solar cell and finally Equation 3.26 was used to simulate the  $JV$ -curves for the different illumination conditions. The simulated curves are in very good agreement

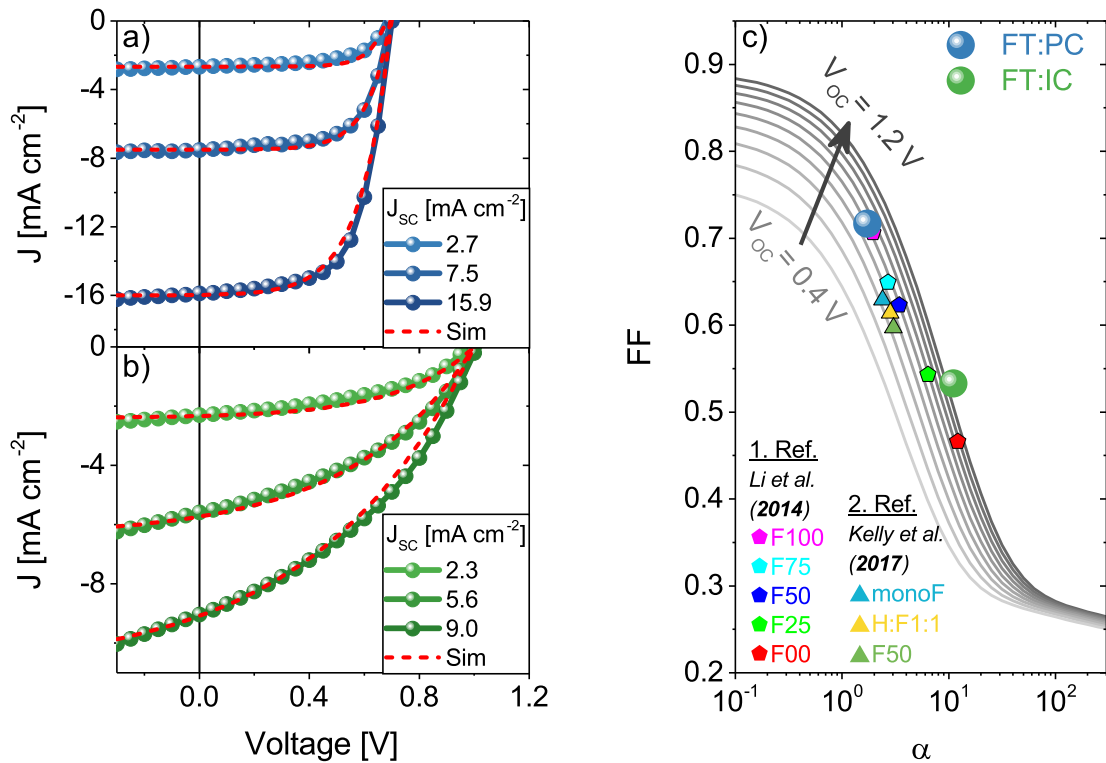


**Figure 6.17.:**  $JV$ -characteristics of a) FTPC and b) FTIC cells illuminated with different intensities of a blue laser diode used for the BACE measurements. The red dashed lines are the simulations according to Equation 3.26. In c) the  $FF$  is plotted as a function of the corresponding alpha value. Full lines denote the model prediction according to Neher et al.[49] for  $V_{OC}$  values ranging from 0.4 to 1.2V. The FTPC and FTIC data are shown as big spheres. Additionally, reference data are plotted which are taken from previous work including FTAZ. The first reference (1.Ref.)[109] compared solar cells comprising PCBM as acceptor and different block-copolymers containing different amounts of fluorinated monomer units (F100, all fluorinated and F00 none fluorinated). The second reference (2. Ref.)[142] includes the data for the 50% systems that were discussed in the previous section.

to the measured data as can be seen from Figure 6.17 a) and b) where the simulated and measured  $JV$ -curves are compared. In Figure 6.17 c) the  $FF$  of both systems is plotted as a function of the parameter  $\alpha$  together with model predictions for different  $V_{OC}$ s (gray lines) according to Neher et al.[49] Furthermore,  $FF(\alpha)$  values are plotted that were calculated for the 50% systems and were calculated from values presented by Li et al.[109] Li et al. investigated similar systems with different amounts of fluorination labeled as F100 (100% fluorination), F75, F50, F25 and F00, accordingly. These solar cells revealed a significant influence of the hole mobilities, which were decreasing with decreasing fluorination, on the  $FF$ . The predicted trend of a significantly decreasing  $FF$  for  $\alpha > 1$  is indeed present for all the investigated systems. For the FTIC solar cells a low electron mobility was measured

which is reflected in a high value for  $\alpha$  of ca. 12. This means the competition between the recombination and extraction is indeed the main parameter determining the  $FF$  in these solar cells.

#### 6.3.6. Conclusion

In this section the performance differences of a FTAZ:PCBM solar cell were compared to a FTAZ:ICBA solar cell. The superior performance of FTTPC compared to FTIC solar cells is explained by a higher generation efficiency of free charges and a better extraction efficiency which is explained by one order of magnitude higher electron mobilities in FTTPC compared to FTIC solar cells. The FTIC solar cell has a higher  $V_{OC}$  by 0.2 V which, however, does not compensate for the low efficiency of both, charge carrier generation and extraction. Electroluminescence and  $EQE_{PV}$  measurements of the two blends reveal that the difference in  $V_{OC}$  corresponds exactly to the shift in the CT energy. That means that  $V_{OC}$  losses due to radiative- and non-radiative recombination are nearly identical in both systems. This finding is in good agreement with the similar absolute values of  $EQE_{EL}$ . The EL-emission from the pure singlet components, measured for FTIC, is indicative of energy transfer from the CT-state to the singlet state, but this additional emission feature has no strong effect on the absolute  $EQE_{EL}$  and with that on the non-radiative voltage loss. This means that the reformation of singlet excitons from the CT-state does not constitute a significant recombination channel. Therefore, it is unlikely that these processes are the cause for the lower  $EGE$  in FTIC, as determined 6 ns after excitation. In accordance with this, BACE experiments reveal similar non-geminate recombination rates at  $V_{OC}$  and one sun standard illumination conditions for both blends. The mobilities, however, do show significant differences between both systems. While the hole mobilities are similar for both systems, the electron mobility in FTIC is about one order of magnitude lower than in the FTTPC solar cell. By modeling the  $JV$ -curves of both cells with an analytical model that considers the competition between charge extraction and bimolecular recombination, it is proven that the lower effective mobility, and thereby worse electron extraction in the FTIC device indeed explains the smaller  $FF$  of the FTIC solar cell. Recent results by Stolterfoht et al. point out that the lower charge carrier mobility has also a significant influence on the charge generation yield and that by increasing the lower mobility, the generation yield also increases.[143] This correlation between lower mobility and charge generation yield is also seen for FTTPC and FTIC. The initial singlet exciton splitting, as determined by PL quenching of photogenerated excitons, is comparable for FTIC and FTTPC and apparently a worse criterion for the charge generation yield in these systems. First morphology experiments that will be outlined to greater detail in a paper that is currently prepared for resubmission indicate that the main difference in these two systems is the intermolecular order in the fullerene-rich domains.[136] The fullerene domain sizes and purities and the donor domains seem to be rather similar in both systems. Though

the morphology picture is not yet fully confirmed and therefore not part of this thesis, these preliminary results are mentioned as they are in full agreement with the findings that were presented in this chapter. The less intermolecular order in the ICBA domains leads to worse electron mobilities while the  $V_{OC}$  losses, PL quenching and non-geminate recombination are similar due to similar domain size and purity.

# Chapter 7

## Effective Bimolecular Recombination in PMDPP3T:PCBM Solar Cells

In section 3.2 the controversy regarding the recombination mechanism in typical organic solar cells was outlined. It was shown in section 3.2 that different conclusions about the recombination mechanism can be drawn by either evaluating the recombination current or the charge carrier densities in the device. In this chapter experimental evidence will be given that prove both approaches to be valid and not necessarily contradictory. It will be shown that drawing rather erroneous conclusions by only taking into account one model cause the contradicting trends in how to treat recombination in typical organic solar cell materials. The experimental work focuses on the PMDPP3T:PCBM solar cell that was introduced in chapter 5. This low band-gap solar cell was examined by means of steady state and transient charge extraction techniques to deduce information about the recombination of the charge carriers in the device; the  $J_{SC}-V_{OC}$  method was employed to measure ideality factors free of series resistance. The PMDPP3T:PCBM solar cells investigated in this chapter had film thicknesses of 120 nm which is slightly thinner than the  $\sim 140$  nm of the PMDPP3T:PCBM cells used in the triple-junction. This is caused by slightly different spin coating conditions. The donor acceptor ratio and the total concentration, as well as the solvents used for preparation of the active layers were however the same as for the PMDPP3T:PCBM cell in the triple-junction. The resemblance of the cells used in the triple-junction or examined in this chapter is also reflected in the similar  $JV$ -characteristics depicted in Figure 7.1 a).

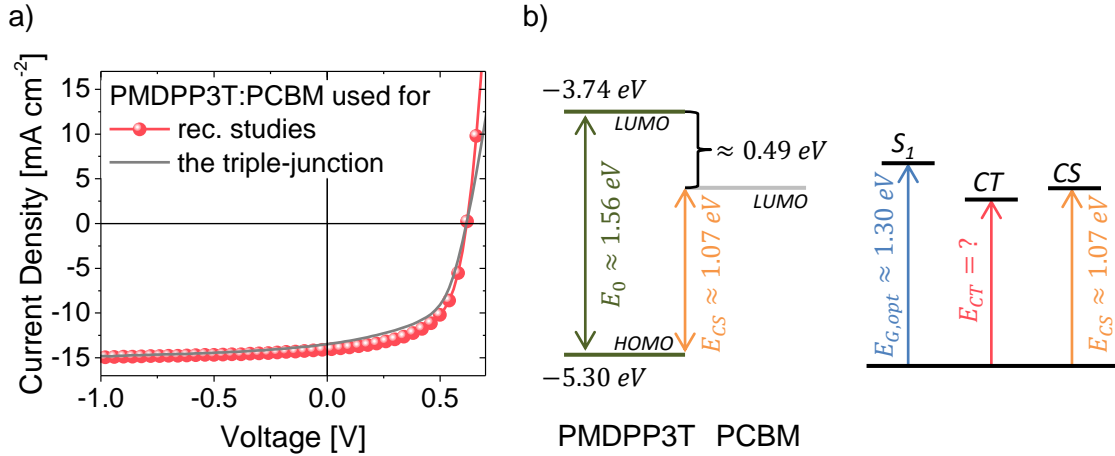


**Figure 7.1.:** a)  $JV$ -curve of a typical PMDPP3T:PCBM solar cell examined in chapter 7 compared to the  $JV$ -curve of the PMDPP3T:PCBM cell used in the triple-junction in chapter 5. b) Energy scheme for the PMDPP3T:PCBM solar cell. Values are adapted from Li et al. and Hendriks et al.[93, 144]. The CT energy needs to be determined.

## 7.1. Energetics and Open Circuit Voltage

Prior to the detailed study of the recombination mechanism by BACE and TDCF the  $V_{OC}$  is examined. In the previous chapter the analysis of the photovoltaic and electroluminescent external quantum efficiency spectra proved to be a useful tool in determining the  $V_{OC}$ , CT-state energies and non-radiative and radiative voltage losses. The  $V_{OC}$  of the PMDPP3T:PCBM solar cell is  $\sim 0.62$  V which is similar to typical P3HT:PCBM solar cells, but PMDPP3T is a low band-gap absorber as shown in Figure 5.1. PMDPP3T has an optical band-gap of  $\sim 1.3$  eV and a LUMO offset to PCBM of  $\sim 0.49$  eV enabling efficient exciton splitting.[93, 144] Energies for the PMDPP3T batch that has been used for this thesis are not known but can be inferred from previous work using PDPP3T.[93, 144] The optical gap of PMDPP3T and PDPP3T – the version of the donor polymer without the methyl groups attached to two of the three thiophene units – is the same and the energy difference between their HOMO and LUMO can be expected to be comparable as well. The HOMO-LUMO difference of PDPP3T is  $\sim 1.56$  eV [93] this however means that the energy difference of the PMDPP3T HOMO and the PCBM LUMO is  $\sim 1.07$  eV. This energy difference is often referred to as charge separated state energy  $E_{CS}$  and the CT-state energy is usually lower by the binding energy of the CT exciton. A scheme of the energetics is depicted in Figure 7.1 b). With these preliminary remarks in mind the focus is now set to the experimental data.

In Figure 7.2 the absolute measured  $EQE_{EL}$  and  $EQE_{PV}$  spectra of a PMDPP3T:PCBM solar cell are plotted together with the black-body photon flux  $\Phi_{BB}$  and the  $EQE_{PV}$  calculated from the  $EQE_{EL}$  at room temperature conditions according to the reciprocity between  $EQE_{EL}$  and  $EQE_{PV}$ . The reciprocity is confirmed by the good match between the measured and calculated  $EQE_{PV}$ . The  $EQE_{EL}$  spectrum peaks at  $\sim 1.07$  eV and it shows a broad

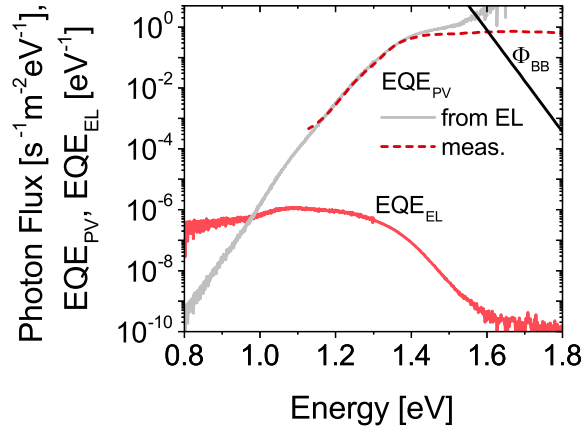


**Figure 7.2.:** The measured  $EQE_{PV}$  and  $EQE_{EL}$  spectra of the PMDPP3T:PCBM solar cell are shown in red (dashed and full lines, respectively). The depicted  $EQE_{EL}$  spectrum is measured at an injection current of  $398 \mu\text{A}$  at  $0.61 \text{ V}$  applied. The gray line shows the  $EQE_{PV}$  spectrum calculated from the  $EQE_{EL}$  spectrum. The photon flux of the black-body spectrum at room temperature is depicted as black line.

shoulder at  $\sim 1.3 \text{ eV}$ . Fitting the  $EQE_{EL}$  and  $EQE_{PV}$  with Gaussian functions to reveal the CT-state energy is ambiguous in this case; in section D.1 this ambiguity is displayed on the basis of two extreme cases either fitting the peak of emission and correspondingly the small shoulder in the calculated  $EQE_{PV}$  resulting in a CT energy of  $1.07 \text{ eV}$  (Figure D.1 b) or fitting the broad shoulder of emission and photocurrent spectrum revealing a CT energy of  $1.35 \text{ eV}$  (Figure D.1 a). That would mean that for the extreme cases the CT-state energy is either larger than the optical band-gap of the donor polymer or that it is more or less equal to the charge separated state energy. Due to this uncertainty, rather than identifying one distinct CT-state energy, the radiative  $V_{OC}$  limit of the solar cell is determined from the black-body photon flux at room temperature and the  $EQE_{PV}$  spectrum, under the assumption of zero non-radiative loss as already conducted in the previous chapters for other systems. The radiative limit of the PMDPP3T:PCBM solar cell is  $1.00 \pm 0.01 \text{ V}$ . The non-radiative voltage loss is determined from the integrated absolute  $EQE_{EL}$ . Figure 7.3 a) shows absolute  $EQE_{EL}$  spectra at different voltages close to one sun  $V_{OC}$ . The integrated  $EQE_{EL}$  values as well as the corresponding non-radiative voltage losses are shown in Figure 7.3 b). Close to  $V_{OC}$  and quasi-equilibrium conditions the measured values deviate by only  $\sim 10 \text{ mV}$  which can partially be explained by the determination of the absolute  $EQE_{EL}$  values as outlined in section D.2. The non-radiative voltage loss at  $V_{OC}$  injection conditions ( $\sim 0.61 \text{ V}$ ) is  $0.376 \text{ V}$  with an approximate error of  $\pm 0.010 \text{ V}$  (section D.2) and it is independent of the injection current within its error. The  $V_{OC}$  calculated from the radiative limit minus the non-radiative loss is  $V_{OC} = 0.624 \pm 0.010 \text{ V}$  which is in perfect agreement with the measured value from the  $JV$ -characteristics (see Figure 7.1).

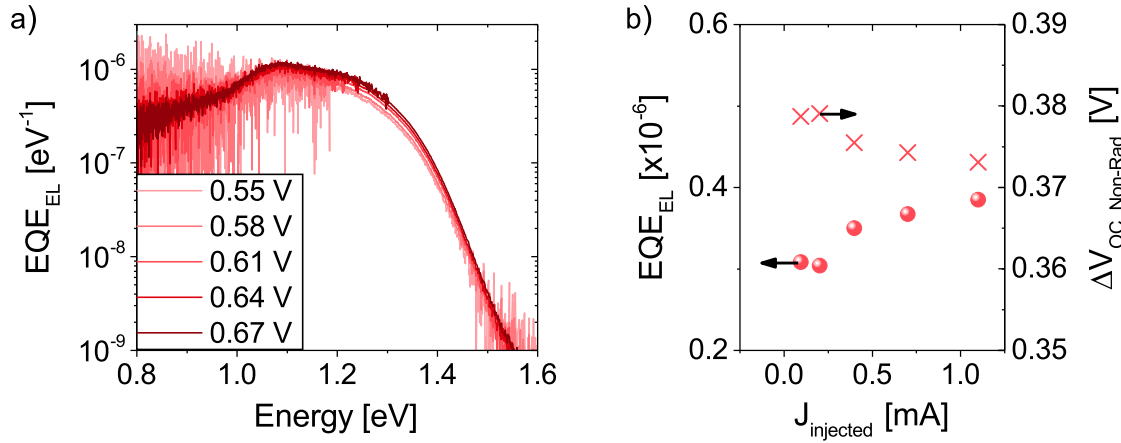


**Figure 7.3.:** a)  $EQE_{EL}$  spectra for different applied voltages. b) the corresponding integrated  $EQE_{EL}$  values as function of the injected current as well as the respective non-radiative voltage loss.

## 7.2. Steady State Recombination evaluated from Recombination Current Measurements

In section 3.2 the series resistance free measurement of the ideality factor was introduced. For this  $J_{SC}-V_{OC}$  method the PMDPP3T:PCBM solar cell is illuminated with different intensities at three temperatures and for each condition a  $JV$ -characteristic is measured. The generated photo current density  $J_G$  is then approximated by the measured current density at the largest applied reversed voltage (deviated between  $-0.3$  V and  $-1$  V). The approximation is valid as the *fill factor* of the PMDPP3T:PCBM solar cell is reasonably high. By plotting  $J_G$  as a function of the respective  $V_{OC}$  the light ideality factor can be determined from the slope of the data according to:

$$n_{id,light} = \frac{q}{k_B T} \frac{dV_{OC}}{d \ln(J_G)}. \quad (7.1)$$

The measured data is plotted in Figure 7.4 a). At lower temperatures the current density seems to increase with higher light intensity without further increasing the  $V_{OC}$ . This has been observed by others before and is attributed to surface recombination.[145] An unambiguous indication of surface recombination is the appearance of light ideality factors smaller than one, which are caused due to a loss of selectivity of the contacts when  $V_{OC}$  approaches the build-in voltage as reasoned by, e.g., Kirchartz et al.[145] To get a good estimate when surface recombination needs to be taken into account the light ideality factor is calculated differentially according to Equation 7.1. The corresponding plot is shown in section D.3 and the onset voltage of surface recombination is estimated from this plot according to section D.3. For the determination of the slope of the linear dependence of  $\log J_G$  vs.  $V_{OC}$  the data points, which

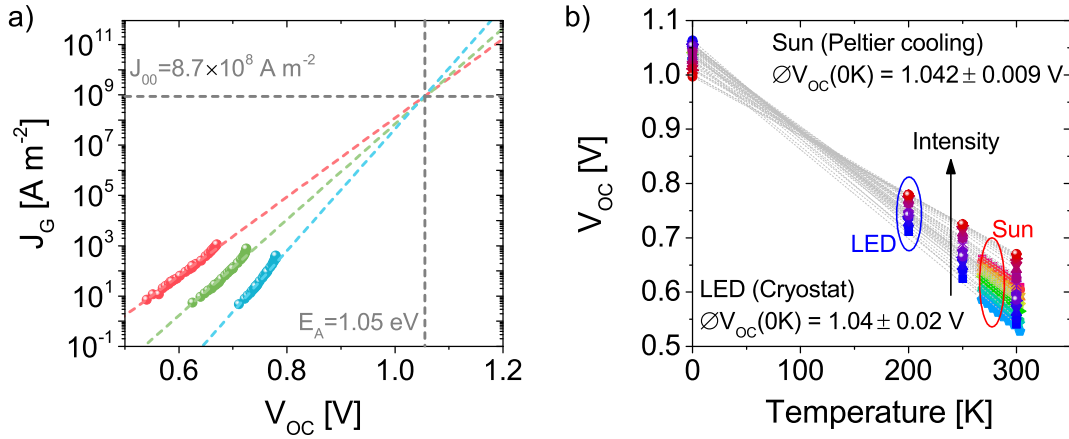


**Figure 7.4.:** a) Generation current as function of  $V_{OC}$  for different illumination intensities and temperatures, fitted with the respective ideality factors. Crossing point of the fits denotes the activation energy for recombination  $E_A$ . If  $V_{OC}$  could reach that effective band-gap energy the potential current  $J_{00}$  would flow.[14] b) Temperature dependent  $V_{OC}$  values measured either at a standardized sun simulator and a Peltier-cooled sample holder with optical density filters for different intensities, or in a helium cooled cryostat and LED illumination. The  $V_{OC}$  extrapolated to zero Kelvin is plotted as well and the averaged values are given in the legend. The extrapolated data measured in the cryostat seem to intersect at about 100 K, whereas the data collected with the Peltier-cooled sample holder intersect rather at 0 K. This can be explained by the temperature measurement in the cryostat where the position of the temperature sensor is likely to cause a slight underestimation of the measured temperature for high intensities in the low temperature regime. Therefore the real temperature for the data points at 200 K and high intensities is probably slightly higher. Hence, the crossing point shifts towards 0 K. Furthermore, measurements were only taken at three different temperatures in the cryostat increasing the effect of this error.

are affected by surface recombination, were neglected. All measured  $J_G(V_{OC})$  data fit best with an light ideality factor very close to 1, as already indicated by the differentially determined ideality factor in section D.3, meaning that bimolecular recombination dominates the recombination current. Even more important, the light ideality factor is temperature independent taking into account measurement uncertainties. These results are in good agreement to literature reports by Tvingstedt et al. where temperature independent ideality factors were found for several typical organic solar cell systems.[14] The rough approximation of the onset of surface recombination is backed up by the fact that all extrapolated  $J_G(V_{OC})$  data, with the respective light ideality factors, intersect at the same voltage of  $\approx 1.05$  eV, corresponding to a hypothetical current density  $J_{00} = 8.7 \times 10^8 \text{ A m}^{-2}$ . The extrapolated  $J_G(V_{OC})$  data actually need to intersect in one point, as this voltage corresponds to the activation energy for recombination ( $E_A \approx 1.05$  eV) and is thereby identified with the effective band-gap of the organic semiconductor system.  $J_{00}$  then denotes the potential current density that would flow if the  $V_{OC}$  could reach its effective band-gap by increasing the charge carrier density in the device.[14] Another way to determine the effective band-gap is by measuring the  $V_{OC}$  as a function of temperature and extrapolating the measured values to 0 K.[34, 47, 146] This was

done at different illumination intensities for the PMDPP3T:PCBM solar cell either conducted at a standardized sun simulator with optical density filters and a Peltier-cooled sample holder or with a high power LED and a helium cooled cryostat. The resulting data is shown in Figure 7.4 b) and the extrapolated averaged values are given for both ways of illumination. For LED and sun simulator illumination the extrapolated values are  $V_{OC}(0K) = 1.04 \pm 0.02$  V and  $V_{OC}(0K) = 1.042 \pm 0.009$  V, respectively. These values are in very good agreement with the extrapolated values obtained from the  $J_G(V_{OC})$  method, strongly supporting the validity of the  $J_{SC}-V_{OC}$  method and the accuracy of the extracted light ideality factors.

The dark ideality factors determined from the dark  $JV$ -characteristics are, however, clearly larger than one and increase with decreasing temperature. The dark ideality factor  $n_{id,dark}$  is determined according to Hawks et al. by:[15]

$$n_{id,dark} = \frac{q}{k_B T} \min \left( \frac{dV}{d \ln J_{dark}(V)} \right). \quad (7.2)$$

The corresponding dark  $JV$ -characteristics are shown in Figure 7.5 a) the differentially determined ideality factors are shown in Figure 7.5 b) and the minima of these values are plotted as a function of temperature in Figure 7.5 c). The usage of this dark ideality factor is however highly questionable as the dark  $JV$ -characteristics are strongly influenced by shunt and series resistance and space charge effects at higher voltages. Only if the slope – and with that the dark ideality factor – is constant over a notable voltage range can the influence of shunt and space charge effects on the minimum value of dark ideality factor be ignored. Even in this case, series resistance can still affect the ideality factor. Nevertheless, good agreement between measured data and simulations including dark ideality factors has been shown before.[15, 56]

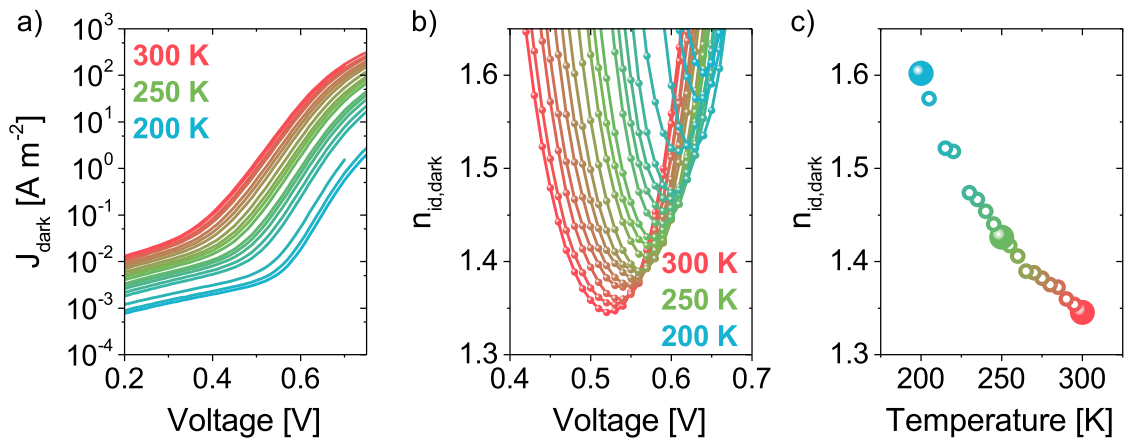


**Figure 7.5.:** a) Dark current of PMDPP3T:PCBM solar cell measured at temperatures between 300 K and 200 K. b) Ideality factors extracted from the dark  $JV$ -characteristics depicted in a). c) Ideality factors determined as the minimum of the values shown in b) as a function of the corresponding Temperature.

To examine the different approaches – either determining the light or dark ideality factor – Equation 3.21 is recalled connecting the parameters  $\beta$  and  $\zeta$  with the ideality factor  $n_{id}$ , with  $\beta$  the recombination order, and  $\zeta$  a parameter describing the energetic disorder in the system, which both can be obtained by charge extraction experiments. Measuring the charge carrier density  $n$  as a function of  $V_{OC}$  for different illumination conditions allows for determination of  $\zeta$  via  $n \propto e^{\zeta V_{OC}}$ . Evaluating  $J_G$  as a function of  $n$  allows for determination of the recombination order  $\beta$  via  $J_G \propto n^\beta$ . As discussed before (section 3.2) the product of  $\beta$  and  $\zeta$  is proportional to  $n_{id}^{-1}$  according to  $\beta\zeta = q/(n_{id}k_B T)$ . In the next section the results of the bias assisted charge extraction experiments will be discussed and  $\beta$ ,  $\zeta$  and  $n_{id}$  are compared on the basis of different recombination models.

### 7.3. Steady State Recombination evaluated from Charge Carrier Density Measurements

In this section BACE measurements on the PMDPP3T:PCBM solar cell are discussed which were conducted to determine the recombination order  $\beta$  and the parameter  $\zeta$ . In the previous chapters the applicability of BACE was proven for different systems and the fundamental concept to extract  $\beta$  from the measurements of the charge carrier density at  $V_{OC}$  conditions was explained. Additionally,  $\zeta$  can be obtained by evaluating the dependence of charge carrier density  $n$  at  $V_{OC}$  for different illumination conditions. Hereby it is especially important to evaluate the measured data free of surface recombination to draw reliable conclusions about the recombination mechanism. Therefore the onset of surface recombination was estimated from the temperature dependent  $J_G(V_{OC})$  data as explained in the previous section. The onset is estimated to be at  $\sim 0.65$  V,  $\sim 0.70$  V and  $\sim 0.75$  V for the 300 K, 250 K and 200 K measurement, respectively and is marked with a dashed line in Figure 7.6. The data and fits that are shown in Figure 7.6 a) are the same as depicted earlier in Figure 7.4 a). The light ideality factors are given in the table in Figure 7.6. With the BACE technique the charges in the device can be extracted at different illumination conditions and at the corresponding  $V_{OC}$ . This was done at the same temperatures (300 K, 250 K and 200 K) for the PMDPP3T:PCBM solar cell. In Figure 7.6 b) the corresponding data are plotted and  $\zeta$  is given as the slope in the log-lin plot of  $n(V_{OC})$  for  $V_{OC}$  up to the onset of surface recombination roughly at a charge carrier density of  $1.0 - 1.3 \times 10^{22} \text{ m}^{-3}$ . The corresponding values are summarized in the table in Figure 7.6. In Figure 7.6 c) the extracted charge carrier density is plotted as a function of the corresponding generated photocurrent density. By determining the slope of the data, again in the range unaffected by surface recombination,  $\beta$  is obtained and the values are also given in the table in Figure 7.6. Clearly, one of the three plots is redundant but by plotting the data in this fashion the importance of surface recombination should be highlighted. Values for  $\beta$ , obtained from  $n(J_G)$ , show some temperature dependence and

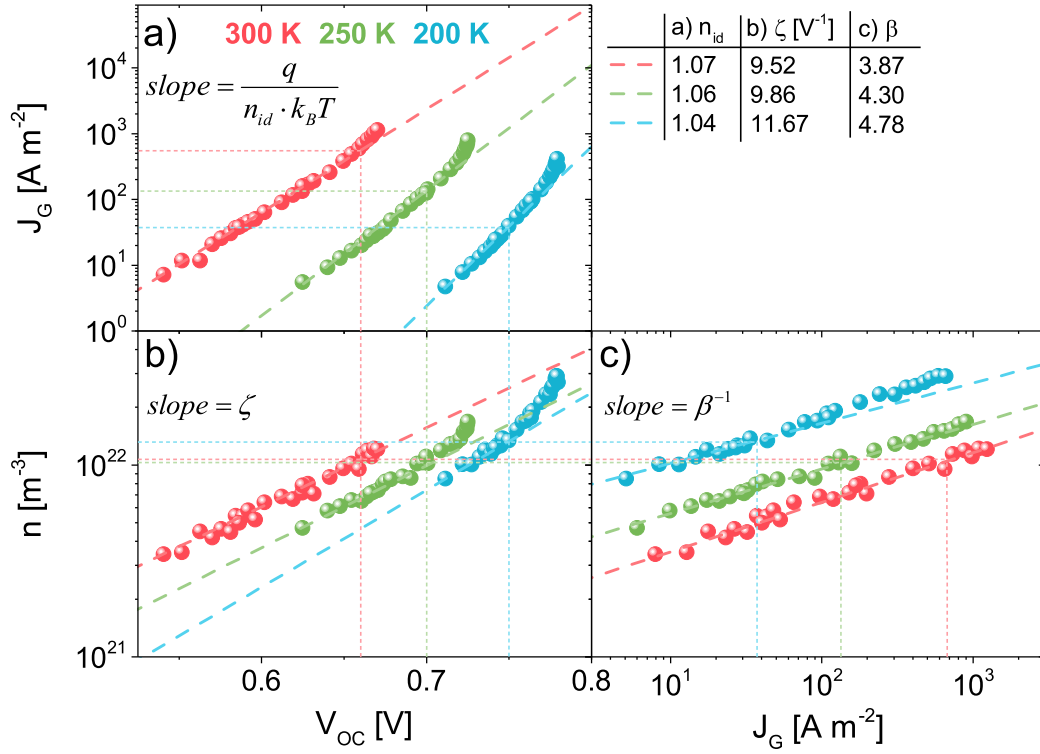


**Figure 7.6.:** Generation current (a) and charge carrier density (b) in dependence of  $V_{OC}$ . c) charge carrier density in dependence of the generation current. Measurements done at 300 K, 250 K and 200 K on the PMDPP3T:PCBM solar cell. Fits to the data are depicted as thick dashed lines. The limiting range affected by surface recombination is given by thin dashed lines which also mark the fitted data range. In the table on the upper right panel all fitting parameters are summed up.

are much larger than 2. As discussed in section 3.2 such high values for  $\beta > 2$  can be reasoned by exponential density of state (DOS) distributions and have been explained by tail-state recombination before.[15, 56] Furthermore, also the disorder parameter  $\zeta$  seems to be slightly temperature dependent. It should be highlighted that this should not be the case if the DOS distributions for electrons and holes both have the same exponential tail-state distribution with  $E_U = k_B T_0$ ,  $m = \frac{T_0}{T}$  and  $\zeta = \frac{q}{2mk_B T} = \frac{q}{2E_U}$ , as discussed in section 3.2 and usually assumed in the literature.[15, 56, 147, 148] However, the light ideality factors which were extracted from Figure 7.6 a) are basically independent of temperature.

In order to gain a better understanding of the recombination mechanism and potential DOS distributions, different model assumptions will be tested which consider two different DOS distributions and recombination either via trapped or free charges. Typically the assumption is made that free electrons recombine with exponentially trapped holes and vice versa. This results in a description of the trapped charge carrier concentration  $n_{tt} \propto \exp(qV_{OC}/2E_U)$  with  $E_U$  describing the tail slope of the valence and conduction bands.[56] This, however, implies

that the parameter  $\zeta$  is independent of temperature and only determined by the exponential tail-slope. On the other hand, assuming that only, e.g., the valance band shows a significant exponential trap state distribution with states well below the Fermi-energy, a different solution for the trapped charge carrier concentration is obtained as outlined in section D.4. The

**Table 7.1.:** Recombination models in dependence of the DOS distributions.

Model	Parameter	free with trapped	free with free
	Rate	$\gamma(n_f p_t + n_t p_f)$	$\gamma n_f p_f$
	$\beta$	$1 + \frac{E_U}{k_B T}$	$2 \frac{E_U}{k_B T}$
	$\zeta$	$\frac{q}{2E_U}$	$\frac{q}{2E_U}$
	$n_{id}$	$\frac{2E_U}{k_B T + E_U}$	1
	Rate	$\gamma n_t p_f$	$\gamma n_f p_f$
	$\beta$	2	$1 + \frac{E_U}{k_B T}$
	$\zeta$	$\frac{q}{E_U + k_B T}$	$\frac{q}{E_U + k_B T}$
	$n_{id}$	$\frac{1}{2} \left( 1 + \frac{E_U}{k_B T} \right)$	1

resulting trapped charge carrier concentration is referred to as  $n_{ft}$  to distinguish it from the case where both charge carriers can be trapped ( $n_{tt}$ ) and  $n_{ft} \propto \exp(qV_{OC}/(k_B T + E_U))$ . Mark and Helfrich furthermore showed that for an exponential trap distribution the free charge carrier density can be related to the trapped charge carrier density by  $n_{free} \propto m^{-1} n_{trap}^m$ , with  $m = \frac{T_0}{T}$  assuming that most charges are trapped and some free charges are present due to thermal excitation.[149]

On the basis of these prerequisites, namely an expression for the charge carrier densities, either free or trapped ones, and either in the situation where both charge carrier types can be trapped or only one, the recombination rates can be derived and, by that, also the recombination currents for each model situation. This will result in four different dependencies of the recombination current on the charge carrier density of electrons  $n$  and holes  $p$  as outlined in Table 7.1 depending on if trapped charges recombine with free ones or if free charges recombine with free ones. The third option of recombination of both trapped charges is not considered as the likelihood of this type of recombination to be dominant is very low.[147] The option with exponentially broadened DOS distributions for both electrons and holes, will be referred to as the Exp-Exp model and the situation where only one of the DOS distribution is exponentially broadened is referred to as Exp-Gauss model. Furthermore, Table 7.1 lists the expected dependencies of  $\beta$ ,  $\zeta$  and  $n_{id}$  on  $E_U$  for each of the cases. In the case of the Exp-Gauss model  $\zeta$  is a function of temperature, while for the Exp-Exp model  $\zeta$  is independent of temperature. Both methods result in ideality factors of one for only free carrier recombination, but at the same time reveal dependencies of  $\zeta$  and  $\beta$  on the exponential tail slope  $E_U$  and for the Exp-Gauss model additionally on temperature. Because the measured light ideality factors are close to one, both methods are tested to simulate  $n(V_{OC})$  and  $n(J_G)$  with  $\zeta$  and  $\beta$  according to the respective  $E_U$  dependency. The results of the simulations are shown in Figure 7.7 for the Exp-Gauss and Exp-Exp model. The measured data are shown as spheres and the best fits presented in Figure 7.6 are denoted as black, dark and light gray lines for 300 K, 250 K and 200 K, respectively. The best simulation of the data is obtained for the Exp-Gauss model at  $E_U = 74$  meV and for the Exp-Exp model at  $E_U = 50$  meV. The best simulations with the aforementioned energies are denoted as full dark colored lines for the Exp-Gauss model and dashed light colored lines for the Exp-Exp model.

At first glance the Exp-Gauss model seems to simulate the measured data slightly better as the temperature dependence of  $\zeta$  is in better agreement with the fits to the data than a constant  $\zeta$  as can also be seen from the table in Figure 7.7. On the other hand, due to the lack of lower  $J_G(V_{OC})$  data at 200 K, there are only few data points that are unaffected by surface recombination, rendering both models suitable to describe the measurement. The approximated values of  $E_U$  for both models allow for calculation of the ideality factors according to Table 7.1 for recombination between free and trapped charge carriers. The results are shown in Figure 7.8 and apparently the Exp-Exp model with  $E_U = 50$  meV also describes the temperature dependence of the dark ideality factor, determined from the dark  $JV$ -curves, reasonably well. This is rather surprising as the slope of the dark  $JV$ -curves did not show any plateau region where the dark ideality factor would be constant (shunt and space charge free) and trustworthy values could be derived.

One could try to distinguish between both models using Kelvin probe measurements. In a Kelvin probe measurement the work function of the active layer is measured as a function of its thickness on either the anode or cathode. Lange et al. showed that by this means the

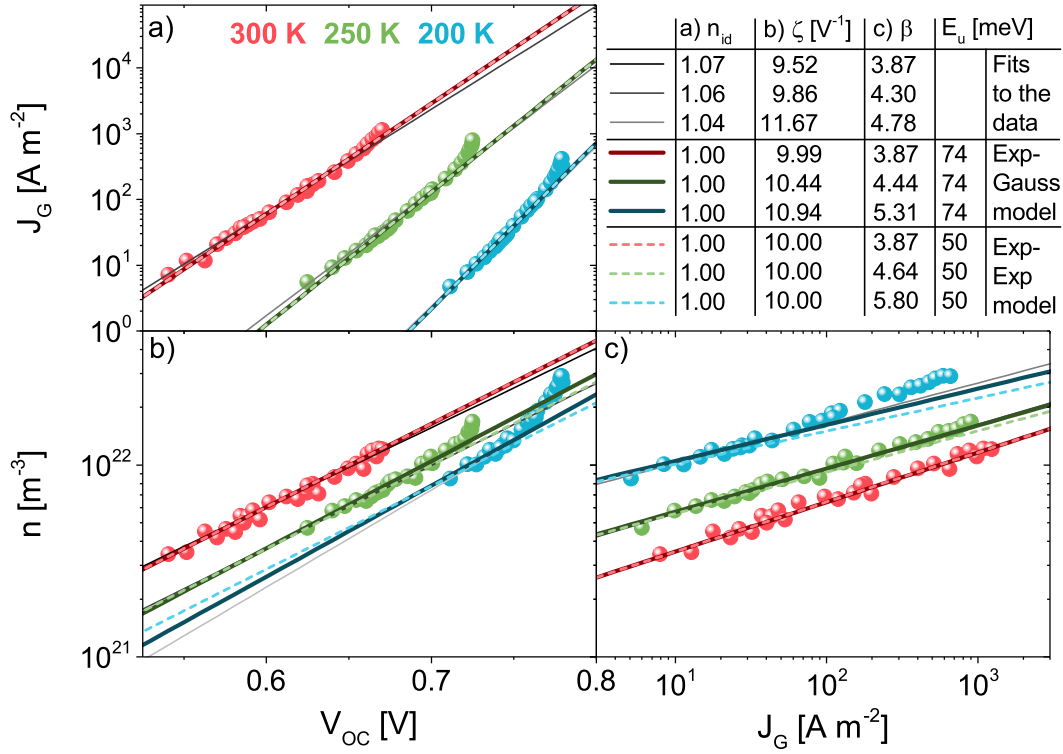


**Figure 7.7.:** Generation current (a) and charge carrier density (b) in dependence of  $V_{OC}$ ; c) charge carrier density in dependence of the generation current according to Figure 7.6. Fits to the data, according to Figure 7.6 and not assuming any model, are depicted as thin full lines (black: 300 K, dark gray: 250 K, light gray: 200 K). Full dark colored lines denote simulations according to the Exp-Gauss model with best agreement to the measured data for  $E_U = 74$  meV. Dashed light colored lines denote optimized simulations with the Exp-Exp model with  $E_U = 50$  meV. The table in the upper right panel lists the corresponding parameters for  $\beta$ ,  $\zeta$  and  $n_{id}$ .

band bending of the HOMO and LUMO towards their respective electrodes can be derived and with that the respective disorder.[150] Unfortunately due to lack of material these experiments were not conducted, but the main conclusion is not altered by the uncertainty as to which model best reflects the real energetics. The finding that light ideality factors of one and trap state distributions are in full agreement with each other, if the recombination channel is assumed to be dominated by the free charges in the device under illumination and not the trapped ones, is of major importance and the main result of this section.

The agreement with the dark ideality factor obtained from the measurement and the Exp-Exp model with  $E_U = 50$  meV can be reasoned with the lower charge carrier density in the dark experiments than in, e.g., the  $J_{SC}$  vs.  $V_{OC}$  measurements. This implies that the dark ideality factor is more relevant for low charge carrier densities with very little free charges in the device meaning that the influence of the trapped-free recombination channel becomes more important.

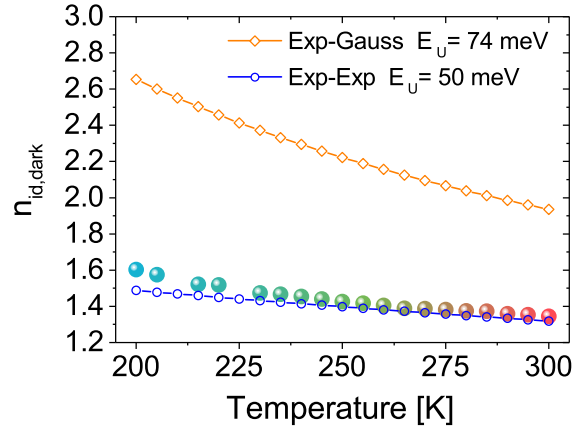


**Figure 7.8.:** Dark ideality factors calculated for the Exp-Gauss (orange) or the Exp-Exp (blue) model.

Another strong argument for recombination being dominated by free to free carrier recombination, despite the presence of trap states in the device, can be derived from the  $EQE_{PV}$  measurements. The  $EQE_{PV}$  is the efficiency of generated photocurrent as a function of wavelength. Thus, from an exponentially decaying absorption below the effective gap energy the Urbach energy can be derived. According to Hawks et al. the slope of the absorbing of the photocurrent generating states should be the same as  $E_U$ , the energy that was extracted from the charge carrier density measurements and a model where both DOS distributions are exponentially broadened.[15] This would imply for the PMDPP3T:PCBM solar cell that the  $EQE_{PV}$  in the low energy regime is fitted best with an Urbach energy of 50 meV, however the slope of the low energy part of the  $EQE_{PV}$ , shown in Figure 7.2, fits to an energy of  $\approx 25$  meV. The slope of 25 meV is in perfect agreement with the  $J_G(V_{OC})$  dependence as shown in Figure 7.6 a) and an ideality factor of one. This becomes clear by referring to Equation 3.20 in which the recombination current density is related to  $V_{OC}$  and accordingly, with  $J_R = J_G$  (valid at  $V_{OC}$ ),  $J_G \propto \exp(\frac{qV_{OC}}{n_{id}k_B T})$ . That means that the recombination current at  $V_{OC}$  is entirely dominated by a bimolecular process and that the slope of the low energy part of the  $EQE_{PV}$  represents exactly this  $J_G(V_{OC})$  dependence.

## 7.4. Transient Recombination - TDCF

In subsection 6.2.3 the differential charge carrier decay was determined with the TDCF technique for the fluorinated organic solar cell systems. The very good agreement between the steady state BACE measurement and the differential data was shown and both measurement techniques confirmed bimolecular recombination. For the PMDPP3T:PCBM system the steady state BACE recombination measurements revealed recombination orders larger

than two assigned to exponential trap distributions, but a recombination mechanism mediated via free states of purely bimolecular nature. These findings should be compared and put into perspective with the results of transient TDCF measurements. In Figure 7.9 the extracted total and pre charge carrier density are plotted as a function of the delay time between laser excitation and extraction with a high reverse voltage. The measurements were done

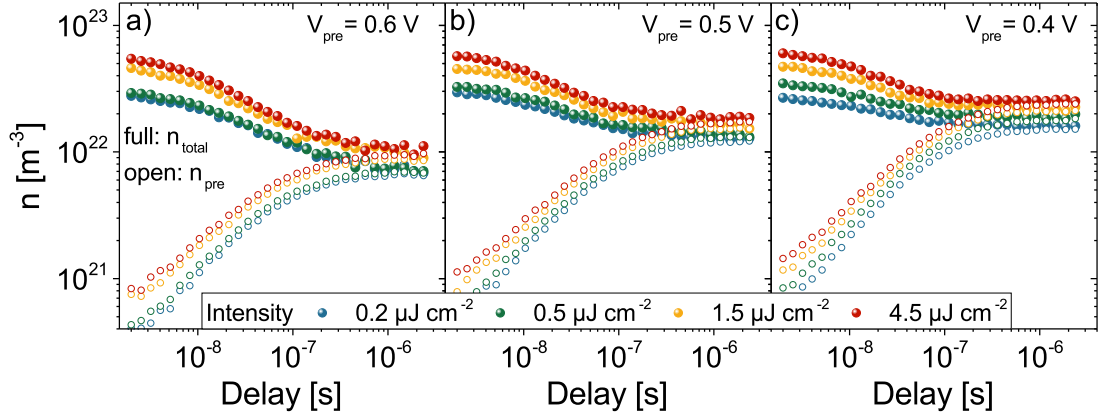


**Figure 7.9.:** Delay dependence of the total charge carrier density of the PMDPP3T:PCBM solar cell extracted at pre biases 0.6 V (a), 0.5 V (b) and 0.4 V (c) and at different fluences.

for three different pre biases (0.6 V, 0.5 V, 0.4 V) and four different intensities in the range of  $\sim 0.2$  to  $\sim 4.5 \mu\text{J cm}^{-2}$  at room temperature. From these data the differential decay can be plotted as function of collected charge carrier density and the resulting differential plots are shown in Figure 7.10. For the extraction after short delay times (high collected charge carrier density) the rates differ and the temporal evolution is different for each fluence. This is likely to be caused by thermalization effects due to fast hot excitation relaxation or other phenomena, which need to be examined more thoroughly in the future. After not more than 20 ns all rates follow a similar dependency on collected charge carrier density independent of fluence. For long delay times (lowest  $n_{coll}$ ) there is no big change in total collected charge anymore, because all charges are already extracted with pre bias. This can be seen in Figure 7.9 where the total and the pre charge are plotted as function of delay time in a range of 2 ns to  $\sim 3 \mu\text{s}$ . As the change in total extracted charge carrier density becomes small, the determination of the differential decay becomes very noisy and unreliable. Therefore, in Figure 7.10 the decay rates are only plotted up to  $\sim 300$  ns.

Apparently, the differential decay data do not follow a straight power law dependence and different regimes with different slopes above and below a charge carrier density of approximately  $2 \times 10^{22} \text{ m}^{-3}$  are found as shown in Figure 7.10. In the previous section it was however shown that the recombination current is dominated by free charge carrier recombination and a model was introduced, which explains high recombination orders from BACE experiments. To compare the steady state BACE results with the TDCF results the recombination rates determined by TDCF were corrected by adding the recombination of the dark injected

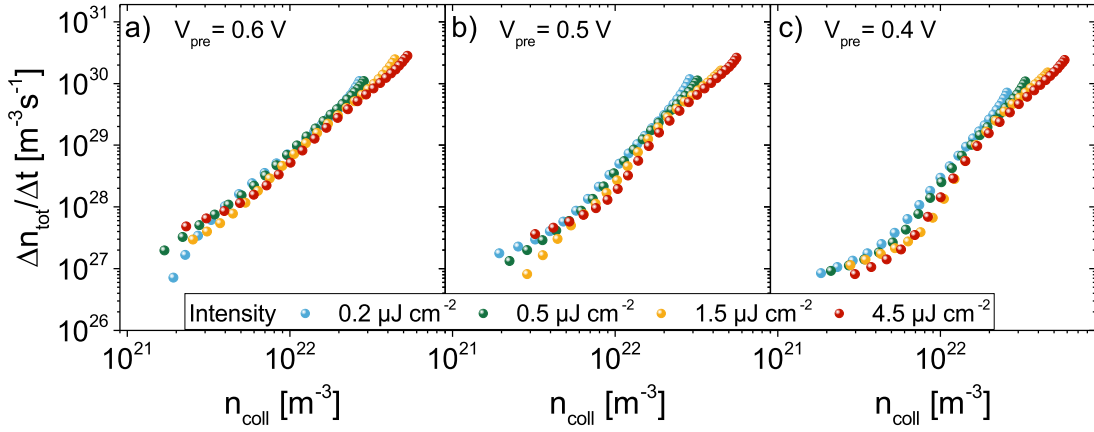


**Figure 7.10.:** Differential charge carrier density decay as a function of the charge carrier density collected with the extraction pulse ( $n_{coll}$ ). Extraction experiments were conducted with pre bias set to 0.6 V (a), 0.5 V (b) and 0.4 V (c) and at four different intensities.

charge carrier density ( $\gamma n_{BG}^\beta$ ) to the rates depicted in Figure 7.10. Furthermore, these rates are plotted as functions of the total ( $n_{tot} = n_{coll} + n_{BG}$ ) and not the collected ( $n_{coll}$ ) charge carrier density. This needs to be done to account for the different measurement techniques, as in a TDCF experiment the recombination of the dark injected charge carrier density is not considered. The BACE data are depicted as black stars in Figure 7.11 together with the corrected TDCF rates. A perfect agreement between TDCF and BACE is obtained; in the charge carrier density range in which rates could be measured with the BACE technique, the recombination data measured with TDCF show the strongest rate increase with charge carrier density and a slope clearly larger than 2. From the BACE measurements at room temperature conditions a recombination order of  $\beta = 3.87$  was determined. The simulation of the recombination rate with  $\beta = 3.87$  is depicted as magenta colored line in Figure 7.11. For charge carrier densities larger than  $\approx 2 \times 10^{22} \text{ m}^{-3}$  the rates determined by TDCF clearly deviate from this dependency. For the charge carrier density range dominated by the higher order, which was already explained and reasoned by a trapped charge carrier distribution in the previous section, a density dependent bimolecular recombination coefficient  $k_2(n)$  can be determined by:

$$R = \gamma n^\beta = R_{BMR} = k_2 n^2 \quad (7.3)$$

$$\Rightarrow k_2(n) = \gamma n^{\beta-2}, \quad (7.4)$$

with the recombination coefficient  $\gamma$  determined for a certain order  $\beta$ . However, in the previous chapter it was shown that the light ideality factor is one and the process that determines the recombination current needs to be bimolecular, meaning that only actual free charges

and not the trapped ones determine the recombination rate. Nevertheless, from the measured data, a charge carrier density dependent bimolecular recombination coefficient can be determined according to Equation 7.3, if  $\beta > 2$ , but this automatically implies that not only free, but all charges are taken into account for the calculation, including the extractable trapped charges. Therefore, by evaluating the recombination rates with a density dependent bimolecular recombination coefficient  $k_2(n)$  the amount of free charges that actually contribute to the recombination current is overestimated while the actual free charge carrier, bimolecular recombination coefficient  $k_{2,eff}$  is underestimated.

Apparently, at very high illumination intensities the differential decay data indeed rather follows a power law with a slope of two ( $\beta = 2$  in the simulation; depicted as green line), meaning that briefly after excitation and an initial thermalization the recombination is dominated by a bimolecular process. The appearance of this bimolecular dependency is explained by high charge carrier densities and concomitantly a higher ratio of free to trapped charges such that free charge carrier recombination dominates the total recombination rate.

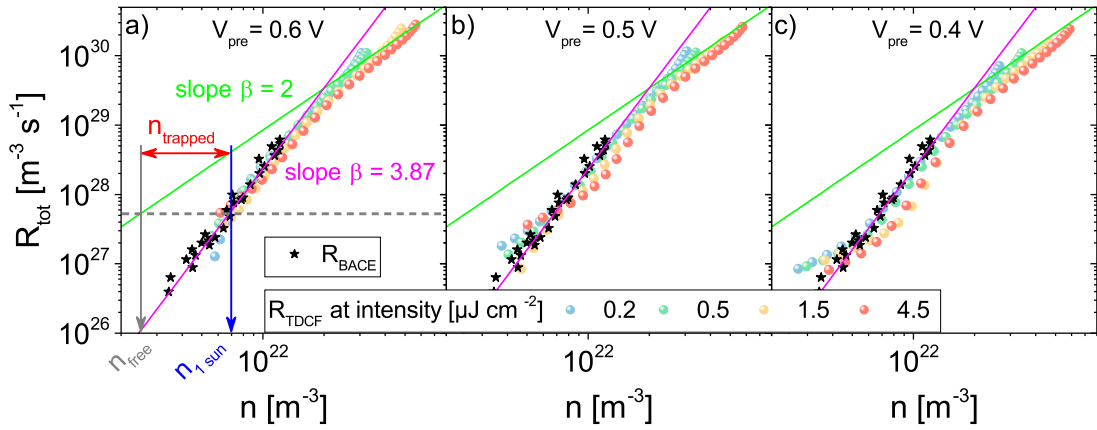


**Figure 7.11.:** The data shown in Figure 7.10 with the corrected BACE recombination rates (black stars) and simulations according to Equation 6.2 with recombination orders  $\beta$ . The charge carrier density at one sun illumination intensity is marked with a blue line. The free charge carrier density and the injected background charge carrier density are marked in light and dark gray, respectively.

This allows for the evaluation of the free charge recombination process and an effective bimolecular recombination coefficient of  $k_{2,eff} = 8.5 \times 10^{-16} \text{ m}^3 \text{ s}^{-1}$  is determined. In Figure 7.11 the according bimolecular recombination rate is depicted as a function of  $n$  which accounts for only free charges in this case. The rates that were measured by TDCF and BACE are depicted as functions of  $n = n_{tot}$  the total charge carrier density which includes trapped and free charges as all charges are extracted in a typical BACE or TDCF experiment. At roughly  $2 \times 10^{22} \text{ m}^{-3}$  the measured and the bimolecular, free carrier rate start merging and the carrier densities in the device are so high that the mistake by accounting for the trapped charges is reduced, although they are not participating in the bimolecular recombination process.

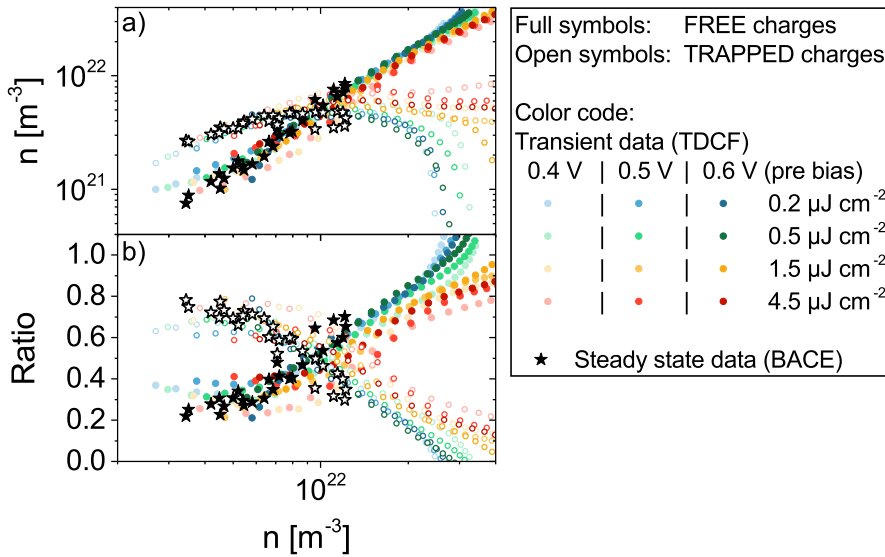


**Figure 7.12.:** a) Free (green) and trapped (red) charge carrier density and b) the ratio of free (green) and trapped (red) charge carrier density to the total charge carrier density as a function of the total charge carrier density. Different symbols denote the different pre bias conditions in the according TDCF extraction experiment. The calculations were only done for the highest injection conditions to have enough free charges in the device so that those charges dominate the recombination rate and a clear effect is becoming visible.

In Figure 7.11 a) the charge carrier density extracted at approximately one sun conditions is marked as blue line. A horizontal dashed line denotes the approximate recombination rate at one sun condition that was determined in the charge extraction experiments. The intersection of this dashed line with the green line (expected free carrier recombination based on  $k_{2,eff}$ ) marks the free charge carrier density which contributes to the bimolecular, free carrier recombination process, that actually dominates the recombination current as demonstrated in the previous chapter. This free charge carrier density is marked with a light gray line. For any fixed rate measured in a TDCF or BACE experiment the total charge carrier density can be divided into free and additionally trapped charges. In Figure 7.12 a) the free and trapped charge carrier densities are plotted as functions of the total charge carrier density ( $n = n_{tot}$ ) and in Figure 7.12 b) the ratios of free and trapped to the total charge carrier density are shown. This evaluation was done for all pre biases and fluences that were used in the TDCF experiments (colored dots in the plot), and as well for the BACE data (black stars). From Figure 7.12 a) it can be seen that for low total charge carrier densities the trapped and free charge carrier density increase with increasing total charge carrier density. The trapped charge carrier density (open symbols in Figure 7.12 a) reaches a plateau value of roughly  $4$  to  $8 \times 10^{21} \text{ m}^{-3}$  when all traps are filled. This plateau region is most prominent for the highest fluences that have been used in the TDCF experiment (red symbols). Also for the BACE data a leveling off of the trapped charge carrier density is identified and the

appearance of such a plateau is in agreement with the prediction of traps that get completely filled. The additional free charge carrier density is constantly increasing and consequently starts to dominate the total recombination rate. Thus it was possible to get an estimate for the effective free charge carrier BMR coefficient in the first place. From Figure 7.12 b) it becomes clear that for low charge carrier densities almost 80% of the charges are trapped and only 20% are really free and contribute to the recombination current. This interpretation of the data is in good agreement with the findings of the previous section where a bimolecular behavior of the recombination current was observed while at the same time trapped charges were identified.

## 7.5. Extraction of Charges - the Effective Mobility

So far it was shown that a single bimolecular process of only free charge carriers dominates the recombination current in these PMDPP3T:PCBM solar cells. This, however, implies that it should be possible to fit the  $JV$ -characteristics, which are measured under different illumination conditions, with one constant bimolecular, free carrier recombination coefficient  $k_{2,eff}$  instead of a charge carrier dependent bimolecular recombination coefficient. The Würfel-Neher model which was introduced in section 3.2 and applied in subsection 6.3.5 is applicable to the PMDPP3T:PCBM solar cells, because it explicitly assumes that the recombination mechanism can be described by free to free charge carrier recombination and that the occupation of tail states can be described by the Boltzmann approximation instead of Fermi-Dirac statistics.[49, 68] This furthermore means that trapped charges have almost no influence on the steady state recombination current. To simulate the  $JV$ -characteristics with this model, not just the free charge carrier recombination coefficient, but also the mobility of these free charges needs to be known. It was shown before, e.g. in section 6.3 or in other publications,[109, 139] that the BACE technique allows one to determine effective mobilities in solar cells. In the BACE experiment also trapped charges are extracted and the effective mobility reflects the mobility of charges with respect to all charges that are extracted and not just the free charge carrier mobility. Nevertheless, for high charge carrier densities and a complete filling of traps the overall effective mobility is increasingly dominated by the rising amount of free charge carriers. Unfortunately, in the experimental BACE setup the illumination intensities are limited and even for the highest illumination condition the influence of trapped charges on the effective mobility is probably still large. Therefore, BACE effective mobilities are determined at high intensities and close to  $V_{OC}$  conditions to get closer to a mobility value which represents the actual free charge carrier mobility. Furthermore, BACE mobilities are found to be more trustworthy and more comparable to SCLC measurements at higher illumination conditions and close to  $V_{OC}$  as shown in the PhD thesis of Juliane Kniepert or the Master thesis of Edgar Nandayapa.[135, 151] The measurements of the charge carrier densities at open circuit conditions or as functions of another applied bias at a fixed intensity

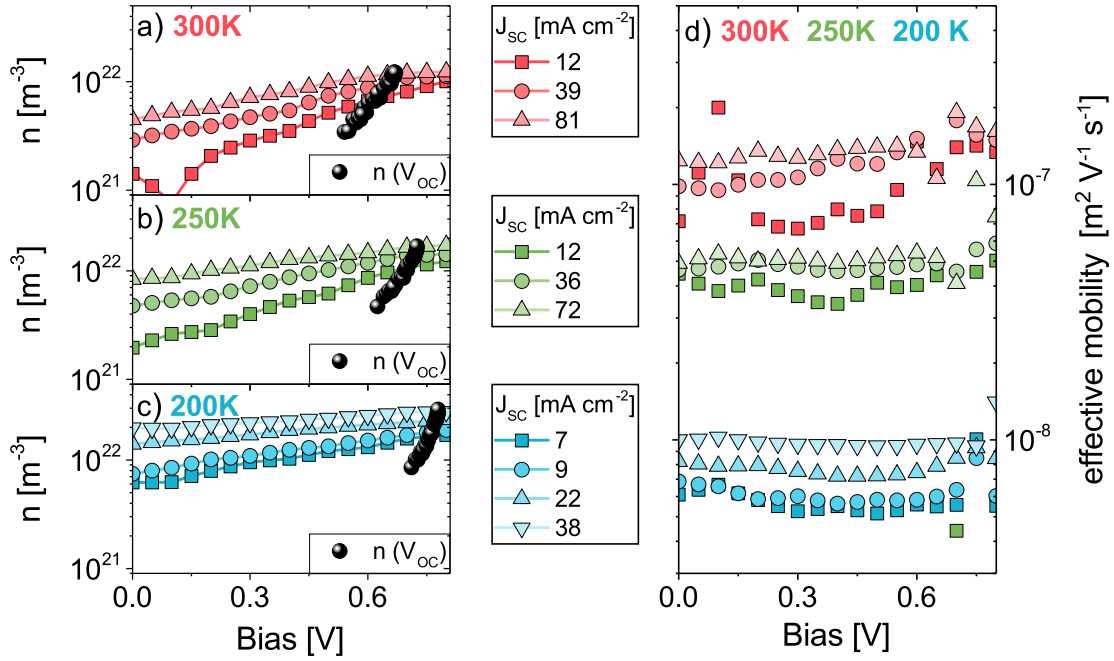


**Figure 7.13.:** BACE data for the PMDPP3T:PCBM solar cell at a) 300 K, b) 250 K and c) 200 K. The black spheres denote the charge carrier density data at different  $V_{OC}$  values according to increasing illumination intensities. For certain illumination intensities the extraction of charges is measured as a function of applied voltage. These data are shown as colored symbols with short circuit current densities as denoted in the legend. d) Effective mobilities of the PMDPP3T:PCBM solar cell as a function of applied bias for 300 K, 250 K and 200 K according to a), b) and c).

are shown in Figure 7.13 for three different temperatures (a) 300 K, b) 250 K and c) 200 K). The data are evaluated in the same way as presented in subsection 6.3.4 for the FTIC system. The extracted effective mobilities are shown as a function of the applied voltage in Figure 7.13 d). The effective mobility is relatively constant over a wide voltage range and increases with increasing the illumination intensity, as expected in case of disorder. The effective mobilities are determined to be  $\mu_{eff} = 1.5 \times 10^{-7} \text{ m}^2 \text{ V}^{-1} \text{ s}^{-1}$ ,  $\mu_{eff} = 4.8 \times 10^{-8} \text{ m}^2 \text{ V}^{-1} \text{ s}^{-1}$  and  $\mu_{eff} = 9 \times 10^{-9} \text{ m}^2 \text{ V}^{-1} \text{ s}^{-1}$  for 300 K, 250 K and 200 K, respectively. As mentioned before, the maximum intensity, which is applicable in the BACE measurement, is lower than what can be applied in the TDCF experiment. This becomes clear by comparing the black stars (BACE) with the measured TDCF data in Figure 7.11. Therefore, the actual effective mobility of the truly free charges will be higher than what is determined by BACE. As a future perspective it would be beneficial to experimentally realize higher illumination intensities in the BACE measurement to attain similar charge carrier density regimes like in TDCF.

## 7.6. Simulation of the *JV*-Characteristics for Different Illumination Intensities

In the previous sections the effective, free charge carrier bimolecular recombination coefficient  $k_{2,eff}$  was introduced and estimated from the TDCF data for the PMDPP3T:PCBM solar cell at 300 K. Additionally the effective mobility was measured with the BACE technique at 300 K, 250 K and 200 K. In order to finally test the applicability of the concept of an effective bimolecular recombination coefficient to describe the recombination process in organic solar cell systems that show a trapped charge carrier distribution, measured *JV*-characteristics will be compared to simulations based on the modified Shockley-equation (section 3.2) according to the Würfel-Neher model. The previously determined, effective, free carrier recombination coefficient  $k_{2,eff}$  is used in these simulations and the free carrier mobility is close to the BACE effective mobility that were measured at high fluences. The modification of the Shockley-equation, accounting for transport limitations, depends on the figure of merit  $\alpha$  (Equation 3.24), which itself depends on the ratio of free charge carrier recombination and the effective mobility, as well as on the generation current, the active layer thickness and temperature.[49] In Figure 7.14 *JV*-characteristics of the PMDPP3T:PCBM solar cells are shown that were measured at three different temperatures and over a wide range of intensities.

**Table 7.2.:** Simulation Parameters for the PMDPP3T:PCBM solar cell.

Temperature [K]	300	250	200
$k_{2,eff}$ [ $\text{m}^3\text{s}^{-1}$ ]	$8.5 \times 10^{-16}$	$1 \times 10^{-16}$	$6 \times 10^{-17}$
$\mu_{eff}$ [ $\text{m}^2 \text{V}^{-1} \text{s}^{-1}$ ]	$3 \times 10^{-7}$	$4.8 \times 10^{-8}$	$9 \times 10^{-9}$

In Figure 7.14 b) the same data are shown as in a) but with a different scaling. The measured data are depicted as colored lines and the simulations according to the modified Shockley-equation are shown as gray dashed lines. In Table 7.2 the parameter values used in the simulation are given for each temperature. The photogenerated current density was used as a fitting parameter as well, because the photocurrent density, measured at reverse bias conditions, was not completely saturated, especially not for the high illumination intensities and low temperature measurements. However, the absolute value of the generated photocurrent density does not influence the *FF* strongly. The actual shape of the *JV*-curve is dominated by the competition of extraction and recombination, reflected by  $k_{2,eff}$  and  $\mu_{eff}$ . The agreement with the measured and simulated data is very good. For 300 K the determined  $k_{2,eff}$  and a  $\mu_{eff}$  of  $3 \times 10^{-7} \text{m}^2 \text{V}^{-1}\text{s}^{-1}$  perfectly describe the *JV*-curves over a large intensity range. The measured effective mobility of  $1.5 \times 10^{-7} \text{m}^2 \text{V}^{-1} \text{s}^{-1}$  is only half the mobility value that was used for the best fit. As mentioned before, the measured effective mobility (BACE) might actually underestimate the real free charge carrier mobility. The overall high effective mobility, which is found for the PMDPP3T:PCBM system, is in good agreement with high mobilities, that have been found in literature for PMDPP3T and

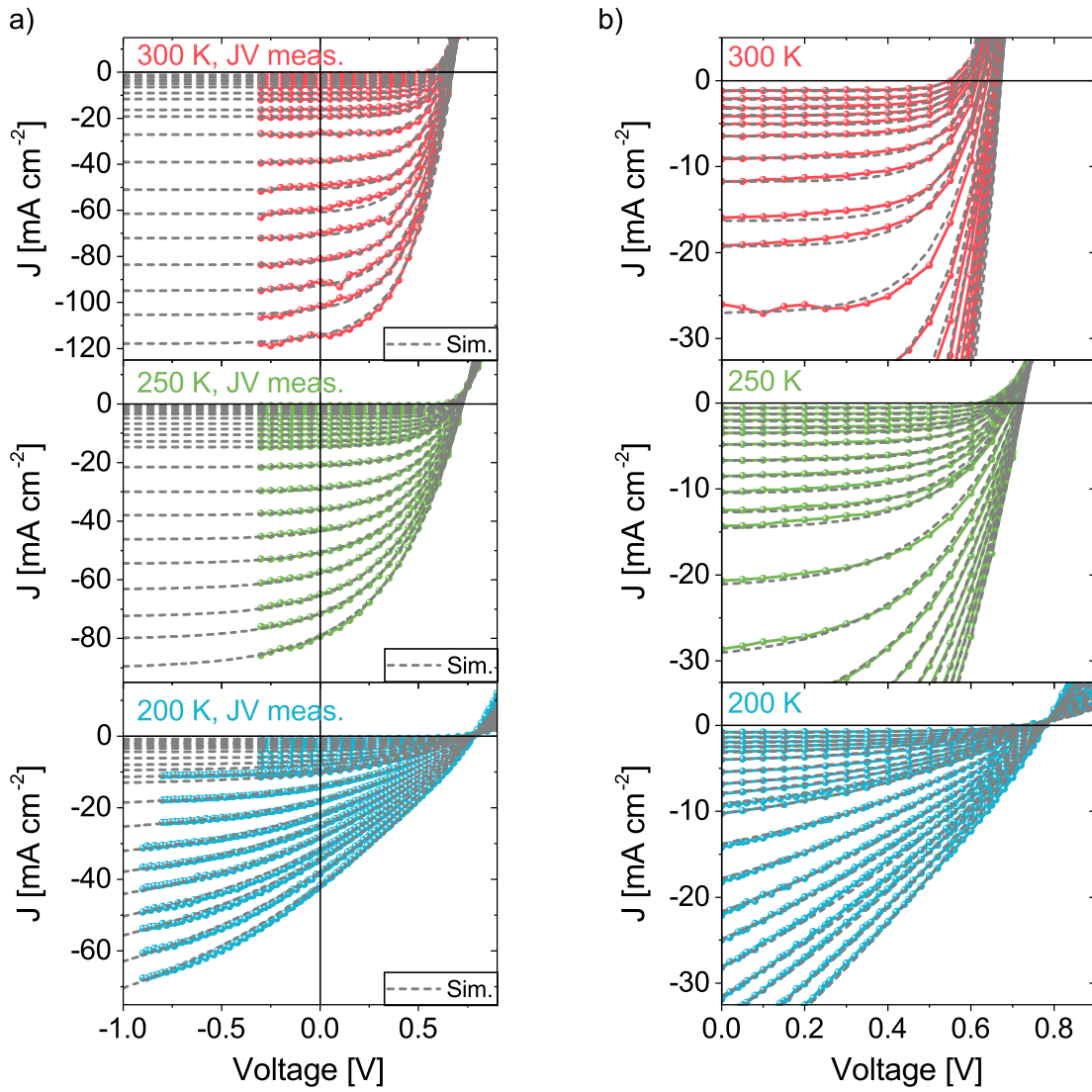


**Figure 7.14.:** Simulation of the  $JV$ -characteristics of the PMDPP3T:PCBM solar cell compared to the measured values at 300 K, 250 K and 200 K. The simulation data is denoted as gray dashed lines. The simulation was done by use of the modified Shockley-Equation (Equation 3.26) and with the measured parameters.

PCBM.[152, 153] Short circuit currents are measured in the range of  $J_{SC} = 1.2 \text{ mA cm}^{-2}$  to  $J_{SC} = 118 \text{ mA cm}^{-2}$  at 300 K. For the simulation of the  $JV$ -curves that were recorded at lower temperatures, no free charge carrier recombination coefficients could be determined as the TDCF measurements could not be performed for the low temperatures. Therefore, both  $k_{2,eff}$  and the effective mobility can be used as free fitting parameters for the simulations at 250 K and 200 K. Nevertheless, for the simulations of the low temperature  $JV$ -curves the measured effective mobilities were taken that had been determined by BACE even though they might actually underestimate the real free charge carrier mobility. This was done to get a reference point for the effective mobility values. As a consequence, also the effective,

free charge carrier recombination coefficients in the solar cell at 250 K and 200 K might be larger than the values that were used in the simulation. Furthermore it is not clear how the mobility of each charge carrier type changes with decreasing temperature and how the free carrier mobility is affected by this.

The uncertainty of correct determination of mobility, generated charge carrier density and effective bimolecular recombination coefficient for the 250 K and 200 K data sets from the simulations that were presented in Figure 7.14 can also be visualized in a different way. Therefore, the  $FF$  of each  $JV$ -curve (measured at different temperatures and light intensities) is plotted as a function of  $\alpha$  that was determined from the fitting parameters which were used to fit those  $JV$ -curves. The corresponding  $FF(\alpha)$  values are shown in Figure 7.15 a), b) and c) for the three temperatures. As expected, and as seen before (subsection 6.3.5), the  $FF$  drops with increasing  $\alpha$  for all temperatures. The  $V_{OC}$  of the different  $JV$ -curves increased with increasing intensities from  $\sim 0.55$  V to  $\sim 0.68$  V at 300 K, from  $\sim 0.62$  V to  $\sim 0.73$  V at 250 K and from  $\sim 0.71$  V to  $\sim 0.78$  V at 200 K. According to Neher et al.  $FF(\alpha)$  values can be calculated for each  $V_{OC}$  based on an empirical  $FF(V_{OC})$  expression.[49] In Figure 7.15 a), b) and c) the predicted  $FF(\alpha)$  values are plotted as gray lines for the respective highest and lowest  $V_{OC}$  values that were measured for the highest and lowest intensity for each temperature. As a consequence the  $FF(\alpha)$  data which were determined from the measured  $FF$ s and the free carrier parameters that were used to fit the  $JV$ -curves should fall in between the respective gray lines. While the  $FF(\alpha)$  values at 300 K nicely confirm this trend, the 250 K and 200 K

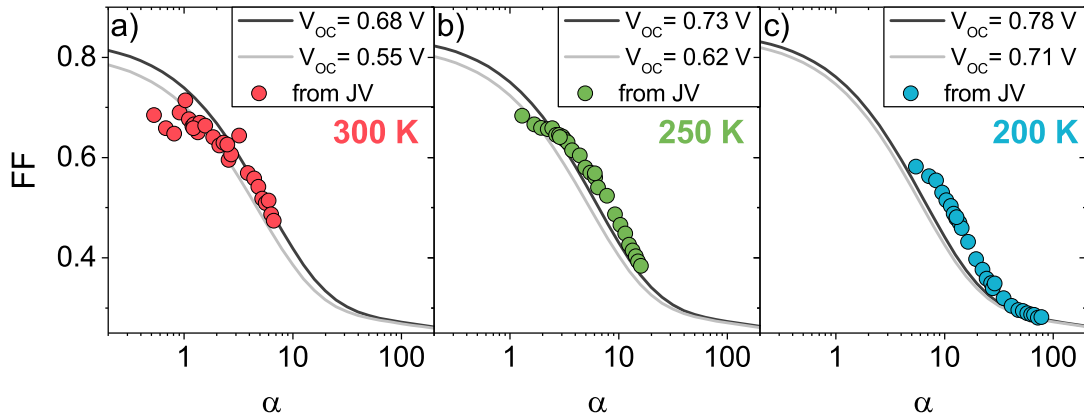


**Figure 7.15.:**  $FF(\alpha)$  values for the PMDPP3T:PCBM solar cell measured at 300 K a), 250 K b) and 200 K c) and different light intensities (Figure 7.14). The gray scaled lines show the prediction of  $FF(\alpha)$  values according to Neher et al. for different  $V_{OC}$  values.[49]

data are shifted to too high  $V_{OC}$  predictions. On the one hand, this underlines the accuracy of the determined free carrier mobility, effective free carrier recombination coefficient and the generated photocurrent values which were determined from the 300 K measurements. On the other hand, it reveals that the actual values for the 250 K and 200 K measurements probably deviate from the values that were used for the simulation of the  $JV$ -curves as displayed in

Figure 7.14. Nevertheless, the trend of a decreasing  $FF$  with increasing  $\alpha$  is confirmed in all cases.

Overall, these findings underline that the effective recombination coefficient is high, this suggests that free charges in PMDPP3T:PCBM solar cells indeed tend to recombine very efficiently. The fact that the PMDPP3T:PCBM solar cells show high  $FF$ s despite their high effective recombination coefficient is in good agreement with the high free carrier mobilities and an efficient extraction of those free charges.

## 7.7. Discussion

In this comprehensive study the recombination process in PMDPP3T:PCBM solar cells was examined. Steady state and transient measurement techniques were employed and the results were explained by a new model of how to interpret the recombination mechanism in these PMDPP3T:PCBM solar cells. The presented model has important implications and might help to shed new light on the question of whether recombination processes in organic solar cells are dominated by free carrier recombination or by traps. For the PMDPP3T:PCBM system a light ideality factor of one is found by evaluating the current density as a function of *open circuit voltage*. This implies that actually only free charges outside the Fermi-gap contribute to the recombination current of these cells. On the other hand, charge extraction experiments revealed a high recombination order that is explained by trapped charges. This shows that conclusions about the recombination mechanism in organic solar cells depend on the measurement technique and the way of how the data is interpreted. The newly introduced model reveals that these, at the first glance, contradicting experimental findings are in agreement with each other under the premise that only the actual free charges contribute to the recombination current. By means of transient and steady state charge extraction experiments the free charge carrier recombination mechanism was identified and a free carrier recombination coefficient  $k_{2,eff}$  has been introduced. Finally,  $JV$ -characteristics which were measured over a broad intensity range could be fit with this newly introduced effective, free charge carrier recombination coefficient. However, the exact trap distribution could not be unambiguously revealed, but the prediction of the temperature dependence of the dark ideality factor with the Exp-Exp model suggests that both, electrons and holes are trapped in the PMDPP3T:PCBM solar cell. Measuring the energetic disorder with the Kelvin probe technology might enable to distinguish more clearly between both suggested trap distributions that were tested in this model. In Figure 7.16 the final results are summed up in a sketch according to Figure 3.1 for this particular case of a PMDPP3T:PCBM solar cell. It can be concluded that the recombination mechanism is not dominated by the trap states in the device and the recombination coefficient  $\gamma$  (dark blue) has no physical meaning in this case. It should be pointed out that the interpretation of the data assuming a charge carrier density dependent  $k_2(n)$  (light blue) would still consider the recombination as mediated by

states outside the Fermi-gap. Hence this picture would be in agreement with the light ideality factors of one, but at the same time a charge carrier density dependent  $k_2(n)$  would require a charge carrier dependent mobility to correctly account for the trapped charges. If  $k_2(n)$  is determined at any extracted charge carrier density  $n$  that is dominated by the trapped charges, then  $k_2(n) < k_{2,eff}$  and the mobility would need to decrease to account for the lower recombination coefficient. The BACE measurements, which take into account all extractable charges, revealed that the effective mobility indeed decreased with decreasing illumination intensity, suggesting that this picture of taking into account all charges in the device is also justified under the premise that the main recombination process is bimolecular. The main advantage of the newly introduced model is that it becomes unnecessary to evaluate density dependent recombination coefficients and mobilities with respect to the total extractable charge carrier densities. By just taking into account the actual free charge carriers a constant recombination coefficient and a constant mobility is found to be adequate to fully describe the  $JV$ -curves of such solar cells. This, however, should not suggest that trap assisted recombination cannot be the main recombination channel in organic solar cell devices, but in cases where the recombination current is clearly dominated by a bimolecular process and the light ideality factor is temperature independent, then dark ideality factors larger than one or the mere presence of traps should not be taken as argument for trap assisted recombination being relevant for the device performance.

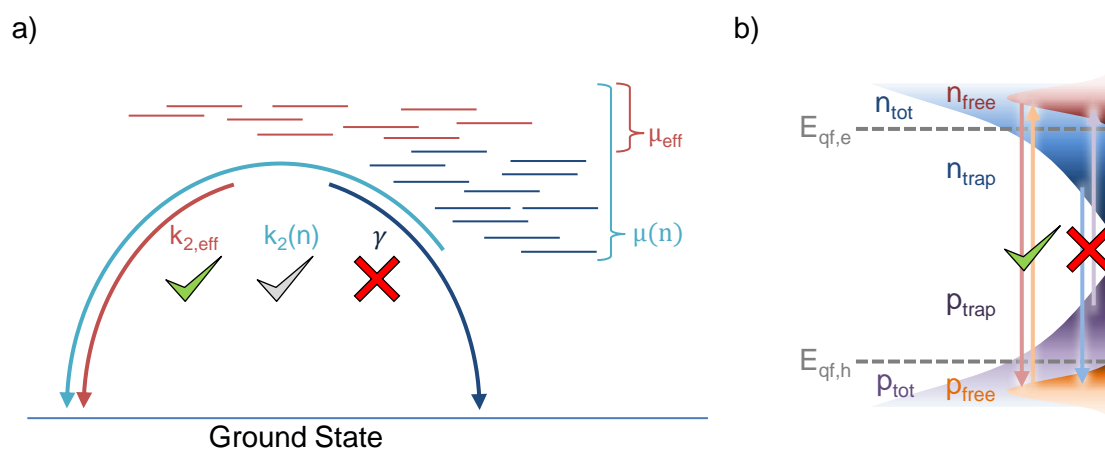


**Figure 7.16.:** a) Pathways for recombination sketched for the PMDPP3T:PCBM system. The effective coefficient and mobility are the best option to describe the recombination behavior; a density dependent depiction of the coefficient and the mobility is in agreement with the effective recombination picture but all charges are considered even if they are not participating in the recombination process; recombination via trap states can be excluded for this system to be relevant. b) Sketched DOS distribution as found for the PMDPP3T:PCBM solar cell. Both charge carrier types can be trapped but the dominant recombination mechanism is mediated via free charges. The recombination of trapped with free charges is unable to explain the experimental findings and is ruled out.

Considering the argument that recombination takes place at the donor acceptor interface via

CT-states and following the argument by Burke et al. who state that a reduced Langevin recombination implies equilibrium between CT- and CS-states and taking into account that organic solar cells with high  $FFs$  usually show strongly reduced Langevin recombination coefficients, then the findings for the PMDPP3T:PCBM system seem to contradict these statements. The PMDPP3T:PCBM solar cell shows reasonably high  $FFs$  but at the same time a very high effective bimolecular recombination coefficient. The reason for this apparent contradiction can be explained by recalling that the effective recombination coefficient is explicitly only valid for the actual free charges and that, if the recombination coefficient would have been determined as a function of  $n$  at a low charge carrier density, it would actually also be reduced compared to the free charge carrier mobility. Furthermore Burke et al. found that an energy cascade in the donor or acceptor material would have beneficial effects on the free charge carrier lifetime.[47] They state that in a situation with and without an energy cascade between the intermixed and pure donor/acceptor regions the CT-state and CS-state densities would be similar in the donor/acceptor interfacial area, but that the total charge carrier density would increase in a situation with an energy cascade as charges would be less likely to reach the donor/acceptor interface. Burke et al. explicitly state that this situation is also comparable to energetic disorder or trap states outside of the mixed donor/acceptor region.[47] This interpretation is similar to the model suggested herein; if the actual morphology shows only little intermixing at the interface between donor and acceptor and if the energetics of the pure domains show trap states, while at the same time the pure domains are not too big, then it would be plausible that there is a high likelihood for recombination if free charges reach the intermixed donor/acceptor region, but most of the charges would be trapped in the domains away from the intermixed regions. As an outlook for future research, morphology studies on the PMDPP3T:PCBM system could help to understand the compatibility of these findings with the model presented by Burke et al.

Concluding, it can be stated that the most important finding of this study is that trap states, revealed by charge extraction experiments, and light ideality factors equal to one, derived via the recombination current, can conclusively be explained by the presented model. The model is backed up by TDCF measurements which actually allow for determination of the effective, free charge carrier recombination coefficient and by simulations of the  $JV$ -characteristics based on this recombination coefficient.

# Chapter 8

## Conclusion

This thesis can be subdivided into three main parts: first the realization of a series connected hybrid multi-junction solar cell was presented; second, different organic solar cell model systems were investigated with respect to their *open circuit voltage*; and in the last section, a detailed analysis of the recombination of charges in a specific organic solar cell system was presented. The initial focus of this thesis, the realization and optimization of the hybrid triple-junction solar cell, initiated the subsequent research on *open circuit voltage* and recombination in organic solar cell systems since the significant voltage loss and low *open circuit voltage* in the organic, low band-gap sub-cell is a major limiting factor that hampers even higher efficiencies in the hybrid triple-junction. While the *fill factor* and *short circuit current density* of the hybrid triple-junction device are comparatively large and further optimization is straight forward and more of an engineering problem, the fundamental voltage losses in organic solar cells in general are still highly debated and not yet fully understood. Therefore, different model systems were chosen in order to examine several aspects and influential factors on *open circuit voltage* to a greater detail. Finally, by additionally studying the recombination dynamics in the low band-gap PMDPP3T:PCBM solar cell system a new model was introduced that unambiguously explains high recombination orders ( $\beta > 2$ ), derived by charge extraction experiments, and recombination currents that clearly are dominated by bimolecular recombination. These findings shed new light on how to picture the recombination process in organic solar cell systems in general.

The first part of this thesis, the optimization of the hybrid multi-junction resulted in, at that time (Jan. 2015), record efficiencies. Inorganic thin film solar cells based on a-Si:H are widely used and their lack of efficiency is partly compensated by low production costs and challenged by the use of multi-junction architectures incorporating, e.g.,  $\mu\text{c-Si:H}$ . This

however hampers fast and cost efficient processing due to the inherent properties of  $\mu\text{c-Si:H}$  processing. Therefore, the use of hybrid multi-junctions is promising and benefits from the long term expertise in inorganic thin film technologies and the favorable processing conditions of organic solar cells. The presented work benefited greatly from the close collaboration with the inorganic research group at the pvComB and their experience in building efficient amorphous silicon solar cells. One major achievement of this collaboration was the incorporation of a light scattering front electrode in combination with a rather thin organic back-cell which was not destroyed by the rough underlying layer stack. For the first time, a significant device improvement was achieved by this means. All results and the progress in developing efficient hybrid multi-junctions was accompanied and facilitated by optical simulations and photovoltaic external quantum efficiency measurements. The optical simulations were employed in order to predict the best thicknesses of each active layer and the photovoltaic external quantum efficiency measurements were used to separately measure the currents in each sub-cell. Thus, the current limiting sub-cells were identified and the effects of different organic sub-cells on the triple-junctions were studied.

In the second part of this work, fundamental processes determining the *open circuit voltage* of organic solar cell systems were studied thoroughly. Three model situations were chosen in order to disentangle different influences on *open circuit voltage*.

First, bilayer solar cells with controllable interface morphologies were used to study the effects of molecular orientation of donor to acceptor. Experimental evidence was found for the influence of the molecular orientation on the non-radiative loss channel. The results are in good agreement with recent density functional theory calculations that also find that the molecular orientation directly influences the non-radiative loss of charges and not just the charge transfer state energetics. These findings are considered very important for future development of high efficiency organic solar cell materials, especially with respect to their molecular design.

Secondly, the fundamental recombination dynamics and charge transfer state properties in three different organic bulk heterojunction solar cell systems were studied. It was shown that the CT-state energetics are determined by long range electrostatics rather than by individual local donor/acceptor pair interactions. This indirect conclusion was drawn because all systems were based on the same donor backbone and incorporated the same total ratio of fluorine to hydrogen atoms but in three distinctly different ways. The studied systems cannot adopt the same local donor/acceptor pair interaction due to the differences induced by structural variations of the donor material. Nevertheless, all measured recombination and CT-state quantities were found to be very similar, which leads to the conclusion that long range electrostatic interactions dictate performance.

Thirdly, the effect of exchanging the fullerene PCBM with the higher adduct fullerene ICBA was investigated in solar cells based on the efficient donor material FTAZ. The exchange of

---

PCBM with ICBA has been studied for a variety of donor materials and many conclusions have been drawn as to what hampers the efficient current generation of ICBA based cells compared to PCBM based cells. In this thesis a conclusive picture of the limiting processes in a typical ICBA based organic solar cell was derived, finding that the *open circuit voltage* differences are solely explained by the shift of CT-state energy corresponding to the LUMO energy shift. Notably, no differences in radiative and non-radiative losses were found. The recombination coefficients at typical one sun illumination conditions were very similar for both systems in agreement with the alike losses. The initial generation of free charges was less efficient in ICBA based cells which correlates with the smaller exciton separation energy measured. The electron mobility in the ICBA based cells is also significantly lower, fully explaining the worse *fill factor*. The findings are supported by *JV*-curve simulations. The measures taken to get reliable results and to draw plausible conclusions highlights the importance of performing comprehensive studies of organic solar cell physics.

The last part of this thesis dealt with the recombination mechanisms that can dominate the device performance of organic solar cells. An apparent controversy in the research community about whether or not, and to what extent, trap states dominate the recombination processes was partially resolved by closely examining the recombination process in a PMDPP3T:PCBM solar cell. In this system, depending on which experiments are conducted, one could either conclude that trap states dictate the recombination mechanism or that a bimolecular recombination process of free charges is dominant. In this thesis the apparent contradiction was conclusively solved by showing that the two pictures do not necessarily contradict each other and rather are a consequence of interpreting measured data of different experiments. By employing two particular trap state models it was shown that conclusions drawn by charge extraction experiments indeed reveal the presence of trapped charge carriers, but that the actual recombination current is still dominated by free charges. Finally, by taking into account these results, a new evaluation of differential charge carrier decay data that came from TDCF measurements was presented. This new approach to assess the possible recombination pathways in organic solar cells is of major importance in understanding and resolving controversies about how and through which states recombination occurs. The simulation of *JV*-characteristics on the basis of this effective recombination coefficient is in perfect agreement with the measured *JV*-curves over a wide intensity and temperature range proving its applicability in accurately describing the recombination process.

In this thesis several important findings were presented and a broad range of topics have been covered. The optimization of hybrid multi-junction solar cells resulted in – at the time of discovery – a record efficiency. The technical difficulties and engineering problems that have been overcome in this work will help future developments of similar hybrid multi-junction devices. Fundamental questions regarding the *open circuit voltage* of organic solar cells were

addressed and a broad range of experimental methods were employed to shed new light on radiative and non-radiative voltage losses and their connection to film morphology. Finally, a new recombination model was presented that is able to unambiguously explain experimental findings which, in the past, were considered to be contradictory. This was achieved by unraveling the recombination pathways in a typical organic solar cell and explaining the influence of trap states on the recombination process for this model system. By this means an important incentive is provided for future research on recombination in organic solar cells in general.

## Bibliography

- [1] K. P. Bhandari, J. M. Collier, R. J. Ellingson, et al. Energy payback time (EPBT) and energy return on energy invested (EROI) of solar photovoltaic systems: A systematic review and meta-analysis, *Renew. Sustain. Energy Rev.* **47** (2015), pp. 133–141. DOI: 10.1016/j.rser.2015.02.057.
- [2] T. Kim, J. H. Jeon, S. Han, et al. Organic-inorganic hybrid tandem multijunction photovoltaics with extended spectral response, *Appl. Phys. Lett.* **98**.18 (2011), p. 183503. DOI: 10.1063/1.3580609.
- [3] J. H. Seo, D.-H. Kim, S.-H. Kwon, et al. High Efficiency Inorganic/Organic Hybrid Tandem Solar Cells, *Adv. Mater.* **24**.33 (2012), pp. 4523–4527. DOI: 10.1002/adma.201201419.
- [4] W. Qin, W. Yu, W. Zi, et al. High efficiency organic/a-Si hybrid tandem solar cells with complementary light absorption, *J. Mater. Chem. A* **2**.37 (2014), pp. 15303–15307. DOI: 10.1039/c4ta02690j.
- [5] S. Roland, S. Neubert, S. Albrecht, et al. Hybrid Organic/Inorganic Thin-Film Multijunction Solar Cells Exceeding 11% Power Conversion Efficiency, *Adv. Mater.* **27** (2015), pp. 1262–1267. DOI: 10.1002/adma.201404698.
- [6] M. A. Green, K. Emery, Y. Hishikawa, et al. Solar cell efficiency tables (version 48), *Prog. Photovoltaics Res. Appl.* **24**.7 (2016), pp. 905–913. DOI: 10.1002/pip.2788.
- [7] W. Zhao, D. Qian, S. Zhang, et al. Fullerene-Free Polymer Solar Cells with over 11% Efficiency and Excellent Thermal Stability, *Adv. Mater.* **28**.23 (2016), pp. 4734–4739. DOI: 10.1002/adma.201600281.
- [8] M. C. Scharber, D. Wuhlbacher, M. Koppe, et al. Design rules for donors in bulk-heterojunction solar cells - Towards 10 % energy-conversion efficiency, *Adv. Mater.* **18**.6 (2006), p. 789. DOI: 10.1002/adma.200501717.
- [9] S. Albrecht, S. Janietz, W. Schindler, et al. Fluorinated Copolymer PCPDTBT with Enhanced Open-Circuit Voltage and Reduced Recombination for Highly Efficient Polymer Solar Cells. English, *J. Am. Chem. Soc.* **134**.36 (2012), pp. 14932–14944. DOI: 10.1021/Ja305039j.
- [10] S. C. Price, A. C. Stuart, L. Q. Yang, et al. Fluorine Substituted Conjugated Polymer of Medium Band Gap Yields 7 % Efficiency in Polymer-Fullerene Solar Cells, *J. Am. Chem. Soc.* **133**.12 (2011), pp. 4625–4631. DOI: 10.1021/Ja1112595.

- 
- [11] H.-Y. Chen, J. Hou, S. Zhang, et al. Polymer solar cells with enhanced open-circuit voltage and efficiency, *Nat. Photonics* **3.11** (2009), pp. 649–653. DOI: 10.1038/nphoton.2009.192.
- [12] Y. Liang, D. Feng, Y. Wu, et al. Highly Efficient Solar Cell Polymers Developed via Fine-Tuning of Structural and Electronic Properties, *J. Am. Chem. Soc.* **131.22** (2009), pp. 7792–7799. DOI: 10.1021/ja901545q.
- [13] Y. Zhang, S.-C. Chien, K.-S. Chen, et al. Increased open circuit voltage in fluorinated benzothiadiazole-based alternating conjugated polymers, *Chem. Commun.* **47.39** (2011), p. 11026. DOI: 10.1039/c1cc14586j.
- [14] K. Tvingstedt and C. Deibel. Temperature Dependence of Ideality Factors in Organic Solar Cells and the Relation to Radiative Efficiency, *Adv. Energy Mater.* **6.9** (2016), p. 1502230. DOI: 10.1002/aenm.201502230.
- [15] S. A. Hawks, G. Li, Y. Yang, et al. Band tail recombination in polymer:fullerene organic solar cells, *J. Appl. Phys.* **116.7** (2014), p. 074503. DOI: 10.1063/1.4892869.
- [16] M. Pope, H. P. Kallmann, and P. Magnante. Electroluminescence in Organic Crystals, *J. Chem. Phys.* **38.8** (1963), p. 2042. DOI: 10.1063/1.1733929.
- [17] H. Shirakawa, E. J. Louis, A. G. MacDiarmid, et al. Synthesis of electrically conducting organic polymers: halogen derivatives of polyacetylene, (CH)<sub>x</sub>, *J. Chem. Soc. Chem. Commun.* **16** (1977), p. 578. DOI: 10.1039/c39770000578.
- [18] C. W. Tang. 2-Layer Organic Photovoltaic Cell, *Appl. Phys. Lett.* **48.2** (1986), pp. 183–185. DOI: 10.1063/1.96937.
- [19] J. J. M. Halls, C. A. Walsh, N. C. Greenham, et al. Efficient Photodiodes from Interpenetrating Polymer Networks, *Nature* **376.6540** (1995), pp. 498–500. DOI: 10.1038/376498a0.
- [20] G. Yu, J. Gao, J. C. Hummelen, et al. Polymer Photovoltaic Cells: Enhanced Efficiencies via a Network of Internal Donor-Acceptor Heterojunctions, *Science (80-. )*. **270.5243** (1995), pp. 1789–1791. DOI: 10.1126/science.270.5243.1789.
- [21] A. Köhler and H. Bässler. *Electronic Processes in Organic Semiconductors*. Weinheim, Germany: Wiley-VCH Verlag GmbH & Co. KGaA, 2015. DOI: 10.1002/9783527685172.
- [22] G. Grancini, M. Maiuri, D. Fazzi, et al. Hot exciton dissociation in polymer solar cells, *Nat. Mater.* **12.1** (2012), pp. 29–33. DOI: 10.1038/nmat3502.
- [23] A. A. Bakulin, D. S. Martyanov, D. Y. Paraschuk, et al. Ultrafast Charge Photogeneration Dynamics in Ground-State Charge-Transfer Complexes Based on Conjugated Polymers, *J. Phys. Chem. B* **112.44** (2008), pp. 13730–13737. DOI: 10.1021/jp8048839.
- [24] K. Vandewal, S. Albrecht, E. T. Hoke, et al. Efficient charge generation by relaxed charge-transfer states at organic interfaces, *Nat. Mater.* **13.1** (2014), pp. 63–68. DOI: 10.1038/nmat3807.

- [25] S. Albrecht, K. Vandewal, J. R. Tumbleston, et al. On the Efficiency of Charge Transfer State Splitting in Polymer:Fullerene Solar Cells, *Adv. Mater.* **26**.16 (2014), pp. 2533–2539. DOI: 10.1002/adma.201305283.
- [26] J. Lee, K. Vandewal, S. R. Yost, et al. Charge Transfer State Versus Hot Exciton Dissociation in Polymer-Fullerene Blended Solar Cells, *J. Am. Chem. Soc.* **132**.34 (2010), pp. 11878–11880. DOI: 10.1021/ja1045742.
- [27] H. Bässler. Charge Transport in Disordered Organic Photoconductors a Monte Carlo Simulation Study, *Phys. status solidi* **175**.1 (1993), pp. 15–56. DOI: 10.1002/pssb.2221750102.
- [28] W. Shockley and H. J. Queisser. Detailed Balance Limit of Efficiency of p-n Junction Solar Cells, *J. Appl. Phys.* **32**.3 (1961), pp. 510–519. DOI: 10.1063/1.1736034.
- [29] T. Ameri, G. Dennler, C. Lungenschmied, et al. Organic tandem solar cells: A review, *Energy Environ. Sci.* **2**.4 (2009), pp. 347–363. DOI: 10.1039/b817952b.
- [30] J. Liu, S. Chen, D. Qian, et al. Fast charge separation in a non-fullerene organic solar cell with a small driving force, *Nat. Energy* **1**.7 (2016), p. 16089. DOI: 10.1038/nenergy.2016.89.
- [31] A. D. Vos. Detailed balance limit of the efficiency of tandem solar cells, *J. Phys. D. Appl. Phys.* **13**.5 (1980), pp. 839–846. DOI: 10.1088/0022-3727/13/5/018.
- [32] M. G. Walter, E. L. Warren, J. R. McKone, et al. Solar Water Splitting Cells, *Chem. Rev.* **110**.11 (2010), pp. 6446–6473. DOI: 10.1021/cr1002326.
- [33] J. Luo, J.-H. Im, M. T. Mayer, et al. Water photolysis at 12.3% efficiency via perovskite photovoltaics and Earth-abundant catalysts, *Science (80-. )*. **345**.6204 (2014), pp. 1593–1596. DOI: 10.1126/science.1258307.
- [34] K. Vandewal, K. Tvingstedt, A. Gadisa, et al. Relating the open-circuit voltage to interface molecular properties of donor:acceptor bulk heterojunction solar cells, *Phys. Rev. B* **81**.12 (2010), p. 125204. DOI: 10.1103/PhysRevB.81.125204.
- [35] K. Vandewal, A. Gadisa, W. D. Oosterbaan, et al. The relation between open-circuit voltage and the onset of photocurrent generation by charge-transfer absorption in polymer: Fullerene bulk heterojunction solar cells, *Adv. Funct. Mater.* **18**.14 (2008), pp. 2064–2070. DOI: 10.1002/adfm.200800056.
- [36] K. Vandewal, K. Tvingstedt, A. Gadisa, et al. On the origin of the open-circuit voltage of polymer-fullerene solar cells, *Nat. Mater.* **8**.11 (2009), pp. 904–909. DOI: 10.1038/nmat2548.
- [37] M. A. Loi, S. Toffanin, M. Muccini, et al. Charge Transfer Excitons in Bulk Heterojunctions of a Polyfluorene Copolymer and a Fullerene Derivative, *Adv. Funct. Mater.* **17**.13 (2007), pp. 2111–2116. DOI: 10.1002/adfm.200601098.
- [38] H. Kim, J. Y. Kim, S. H. Park, et al. Electroluminescence in polymer-fullerene photovoltaic cells, *Appl. Phys. Lett.* **86**.18 (2005), p. 183502. DOI: 10.1063/1.1924869.

- 
- [39] K. Tvingstedt, K. Vandewal, A. Gadisa, et al. Electroluminescence from Charge Transfer States in Polymer Solar Cells, *J. Am. Chem. Soc.* **131.33** (2009), pp. 11819–11824. DOI: 10.1021/ja903100p.
- [40] G. Kirchhoff. Ueber das Verhältniss zwischen dem Emissionsvermögen und dem Absorptionsvermögen der Körper für Wärme und Licht, *Ann. der Phys. und Chemie* **185.2** (1860), pp. 275–301. DOI: 10.1002/andp.18601850205.
- [41] M. Planck. Ueber das Gesetz der Energieverteilung im Normalspectrum, *Ann. Phys.* **309.3** (1901), pp. 553–563. DOI: 10.1002/andp.19013090310.
- [42] P. Würfel. The Physics of Solar Cells, *Wiley* (2007).
- [43] P. Würfel. The Chemical Potential of Radiation, *J. Phys. C* **15** (1982), pp. 3967–3985.
- [44] U. Rau. Reciprocity relation between photovoltaic quantum efficiency and electroluminescent emission of solar cells, *Phys. Rev. B* **76.8** (2007), p. 85303. DOI: 10.1103/PhysRevB.76.085303.
- [45] R. A. Marcus. Relation between charge transfer absorption and fluorescence spectra and the inverted region, *J. Phys. Chem.* **93.8** (1989), pp. 3078–3086. DOI: 10.1021/j100345a040.
- [46] I. R. Gould, D. Noukakis, L. Gomez-Jahn, et al. Radiative and nonradiative electron transfer in contact radical-ion pairs, *Chem. Phys.* **176.2-3** (1993), pp. 439–456. DOI: 10.1016/0301-0104(93)80253-6.
- [47] T. M. Burke, S. Sweetnam, K. Vandewal, et al. Beyond Langevin Recombination: How Equilibrium Between Free Carriers and Charge Transfer States Determines the Open-Circuit Voltage of Organic Solar Cells, *Adv. Energy Mater.* **5.11** (2015), p. 1500123. DOI: 10.1002/aenm.201500123.
- [48] D. Bartsaghi, I. D. C. Pérez, J. Kniepert, et al. Competition between recombination and extraction of free charges determines the fill factor of organic solar cells. *Nat. Commun.* **6**.May (2015), p. 7083.
- [49] D. Neher, J. Kniepert, A. Elimelech, et al. A New Figure of Merit for Organic Solar Cells with Transport-limited Photocurrents, *Sci. Rep.* **6** (2016), p. 24861. DOI: 10.1038/srep24861.
- [50] W. Shockley and W. T. Read. Statistics of the Recombinations of Holes and Electrons, *Phys. Rev.* **87.5** (1952), pp. 835–842. DOI: 10.1103/PhysRev.87.835.
- [51] R. N. Hall. Electron-Hole Recombination in Germanium, *Phys. Rev.* **87.2** (1952), pp. 387–387. DOI: 10.1103/PhysRev.87.387.
- [52] P. Langevin. Recombination et Mobilites Des Ions Dans Les Gaz, *Ann. Chim. Phys.* **28** (1903), pp. 433–530.
- [53] J. Kniepert, I. Lange, N. J. van der Kaap, et al. A Conclusive View on Charge Generation, Recombination, and Extraction in As-Prepared and Annealed P3HT:PCBM

- Blends: Combined Experimental and Simulation Work, *Adv. Energy Mater.* **4.7** (2014), p. 1301401. DOI: 10.1002/aenm.201301401.
- [54] C. Deibel, A. Wagenpfahl, and V. Dyakonov. Origin of reduced polaron recombination in organic semiconductor devices, *Phys. Rev. B* **80.7** (2009). DOI: 10.1103/PhysRevB.80.075203.
- [55] A. Foertig, A. Baumann, D. Rauh, et al. Charge carrier concentration and temperature dependent recombination in polymer-fullerene solar cells, *Appl. Phys. Lett.* **95.5** (2009), p. 052104. DOI: 10.1063/1.3202389.
- [56] T. Kirchartz, B. E. Pieters, J. Kirkpatrick, et al. Recombination via tail states in polythiophene:fullerene solar cells, *Phys. Rev. B* **83.11** (2011), p. 115209. DOI: 10.1103/PhysRevB.83.115209.
- [57] C. van Berkel, M. J. Powell, A. R. Franklin, et al. Quality factor in a-Si:H nip and pin diodes, *J. Appl. Phys.* **73.10** (1993), p. 5264. DOI: 10.1063/1.353755.
- [58] R. A. Street, M. Schoendorf, A. Roy, et al. Interface state recombination in organic solar cells, *Phys. Rev. B* **81.20** (2010), p. 205307. DOI: 10.1103/PhysRevB.81.205307.
- [59] R. A. Street, A. Krakaris, and S. R. Cowan. Recombination Through Different Types of Localized States in Organic Solar Cells, *Adv. Funct. Mater.* **22.21** (2012), pp. 4608–4619. DOI: 10.1002/adfm.201200031.
- [60] C. Deibel and A. Wagenpfahl. Comment on “Interface state recombination in organic solar cells”, *Phys. Rev. B* **82.20** (2010), p. 207301. DOI: 10.1103/PhysRevB.82.207301.
- [61] R. A. Street. Reply to “Comment on ‘Interface state recombination in organic solar cells’ ”, *Phys. Rev. B* **82.20** (2010), p. 207302. DOI: 10.1103/PhysRevB.82.207302.
- [62] G. A. H. Wetzelaer, M. Kuik, M. Lenens, et al. Origin of the dark-current ideality factor in polymer:fullerene bulk heterojunction solar cells, *Appl. Phys. Lett.* **99.15** (2011), p. 153506. DOI: 10.1063/1.3651752.
- [63] G.-J. A. H. Wetzelaer, M. Kuik, and P. W. M. Blom. Identifying the Nature of Charge Recombination in Organic Solar Cells from Charge-Transfer State Electroluminescence, *Adv. Energy Mater.* **2.10** (2012), pp. 1232–1237. DOI: 10.1002/aenm.201200009.
- [64] M. Wolf and H. Rauschenbach. Series resistance effects on solar cell measurements, *Adv. Energy Convers.* **3.2** (1963), pp. 455–479. DOI: 10.1016/0365-1789(63)90063-8.
- [65] R. Sinton and A. Cuevas. “A Quasi-Steady-State Open-Circuit Voltage Method for Solar Cell Characterization”, R. A. Sinton, A. Cuevas, *Proc. 16th Eur. Photovolt. Sol. Energy Conf., Glas. 2000, 1152*. Vol. 5. 2000.
- [66] S. Schiefer, B. Zimmermann, and U. Würfel. Determination of the intrinsic and the injection dependent charge carrier density in organic solar cells using the Suns-Voc method, *J. Appl. Phys.* **115.4** (2014), p. 044506. DOI: 10.1063/1.4862960.

- 
- [67] S. Schiefer, B. Zimmermann, S. W. Glunz, et al. Applicability of the Suns-Voc Method on Organic Solar Cells, *IEEE J. Photovoltaics* **4.1** (2014), pp. 271–277. DOI: 10.1109/JPHOTOV.2013.2288527.
- [68] U. Wurfel, D. Neher, A. Spies, et al. Impact of charge transport on current-voltage characteristics and power-conversion efficiency of organic solar cells, *Nat. Commun.* **6** (2015). DOI: 10.1038/ncomms7951.
- [69] J. Gilot, M. M. Wienk, and R. A. J. Janssen. Measuring the External Quantum Efficiency of Two-Terminal Polymer Tandem Solar Cells, *Adv. Funct. Mater.* **20.22** (2010), pp. 3904–3911. DOI: 10.1002/adfm.201001167.
- [70] J. Kniepert, M. Schubert, J. C. Blakesley, et al. Photogeneration and Recombination in P3HTPCBM Solar Cells Probed by Time-Delayed Collection Field Experiments. English, *J. Phys. Chem. Lett.* **2.7** (2011), pp. 700–705. DOI: 10.1021/Jz200155b.
- [71] J. Kurpiers, D. M. Balazs, A. Paulke, et al. Free Carrier Generation and Recombination in PbS Quantum Dot solar cells, *submitted* (2016).
- [72] H. Tan, A. Furlan, W. Li, et al. Highly Efficient Hybrid Polymer and Amorphous Silicon Multijunction Solar Cells with Effective Optical Management, *Adv. Mater.* **28.11** (2016), pp. 2170–2177. DOI: 10.1002/adma.201504483.
- [73] H. Sai, T. Matsui, T. Koida, et al. Triple-junction thin-film silicon solar cell fabricated on periodically textured substrate with a stabilized efficiency of 13.6%, *Cit. Appl. Phys. Lett. Appl. Phys. Lett. Appl. Phys. Lett.* **106.96** (2015), pp. 213902–213504. DOI: 10.1063/1.3432739.
- [74] A. V. Shah, H. Schade, M. Vanecek, et al. Thin-film silicon solar cell technology, *Prog. Photovoltaics Res. Appl.* **12.2-3** (2004), pp. 113–142. DOI: 10.1002/pip.533.
- [75] Heliatek. “Heliatek sets new Organic Photovoltaic world record efficiency of 13.2% - Heliatek – The future is light”. Press-release. <http://www.heliatek.com/en/press/press-releases/de>, 2016, <http://www.heliatek.com/en/press/press-releases/de>.
- [76] C.-C. Chen, W.-H. Chang, K. Yoshimura, et al. An Efficient Triple-Junction Polymer Solar Cell Having a Power Conversion Efficiency Exceeding 11%, *Adv. Mater.* **26** (2014), pp. 5670–5677. DOI: 10.1002/adma.201402072.
- [77] G. Zhao, Y. He, and Y. Li. 6.5% Efficiency of Polymer Solar Cells Based on poly(3-hexylthiophene) and Indene-C60 Bisadduct by Device Optimization, *Adv. Mater.* **22.39** (2010), pp. 4355–4358. DOI: 10.1002/adma.201001339.
- [78] S. Albrecht, B. Grootoink, S. Neubert, et al. Efficient hybrid inorganic/organic tandem solar cells with tailored recombination contacts, *Sol. ENERGY Mater. Sol. CELLS* **127.0** (2014), pp. 157–162. DOI: 10.1016/j.solmat.2014.04.020.
- [79] P. Buehlmann, J. Bailat, D. Dominé, et al. In situ silicon oxide based intermediate reflector for thin-film silicon micromorph solar cells, *Appl. Phys. Lett.* **91.14** (2007), pp. 1–3. DOI: 10.1063/1.2794423.

- [80] P. Cuony, D. T. L. Alexander, I. Perez-Wurfl, et al. Silicon Filaments in Silicon Oxide for Next-Generation Photovoltaics, *Adv. Mater.* **24.9** (2012), pp. 1182–1186. DOI: 10.1002/adma.201104578.
- [81] M. C. Scharber, M. Koppe, J. Gao, et al. Influence of the Bridging Atom on the Performance of a Low-Bandgap Bulk Heterojunction Solar Cell, *Adv. Mater.* **22.3** (2010), pp. 367–370. DOI: 10.1002/adma.200900529.
- [82] W. Li, A. Furlan, K. H. Hendriks, et al. Efficient Tandem and Triple-Junction Polymer Solar Cells, *J. Am. Chem. Soc.* **135.15** (2013), pp. 5529–5532. DOI: 10.1021/ja401434x.
- [83] G. F. Burkhard, E. T. Hoke, and M. D. McGehee. Accounting for Interference, Scattering, and Electrode Absorption to Make Accurate Internal Quantum Efficiency Measurements in Organic and Other Thin Solar Cells, *Adv. Mater.* **22.30** (2010), pp. 3293–3297. DOI: 10.1002/adma.201000883.
- [84] M. Gohlke. *Documentation of the APCSA Program*. Tech. rep. 2014.
- [85] K. Ding, T. Kirchartz, B. E. Pieters, et al. Characterization and simulation of a-Si:H/ $\mu$ c-Si:H tandem solar cells, *Sol. ENERGY Mater. Sol. CELLS* **95.12** (2011), pp. 3318–3327. DOI: 10.1016/j.solmat.2011.07.023.
- [86] E. T. Hoke and G. F. Burkhard. *Transfer Matrix model*. 2010.
- [87] P. Peumans, A. Yakimov, and S. R. Forrest. Small molecular weight organic thin-film photodetectors and solar cells, *J. Appl. Phys.* **93.7** (2003), pp. 3693–3723. DOI: 10.1063/1.1534621.
- [88] L. A. A. Pettersson, L. S. Roman, and O. Inganaes. Modeling photocurrent action spectra of photovoltaic devices based on organic thin films, *J. Appl. Phys.* **86.1** (1999), pp. 487–496. DOI: 10.1063/1.370757.
- [89] A. Shah. *Thin-film silicon solar cells*. Lausanne: EPFL press, 2010.
- [90] S. Kirner, S. Calnan, O. Gabriel, et al. An improved silicon-oxide-based intermediate-reflector for micromorph solar cells, *Phys. status solidi* **9.10-11** (2012), pp. 2145–2148. DOI: 10.1002/pssc.201200243.
- [91] M. Despeisse, G. Bugnon, A. Feltrin, et al. Resistive interlayer for improved performance of thin film silicon solar cells on highly textured substrate, *Appl. Phys. Lett.* **96.7** (2010), p. 73507. DOI: 10.1063/1.3324704.
- [92] J. Kim, Z. Hong, G. Li, et al. 10.5% efficient polymer and amorphous silicon hybrid tandem photovoltaic cell, *Nat. Commun.* **6** (2015), p. 6391. DOI: 10.1038/ncomms7391.
- [93] K. H. Hendriks, G. H. L. Heintges, V. S. Gevaerts, et al. High-Molecular-Weight Regular Alternating Diketopyrrolopyrrole-based Terpolymers for Efficient Organic Solar Cells, *Angew. Chemie Int. Ed.* **52.32** (2013), pp. 8341–8344. DOI: 10.1002/anie.201302319.

- 
- [94] L. Dou, C.-C. Chen, K. Yoshimura, et al. Synthesis of 5H-Dithieno[3,2-b:2',3'-d]pyran as an Electron-Rich Building Block for Donor-Acceptor Type Low-Bandgap Polymers, *Macromolecules* **46.9** (2013), pp. 3384–3390. DOI: 10.1021/ma400452j.
- [95] C. Poelking, M. Tietze, C. Elschner, et al. Impact of mesoscale order on open-circuit voltage in organic solar cells, *Nat. Mater.* **14.4** (2014), pp. 434–439. DOI: 10.1038/nmat4167.
- [96] F. C. Jamieson, E. B. Domingo, T. McCarthy-Ward, et al. Fullerene crystallisation as a key driver of charge separation in polymer/fullerene bulk heterojunction solar cells, *Chem. Sci.* **3.2** (2012), pp. 485–492. DOI: 10.1039/C1SC00674F.
- [97] U. Hörmann, C. Lorch, A. Hinderhofer, et al. Voc from a Morphology Point of View: the Influence of Molecular Orientation on the Open Circuit Voltage of Organic Planar Heterojunction Solar Cells, *J. Phys. Chem. C* **118.46** (2014), pp. 26462–26470. DOI: 10.1021/jp506180k.
- [98] W. Chen, D.-C. Qi, H. Huang, et al. Organic-Organic Heterojunction Interfaces: Effect of Molecular Orientation, *Adv. Funct. Mater.* **21.3** (2011), pp. 410–424. DOI: 10.1002/adfm.201000902.
- [99] L. Zhang, S. S. Roy, R. J. Hamers, et al. Molecular Orientation-Dependent Interfacial Energetics and Built-in Voltage Tuned by a Template Graphene Monolayer, *J. Phys. Chem. C* **119.1** (2015), pp. 45–54. DOI: 10.1021/jp508931e.
- [100] B. Yang, Y. Yi, C.-R. Zhang, et al. Impact of Electron Delocalization on the Nature of the Charge-Transfer States in Model Pentacene/C 60 Interfaces: A Density Functional Theory Study, *J. Phys. Chem. C* **118.48** (2014), pp. 27648–27656. DOI: 10.1021/jp5074076.
- [101] Y. Yi, V. Coropceanu, and J.-L. Brédas. Exciton-Dissociation and Charge - Recombination Processes in Pentacene/C 60 Solar Cells: Theoretical Insight into the Impact of Interface Geometry, *J. Am. Chem. Soc.* **131.43** (2009), pp. 15777–15783. DOI: 10.1021/ja905975w.
- [102] B. P. Rand, D. Cheyns, K. Vasseur, et al. The Impact of Molecular Orientation on the Photovoltaic Properties of a Phthalocyanine/Fullerene Heterojunction, *Adv. Funct. Mater.* **22.14** (2012), pp. 2987–2995. DOI: 10.1002/adfm.201200512.
- [103] J. Idé, S. Mothy, A. Savoyant, et al. Interfacial dipole and band bending in model pentacene/C 60 heterojunctions, *Int. J. Quantum Chem.* **113.4** (2013), pp. 580–584. DOI: 10.1002/qua.24006.
- [104] S. Verlaak, D. Beljonne, D. Cheyns, et al. Electronic Structure and Geminate Pair Energetics at Organic-Organic Interfaces: The Case of Pentacene/C 60 Heterojunctions, *Adv. Funct. Mater.* **19.23** (2009), pp. 3809–3814. DOI: 10.1002/adfm.200901233.

- [105] B. Kitchen, O. Awartani, R. J. Kline, et al. Tuning Open-Circuit Voltage in Organic Solar Cells with Molecular Orientation, *ACS Appl. Mater. Interfaces* **7.24** (2015), pp. 13208–13216. DOI: 10.1021/am508855s.
- [106] J. R. Tumbleston, B. A. Collins, L. Yang, et al. The influence of molecular orientation on organic bulk heterojunction solar cells, *Nat Phot.* **8.5** (2014), pp. 385–391.
- [107] N. D. Treat, M. A. Brady, G. Smith, et al. Interdiffusion of PCBM and P3HT Reveals Miscibility in a Photovoltaically Active Blend, *Adv. Energy Mater.* **1.1** (2011), pp. 82–89. DOI: 10.1002/aenm.201000023.
- [108] G. O. Ngongang Ndjawa, K. R. Graham, R. Li, et al. Impact of Molecular Orientation and Spontaneous Interfacial Mixing on the Performance of Organic Solar Cells, *Chem. Mater.* **27.16** (2015), pp. 5597–5604. DOI: 10.1021/acs.chemmater.5b01845.
- [109] W. Li, S. Albrecht, L. Yang, et al. Mobility-controlled performance of thick solar cells based on fluorinated copolymers, *J. Am. Chem. Soc.* **136.44** (2014), pp. 15566–15576.
- [110] S. A. Mollinger, K. Vandewal, and A. Salleo. Microstructural and Electronic Origins of Open-Circuit Voltage Tuning in Organic Solar Cells Based on Ternary Blends, *Adv. Energy Mater.* **5.23** (2015), p. 1501335. DOI: 10.1002/aenm.201501335.
- [111] L. Yang, H. Zhou, S. C. Price, et al. Parallel-like Bulk Heterojunction Polymer Solar Cells, *J. Am. Chem. Soc.* **134.12** (2012), pp. 5432–5435. DOI: 10.1021/ja211597w.
- [112] S. Kouijzer, W. Li, M. M. Wienk, et al. Charge transfer state energy in ternary bulk-heterojunction polymer–fullerene solar cells, *J. Photonics Energy* **5.1** (2014), p. 057203. DOI: 10.1117/1.JPE.5.057203.
- [113] R. A. Street, D. Davies, P. P. Khlyabich, et al. Origin of the Tunable Open-Circuit Voltage in Ternary Blend Bulk Heterojunction Organic Solar Cells, *J. Am. Chem. Soc.* **135.3** (2013), pp. 986–989. DOI: 10.1021/ja3112143.
- [114] X. M. He, F. Gao, G. L. Tu, et al. Formation of Nanopatterned Polymer Blends in Photovoltaic Devices. English, *Nano Lett.* **10.4** (2010), pp. 1302–1307. DOI: 10.1021/N1904098m.
- [115] J.-H. Huang, Y.-S. Hsiao, E. Richard, et al. The investigation of donor-acceptor compatibility in bulk - heterojunction polymer systems, *Appl. Phys. Lett.* **103.4** (2013), p. 043304. DOI: 10.1063/1.4816056.
- [116] H. Xin, S. Subramaniyan, T.-W. Kwon, et al. Enhanced Open Circuit Voltage and Efficiency of Donor-Acceptor Copolymer Solar Cells by Using Indene-C60 Bisadduct, *Chem. Mater.* **24.11** (2012), pp. 1995–2001. DOI: 10.1021/cm300355e.
- [117] T. E. Kang, H.-H. Cho, C.-H. Cho, et al. Photoinduced Charge Transfer in Donor-Acceptor (DA) Copolymer: Fullerene Bis-adduct Polymer Solar Cells, *ACS Appl. Mater. Interfaces* **5.3** (2013), pp. 861–868. DOI: 10.1021/am302479u.

- 
- [118] P. Cheng, Y. Li, and X. Zhan. Efficient ternary blend polymer solar cells with indene-C60 bisadduct as an electron-cascade acceptor, *Energy Environ. Sci.* **7.6** (2014), p. 2005. DOI: 10.1039/c3ee44202k.
- [119] D. C. Coffey, B. W. Larson, A. W. Hains, et al. An Optimal Driving Force for Converting Excitons into Free Carriers in Excitonic Solar Cells, *J. Phys. Chem. C* **116.16** (2012), pp. 8916–8923. DOI: 10.1021/jp302275z.
- [120] M. A. Faist, T. Kirchartz, W. Gong, et al. Competition between the Charge Transfer State and the Singlet States of Donor or Acceptor Limiting the Efficiency in Polymer:Fullerene Solar Cells. English, *J. Am. Chem. Soc.* **134.1** (2012), pp. 685–692. DOI: 10.1021/Ja210029w.
- [121] M. A. Faist, S. Shoaee, S. Tuladhar, et al. Understanding the Reduced Efficiencies of Organic Solar Cells Employing Fullerene Multiadducts as Acceptors, *Adv. Energy Mater.* **3.6** (2013), pp. 744–752. DOI: 10.1002/aenm.201200673.
- [122] E. T. Hoke, K. Vandewal, J. A. Bartelt, et al. Recombination in Polymer:Fullerene Solar Cells with Open-Circuit Voltages Approaching and Exceeding 1.0 V, *Adv. Energy Mater.* **3.2** (2013), pp. 220–230. DOI: 10.1002/aenm.201200474.
- [123] N. C. Miller, S. Sweetnam, E. T. Hoke, et al. Molecular Packing and Solar Cell Performance in Blends of Polymers with a Bisadduct Fullerene, *Nano Lett.* **12.3** (2012), pp. 1566–1570. DOI: 10.1021/nl204421p.
- [124] W. Li, L. Yang, J. R. Tumbleston, et al. Controlling Molecular Weight of a High Efficiency Donor-Acceptor Conjugated Polymer and Understanding Its Significant Impact on Photovoltaic Properties, *Adv. Mater.* **26** (2014), pp. 4456–4462. DOI: 10.1002/adma.201305251.
- [125] J. A. Love, I. Nagao, Y. Huang, et al. Silaindacenodithiophene-Based Molecular Donor: Morphological Features and Use in the Fabrication of Compositionally Tolerant, High-Efficiency Bulk Heterojunction Solar Cells, *J. Am. Chem. Soc.* **136.9** (2014), pp. 3597–3606. DOI: 10.1021/ja412473p.
- [126] N. A. Ran, S. Roland, J. A. Love, et al. Impact of Interfacial Molecular Orientation on Radiative Recombination and Charge Generation Efficiencies, *Submitt. to Nat. Energy* (2017).
- [127] X.-K. Chen, M. K. Ravva, H. Li, et al. Effect of Molecular Packing and Charge Delocalization on the Nonradiative Recombination of Charge-Transfer States in Organic Solar Cells, *Adv. Energy Mater.* (2016), p. 1601325. DOI: 10.1002/aenm.201601325.
- [128] N. Felekidis, E. Wang, M. Kemerink, et al. Open circuit voltage and efficiency in ternary organic photovoltaic blends, *Energy Environ. Sci.* **9.1** (2016), pp. 257–266. DOI: 10.1039/C5EE03095A.
- [129] M. L. Tietze, W. Tress, S. Pfützner, et al. Correlation of open-circuit voltage and energy levels in zinc-phthalocyanine: C 60 bulk heterojunction solar cells with varied

- mixing ratio, *Phys. Rev. B* **88.8** (2013), p. 085119. DOI: 10.1103/PhysRevB.88.085119.
- [130] A. C. Stuart, J. R. Tumbleston, H. Zhou, et al. Fluorine Substituents Reduce Charge Recombination and Drive Structure and Morphology Development in Polymer Solar Cells, *J. Am. Chem. Soc.* **135.5** (2013), pp. 1806–1815. DOI: 10.1021/ja309289u.
- [131] Q. Zhang, M. A. Kelly, A. Hunt, et al. Comparative Photovoltaic Study of Physical Blending of Two Donor Acceptor Polymers with the Chemical Blending of the Respective Moieties, *Macromolecules* **49.7** (2016), pp. 2533–2540. DOI: 10.1021/acs.macromol.5b02586.
- [132] S. Sweetnam, R. Prasanna, T. M. Burke, et al. How the Energetic Landscape in the Mixed Phase of Organic Bulk Heterojunction Solar Cells Evolves with Fullerene Content, *J. Phys. Chem. C* **120.12** (2016), pp. 6427–6434. DOI: 10.1021/acs.jpcc.6b00753.
- [133] A. K. Ko Kyaw, D. Gehrig, J. Zhang, et al. High open-circuit voltage small-molecule p-DTS(FBTTh2):ICBA bulk heterojunction solar cells - morphology, excited-state dynamics, and photovoltaic performance, *J. Mater. Chem. A* **3.4** (2015), pp. 1530–1539. DOI: 10.1039/c4ta06256f.
- [134] S. Albrecht, W. Schindler, J. Kurpiers, et al. On the Field Dependence of Free Charge Carrier Generation and Recombination in Blends of PCPDTBT/PC70BM: Influence of Solvent Additives, *J. Phys. Chem. Lett.* **3.5** (2012), pp. 640–645. DOI: 10.1021/jz3000849.
- [135] Juliane Kniepert. “Correlation between Dynamic Parameters and Device Performance of Organic Solar Cells”. PhD thesis. University of Potsdam, 2016.
- [136] S. Roland, L. Yan, Q. Zhang, et al. Charge Generation and Mobility-limited Performance of Bulk Heterojunction Solar Cells with a Higher Adduct Fullerene, *Prep. resubmission to J. Mater. Chem. C* (2017).
- [137] V. D. Mihailetschi, L. J. A. Koster, J. C. Hummelen, et al. Photocurrent Generation in Polymer-Fullerene Bulk Heterojunctions, *Phys. Rev. Lett.* **93.21** (2004), p. 216601. DOI: 10.1103/PhysRevLett.93.216601.
- [138] M. Mingebach, S. Walter, V. Dyakonov, et al. Direct and charge transfer state mediated photogeneration in polymer–fullerene bulk heterojunction solar cells, *Appl. Phys. Lett.* **100.19** (2012), p. 193302. DOI: 10.1063/1.4711849.
- [139] S. Albrecht, J. R. Tumbleston, S. Janietz, et al. Quantifying Charge Extraction in Organic Solar Cells: The Case of Fluorinated PCPDTBT, *J. Phys. Chem. Lett.* **5.7** (2014), pp. 1131–1138. DOI: 10.1021/jz500457b.
- [140] N. F. Mott and R. W. Gurney. *Electronic processes in ionic crystals*. Dover, 1964.
- [141] P. N. Murgatroyd. Theory of space-charge-limited current enhanced by Frenkel effect, *J. Phys. D. Appl. Phys.* **3.2** (1970), p. 308. DOI: 10.1088/0022-3727/3/2/308.

- 
- [142] M. A. Kelly, S. Roland, Q. Zhang, et al. Incorporating Fluorine Substitution into Conjugated Polymers for Solar Cells: Three Different Means, Same Results, *J. Phys. Chem. C* **121** (2017), pp. 2059–2068. DOI: 10.1021/acs.jpcc.6b10993.
- [143] M. Stolterfoht, A. Armin, S. Shoaee, et al. Slower carriers limit charge generation in organic semiconductor light-harvesting systems, *Nat. Commun.* **7** (2016), p. 11944. DOI: 10.1038/ncomms11944.
- [144] W. Li, K. H. Hendriks, M. M. Wienk, et al. Diketopyrrolopyrrole Polymers for Organic Solar Cells, *Acc. Chem. Res.* **49.1** (2016), pp. 78–85. DOI: 10.1021/acs.accounts.5b00334.
- [145] T. Kirchartz, F. Deledalle, P. S. Tuladhar, et al. On the Differences between Dark and Light Ideality Factor in Polymer:Fullerene Solar Cells, *J. Phys. Chem. Lett.* **4.14** (2013), pp. 2371–2376. DOI: 10.1021/jz4012146.
- [146] S. D. Collins, C. M. Proctor, N. A. Ran, et al. Understanding Open-Circuit Voltage Loss through the Density of States in Organic Bulk Heterojunction Solar Cells, *Adv. Energy Mater.* **6.4** (2016), p. 1501721. DOI: 10.1002/aenm.201501721.
- [147] J. C. Blakesley and D. Neher. Relationship between energetic disorder and open-circuit voltage in bulk heterojunction organic solar cells, *Phys. Rev. B* **84.7** (2011). DOI: 10.1103/PhysRevB.84.075210.
- [148] T. Kirchartz and J. Nelson. Meaning of reaction orders in polymer:fullerene solar cells, *Phys. Rev. B* **86.16** (2012), p. 165201. DOI: 10.1103/PhysRevB.86.165201.
- [149] P. Mark and W. Helfrich. Space Charge Limited Currents in Organic Crystals, *J. Appl. Phys.* **33.1** (1962), pp. 205–215. DOI: 10.1063/1.1728487.
- [150] I. Lange, J. Kniepert, P. Pingel, et al. Correlation between the Open Circuit Voltage and the Energetics of Organic Bulk Heterojunction Solar Cells, *J. Phys. Chem. Lett.* **4.22** (2013), pp. 3865–3871. DOI: 10.1021/jz401971e.
- [151] E. Nandayapa. “Simulation of Charge Extraction in Organic Solar Cells”. Master Thesis. 2015.
- [152] Z. Yi, S. Wang, and Y. Liu. Design of High-Mobility Diketopyrrolopyrrole-Based  $\pi$ -Conjugated Copolymers for Organic Thin-Film Transistors, *Adv. Mater.* **27.24** (2015), pp. 3589–3606. DOI: 10.1002/adma.201500401.
- [153] J. Y. Back, H. Yu, I. Song, et al. Investigation of Structure-Property Relationships in Diketopyrrolopyrrole Based Polymer Semiconductors via Side-Chain Engineering, *Chem. Mater.* **27.5** (2015), pp. 1732–1739. DOI: 10.1021/cm504545e.

# Appendix A

## Appendix Chapter 4

### A.1. Calibration Routine for Absolute EL Measurements

In order to correctly determine the emitted photon flux density from the solar cell at certain injection conditions, a calibrated Silicon photodiode was placed parallel in front of the solar cell. The initial distance of OSC and detector was minimized but not precisely measured due to mechanical limitations. A few assumptions are made to anyhow determine the emitted photon flux leaving the OSC. Firstly, it can be assumed that the OSC is a Lambert's emitter. This means that the radiance in dependence of the angle  $\Theta_0$  (with respect to the surface normal as shown in Figure A.1)  $I(\Theta_0)$  is related to radiance perpendicular to the surface  $I_0$  as

$$I(\Theta) = I_0 \cos\Theta. \quad (\text{A.1})$$

The radiant flux  $\Phi_0$  into a solid angle increment  $d\Omega$  is then given in dependence of the angle  $\Theta_0$  as follows:

$$\Phi_0 = \int_0^{2\pi} d\phi \int_0^{\Theta_0} I(\Theta) \sin\Theta d\Theta \quad (\text{A.2})$$

$$= 2\pi I_0 \int_0^{\Theta_0} \cos\Theta \sin\Theta d\Theta \quad \left| \quad x = \cos\Theta \Rightarrow d\Theta = \frac{dx}{-\sin\Theta} \right. \quad (\text{A.3})$$

$$= 2\pi I_0 \int_1^{\cos\Theta_0} -x dx \quad (\text{A.4})$$

$$= \pi I_0 \sin^2\Theta_0. \quad (\text{A.5})$$

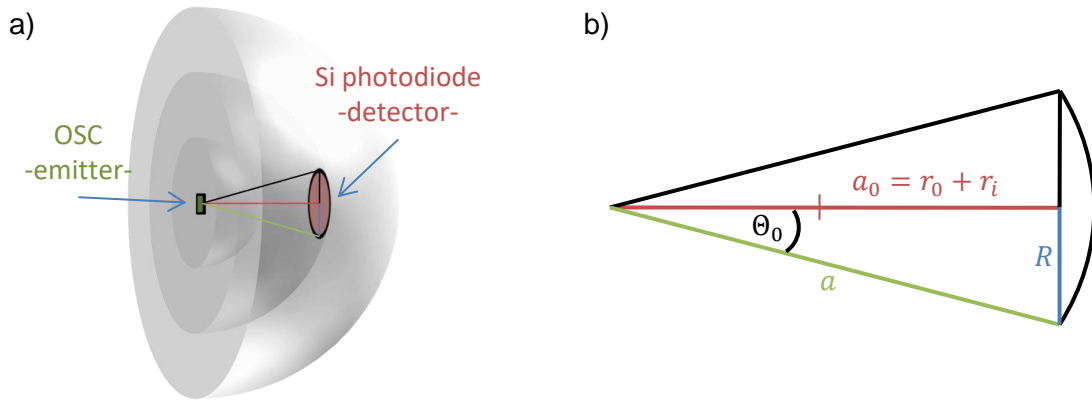


**Figure A.1.:** a) Sketched picture of the OSC emitting into the half sphere denoted for three different distances with the detector and the relevant lengths depicted for one particular distance. b) Zoomed in version of the length scales shown in a) with the relevant measures labeled.

This results in a radiant flux for the half sphere of  $\Phi = I_0\pi$ . The radiant flux hitting the Silicon photodiode depends on the distance  $a_0$  of the diode to the OSC and the radius  $R$  of the photodiode as depicted in Figure A.1. The ratio of the current expected for the emission into the half sphere  $i$  and the actual measured current  $i_m$  is then given by

$$\frac{i}{i_m} = \frac{\Phi}{\Phi_0} = \frac{I_0\pi}{I_0\pi\sin^2\Theta_0} = \frac{1}{\sin^2\Theta_0}. \quad (\text{A.6})$$

According to Figure A.1  $\sin\Theta_0$  can be described in dependence of  $R$  and the distance  $a_0$  between detector and solar cell, with  $a_0 = r_0 + r_i$  ( $r_0$  denoting the unknown minimum distance between detector and OSC;  $r_i$  can be measured). This finally results in a dependence of the total expected current for collection of the emission into the whole half sphere on the actually measured current and the minimum distance  $r_0$ .

$$i = i_m \cdot \left( \frac{\sqrt{(r_0 + r_i)^2 + R^2}}{R} \right)^2. \quad (\text{A.7})$$

By this means the total current can be determined if  $i_m$  is measured for different distances  $r_i$ . The total current needs to be same no matter how far the detector is placed and therefore the unknown shortest detector to OSC distance  $r_0$  is kept as free fitting parameter to guarantee the total current to be equal for all distances.

# Appendix B

## Appendix Chapter 5

### B.1. Triple-Junction Layer Stack

**Table B.1.:** Full layer stack of TJs with a flat front electrode.

layer	stack	thickness [nm]	opt.data
front electrode	AZO (flat)	700	✓
front-cell p	p- $\mu$ C-Si seed	$\sim 5$	—
	p- $\mu$ C-SiO <sub>x</sub>	22	✓
	p-a-SiC <sub>x</sub> buffer	$\sim 6$	—
front-cell i	i-a-Si	65	✓
front-cell n	n-a-Si	$\sim 2$	—
	n- $\mu$ C-Si	27	✓
middle-cell p	p- $\mu$ C-Si seed	$\sim 10$	—
	p- $\mu$ C-Si	23	✓
	p-a-SiC <sub>x</sub> buffer	$\sim 5$	—
middle-cell i	i-a-Si	400	✓
middle-cell n	n-a-Si	$\sim 2$	—
	n- $\mu$ C-Si	27	✓
rec. contact	ITO or AZO	130 or 100	✓
	PEDOT or Ag/MoO <sub>x</sub>	$\sim 30$ or 1/10	✓
back-cell organic	Si-PCPDTBT:PCBM or PMDPP3T:PCBM blend	both $\sim 140$	✓
back electrode	Ca/Ag	10/1000	✓

For the optical modeling the thickness of each p- and n-layer was taken as the sum of the whole stack. The refractive indexes were taken as available. That means for, e.g., the front p-layer the refractive index of the p- $\mu$ C-SiO<sub>x</sub> layer was taken for the whole p-layer. The error

**Table B.2.:** Full layer stack of TJs with a rough front electrode.

layer	stack	thickness [nm]	opt.data
front electrode	AZO (rough)	$\leq 700$	✓
front-cell p	p- $\mu$ c-Si seed	$\sim 5$	—
	p- $\mu$ c-SiO <sub>x</sub>	22	✓
	p-a-SiC <sub>x</sub> buffer	$\sim 6$	—
front-cell i	i-a-Si	60	✓
front-cell n	n-a-Si	$\sim 2$	—
	n- $\mu$ c-SiO <sub>x</sub>	20	✓
middle-cell p	p- $\mu$ c-Si seed	$\sim 10$	—
	p- $\mu$ c-Si	23	✓
	p-a-SiC <sub>x</sub> buffer	$\sim 5$	—
middle-cell i	i-a-Si	500	✓
middle-cell n	n-a-Si	$\sim 2$	—
	n- $\mu$ c-Si	27	✓
rec. contact	ITO or AZO	130 or 100	✓
	PEDOT or Ag/MoO <sub>x</sub>	$\sim 30$ or 1/10	✓
back-cell organic	PMDPP3T:PCBM blend	$\sim 140$	✓
back electrode	Ca/Ag	10/1000	✓

is considered negligible. The thick silver capping layer of the back electrode is required for protecting the organic layer as the pixels are contacted directly in the experimental setup.

## B.2. Contour Pots of PMDPP3T:PCBM based Triple-Junction

Calculated thickness dependence of  $J_{SC}$  for each sub-cell in the PMDPP3T:PCBM based TJ.

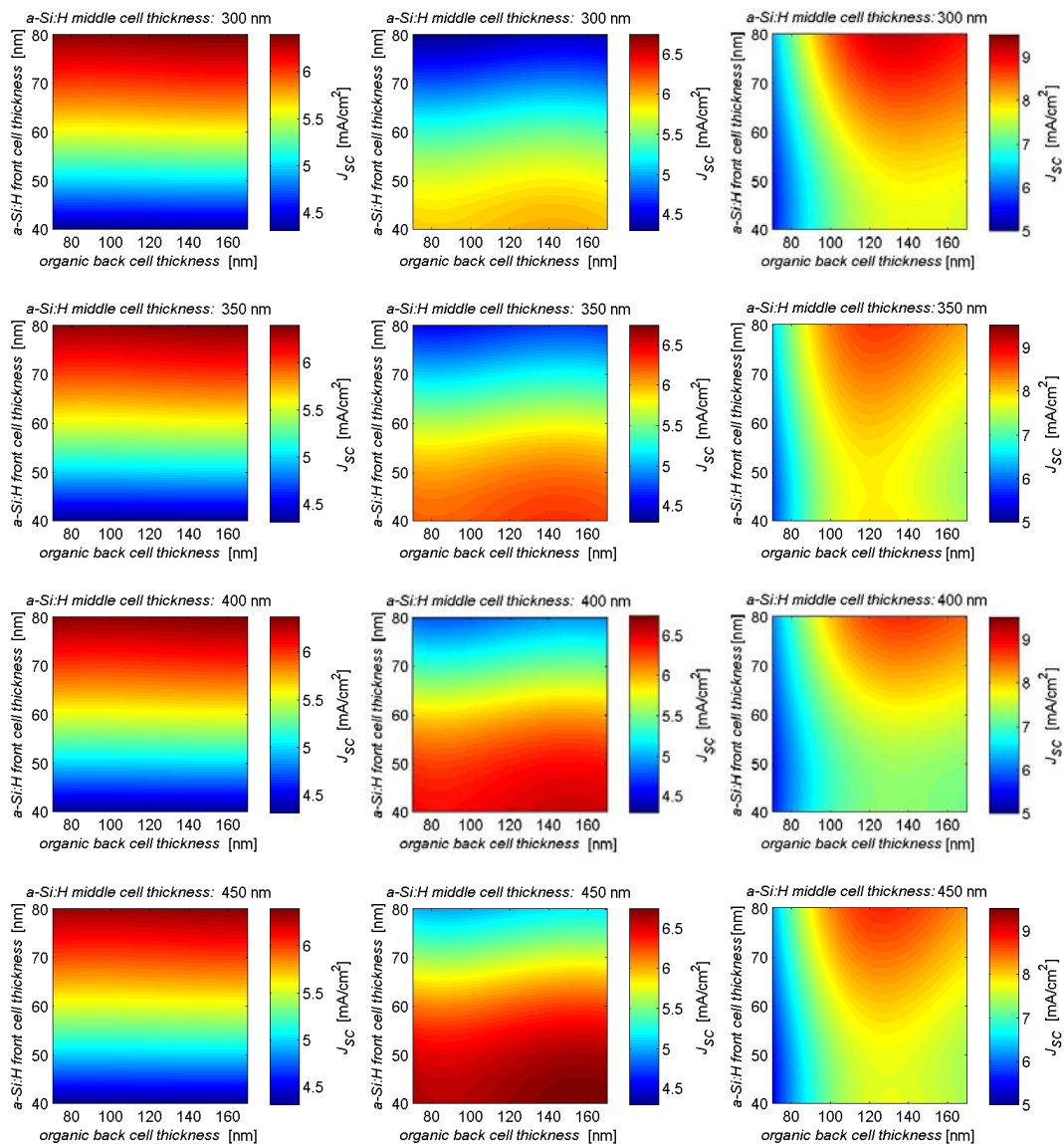


**Figure B.1.:** Contour plots showing  $J_{SC}$  in dependence of the a-Si:H front- and organic back cell thickness for four fixed a-Si:H middle cell thicknesses (rows). The three columns show the expected  $J_{SC}$  of all three sub-cells. First column for the a-Si:H front cell. Second column the a-Si:H middle cell. Third column the organic back cell.

### B.3. Contour Plots of Si-PCPDTBT:PCBM based Triple-Junctions

Calculated thickness dependence of  $J_{SC}$  for each sub-cell in the Si-PCPDTBT:PCBM based TJ.

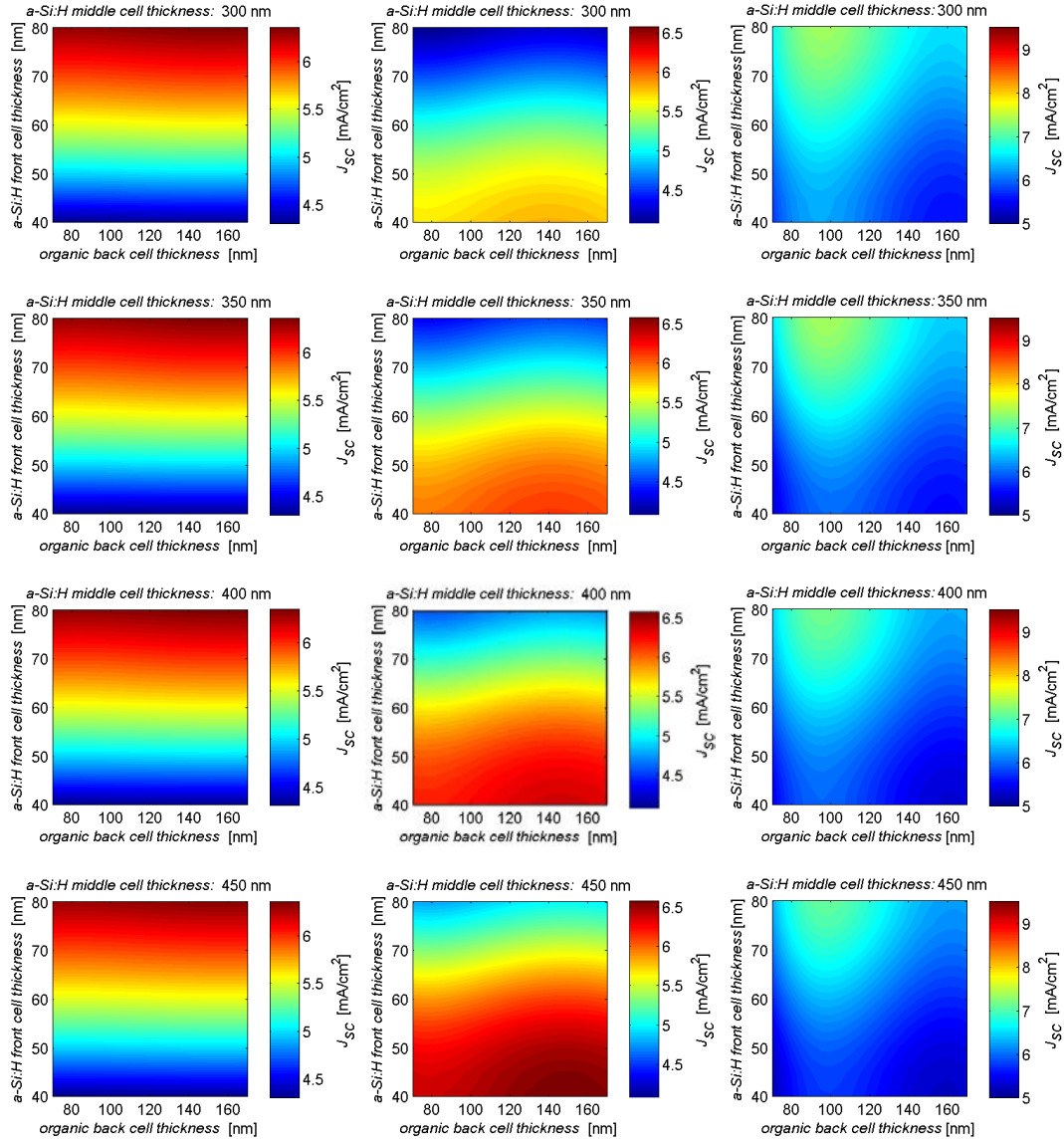


**Figure B.2.:** Contour plots showing  $J_{SC}$  in dependence of the a-Si:H front- and organic back cell thickness for four fixed a-Si:H middle cell thicknesses (rows). The three columns show the expected  $J_{SC}$  of all three sub-cells. First column for the a-Si:H front cell. Second column the a-Si:H middle cell. Third column the organic back cell.

### B.4. SEM pictures of flat or rough a-Si:H tandem

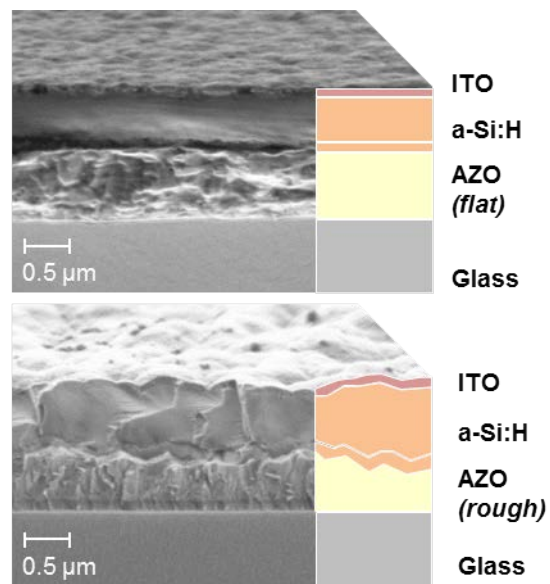


**Figure B.3.:** a) SEM picture of the a-Si:H tandem cell with either a flat or a rough front AZO.

# Appendix C

## Appendix Chapter 6

### C.1. Molecular Orientation of p-SIDT(FBTTh<sub>2</sub>)<sub>2</sub> Films

Analysis of the GIWAXS data in order to quantify the ratio of face- vs. edge-on oriented molecules in the film. The anisotropy of the  $\pi$ -stacking peak is evaluated as a function of the angle  $\chi$  as denoted in Figure C.1. The intensities have been corrected for sensitivity differences between out of plane and in plane scattering.[126].

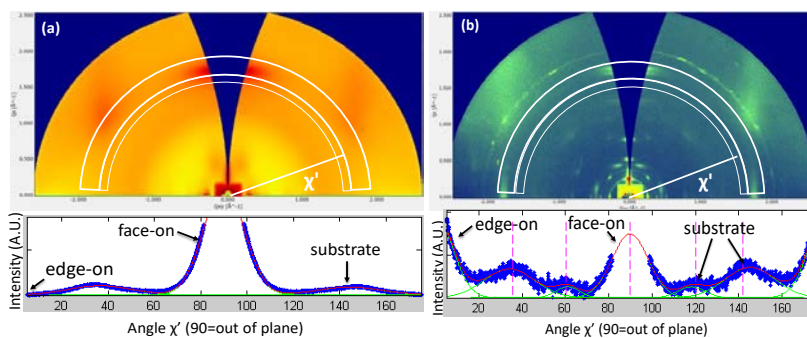


**Figure C.1.:** a) GIWAXS of p-SIDT(FBTTh<sub>2</sub>)<sub>2</sub> cast from chlorobenzene. b) GIWAXS of p-SIDT(FBTTh<sub>2</sub>)<sub>2</sub> cast from chlorobenzene with 0.4% v/v solvent additive DIO.

## C.2. Interfacial Mixing of $C_{60}$ into edge-or face-on oriented p-SIDT(FBTTh<sub>2</sub>)<sub>2</sub> layers

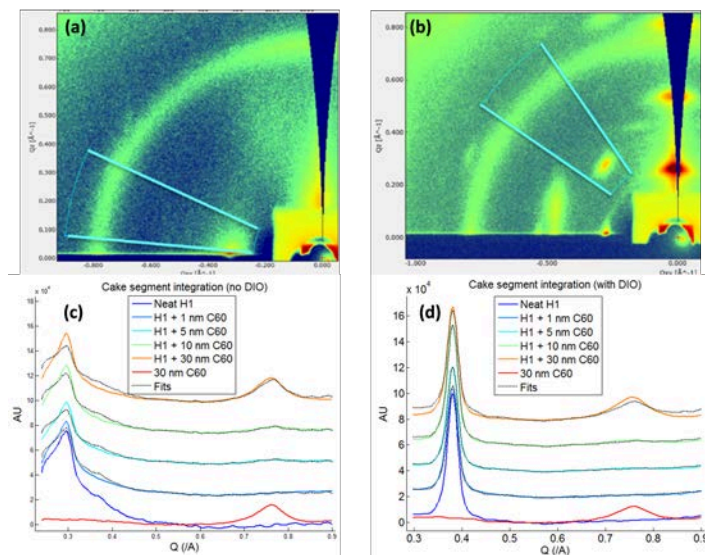


**Figure C.2.:** Interfacial mixing of  $C_{60}$  into either the face-on (a,c) or edge-on (b,d) oriented p-SIDT(FBTTh<sub>2</sub>)<sub>2</sub> layer. The cake slices in a) and b) show where the p-SIDT(FBTTh<sub>2</sub>)<sub>2</sub> and  $C_{60}$  signals were compared by integrating the intensity of the corresponding scattering peaks. In c) and d) signals are plotted for different  $C_{60}$  thicknesses as a function of  $q$ . Integration of these cross sections yields the data shown in Figure 6.2

## C.3. Pinholes in the neat Edge-On oriented p-SIDT(FBTTh<sub>2</sub>)<sub>2</sub> Layer

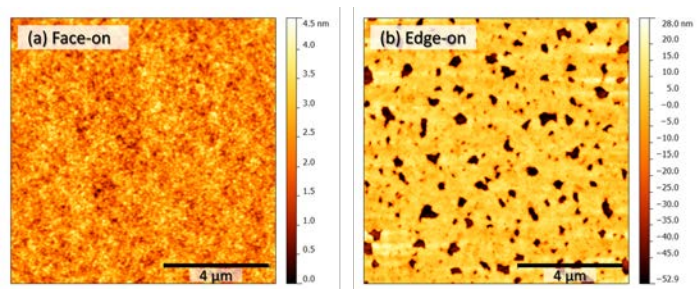


**Figure C.3.:** Atomic Force Microscope (AFM) pictures of neat face-on (a) or edge-on (b) p-SIDT(FBTTh<sub>2</sub>)<sub>2</sub> films.

## C.4. *JV*-Characteristics of the Bilayer Devices at UCSB and UP

Bilayer devices comprising of p-SIDT(FBTTh<sub>2</sub>)<sub>2</sub> and C<sub>60</sub> were build and characterized at UCSB and UP. The device performance of the devices shipped to Potsdam showed slightly increased  $V_{OC}$  values especially for the edge-on devices. This can be reasoned with less edge-on orientation of p-SIDT(FBTTh<sub>2</sub>)<sub>2</sub> with respect to C<sub>60</sub> speculating that with time the less stable edge-on configuration gets distorted at the interface and the fraction of face-on oriented p-SIDT(FBTTh<sub>2</sub>)<sub>2</sub> to C<sub>60</sub> molecules increases. This has an immediate effect on the non-radiative loss that is decreasing in the face-on orientation and subsequently a higher  $V_{OC}$  is measured at UP. All in all, the total performance values are comparable and especially the  $V_{OC}$  values measured for the different cells at UP are similar. In Figure C.4 (left) the *JV*-curves for three different edge- and face-on devices, each averaged over six pixels, are shown. The pink and cyan lines in Figure C.4 (left) show the averaged *JV*-curves measured at UCSB. In Table C.1 the mean performance values are shown; the higher current densities measured at UP are partially due to different pixel sizes with 4 small (1 mm<sup>2</sup>) and 2 big (16 mm<sup>2</sup>) pixels on each device. The big pixels have lower currents compared to the small ones, which is related to edge effects as no aperture was used for the measurements. In Figure C.4 (right) the performance of edge- and face-on cells prepared on a MoO<sub>3</sub> electrode are shown. The preparation and measurements were conducted by Niva Ran at UCSB.

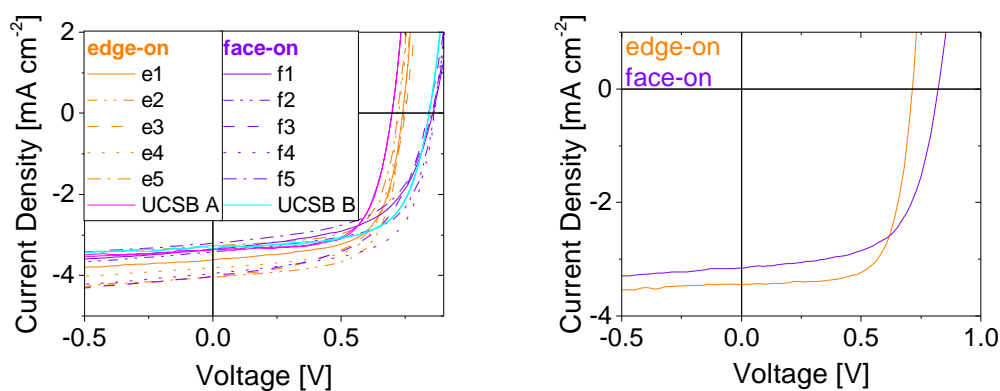


**Figure C.4.:** left: *JV*-curves of three devices each averaged over six pixels as measured at UP. In pink and cyan the averaged *JV*-curves, as measured at UCSB are shown for comparison. right: Averaged *JV*-curves of edge- and face-on devices prepared on a Molybdenum Oxide (MoO<sub>3</sub>) electrode. Measurements by Niva Ran at UCSB.

**Table C.1.:** Bilayer performance averages of three devices measured at UP and the averaged values for devices prepared and measured at UCSB

University	Orientation	Device	$J_{SC}$ [mA cm <sup>-2</sup> ]	$V_{OC}$ [V]	FF [%]
UCSB	edge-on	A	$-3.03 \pm 0.4$	$0.69 \pm 0.04$	$68 \pm 3$
	face-on	B	$-2.97 \pm 0.3$	$0.84 \pm 0.03$	$66 \pm 5$
UP	edge-on	R1	$-3.6 \pm 0.2$	$0.741 \pm 0.004$	$65 \pm 2$
		R3	$-3.5 \pm 0.1$	$0.746 \pm 0.004$	$65 \pm 1$
		R5	$-3.8 \pm 0.1$	$0.725 \pm 0.004$	$67 \pm 1$
		R7	$-3.3 \pm 0.1$	$0.720 \pm 0.006$	$67 \pm 1$
		N3	$-4.0 \pm 0.2$	$0.749 \pm 0.002$	$59 \pm 2$
	face-on	R2	$-3.4 \pm 0.2$	$0.856 \pm 0.008$	$57 \pm 1$
		R4	$-4.0 \pm 0.2$	$0.867 \pm 0.003$	$62 \pm 1$
		R6	$-4.0 \pm 0.3$	$0.865 \pm 0.005$	$62 \pm 3$
		R8	$-3.8 \pm 0.1$	$0.863 \pm 0.006$	$67 \pm 9$
		N4	$-4.0 \pm 0.4$	$0.840 \pm 0.006$	$55 \pm 1$

## C.5. UPS measurements of Edge- or Face-On oriented Films of p-SIDT(FBTTh<sub>2</sub>)<sub>2</sub>.

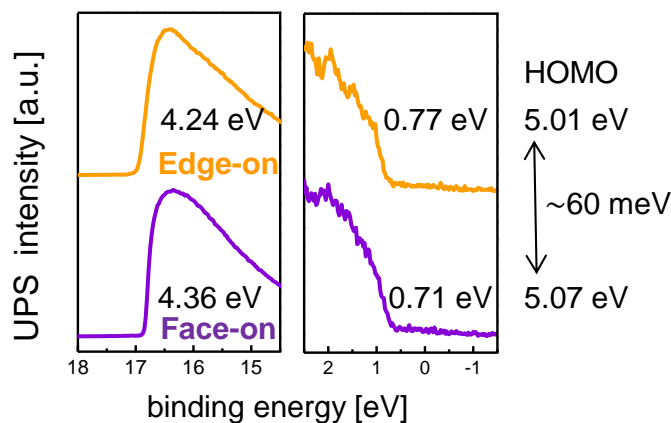


**Figure C.5.:** UPS data of edge- or face-on oriented p-SIDT(FBTTh<sub>2</sub>)<sub>2</sub>.

## C.6. Field dependence of Charge Carrier Generation of the Bilayer Systems

To measure the effect of the electric field on the free charge carrier generation TDCF experiments with 600 nm laser excitation were conducted and the free charges formed were extracted 10 ns after excitation by a sufficiently high ( $-3$  V) voltage pulse. The solar cells were kept at a certain pre bias while excitation for different electric field conditions. The extracted charges are shown in Figure C.7 a) as a function of applied pre bias. The field dependence is similar for both bilayers and overall weak. To further examine the effect of the applied field on the generation of charges and extractable photocurrent,  $EQE_{PV}$  measurements were conducted for different applied voltages. According to Equation 2.4 the short circuit current density can be obtained from the sun spectrum and the measured  $EQE_{PV}$ . By applying different voltages while measuring the  $EQE_{PV}$  the  $JV$ -characteristics can be remodeled. This has been done with the help of the  $EQE_{PV}$  spectra for the edge- and face-on devices shown in Figure C.6 a) and b) and the integrated current densities according to Equation 2.4 are shown in Figure C.7 b). The spectra have been separated into two parts for wavelengths above and below 500 nm. This was done to account for the current generated by excitons primarily generated in the p-SIDT(FBTTh<sub>2</sub>)<sub>2</sub> donor or the C<sub>60</sub> acceptor. The separately integrated current densities are depicted in Figure C.7 b) as well. The stronger field dependence is visible here for primarily exciting the C<sub>60</sub> indicating that the weak field dependence of charge carrier generation is likely to be caused by splitting excitons in the pure acceptor phase of the bilayer. This effect is again similar for both bilayer systems. This is expected as the C<sub>60</sub> layer is the same

for both molecular orientations of p-SIDT(FBTTh<sub>2</sub>)<sub>2</sub>.

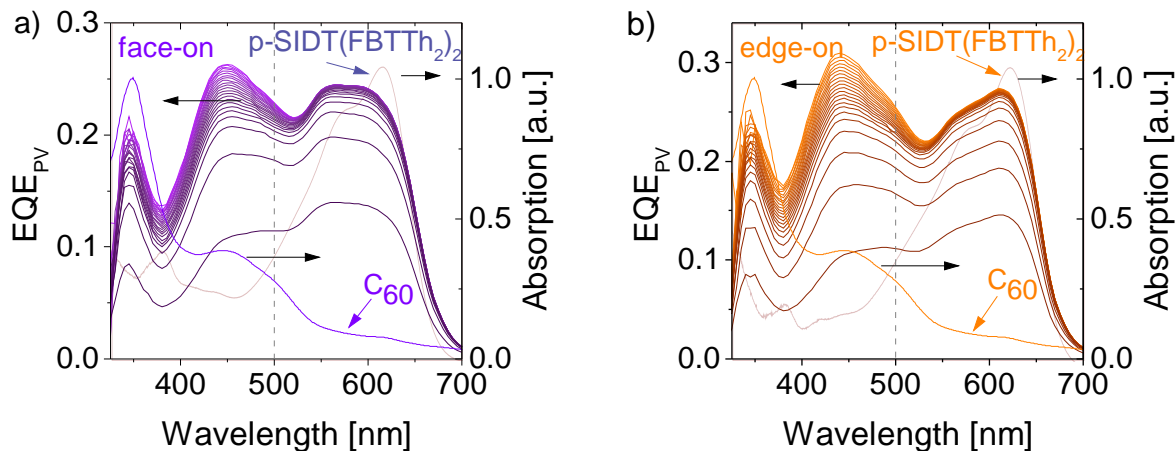


**Figure C.6.:** Voltage dependent  $EQE_{PV}$  data of a) the face-on and b) the edge-on oriented bilayer solar cells. Additionally the absorption spectra of pure p-SIDT(FBTTh<sub>2</sub>)<sub>2</sub> and pure C<sub>60</sub> films are shown to indicate which parts of the  $EQE_{PV}$  are dominated by which molecules.

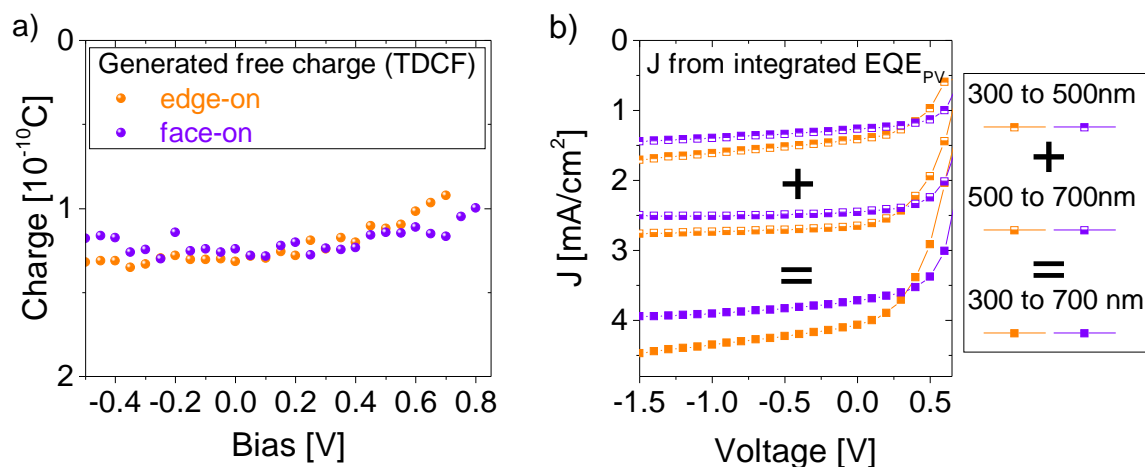


**Figure C.7.:** a) Extracted charges from TDCF measurements. Excitation with 600 nm laser pulses at different pre voltages. Extraction after a short delay time of 10 ns with a -3V extraction voltage. b)  $JV$ -curves from integrated  $EQE_{PV}$  spectra. The  $EQE_{PV}$  is partially integrated from 300-500 nm and from 500-700 nm.

## C.7. Electroluminescence and Photovoltaic External Quantum Efficiency Spectra

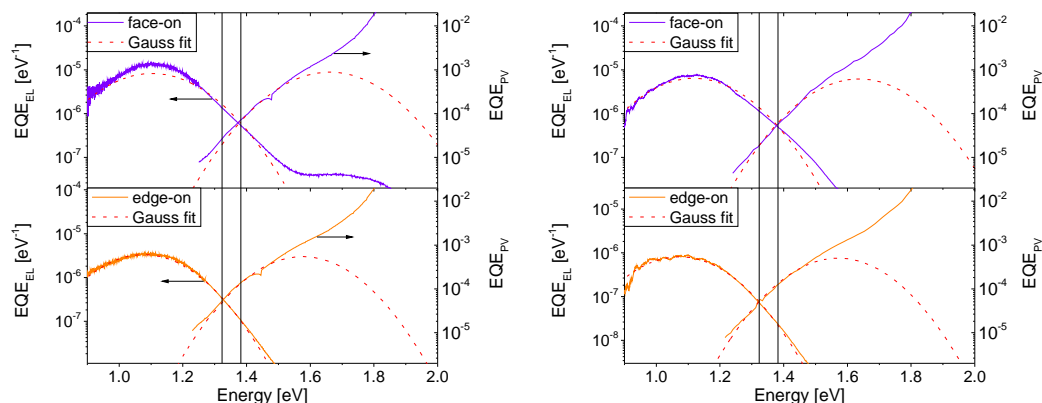


**Figure C.8.:** left: Photovoltaic and electroluminescence external quantum efficiency spectra of the edge- and face-on oriented bilayer systems (e1 and f1, respectively). The red dashed lines denote the Gaussian fits to the data according to Equation 3.9 and Equation 3.10. right: Photovoltaic and electroluminescence external quantum efficiency spectra of the edge- and face-on oriented bilayer systems (e2 and f2, respectively). The red dashed lines denote the Gaussian fits to the data according to Equation 3.9 and Equation 3.10.

## C.8. CT-Emission of FTAZ:PCBM Solar Cells in Dependence of the Active Layer Thickness

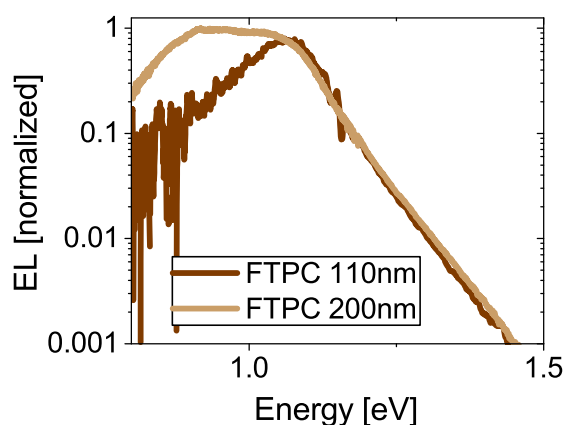


**Figure C.9.:** Electroluminescence spectra of  $\sim 100$  and  $\sim 200$  nm thick FTAZ:PCBM Devices.

## C.9. Transmission Electron Microscopy of the 50% Blends

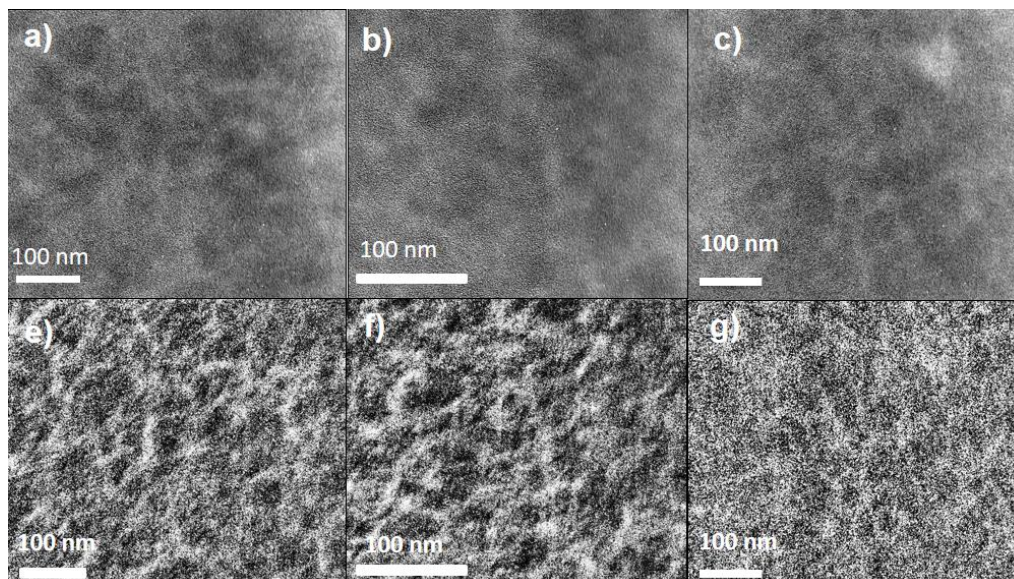


**Figure C.10.:** Transmission electron microscopy pictures of the 50% blends with layer thicknesses of  $\sim 200$  nm. a)-c) show bright field images and e)-g) show sulfur maps of either H:F 1:1 a),e) or monoF b),f) or F50 c),g).

## C.10. Photoluminescence measurements of pure FTAZ or FTPC or FTIC blends

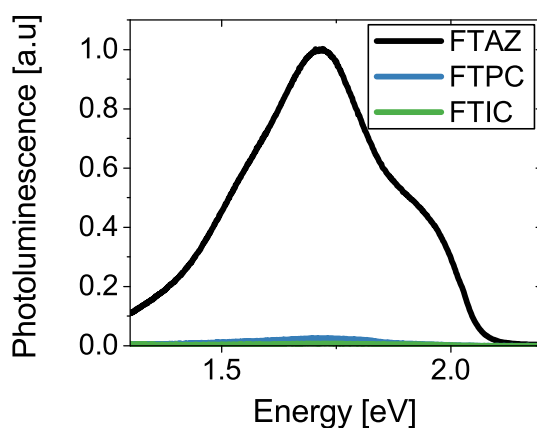


**Figure C.11.:** Photoluminescence spectra of  $\sim 200$  nm thick layers of either pure FTAZ or blend films of FTAZ:PCBM or FTAZ:ICBA

### C.11. SCLC measurements of FTPC and FTIC devices at UNC

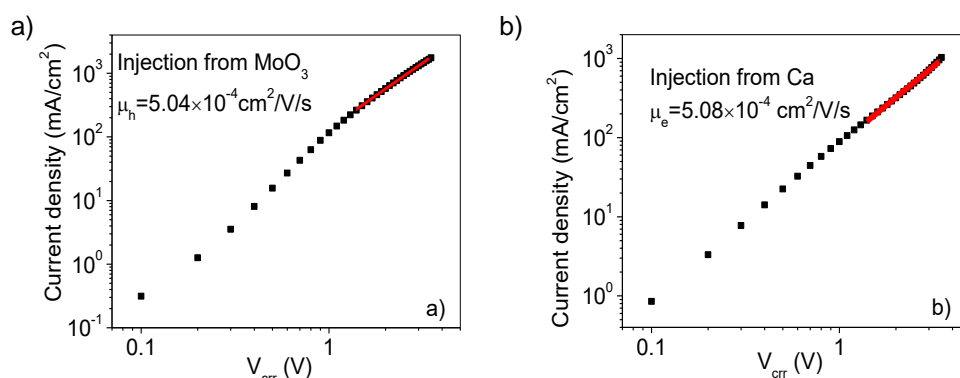


**Figure C.12.:** Space Charge Limited Currents for a) FTPC hole only devices and b) FTPC electron only devices measured at UNC

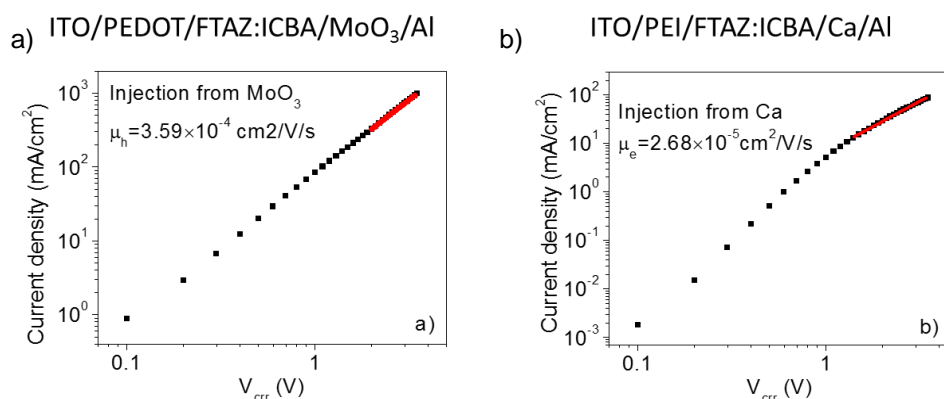


**Figure C.13.:** Space Charge Limited Currents for a) FTIC hole only devices and b) FTIC electron only devices measured at UNC

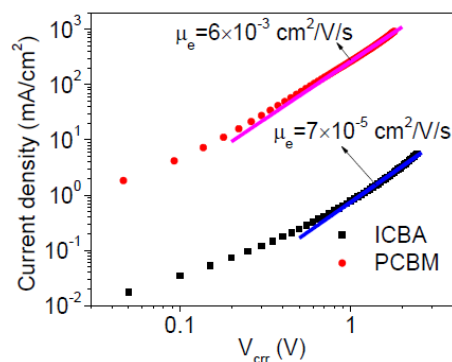


**Figure C.14.:** Space Charge Limited Currents for ICBA and PCBM measured at UNC

# Appendix D

## Appendix Chapter 7

### D.1. Gaussian Fits of the External Quantum Efficiency Spectra of the PMDPP3T:PCBM Solar Cell

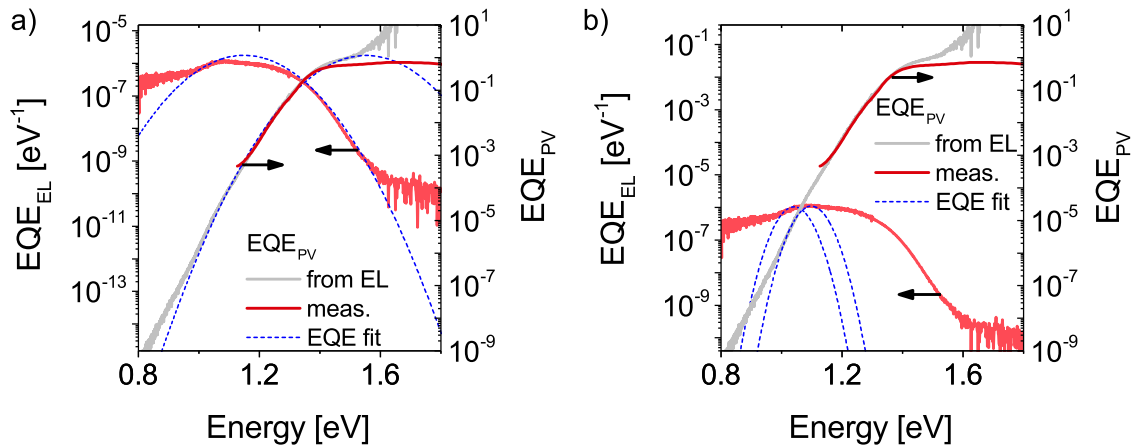


**Figure D.1.:** Gaussian fits to the  $EQE_{EL}$  and  $EQE_{PV}$  with respect to a) the broad emission shoulder at  $\sim 1.3$  eV or b) the emission peaking at  $\sim 1.07$  eV.

### D.2. Uncertainty in the Determination of the Absolute $EQE_{EL}$

The determination of the absolute values of the  $EQE_{EL}$  depends on the separate measurements of the emission spectrum and the determination of the emitted photons at the same current injection conditions as outlined in section A.1. The measured spectra at those injection conditions are normalized and scaled according to the number of emitted photons.

At low injection currents however the emission spectra are more noisy and the normalization causes some error. This error was not determined in detail but deviations of 20 mV in the non-radiative loss especially for injection conditions below  $V_{OC}$  are likely to be caused by this determination uncertainty. The value at injection conditions close to  $V_{OC}$  is already less influenced by the measurement noise and is set as the non-radiative voltage loss.

### D.3. Differentially Determined Light Ideality Factor for the PMDPP3T:PCBM Solar Cell

The differentially determined ideality factor gives a rough estimate of when surface recombination becomes severe. When the ideality factor is smaller than one, surface recombination is present.[145] The scattering of the differentially determined ideality factor data is quite strong and the onset of surface recombination is estimated as the voltage where the respective ideality factors are at least 10 % below one. The onset is estimated to be at  $\sim 0.65$  V,  $\sim 0.70$  V and  $\sim 0.75$  V for the 300 K, 250 K and 200 K measurement, respectively.

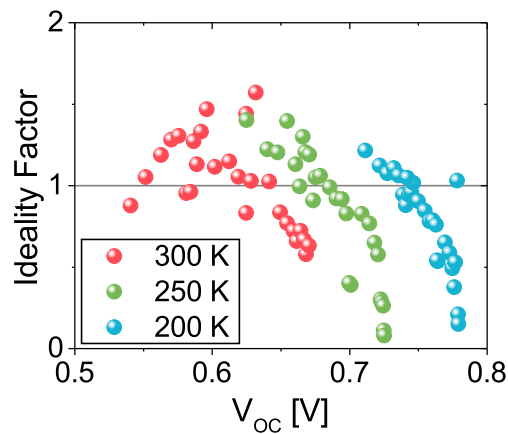


**Figure D.2.:** Differentially determined ideality factor for the PMDPP3T:PCBM solar cell measured at 300 K, 250 K and 200 K.

## D.4. Derivation of the Trapped Charge Carrier Density Concentration in the Case of either Electron or Hole Traps

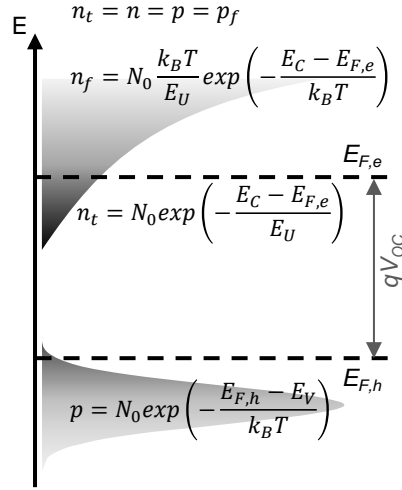


**Figure D.3.:** Initial situation of the Exp-Gauß model

Derivation of the charge carrier density of exponentially trapped electrons in dependence of the *open circuit voltage* according to Professor Neher. The derivation for trapped holes can be done accordingly and will not be shown in detail. The tail slope energy is depicted as  $E_U = k_B T_0$ , the open circuit voltage can be expressed as  $V_{OC} = E_{F,e} - E_{F,h}$  and the gap energy  $E_G = E_C - E_V$  is expressed by the difference between conduction ( $E_C$ ) and valence ( $E_V$ ) band energies. From the charge carrier densities as defined in Figure D.3 the following equation can be derived:

$$\begin{aligned}
 n = p &\Rightarrow & p_f = n_t \\
 &\Rightarrow & N_0 \exp\left(-\frac{E_{F,h} - E_V}{k_B T}\right) = N_0 \exp\left(-\frac{E_C - E_{F,e}}{k_B T_0}\right) & | E_{F,e} = E_{F,h} + qV_{OC} \\
 &\Rightarrow & \frac{E_{F,h}}{T} - \frac{E_V}{T} = \frac{E_C}{T_0} - \frac{E_{F,h}}{T_0} - \frac{qV_{OC}}{T_0} & | + \frac{E_V}{T} + \frac{E_{F,h}}{T_0} \\
 &\Rightarrow & E_{F,h} \left(\frac{1}{T} + \frac{1}{T_0}\right) = \frac{E_C}{T_0} + \frac{E_V}{T} - \frac{qV_{OC}}{T_0} & | \cdot \frac{T_0}{T_0 + T} \\
 &\Rightarrow & \frac{E_{F,h}}{T} = \frac{E_C}{T_0 + T} + \frac{E_V T_0}{T(T_0 + T)} - \frac{qV_{OC}}{T_0 + T}.
 \end{aligned}$$

With this expression for  $\frac{E_{F,h}}{T}$  the hole charge carrier density  $p$ , which equals  $n_t = n = p_f$  per definition in this case, can be written as:

$$\begin{aligned}
 p &= N_0 \exp\left(-\frac{E_{F,h} - E_V}{k_B T}\right) \\
 &= N_0 \exp\left(-\frac{E_C}{k_B(T_0 + T)} - \frac{E_V T_0}{k_B T(T_0 + T)} + \frac{qV_{OC}}{k_B(T_0 + T)} + \frac{E_V}{k_B T}\right) \\
 &= N_0 \exp\left(-\frac{E_C}{k_B(T_0 + T)} + \frac{E_V(T_0 + T - T_0)}{k_B T(T_0 + T)} + \frac{qV_{OC}}{k_B(T_0 + T)}\right) \\
 &= N_0 \exp\left(-\frac{E_C}{k_B(T_0 + T)} + \frac{E_V}{k_B(T_0 + T)} + \frac{qV_{OC}}{k_B(T_0 + T)}\right) \\
 &= N_0 \exp\left(-\frac{E_G}{k_B(T_0 + T)}\right) \exp\left(\frac{qV_{OC}}{k_B(T_0 + T)}\right)
 \end{aligned}$$

This defines  $\zeta$  in the Exp-Gauß model and with  $n_f = N_0^{1-\alpha} \frac{k_B T}{E_U} \cdot n_t^{E_U/k_B T}$  the free charge carrier density can be determined as described in section 7.3.

# Publications and Conference Contributions

## Publications

- "Influence of Aggregation on the Performance of All-Polymer Solar Cells Containing Low-Bandgap Naphthalenediimide Copolymers "  
*Marcel Schubert, Daniel Dolfen, Johannes Frisch, Steffen Roland, Robert Styrleuthner, Burkhard Stiller, Zhihua Chen, Ullrich Scherf, Norbert Koch, Antonio Facchetti, and Dieter Neher, **Advanced Energy Materials**, 2, 369-380, (2012)*
- "Fullerene-Free Polymer Solar Cells with Highly Reduced Bimolecular Recombination and Field-Independent Charge Carrier Generation "  
*Steffen Roland, Marcel Schubert, Brian A. Collins, Jona Kurpiers, Zhihua Chen, Antonio Facchetti, Harald Ade, and Dieter Neher, **The Journal of Physical Chemistry Letters**, 5, 2815-2822, (2014)*
- "Correlated Donor/Acceptor Crystal Orientation Controls Photocurrent Generation in All-Polymer Solar Cells "  
*Marcel Schubert, Brian A. Collins, Hannah Mangold, Ian A. Howard, Wolfram Schindler, Koen Vandewal, Steffen Roland, Jan Behrends, Felix Kraffert, Robert Styrleuthner, Zhihua Chen, Konstantinos Fostiropoulos, Robert Bittl, Alberto Salleo, Antonio Facchetti, Frédéric Laquai, Harald W. Ade, and Dieter Neher, **Advanced Functional Materials**, 24, 4068–4081, (2014)*
- "Efficiency-Limiting Processes in Low-Bandgap Polymer:Perylene Diimide Photovoltaic Blends "  
*Dominik W. Gehrig, Steffen Roland, Ian A. Howard, Valentin Kamm, Hannah Mangold, Dieter Neher, and Frédéric Laquai, **The Journal of Physical Chemistry C**, 118, 20077-20085, (2014)*
- "Efficient hybrid inorganic/organic tandem solar cells with tailored recombination contacts "  
*Steve Albrecht, Bjorn Grootenk, Sebastian Neubert, Steffen Roland, Jan Wordenweber, Matthias Meier, Ruttger Schlatmann, Aad Gordijn, Dieter Neher, **Solar Energy Materials & Solar Cells**, 127, 157-162, (2014)*

- "Mobility-Controlled Performance of Thick Solar Cells Based on Fluorinated Copolymers"  
*Wentao Li, Steve Albrecht, Liqiang Yang, Steffen Roland, John R. Tumbleston, Terry McAfee, Liang Yan, Mary Allison Kelly, Harald Ade, Dieter Neher, and Wei You, **Journal of the American Chemical Society**, 136, 15566-15576, (2014)*
- "Competition between recombination and extraction of free charges determines the fill factor of organic solar cells "  
*Davide Bartesaghi, Irene del Carmen Pérez, Juliane Kniepert, Steffen Roland, Methieu Turbiez, Dieter Neher & L. Jan Anton Koster, **Nature Communications**, 6, 7083, (2015)*
- "Hybrid Organic/Inorganic Thin-Film Multijunction Solar Cells Exceeding 11% Power Conversion Efficiency "  
*Steffen Roland, Sebastian Neubert, Steve Albrecht, Bernd Stannowski, Mark Seger, Antonio Facchetti, Rutger Schlatmann, Bernd Rech, and Dieter Neher, **Advanced Materials**, 27, 1262-1267, (2015)*
- "Generation and mobility-limited performance of bulk heterojunction solar cells with a higher adduct fullerene"  
*Steffen Roland, Liang Yan, Qianqian Zhang, Xuechen Jiao, Harald Ade, Wei You, Dieter Neher, **in preparation for resubmission to Journal of Materials Chemistry C**(2017)*
- "Incorporating Fluorine Substitution into Conjugated Polymers for Solar Cells: Three Different Means, Same Result "  
*Mary Allison Kelly, Steffen Roland Qianqian Zhang, YOUNGMIN Lee, Bernd Kabius, Qing Wang, Enrique D. Gomez, Dieter Neher, Wei You, Accepted to **The Journal of Physical Chemistry C** (2017)*
- "Impact of Interfacial Molecular Orientation on Radiative Recombination and Charge Generation Efficiencies"  
*Niva A. Ran, Steffen Roland, John A. Love, Victoria Savikhin, Christopher J. Takacs, Yao-Tsung Fu, Hong Li, Veaceslav Coropceanu, Xiaofeng Liu, Jean-Luc Brédas, Guillermo C. Bazan, Michael F. Toney, Dieter Neher, Thuc-Quyen Nguyen, **ready for resubmission to Nature Energy** (2017)*

## Presentations

- Talk: "Reduced Recombination and Field Independent Charge Carrier Generation in Polymer-Polymer Solar Cells "  
*Steffen Roland et al.*, **DPG Spring Meeting 2013**, Regensburg, Germany
- Poster: "Reduced Recombination and Field Independent Charge Carrier Generation in Polymer-Polymer Solar Cells "  
*Steffen Roland et al.*, **SPP1355 Spring School 2013**, Dresden-Weinböhla, Germany
- Talk: "Reduced Recombination and Field Independent Charge Carrier Generation in Polymer-Polymer Solar Cells "  
*Steffen Roland et al.*, **Next Generation Organic Photovoltaics 2013**, Groningen, Netherlands
- Talk: "High Efficiency Hybrid Triple Junction Solar Cells Comprising of Amorphous Silicon and Low Band Gap Polymers "  
*Steffen Roland et al.*, **Hybrid and Organic Photovoltaics 2014**, Lausanne, Switzerland
- Talk: "High Efficiency Hybrid Triple Junction Solar Cells Comprising of Amorphous Silicon and Low Band Gap Polymers exceeding 11% Power Conversion Efficiency "  
*Steffen Roland et al.*, **DPG Spring Meeting 2015**, Berlin, Germany
- Talk: "High Efficiency Hybrid Triple Junction Solar Cells Comprising of Amorphous Silicon and Low Band Gap Polymers reaching 11% Power Conversion Efficiency "  
*Steffen Roland et al.*, **MRS Spring Meeting 2015**, San Francisco, USA
- Poster: "Effect of the Donor Orientation on the  $V_{OC}$  Losses in Small Molecule Organic Bilayer Solar Cells "  
*Steffen Roland et al.*, **DPG Spring Meeting 2016**, Regensburg, Germany
- Talk: "Role of Trapped and Free Charges on the Recombination in a Low Band-Gap Organic Solar Cell "  
*Steffen Roland et al.*, **submitted to DPG Spring Meeting 2017**, Dresden, Germany

# Danksagung

Zuallererst möchte ich mich ganz herzlich bei Prof. Dr. Dieter Neher bedanken. Du hast es mir ermöglicht, in einem sehr angenehmen Arbeitsumfeld und unter besten technischen Voraussetzungen zu forschen. Du hast meine Arbeit immer mit Interesse verfolgt, hast dir viel Zeit für Besprechungen genommen und immer neue Anreize geschaffen, den eigenen wissenschaftlichen Horizont zu erweitern.

Darüberhinaus gilt mein besonderer Dank Prof.Dr. Carsten Deibel und Prof.Dr. Elizabeth von Hauff, die sich bereit erklärt haben die Begutachtung dieser Arbeit zu übernehmen.

Des Weiteren möchte ich mich bei all meinen aktuellen und auch ehemaligen Kollegen in der Arbeitsgruppe *Physik weicher Materie* für eine tolle Arbeitsatmosphäre und die gute Stimmung bedanken. Insbesondere möchte ich an dieser Stelle Marcel erwähnen. Meine Arbeit als deine studentische Hilfskraft war mein Einstieg in die Welt der organischen Solarzellen. Unser guter Draht zueinander und der Spaß, den wir im Labor hatten, hat großen Anteil an meinem weiteren Werdegang. Steve danke ich für die gute Zusammenarbeit im Bereich der hybriden Mehrschicht solarzellen. Ich habe gerade zu Beginn meiner Arbeit viel von dir gelernt. Jona, unsere gemeinsame Zeit als Doktoranden und die gemeinsamen Konferenzen werde ich immer in positiver Erinnerung behalten, deine technische Versiertheit und Expertise haben viele Experimente in meiner Arbeit und in dieser Arbeitsgruppe im Allgemeinen überhaupt erst möglich gemacht – dafür gebührt dir ein besonderer Dank. Ein spezieller Dank gilt natürlich auch dir, Frank. Ich glaube, man darf zu Recht behaupten, dass du die gute Seele der Arbeitsgruppe *Physik weicher Materie* bist und für alle Probleme technischer, organisatorischer und auch bürokratischer Natur nicht nur ein offenes Ohr, sondern auch meistens eine Lösung parat hast. Ganz besonders möchte ich mich auch bei dir, Jack, bedanken. Du hast nicht nur diese Arbeit Korrektur gelesen, sondern warst auch immer an Diskussionen aller Art interessiert und hast somit, neben wissenschaftlicher Unterstützung, auch für gute Stimmung und Abwechslung gesorgt. Ein gesonderter Dank gilt auch euch Edgar, Malavika und Pietro für die gute Zusammenarbeit an diversen Projekten, dem gesamten technischen Personal, insbesondere Apu, unserer Sekretärin Elke und allen anderen, nicht namentlich genannten Kollegen. Es war eine schöne Zeit mit euch.

Außerdem möchte ich mich auch bei den vielen Menschen bedanken, die auf die eine oder andere Weise am Gelingen dieser Arbeit beteiligt waren. Zunächst möchte ich die zahlreichen Projektpartner erwähnen, ohne die viele der Ergebnisse dieser Arbeit so nicht zustande

gekommen wären. Der wissenschaftliche Austausch und die gute Zusammenarbeit war mir stets eine Freude. Sebastian Neubert und Bernd Stannowski vom *pvComB* in Berlin danke ich für die amorphen Siliziumsolarzellen, die in den Mehrschicht solarzellen verbaut sind. Prof. Antonio Facchetti von der *Northwestern University* möchte ich für das donor Polymer PMDPP3T danken. Niva Ran aus der Arbeitsgruppe von Prof. Thuc-Quyen Nguyen von der *University of California Santa Barbara* danke ich für die Bilayer Solarzellen. Liang Yan, Allison Kelly, Liqiang Yan und Prof. Wei You von der *University of North Carolina at Chapel Hill* danke ich für die enge Zusammenarbeit und die fluorinierten Solarzellensysteme.

Trotz all der Unterstützung von Kollegen und Projektpartnern würde diese Arbeit ohne den Rückhalt meiner Familie und Freunde und besonders dir, Vanessa, so wohl nicht existieren.

# Eigenständigkeitserklärung

Hiermit erkläre ich, dass ich diese Arbeit selbstständig verfasst habe, keine anderen als die angegebenen Hilfsmittel benutzt habe und die in dieser Arbeit präsentierten Ergebnisse bei keiner anderen Universität eingereicht wurden.

Berlin, den 24.02.2017

Steffen Roland